



Abdul Shakoor  
Kerry Cato *Editors*

# IAEG/AEG Annual Meeting Proceedings, San Francisco, California, 2018—

## Volume 4

Dams, Tunnels, Groundwater Resources,  
Climate Change



 Springer

---

IAEG/AEG Annual Meeting Proceedings,  
San Francisco, California, 2018—Volume 4

---

Abdul Shakoor • Kerry Cato  
Editors

# IAEG/AEG Annual Meeting Proceedings, San Francisco, California, 2018—Volume 4

Dams, Tunnels, Groundwater Resources,  
Climate Change



 Springer

*Editors*

Abdul Shakoor  
Department of Geology  
Kent State University  
Kent, OH, USA

Kerry Cato  
Department of Geological Sciences  
California State University  
San Bernardino, CA, USA

ISBN 978-3-319-93132-6      ISBN 978-3-319-93133-3 (eBook)  
<https://doi.org/10.1007/978-3-319-93133-3>

Library of Congress Control Number: 2018947486

© Springer Nature Switzerland AG 2019

This work is subject to copyright. All rights are reserved by the Publisher, whether the whole or part of the material is concerned, specifically the rights of translation, reprinting, reuse of illustrations, recitation, broadcasting, reproduction on microfilms or in any other physical way, and transmission or information storage and retrieval, electronic adaptation, computer software, or by similar or dissimilar methodology now known or hereafter developed.

The use of general descriptive names, registered names, trademarks, service marks, etc. in this publication does not imply, even in the absence of a specific statement, that such names are exempt from the relevant protective laws and regulations and therefore free for general use.

The publisher, the authors and the editors are safe to assume that the advice and information in this book are believed to be true and accurate at the date of publication. Neither the publisher nor the authors or the editors give a warranty, express or implied, with respect to the material contained herein or for any errors or omissions that may have been made. The publisher remains neutral with regard to jurisdictional claims in published maps and institutional affiliations.

Cover illustration: Golden Gate Bridge at night. Frederic Prochasson © 123rf.com

This Springer imprint is published by the registered company Springer Nature Switzerland AG  
The registered company address is: Gewerbestrasse 11, 6330 Cham, Switzerland

---

## Preface

The XIII IAEG Congress and 61st AEG Annual Meeting, San Francisco, USA, chose *Engineering Geology for a Sustainable World* as the theme for 2018. Based on the topical symposia and technical sessions, the proceedings are organized into six volumes and sub-categories as follows:

Volume 1: Slope Stability: Case Histories, Landslide Mapping, Emerging Technologies

Volume 2: Geotechnical and Environmental Site Characterization

Volume 3: Mining, Aggregates, Karst

Volume 4: Dams, Tunnels, Groundwater Resources, Climate Change

Volume 5: Geologic Hazards: Earthquakes, Land Subsidence, Coastal Hazards, and  
Emergency Response

Volume 6: Advances in Engineering Geology: Education, Soil and Rock Properties, Modeling

Participants of this joint meeting had the option to submit either a full paper or only an abstract. The editors would like to thank the authors for their valuable contributions. One hundred eighty-six full papers were submitted for review, and 153 papers successfully completed the process. Each paper submitted for the proceedings was peer-reviewed by two reviewers. Authors revised their papers in accordance with reviewers' comments. The reviewers, from across the globe, included professional experts as well as authors of other papers. The editors greatly appreciate the help provided by reviewers. A list of reviewers follows.

The editors are also very grateful to Karen Smith and Paisley Cato for their assistance throughout the review process.

Kent, OH, USA  
San Bernardino, CA, USA  
2018

Abdul Shakoor  
Kerry Cato

---

# Organization

## **General Meeting Chairs**

Sarah Kalika, Cornerstone Earth Group  
Gary Luce, Resource Concepts, Inc.  
Coralie Wilhite, United States Army Corps of Engineers

## **Field Course Chairs**

Chase White, California Geological Survey  
Drew Kennedy, Sage Engineers

## **IAEG Planning Committee Heads**

Scott Burns, Portland State University  
Jeffrey R. Keaton, Wood

## **Proceedings Editors**

Abdul Shakoor, Kent State University  
Kerry Cato, Cato Geoscience, Inc./California State University, San Bernardino

## **Editorial Assistants**

Karen Smith, Kent State University  
Paisley Cato, Cato Geoscience, Inc.

## **Short Course Chairs**

E. Morley Beckman, Kleinfelder  
Byron Anderson, Kleinfelder  
Chrissey Villeneuve, Shannon & Wilson, Inc.

## **Technical Program Committee**

Abdul Shakoor, Kent State University  
Kerry Cato, Cato Geoscience, Inc./California State University, San Bernardino  
William Godwin, Consulting Geologist  
Sarah Kalika, Cornerstone Earth Group

## **Symposium Chairs**

Robert E. Tepel, Retired Professional Geologist and Certified Engineering Geologist  
Brian H. Greene, United States Army Corps of Engineers  
Donald Bruce, Geosystems, L.P.  
Holly Nichols, California Department of Water Resources  
Keith Turner, Colorado School of Mines  
Fred Baynes, Consulting Engineering Geologist  
Kevin McCoy, Colorado Geological Survey

Hilary Whitney, Environmental Resources Management  
Michelle Sneed, United States Geological Survey  
Thomas Oommen, Michigan Technological University  
Julien Waeber, AECOM  
Ed Medley, Consulting Geological Engineer  
Mark Bailey, Asbestos TEM Labs  
Atiye Tugrul, Istanbul University, Avcilar Campus, Turkey  
Lindsay Swain, Dudek  
Ike Isaacson, Brierley Associates  
Mike Piepenburg, Aldea Services, LLC  
Bruce Hilton, Kleinfelder  
Anne Rosinski, California Geological Survey  
Steve Parry, Parry Engineering Geological Services  
Jan Novotny, Ceska Geologicka Sluzba, Czech Republic  
Xiaolei Liu, Shandong Provincial Key Laboratory of Marine Environment and Geological Engineering (Ocean University of China), China

### **Field Course Leaders and Contributors**

William Godwin, Consulting Geologist  
William McCormick, Kleinfelder  
Bradley Erskine, Kleinfelder  
Marina Mascorro, Langan  
Frank Rollo, Rollo & Ridley  
John Egan, Sage Engineers  
Ken Johnson, WSP  
John Wallace, Cotton, Shires and Associates, Inc.  
Ryan Seelbach, Geosyntec  
Tom Barry, California Department of Conservation, Division of Oil, Gas and Geothermal Resources  
John Wakabayashi, Fresno State University  
Greg Stock, Yosemite National Park  
Janet Sowers, Fugro  
Jim Lienkaemper, United States Geological Survey  
Keith Kelson, United States Army Corps of Engineers  
Carol Prentice, United States Geological Survey  
Gordon Seitz, California Department of Conservation  
Chris Madugo, Pacific Gas & Electric Company  
Mike Jewett, Miller Pacific Engineers  
Ray Sullivan, San Francisco State University  
George Ford, Geosyntec  
Wayne Akiyama, APTIM  
Ryan Coe, Terracon  
Kate Zeiger, AECOM  
John Murphy, California State Water Resources Control Board  
Jennifer Gomez, Syar Industries  
Mike George, BGC Engineering  
Nick Sitar, University of California, Berkeley  
Peter Holland, California Geological Survey  
Chris Hundemer, C2earth  
Jake Hudson, Holdrege & Kull/NV5  
Shane Cummings, Holdrege & Kull/NV5  
Chris Hitchcock, InfraTerra  
Roxanne Renedo, BSK Associates  
Tim Dawson, California Department of Conservation

Margaret Doolittle, Kleinfelder  
Kevin Clahan, Lettis Consultants  
Donald Wells, AMEC/Foster Wheeler  
Jennifer Dean, California State Water Resources Control Board  
Felix Desperrier, Lettis Consultants  
Karen Grove, San Francisco State University

**Guest Tour Chairs**

Alice Tepel  
Linda Upp

**Publicity Committee**

Nathan Saraceno, DiGioia Gray & Associates  
Courtney Johnson, Sage Engineers  
Maggie Parks, ENGEO

**Sponsorship Chair**

Courtney Johnson, Sage Engineers

**Technical Session Editing**

Bill Yu, Case Western Reserve University

**Guidebook App**

Clayton Johnson, Golder Associates  
Nathan Saraceno, DiGioia Gray & Associates

**Fed IGS**

Jean-Louis Briaud, Texas A&M University

**K-12 Teacher Workshop**

Cynthia Pridmore, California Geological Survey

**Special Event**

E. Morley Beckman, Kleinfelder

**AEG Meeting Manager**

Heather Clark, Association of Environmental & Engineering Geologists

**AEG Headquarters**

AMR Management



---

## List of Reviewers

David Abbott, USA  
Biljana Abolmasov, Serbia  
Okechukwu Aghamelu, Nigeria  
M. Farooq Ahmed, Pakistan  
Paolo Allasia, Italy  
Priyanthi Amarasinghe, USA  
Sofia Anagnostopoulou, Greece  
Pedro Andrade, Portugal  
Luis Bacellar, Brazil  
Marco Baldo, Italy  
Elizabeth Beckman, USA  
Zbigniew Bednarczyk, Poland  
Eduardo Bergillos Navarro, Spain  
David Bieber, USA  
Candan BiLen, Turkey  
Andrée Blais-Stevens, Canada  
Peter Bobrowsky, Canada  
Nana Bolashvili, Georgia  
James Borchers, USA  
Anika Braun, Germany  
Stephanie Briggs, USA  
Luke Brouwers, United Arab Emirates  
Brian Bruckno, USA  
Matthias Brugger, Germany  
Fintan Buggy, Ireland  
Domenico Calcaterra, Italy  
Michael Carpenter, USA  
Kerry Cato, USA  
Andrea Cevasco, Italy  
Hannah Chapella, USA  
Xiaoli Chen, China  
Sibonakaliso Chiliza, South Africa  
Jeff Coe, USA  
Mike Collins, USA  
Brian Conway, USA  
Jasper Cook, UK  
Isabela Coutinho, Brazil  
John Cripps, UK  
Balázs Czinder, Hungary  
Ranjan Kumar Dahal, Nepal  
Jerome De Graff, USA  
Rachael Delaney, USA  
Artem Demenev, Russia

---

Diego Di Martire, Italy  
Matthys Dippenaar, South Africa  
Angelo Doglioni, Italy  
Anastasia Dorozhko, Russia  
Peter Ellecosta, Germany  
Selman Er, Turkey  
Olga Eremina, Russia  
Georg Erharter, Austria  
Moises Failache, Brazil  
Andrew Farrant, UK  
Zhen Feng, China  
Clark Fenton, New Zealand  
Maria Ferentinou, South Africa  
Kenneth Ferguson, USA  
Isabel Fernandes, Portugal  
Paz Fernandez, Spain  
Mohammad Feruj Alam, Bangladesh  
Phil Flentje, Australia  
Yannis Fourniadis, UK  
Edwin Friend, USA  
Irina Galitskaya, Russia  
George Gaprindashvili, Georgia  
George Gardner, USA  
Jesus Garrido Manrique, Spain  
Eldon Gath, USA  
Ben Gilson, UK  
Daniele Giordan, Italy  
William Godwin, USA  
Robert Goldsmith, Australia  
Dick Gray, USA  
Brian Greene, USA  
James Hamel, USA  
Hans-Balder-Havenith, Belgium  
Greg Hempen, USA  
Egerton Hingston, South Africa  
Peter Hudec, Canada  
Matthew Huebner, USA  
Maria Ingunza, Brazil  
Upali De Silva Jayawardena, Sri Lanka  
Filipe Jeremias, Portugal  
Brendon Jones, South Africa  
Frank Jordan, USA  
Kumud Raj Kafle, Nepal  
Sarah Kalika, USA  
Efstratios Karantanellis, Greece  
Ekaterina Karfidova, Russia  
Hamza Karrad, Algeria  
Heiko Käsling, Germany  
Brian Katz, USA  
Katerina Kavoura, Greece  
Andrey Kazeev, Russia  
Jeffrey Keaton, USA  
Klaus-Peterkeilig, Germany  
Alexey Kindler, Russia  
Matheus Klein Flach, Brazil

Aliko Kokkala, Greece  
Goh Thian Lai, Malaysia  
Hana Lee, Austria  
Nkopane Lefu, South Africa  
Leticia Lescano, Argentina  
Cheng Li, China  
Wenping Li, China  
Qian Liu, Austria  
José Lollo, Brazil  
Silvina Marfil, Argentina  
Vassilis Marinos, Greece  
Milos Marjanovic, Serbia  
Kristofer Marsch, Germany  
Pedro Martins, New Zealand  
Flora Menezes, Germany  
Amira Merchichi, Algeria  
Olga Meshcheriakova, Russia  
Stuart Millis, Hong Kong  
Omar Mimouni, Algeria  
Oleg Mironov, Russia  
Matthew Morris, USA  
Tim Mote, Australia  
Elena Mraz, Germany  
Marcos Musso, Uruguay  
Masashi Nakaya, Japan  
Arpita Nandi, USA  
Marivaldo Dos Nascimento, Brazil  
Monique Neves, Brazil  
Holly Nichols, USA  
Vanessa Noveletto, Brazil  
Takehiro Ohta, Japan  
Kazuhiro Onuma, Japan  
Thomas Oommen, USA  
Rolando Orense, New Zealand  
Ibrahim Oyediran, Nigeria  
George Papathanasiou, Greece  
Steve Parry, UK  
Darren Paul, Australia  
Osni Jose Pejon, Brazil  
Giacomo Pepe, Italy  
Regina Pläskén, Germany  
Lindsay Poluga, USA  
Joaquim Pombo, Portugal  
Martin Potten, Germany  
Constantin Prins, Germany  
Mário Quinta-Ferreira, Portugal  
Rute Ramos, Portugal  
Emanuele Raso, Italy  
Liana Rocha, Brazil  
Valéria Rodrigues, Brazil  
Michael Rucker, USA  
Nicholas Sabatakakis, Greece  
Rosanna Saindon, USA  
Mahin Salimi, Iran  
Ligia Sampaio, Brazil

---

Paul Santi, USA  
Regiane Sbroglia, Brazil  
David Scarpato, USA  
Malcolm Schaeffer, USA  
William Schulz, USA  
Jorge Sfragulla, Argentina  
Sachin Shah, USA  
Abdul Shakoor, USA  
Timothy Shevlin, USA  
Anna Shidlovskaya, Russia  
Roy Shlemon, USA  
Zachary Simpson, South Africa  
Alessandra Siqueira, Brazil  
Young-Suk Song, South Korea  
Georg Stockinger, Germany  
Alexander Strom, Russia  
Wanghua Sui, China  
Valentina Svalova, Russia  
Debora Targa, Brazil  
Ashley Tizzano, USA  
Ákos Török, Hungary  
Emil Tsereteli, Georgia  
Ryosuke Tsuruta, Japan  
Atiye Tugrul, Turkey  
Alan Keith Turner, USA  
Anatiliï Tushev, Ukraine  
Resat Ulusay, Turkey  
Isabella Magalhães Valadares, Brazil  
Lazaro Valezuquette, Brazil  
J. Louis Van Rooy, South Africa  
Ioannis Vazaïos, Canada  
Marlene Villeneuve, New Zealand  
Nicholas Vlachopoulos, Canada  
Yasuhiko Wakizaka, Japan  
Chester (Skip) Watts, USA  
Luke Weidner, USA  
Baoping Wen, China  
Charles Wilk, USA  
Stephen Wilkinson, UK  
John Williams, USA  
Louis Wong, Hong Kong  
Martin Woodard, USA  
Richard Wooten, USA  
Yang Yang, China  
Katherine Yates, New Zealand  
Julia Yeakley, USA  
Murat Yilmaz, Turkey  
Zelin Zhang, China

---

# Contents

## Part I Dams

<b>Microbial Activity Within the Earth Dam: Consequences and the Suppression Strategy</b> .....	3
Nikolay G. Maksimovich, Vadim T. Khmurchik, Artem D. Demenev, and Alexey M. Sedinin	
<b>Wave Modeling and Coastal Erosion in Upstream Dams</b> .....	9
A. G. Siqueira, M. F. M. Fiedler, E. A. Yassuda, and L. A. P. Sousa	
<b>Delft3D Morphological Modeling Downstream of Sergio Motta Reservoir Dam</b> .....	17
A. G. Siqueira, M. F. M. Fiedler, and E. A. Yassuda	
<b>Estimation of Continuity of a Fault Based on Composite Planar Fabric</b> .....	25
Yasuhiko Wakizaka, Atsushi Kajiyama, Hiroyuki Watatani, and Mutsuo Kozuma	
<b>Geologic Influences on Slope Stability and Foundation Design, Oroville Dam Spillway, California</b> .....	33
Stephanie Briggs, Matthew Huebner, Hans AbramsonWard, Justin Cox, Jennifer Dean, Bryan Dussell, Holly Nichols, Brad von Dessonneck, Coralie Wilhite, and Justin Zumbro	
<b>Microbial Changes of the Earth Dam Mechanical Properties and the Improvement of Them</b> .....	41
Artem D. Demenev, Nikolay G. Maksimovich, Vadim T. Khmurchik, and Aleksey M. Sedinin	

## Part II Tunnels

<b>Development of a System for Automatic Evaluation of the Geological Conditions of Tunnel Faces Using Artificial Intelligence and Application to a Construction Site</b> .....	49
Ryosuke Tsuruta, Shinji Utsuki, and Masashi Nakaya	
<b>Wear Phenomena in Tunnel Boring Machine (TBM) Hard Rock Drilling—Reasons and Consequences</b> .....	57
Peter Ellecosta, Heiko Käsling, and Kuroschi Thuro	

## Part III Groundwater Resources

<b>Diagenesis of the Upper Jurassic Carbonate Rocks Within Deep Geothermal Boreholes of the North Alpine Foreland Basin in Germany</b> .....	67
Elena Mraz, Markus Wolfgramm, Inga S. Moeck, and Kuroschi Thuro	

<b>Assessment of the Hydrogeological Windows Impact on Groundwater Contamination in Moscow</b> .....	75
Irina Galitskaya, Irina Pozdnyakova, Irina Kostikova, Oleg Mironov, and Leonid Toms	
<b>On the Differing Role of Contact Obstacles on Variably Saturated Flow in Vertical and Horizontal Fractures</b> .....	83
Brendon R. Jones, J. Louis Van Rooy, and Matthys A. Dippenaar	
<b>Experimental and Numerical Study of the Groundwater Quality in Altered Volcanic Rock Area</b> .....	89
Takehiro Ohta, Shuichi Hattori, Yoshihiro Kikuchi, and Dai Shimofusa	
<b>Secondary Groundwater Resources Exploited by Traditional Knowledge Systems in a Semiarid Region of Southern Italy</b> .....	97
Vincenzo Simeone and Antonio Graziadei	
<b>Part IV Climate Change</b>	
<b>Effects of Climatic Changes on Groundwater Availability in a Semi-arid Mediterranean Region</b> .....	105
Angelo Doglioni and Vincenzo Simeone	
<b>Estimating Sustainability Benefits from Use of Blended Cements and Slag Cement at Geotechnical Projects</b> .....	111
Josh Patterson and Charles M. Wilk	
<b>Author Index</b> .....	117

---

**Part I**  
**Dams**



# Microbial Activity Within the Earth Dam: Consequences and the Suppression Strategy

Nikolay G. Maksimovich, Vadim T. Khmurchik,  
Artem D. Demenev, and Alexey M. Sedinin

## Abstract

We studied some geochemical parameters at the earth dam of the Kama River water reservoirs, Russian Federation. The dam's body consisted of sand-gravel soil, alluvial and peat-bearing lacustrine marsh sediments were disposed at its basement. The system of vertical and horizontal drains mounted within dam's body withdrew filtering river water to reduce hydrostatic loading on the dam. Changes of cation and anion content of filtering river water, gas content of subsurface air, and mineral content of the dam's material were measured. Some indications of suffosion process were detected. We hypothesize that microorganisms living within the dam's body use river-water dissolved organic matter in their metabolism, and thus influence these changes. We hypothesize also that the rise of organic matter content in river water could lead to the intensification of microflora's activity, which in turn could lead to dangerous circumstances, such as weakening or failure of the dam. To avoid this situation, we studied possible techniques to suppress metabolic activity of ground's microflora. The main goal was to reduce microflora's gas-forming activity (mostly methanogenesis) as it dramatically reduces the strength of the dam. This paper describes both theoretical considerations and the results of our laboratory experiments aiming to suppress methanogenesis within the dam's body. The developed technique

of methanogenesis suppression was proposed to the dam's officials.

## Keywords

Earth dam • Microbial methanogenesis •  
Suppression

## 1 Introduction

Microbes take an active part in the transformation of the geological environment. The physiological peculiarities of microorganisms and their capability to act on minerals, organic and inorganic substances contribute to their considerable influence on soil and rock properties: structure, mineralogical content, bearing strength, and other parameters (Bolotina and Sergeev 1987; Kuznetsov et al. 1962; Maksimovich and Khmurchik 2012, 2013; Radina 1973).

The activity of microorganisms can change physical-mechanical properties of soils and rocks due to the following processes and factors: the formation of gases, which causes soils and rocks deconsolidation and alters their bearing strength; the leaching of the chemical elements from the rock that leads to the destruction of rock's mineral skeleton and subsequent decrease in mechanical strength of the rock; the change of microaggregate and chemical compositions of the soil, including the dispersion of clay aggregates, which increases the hydrophilicity and the deterioration of the strength and deformation properties of the soil as the result; the excretion of microbial metabolites exhibiting surface-active properties which reduce the strength of the structural bounds in the soil (Moavad et al. 1976; DeJong et al. 2006; Hendry 1993; O'Reill et al. 2005; Yang et al. 1993). Microbiological activity can considerably increase during anthropogenic influence on the soil.

So metabolic activity of microorganisms can change the geochemical parameters of soil and water and lead to undesirable consequences after the building of

---

N. G. Maksimovich · V. T. Khmurchik (✉) · A. D. Demenev  
A. M. Sedinin  
Natural Science Institute of Perm State University,  
Genkel St. 4, 614990 Perm, Russia  
e-mail: khmurchik.vadim@mail.ru

N. G. Maksimovich  
e-mail: nmax54@gmail.com

A. D. Demenev  
e-mail: demenevartem@gmail.com

A. M. Sedinin  
e-mail: sedinin\_alexey@mail.ru



hyrotechnical constructions and during their lifespan (Koff and Kozhevina 1981; Maksimovich et al. 2001).

The aim of our study was the investigation of the dam's soil and water to reveal deviations in their characteristics caused by possible microbial activity and to develop the technique preventing the progress of potentially dangerous microbial processes to keep the stability of the dam.

---

## 2 Geologic Background

The studied dam is one of a series of dams on the Kama River located in the Russian Federation. The earth dam was constructed of sand-gravel soil via hydraulic inwash up to a height of 19 m. The basement of the dam is presented of alluvial sediments, and is up to 14–17 m in thickness. The sediments are consisted of clays, loams, sandy loams, and fine sands. Sand bands are observed in clays and loams. Sand and gravel deposits are located in the lower part of geological column. The distribution and the composition of gravel-pebble strata are not uniform. Lenses of fine sand and interlayers of clays are observed in the gravel-pebble strata, peat is presented in the strata too. Clays exhibit high physical and chemical activity and contain an elevated quantity of organic substances (up to 8%) and trace chemical elements. Drilling has shown that the dam's material located below the seepage water level has a blue-gray-to-gray hue, and is up to 8 m in overall thickness. Blue-gray, green, bluish, and mottled (ocher-blue-gray, etc.) hues are typical of soils that have undergone gleyfication, which usually occurs as a result of the anaerobic microbial processes development (Perel'man 1965). The hydrological and hydrochemical conditions before and after the dam construction were described earlier (Maksimovich and Khmurchik 2015).

---

## 3 Methods

This study evaluated the microbial activity within the earth dam and assessed the risk of microbiological processes to the dam stability. The study included standard hydro-chemical analysis of water samples from the dam's body and upstream water reservoir during the main hydrological periods of year (i.e. high water level and low water level periods). Analysis of water-dissolved organic matter in these samples was made on gas chromatography–mass spectrometry system “Agilent 6890/5973N” (Agilent Technologies, Inc., USA). 48 water samples from the dam's body and 8 samples from the water reservoir were analyzed.

The gas-analyzer “Ecoprobe-5” (RS Dynamics, Czech Republic) was used to study the content of dam's subsurface air and gas content of the drain system. Subsurface gases

were sampled from the depth of 0.5–0.7 m using sampling holes which were bored by auger along the central horizontal line of the dam's downstream slope at 10 m distance from each other.

Sediment of the system of vertical and horizontal drains was sieved and microscoped, and its mineralogical analysis was performed on the X-ray diffraction analyzer “D2 Phaser” (Bruker, USA).

Analysis of physical-mechanical properties of the dam's soil, and laboratory microbiological studies of dam's water and soil were done also. More proper description of probe sampling and analyzing were described earlier (Maksimovich et al. 2014).

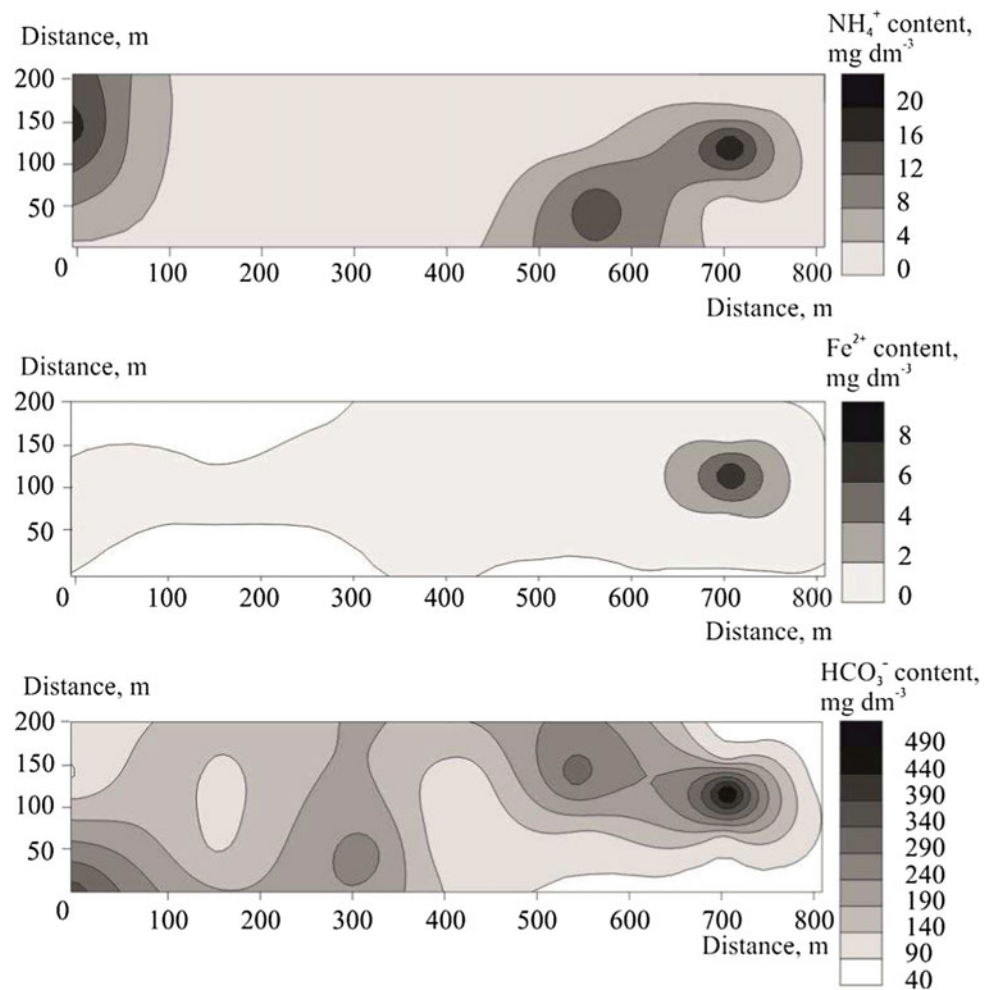
---

## 4 Geochemical Consequences of Microbial Activity Within the Earth Dam

The chemical analysis of dam's seepage water showed that its turbidity index exceeded one of the reservoir water by more than 6 times. Precipitate from seepage water samples was ocher in color and consisted of finely dispersed mineral particles, while the solid from a reservoir water sample was of a dark-brown color and consisted primarily of flaky particles and organic debris. The seepage water precipitate was formed as a result of long-duration contact with air and represented by trivalent iron hydroxide. The source of these trivalent iron ions was the dam's soil in which the gleying process was ongoing. The gleying process, one of the most widespread processes in the saturated zone, consists in the reduction of trivalent iron to a divalent state by microorganisms with subsequent removal of iron from gleyed horizons. A typical sign of gleying process is trivalent iron hydroxide, which is formed during subsequent oxidation processes, when former gleyed horizons are exposed to oxidation (Perel'man 1965).

The chemical analysis of water samples revealed the zones of elevated distribution of  $\text{NH}_4^+$ ,  $\text{NO}_2^-$ ,  $\text{NO}_3^-$ , as well as  $\text{Fe}^{2+}$  ions. The zone of elevated  $\text{NH}_4^+$  ions content roughly coincided with the zone of elevated  $\text{Fe}^{2+}$  ions content. The  $\text{HCO}_3^-$  ions content was also elevated there (see Fig. 1). The presence of spatially coincident zones of elevated  $\text{NH}_4^+$  and  $\text{Fe}^{2+}$  ions content suggests the occurrence of microbiological processes that anaerobically decompose water-dissolved organic substances. Herewith, the source of  $\text{NH}_4^+$  ions is an organic substance, while  $\text{Fe}^{2+}$  ions come from trivalent iron-containing minerals and rocks of the dam's material. It is known that microorganisms reductively dissolve iron(III) minerals under anoxic conditions and produce  $\text{Fe}^{2+}$  ions (Bonneville et al. 2004). Thus, the existence of the zone of elevated  $\text{Fe}^{2+}$  ions content may be the evidence of a microbiological transformation of iron

**Fig. 1** The distribution of  $\text{NH}_4^+$ ,  $\text{Fe}^{2+}$ , and  $\text{HCO}_3^-$  ions in the dam's groundwater,  $\text{mg dm}^{-3}$



minerals and rocks of the dam's material that results in the reduction of  $\text{Fe}^{3+}$  ions to  $\text{Fe}^{2+}$  ions which actively migrate in water solution and precipitate in the form of trivalent iron hydroxide when gleyed water emerges onto the surface. This explains the considerable increase in the turbidity of water seeping through the dam's body as compared to water from the upstream reservoir.

Water of reservoir seeping through the dam's body was characterized by an elevated content of water-dissolved organic substances ( $C_{\text{org}}$ )—the  $C_{\text{org}}$  content was 108–122  $\text{mg dm}^{-3}$ , while the average  $C_{\text{org}}$  content in surface water usually did not exceed 30–40  $\text{mg dm}^{-3}$ . Mass-spectrometer studies showed that the organic substance dissolved in water is of primarily anthropogenic origin. In our opinion, one of the potential sources of the organic substance entering the reservoir and the dam's body is wastewater discharge from an upstream pulp-and-paper plant.

The analysis of subsurface gases of the dam revealed the occurrence of regions with elevated contents of  $\text{CH}_4$ ,  $\text{C}_2\text{--C}_5$  hydrocarbons and volatile organic compounds (see Fig. 2).

The studies of the mineralogical composition of the sediment settled at the bottom of dam's drain system revealed a predominance of authigenic minerals (calcite, amorphous iron hydroxides, goethite, hydrogoethite, and pyrite) over allotigenic one (quartz minerals). The newly-formed minerals—intergrowths of calcite and pyrite—were detected (see Fig. 3).

Microbiological investigations of the dam's soil and water revealed the presence of an active metabolizing microbiota in them. Bacteria, isolated from the core and water samples, consumed organic substances, produced gases and leached Fe ions from the dam's material. We detected microorganisms capable to  $\text{NO}_3^-$ -reduction,  $\text{Fe}^{3+}$ -reduction,  $\text{SO}_4^{2-}$ -reduction, and methanogenesis in dam's soil and water samples and isolated the enrichment cultures of these microorganisms.

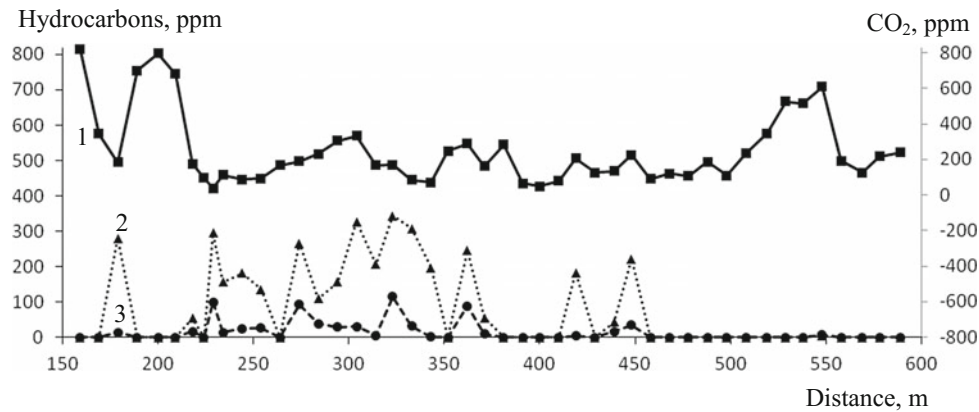


**Fig. 2** The content of gases in subsurface air of the dam, ppm (1—CO<sub>2</sub>, 2—CH<sub>4</sub>, 3—C<sub>2</sub>–C<sub>5</sub> hydrocarbons)

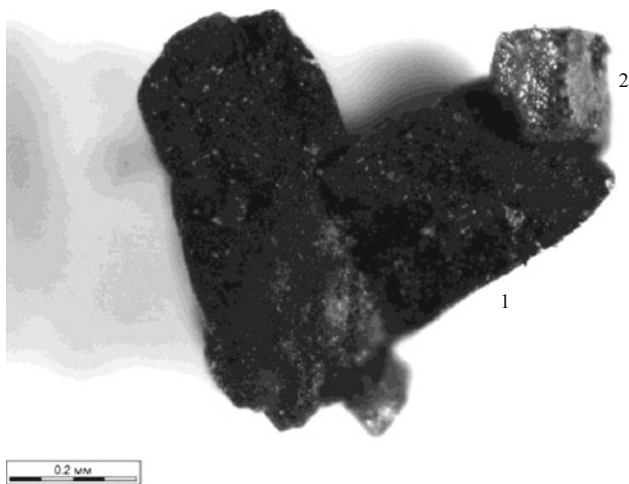


**Fig. 3** The intergrowth of calcite (1) and pyrite (2) from the dam's drain system sediment

## 5 Potential Microbial Activity Suppression Strategies for the Earth Dam

The results of the investigation demonstrate the presence of an active microbiota in dam's soil and water. So, the intensification of bacterial processes, which could be caused by the supply of additional amounts of organic matter, could lead to hazardous changes in physical-mechanical properties of dam's material and, eventually, the unstable state of the dam itself. One of the hazardous changes in the properties of dam's material is the change of bearing strength of the soil as result of gas-forming activity of soil microbiota. Because the content of NO<sub>3</sub><sup>-</sup> ions in water samples from the water reservoir and the dam's ground, along with soil samples from the dam's core were negligible, we hypothesized that methanogenesis was the main gas-forming microbial process

within the dam. This hypothesis was confirmed with the analysis of subsurface air.

It is known that microbial metabolism of organic matter with Fe<sup>3+</sup> ions as the electron acceptor is theoretically possible and is more thermodynamically favorable than microbial mineralization of organic matter with sulfate reduction or methane production as the terminal step (Froelich et al. 1979). Moreover, bacteria reducing Fe<sup>3+</sup> ions successfully outcompete methanogenic bacteria for organic matter (Lovley and Klug 1982), thereby suppressing rates of methane production in environments where Fe<sup>3+</sup>-containing components are abundant (Lovley and Phillips 1987).

This knowledge allows us to develop the technique to suppress the process of bacterial methane production within the dam's body by amending the soil with a Fe<sup>3+</sup>-containing substance, FeCl<sub>3</sub>. Preliminary laboratory experiments using various concentration of aqueous FeCl<sub>3</sub> indicated that a minimal 2.5 mg dm<sup>-3</sup> concentration of aqueous FeCl<sub>3</sub> was required to completely inhibit methane production. The efficiency of this FeCl<sub>3</sub> concentration was approved in experiment with the dam's material. The technique to suppress gas-forming microbial processes (methanogenesis, in general) was proposed to the dam's officials.

**Acknowledgments** This work was financially supported by the Ministry of Education and Science of the Russian Federation (Assignment No 5.6881.2017/8.9).

## References

- Bolotina, I.N., Sergeev, E.M.: Microbiological studies in engineering geology. *Eng. Geol.* **5**, 3–17 (1987) (in Russian)
- Bonneville, S., Van Cappelen, P., Behrends, T.: Microbial reduction of iron (III) oxyhydroxides: effects of mineral solubility and availability. *Chem. Geol.* **212**, 255–268 (2004)

- DeJong, J.T., Fritzges, M.B., Nusslein, K.: Microbially induced cementation to control sand response to undrained shear. *J. Geotech. Geoenviron. Eng.* **12**, 1381–1392 (2006)
- Froelich, P.N., Klinkhammer, G.P., Bender, M.L., Luedtke, A., Heath, G.R., Culien, D., Dauphin, P., Hammond, D., Hartman, B., Maynard, V.: Early oxidation of organic matter in pelagic sediments of the eastern equatorial Atlantic: suboxic diagenesis. *Geochim. Cosmochim. Acta* **43**, 1075–1090 (1979)
- Hendry, J.P.: Calcite cementation during bacterial manganese, iron and sulphate reduction in Jurassic shallow marine carbonates. *Sedimentology* **40**, 87–106 (1993)
- Koff, G.L., Kozhevina, L.S.: The role of microorganisms in the change of geological environment. *Eng. Geol.* **6**, 63–74 (1981) (in Russian)
- Kuznetsov, S.I., Ivanov, M.V., Lyalikova, N.N.: *The Introduction to Geological Microbiology*. The USSR Academy of Sciences, Moscow (1962) (in Russian)
- Lovley, D.R., Klug, M.J.: Intermediary metabolism of organic matter in the sediments of an eutrophic lake. *Appl. Environ. Microbiol.* **43**, 552–560 (1982)
- Lovley, D.R., Phillips, E.J.P.: Competitive mechanisms for inhibition of sulfate reduction and methane production in the zone of ferric iron reduction in sediments. *Appl. Environ. Microbiol.* **53**, 2636–2641 (1987)
- Maksimovich, N.G., Khmurchik, V.T.: The influence of microorganisms on the mineral composition and properties of grounds. *Perm State Univ. Bull. Ser. Geol.* **3**(16), 47–54 (2012) (in Russian)
- Maksimovich, N.G., Khmurchik, V.T.: Microbiological processes within ground dams. *Eng. Surv.* **9**, 66–71 (2013) (in Russian)
- Maksimovich, N.G., Khmurchik, V.T.: The influence of microbiological processes on subsurface waters and grounds in river dam basement. In: Lollino, G. et al. (eds.) *Engineering Geology for Society and Territory*, vol. 6, pp. 563–565. Springer, Berlin (2015)
- Maksimovich, N.G., Menshikova, E.A., Kazakevich, S.V.: Possibility of increasing the aggressiveness of groundwater during construction on pyrite-containing clay soils. In: *Proceedings of the International Symposium on Engineering-Geological Problems of Urban Areas*, vol. 2, pp. 545–551. Aqua-Press, Ekaterinburg (2001)
- Maksimovich, N.G., Khmurchik, V.T., Lazdovskaya, M.A., Demenev, A.D.: The complex of studying of microbiological activity in ground dams. *St.-Petersburg State Univ. Bull. Geol. Geogr.* **4**, 88–100 (2014) (in Russian)
- Moavad, H., Bab'eva, I.P., Gorin, S.E.: Soil aggregation under the influence of *Lypomyces lipofer* extracellular polysaccharide. *Soil Sci.* **9**, 65–68 (1976) (in Russian)
- O'Reill, E.S., Watkins, J., Furukawa, Y.: Secondary mineral formation associated with respiration of nontronite, NAu-1 by iron reducing bacteria. *Geochem. Trans.* **6**(4), 67–76 (2005)
- Perel'man, A.I.: *Geochemistry of Epigenetic Processes*. Nedra, Moscow (1965) (in Russian)
- Radina, V.V.: The role of microorganisms in the formation of ground properties and their tense state. *Hydrotech. Eng.* **9**, 22–24 (1973) (in Russian)
- Yang, I.C.-Y., Li, Y., Park, J.K., Yen, T.F.: The use of slime-forming bacteria to enhance the strength of the soil matrix. In: *Microbial Enhanced Oil Recovery—Recent Advances*, pp. 89–96. Elsevier, Amsterdam (1993)

# Wave Modeling and Coastal Erosion in Upstream Dams

A. G. Siqueira, M. F. M. Fiedler, E. A. Yassuda, and L. A. P. Sousa

## Abstract

A surface wave modeling was applied on the right margin of Sergio Motta Dam Reservoir (Porto Primavera Dam), Brazil, to investigate the behavior of breakwaters against impact of incoming waves. The Simulating WAVes Nearshore (SWAN) spectral wave model was applied to simulate waves generated by wind in the reservoir. Between 2009 and 2012 researchers from the Brazilian Institute of Technological Research (IPT) conducted several studies and developed an experimental project to protect reservoir banks from erosion caused by waves. Three different kinds of submerged breakwaters were installed in 2009, 1.0 km along the shoreline, in five stretches of 100 m length each, with an interval of 100 m between them. Two breakwaters were made of concrete (with an innovative arrangement) and the third one was made from geotextile tubes. The objective of the study was to compare and validate the modeling results with those observed in situ. Different simulations were done: 1—for the same arrangements of breakwaters installed on a segment in the reservoir, 2—for each structure, with a single side-by-side arrangement. The results indicate that the structures reduce wave heights by 35–40% compared to no breakwater. The single side-by-side structure arrangement showed better performance results when compared to the original in situ configuration installed. Wave height attenuation was found to be highly dependent on the

incident wave direction relative to breakwater orientation, and even considering a single structure configuration, the differences in performance depends on the wind direction and speed relative to the structure position.

## Keywords

Morphological modeling • Downstream • Dam • Delft3D • SWAN

## 1 Introduction

Erosion of reservoir banks involves a complex relationship of processes that contribute to the occurrence of different problems related to physical issues directly in the affected areas, as well as social ones, such as the impacts on the activities resulting from human occupation. The main agents of erosion are the wave's action, the surface runoff and the elevation of the water level (aquifer). Among these agents, the wave represent the most devastating erosive process and occurs mainly in large reservoirs, whose extensive surface area presents significant and propitious fetches to the generation of these waves.

In this work, the Simulating WAVes Nearshore (SWAN) spectral wave model was applied on the right margin of Sergio Motta Dam Reservoir (Porto Primavera Dam), Brazil, to simulate waves generated by wind in the reservoir lake.

## 2 Study Area and Objectives

The Sergio Motta Dam Reservoir (Porto Primavera Dam) is located half way down the Paraná River, on the borders of the states of São Paulo and Mato Grosso do Sul, in Brazil, downstream of the Jupiá dam and upstream of the Itaipu dam (Fig. 1). The drainage area of the basin is 574,000 km<sup>2</sup>; the reservoir surface and capacity are 2044 km<sup>2</sup> and 15.7 km<sup>3</sup> respectively (Celeri et al. 2005).

A. G. Siqueira (✉) · L. A. P. Sousa  
Institute for Technological Research, Sao Paulo, Brazil  
e-mail: agsique@ipt.br

L. A. P. Sousa  
e-mail: laps@ipt.br

M. F. M. Fiedler (✉) · E. A. Yassuda  
Tetra Tech Brazil, Sao Paulo, Brazil  
e-mail: MariaFernanda.Fiedler@tetrattech.com

E. A. Yassuda  
e-mail: Eduardo.Yassuda@tetrattech.com

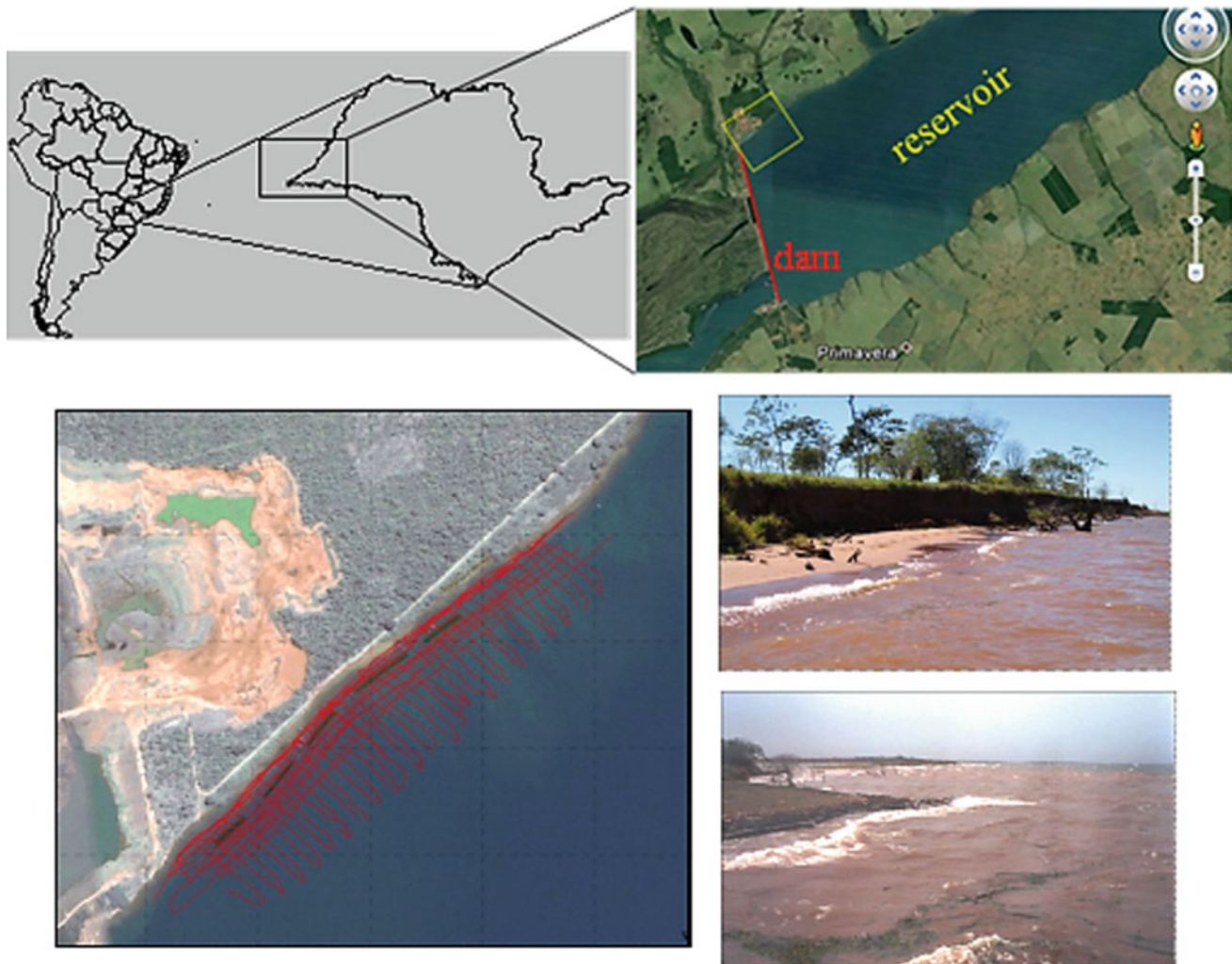


**Fig. 1** Detail of the study area in the reservoir, where the Simulating WAVes Nearshore (SWAN) spectral wave model was applied. Images show the geophysical survey around the breakwaters and the reservoir margin

Between 2009 and 2012 researchers from Brazilian Institute of Technological Research (IPT 2012) conducted several studies and developed an experimental project to protect banks from erosion caused by waves in the reservoir. Three different kinds of submerged breakwaters were installed in 2009, 1.0 km along the shoreline, in five stretches of 100 m length each and with an interval of 100 m between them (Fig. 2).

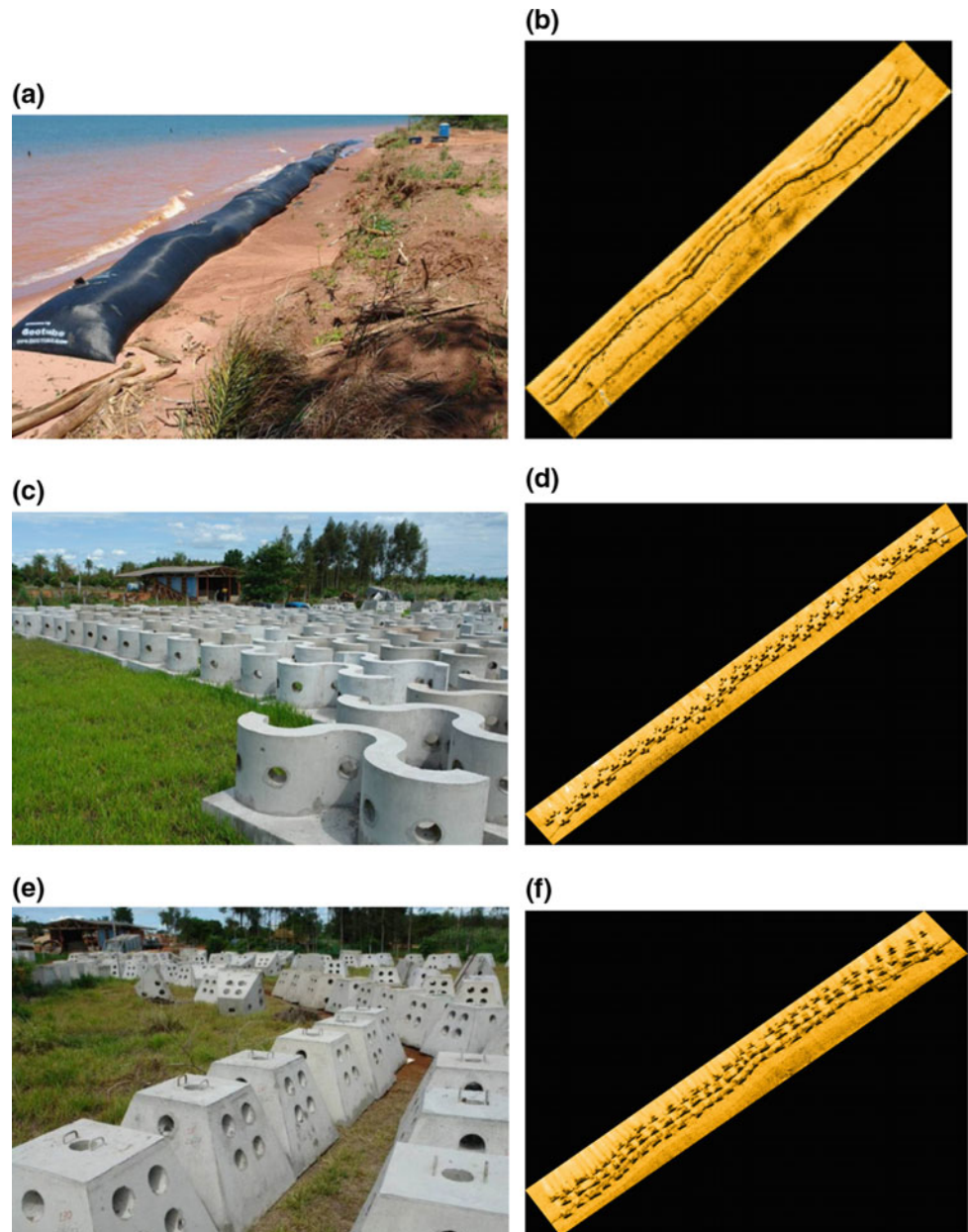
The objective of this study is to compare the surface wave modeling results with the performance of the breakwaters installed in the experimental area on the right reservoir margin (IPT 2012) and verify the behavior of the structures in a single side-by-side arrangement.

## 3 Materials and Methods

### 3.1 Model Set-Up

The grid implemented in the studied area was generated from the physical contours of the preexisting cartographic base (level contours and reservoir margin line). The grid was built using RFGGRID tool of the Delft3D software package. Around the area of the submerged breakwaters the grid is more detailed (presents a higher resolution) in order to enable better representation of the structures. The breakwaters were reproduced in the model exactly in the same position and

**Fig. 2** Types of breakwaters: **a, c, e** geotextile tube and concrete (sinuos and pyramidal); **b, d, f** the sonographic survey images show the installed configuration (multiple lines for concrete breakwater and single line for geotextile tube)



arrangement installed, according to the sonographic survey images, obtained in 2012. The final grid shows 12,389 cells, with horizontal resolution of  $66 \times 199$  cells.

Bathymetry survey data collected in 2012 were projected onto the model grid using triangular interpolation of the survey points using the QUICKIN tool. The grid and bathymetry of the model are shown in Figs. 3 and 4. Two breakwaters were composed of concrete and the third one of geotextile tubes.

The installation arrangements were: breakwaters, side by side, aligned in a single line for geotextile tubes and aligned

in multiple lines for the breakwaters made of concrete. All breakwaters were submerged (water column of 0.80 m). The wave parameters were measured in the reservoir previously and the values adopted for the upstream dam model were the same as those specified for the experimental erosion control project, i.e. a 1.5 m wave height, with a period of 5 s. The wind speed used was 10 and 20 m/s with an incidence direction of  $180^\circ$ , considering the true South.

The structures were represented as Dam type obstacles. In this option, the model admits that the transmission coefficient depends on the condition of the wave incident on the

obstacle as well as its height. The values used for the transmission coefficients  $\alpha$  and  $\beta$  (used in the mathematical formulation when processing the modeling) were 1.8 and 0.1, respectively.

Wave simulations were performed for three scenarios: 1—margin without breakwater to obtain the initial wave condition in the studied section; 2—the same arrangements of breakwaters installed on a segment in the reservoir and 3—different arrangement from the original installed, with simulations for each structure, aligned side-by-side.

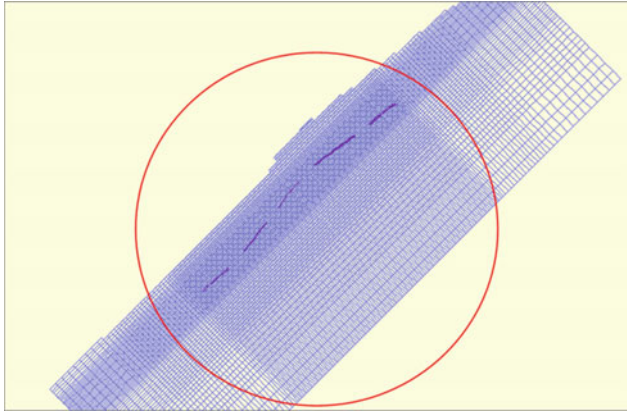
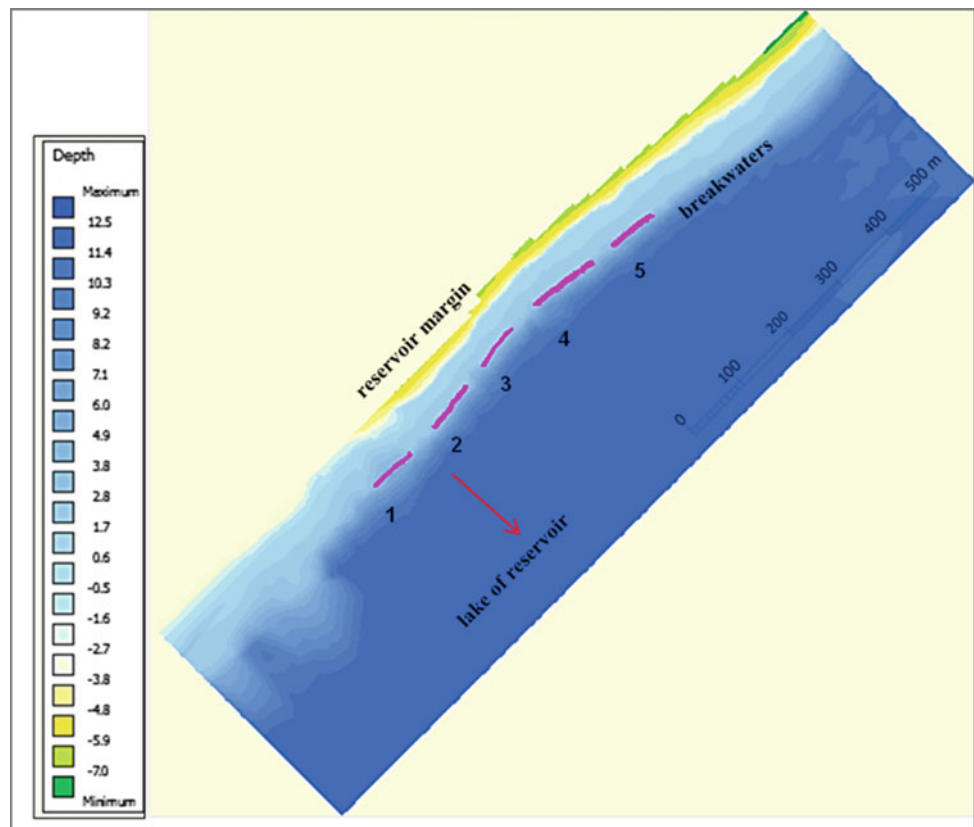


**Fig. 3** Delft3D model grid and submerged breakwaters contour

**Fig. 4** Bathymetry interpolated in the numerical grid with their depth and submerged breakwaters contours. 1—geotextile tube; 2—sinuous aligned; 3—pyramidal aligned; 4—sinuous multiple lines and 5—pyramidal multiple lines



## 4 Results and Discussion

The simulation for scenario 1 considered significant wave heights ( $H_{sig}$ ) varying between 0.8 and 1.3 m in the studied area, without structures. Scenario 2 represents the situation after the installation of the breakwaters and the wave heights were reduced to values between 0.6 and 0.8 m and 0.7 and 0.85 m; the winds velocities considered were 10 and 20 m/s, respectively (Fig. 5).

The geotextile tube and pyramidal with multiple lines structures showed the best performance in reducing the significant wave height, with rates of 42%.

Some points were chosen in the numerical grid to measure the values of significant wave heights after the breakwaters for the scenario 2 simulation. The values are show in Table 1.

The simulations for scenario 3 considered a different arrangement from the original installed. Only one structure was simulated at a time, repeated side by side in the same extension area.

The significant wave height reduction was evaluated in sections behind the breakwater (considering a grid cell behind the breakwater inside the final grid).

The results show that all the breakwaters, even individually, have reduced the significant wave heights from 1.2 m to values between 0.6 and 0.8 m (Fig. 6 and Table 2).



**Fig. 5** Results from scenario 2 simulation with wind speed of 10 m/s (a) and 20 m/s (b). The color bar shows the significant wave heights reduction (m) after breakwaters. 1—geotextile tube; 2—sinuous aligned; 3—pyramidal aligned; 4—sinuous multiple lines and 5—pyramidal multiple lines

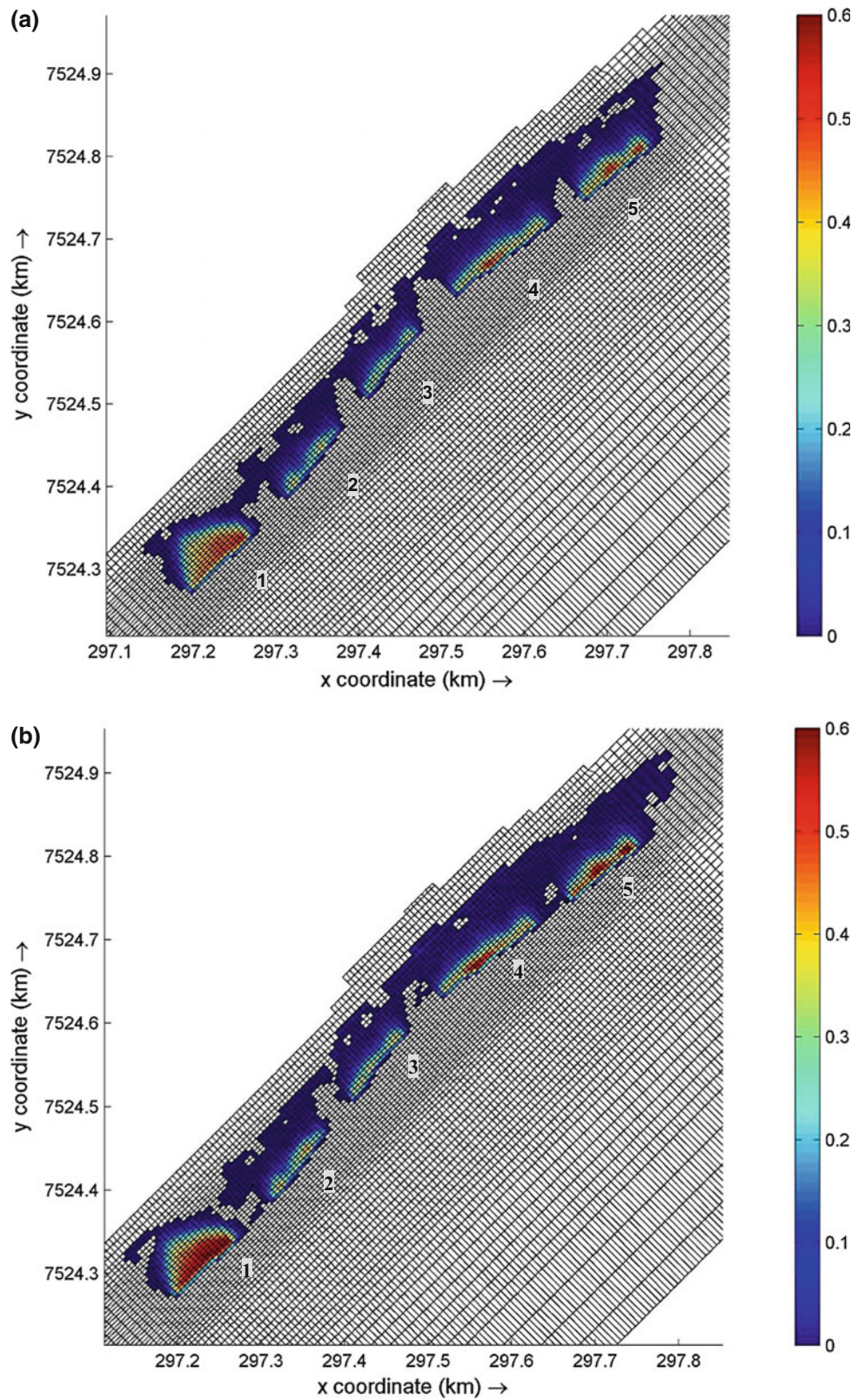


**Table 1** Significant wave height and reduction in the  $s$  values (%) obtained in scenario 2

Breakwater/wind speed		Significant wave heights (m)	Significant wave heights reduction after breakwater (%)
Geotextile tube	Out	1.25	
10 m/s	In	0.72	42.40
Geotextile tube	Out	1.29	
20 m/s	In	0.74	42.64
Sinuos aligned	Out	1.01	
10 m/s	In	0.79	30.68
Sinuos aligned	Out	1.09	
20 m/s	In	0.84	22.94
Pyramidal aligned	Out	0.92	
10 m/s	In	0.74	19.57
Pyramidal aligned	Out	1.1	
20 m/s	In	0.85	22.73
Sinuos multiple lines	Out	1.02	
10 m/s	In	0.7	31.40
Sinuos multiple lines	Out	1.22	
20 m/s	In	0.79	35.25
Pyramidal multiple lines	Out	1.01	
10 m/s	In	0.63	37.62
Pyramidal multiple lines	Out	1.18	
20 m/s	In	0.68	42.37

*In* with breakwater; *Out* without breakwater

## 5 Final Considerations

The Simulating WAVes Nearshore (SWAN) spectral wave model was applied to simulate waves generated by wind in the reservoir lake of Porto Primavera, Brazil. The results obtained with this study were satisfactory and show the model efficiency in this sort of study. The more significant wave height (m) reductions were obtained with the geotextile tube and the pyramidal concrete breakwaters (42% of reduction). These results are similar to those verified in the breakwaters installed in reservoir margin and in the hydrodynamic laboratory tests performed at the Institute for

Technological Research (Instituto de Pesquisas Tecnológicas—IPT).

Each breakwater has a specific configuration, with different shapes and sizes. When installed side-by-side their performance in response to incoming waves may be adversely affected by their structural differences and different wave incident directions. Simulations for only one type of breakwater, aligned, at first, exhibited better performance when compared to the original configuration installed (different types side-by-side) in the reservoir margin. Even in the individual configuration, differences in performance are observed in the reduction of significant wave height, because the structures are submitted to different wave spectra, with

**Fig. 6** Significant wave height reduction considering the breakwaters for scenario 3 simulations (wind speed of the 10 m/s). Breakwaters: **a** sinuous concrete in multiple lines and in a single line; **b** pyramidal concrete in multiple lines and in a single line; **c** geotextile. Values displayed on the scale (0.0–0.6 m) show how much the incident wave height has been reduced after the breakwater (difference between the scenarios with and without breakwaters)

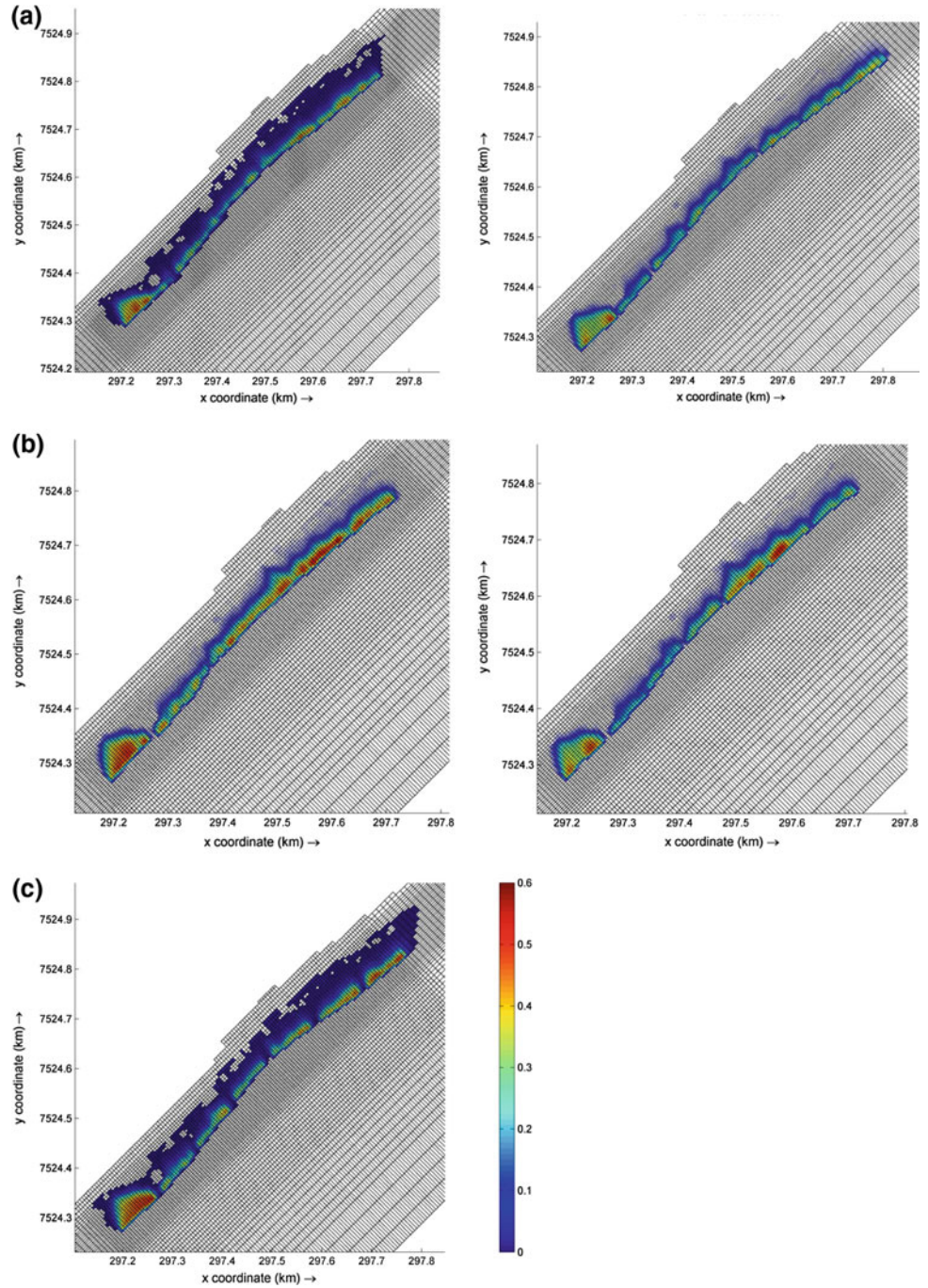


**Table 2** Significant wave height reduction values (%) obtained in scenario 3

Segment*	Significant wave heights (m) without/with structures	Significant wave heights reduction after breakwater (%)	
	Out	In	
<i>Sinuuous concrete in multiple lines</i>			
1	1.05	0.79	25.0
2	1.00	0.80	20.0
3	0.82	0.65	21.0
4	0.97	0.77	20.6
5	1.18	0.80	32.2
<i>Sinuuous concrete in a single line</i>			
1	1.23	0.87	29.0
2	1.10	0.84	23.6
3	1.00	0.79	21.0
4	0.95	0.77	19.0
5	1.10	0.83	24.5
<i>Pyramidal concrete in multiple lines</i>			
1	1.20	0.78	35.0
2	0.82	0.69	16.0
3	0.97	0.67	31.0
4	1.18	0.70	40.5
<i>Pyramidal concrete in a single line</i>			
1	1.20	0.82	31.6
2	0.82	0.71	13.0
3	0.97	0.78	19.0
4	1.18	0.78	33.8
<i>Geotextile in a single line</i>			
1	1.14	0.77	32.5
2	1.00	0.75	25.0
3	0.82	0.63	23.0
4	0.97	0.72	26.0
5	1.18	0.72	39.0

\*Sections evaluated behind of each type of breakwater

different energies. Breakwaters simulations are recommended prior the implementation in the reservoirs should be considered as an alternative, as it assists in the best planning and management of the work that will be performed, and thus also minimizing costs.

## References

Celeri, A., Alves, C.F.C., Carvalho, N.O.: Study of Protection alternatives for the control of erosion in the margins of Sergio

Motta dam. Technical Report n° 130 968-205, Sao Paulo, Brazil (2005) (in Portuguese)  
 Institute for Technological Research.: Study of protection alternatives for the control of erosion on the margins of the Sergio Motta dam (Porto Primavera). Technical Report 130 968–205. Research and Development Funding CESP/Brazilian Electric Power Agency—ANEEL (2012) (in Portuguese)



# Delft3D Morphological Modeling Downstream of Sergio Motta Reservoir Dam

A. G. Siqueira, M. F. M. Fiedler, and E. A. Yassuda

## Abstract

Delft3D hydrodynamic and morphological modeling were applied to simulate flow and sediment transport in Parana River, considering 20 km downstream of Sergio Motta Reservoir Dam, located in São Paulo, Brazil. The objective of this study is to investigate and compare the results of Delft3D morphological model with the verified modifications of the region. The simulations were made for a previously studied time interval (1996–2010) in which hydrodynamic and morphodynamic patterns were known through other studies, such as multi-temporal aerial image analysis (IPT 2001, 2012), hydraulic, geometric, bathymetric and sediment information of islands and sand banks of Parana River and Porto Rico hydrometric station. This period of simulation comprise the final stage of rising of the spillways, the floodgate's closing for filling of the reservoir and the operation of the turbines. The model was forced with measured discharge information of Sergio Motta Dam ( $\text{m}^3/\text{s}$ ) and calibrated with discharge and velocity distributions from field survey and Porto Rico hydrometric station. The Morphological Acceleration Factor (MORFAC) was applied due to the long time interval simulation (14 years), nevertheless the seasonal variability was considered for each of the 14 years simulated. The results were satisfactory and able to reproduce the reality downstream of the reservoir, both in the sediment transport and deposition patterns of the sandbanks and in the erosion sites identified at the islands located in the study area and monitored in the previously studies.

## Keywords

Morphological modeling • Downstream • Dam • Delft3D

## 1 Introduction

Studies involving changes in fluvial dynamics downstream of dams have been little discussed in Brazil although it is a concerning theme, particularly in environmental and safety terms. Modifications in the area associated with the operation activities of hydroelectric plants are topics of interest in this study, such as discharge control (frequency and magnitude) and the effects of water released from the turbines, with reduction of sediment supply and high erosive capacity (hungry waters).

In this work, the mathematical modeling of the sediment transport modifications downstream of the Porto Primavera dam, Brazil, was carried out for the period that comprises the final stage of rising of the spillways, the floodgate's closing for filling of the reservoir and the operation of the turbines (1996–2010). The hydrodynamic and morphodynamic patterns were known through other studies, such a multi-temporal aerial image analysis, hydraulic, geometric, bathymetric and sediment information of islands and sand banks of Parana River and Porto Rico hydrometric station.

## 2 Study Area and Objectives

The Porto Primavera dam is located half way of Paraná River, on the borders of the states of São Paulo and Mato Grosso do Sul, in Brazil, downstream of the Jupiá dam and upstream of the Itaipu dam. The drainage area of the basin is  $574,000 \text{ km}^2$ ; the reservoir surface and capacity are  $2044 \text{ km}^2$  and  $15.7 \text{ km}^3$  respectively, considering the reservoir full state (Celeri et al. 2005). The main channel—Paraná River—is characterized as a multichannel system,

A. G. Siqueira (✉)  
Institute for Technological Research, Sao Paulo, Brazil  
e-mail: agsique@ipt.br

M. F. M. Fiedler (✉) · E. A. Yassuda  
Tetra Tech Brazil, Sao Paulo, Brazil  
e-mail: MariaFernanda.Fiedler@tetrattech.com

E. A. Yassuda  
e-mail: Eduardo.Yassuda@tetrattech.com

presenting two main channels and several secondary channels, with islands and sand banks meeting and dividing it again.

The hydrodynamic and morphological modeling were implemented in the segment of the Paraná River that comprises the neighborhood of the Porto Primavera dam and the Comissão Geografica island, near Sao Jose harbor, about 20 km downstream of the Porto Primavera dam (Fig. 1).

The objective of this study is to investigate and compare the results of Delft3D morphological model with the verified modifications of the region previously studied by multi-temporal analyses by Siqueira et al. (2010).

### 3 Materials and Methods

#### 3.1 Model Set-Up

The numerical grid was generated from the physical contour of the river, islands, banks and sand banks, obtained from georeferenced aerial photogrammetric mosaics of 1996. The grid was built using RFGRID tool of Delft3D software package. The final grid shows 16,240 cells, with horizontal resolution of  $43 \times 378$  cells.

Bathymetry survey was also collected in 1996 and comprises 120 sections scattered along the main and secondary channels, around the islands and the sand banks. The bathymetry data was projected onto the model grid using triangular interpolation of the survey points using QUICKIN

tool. The grid and bathymetry of the model are shown in Fig. 2.

The information of the spillway heights of the dam was used to calibrate the hydraulic conditions. The spillway block has 20 m wide each, which includes 15 m for flood-gate wide and 5 m for pillars. All the structures have been defined as the non-erodible cells.

The model includes two open boundaries at its northeast and southwest extents. These boundaries are forced with averaged monthly discharge, extracted from the registered data at Porto Primavera dam station, for the period between January 1996 and January 2010. A statistical evaluation of the discharge distribution (Fig. 3) was made and two groups of homogeneous months were identified: January to April (wet season) and May to December (dry season).

To run the sediment transport model in Delft3D the grain size distribution was considered and was based on laboratorial analyzes of the sediment collected in the studied river reach. Each sediment class was calibrated to their respective particle size, which resulted in six sediment types: fine and medium sands for channel and sand banks, limonitic agglomerate in the bottom for some areas of the channel, fine sands, silt and clay for islands composition. The sediment class percentages and thickness for each island and each sand bank were imputed one by one and the interpolation of sediment distribution was made using QUICKIN tool of Delft3D software package. A constant Manning's friction coefficient value of 0.022 has been adopted for the entire segment of the studied river, obtained in the calibration

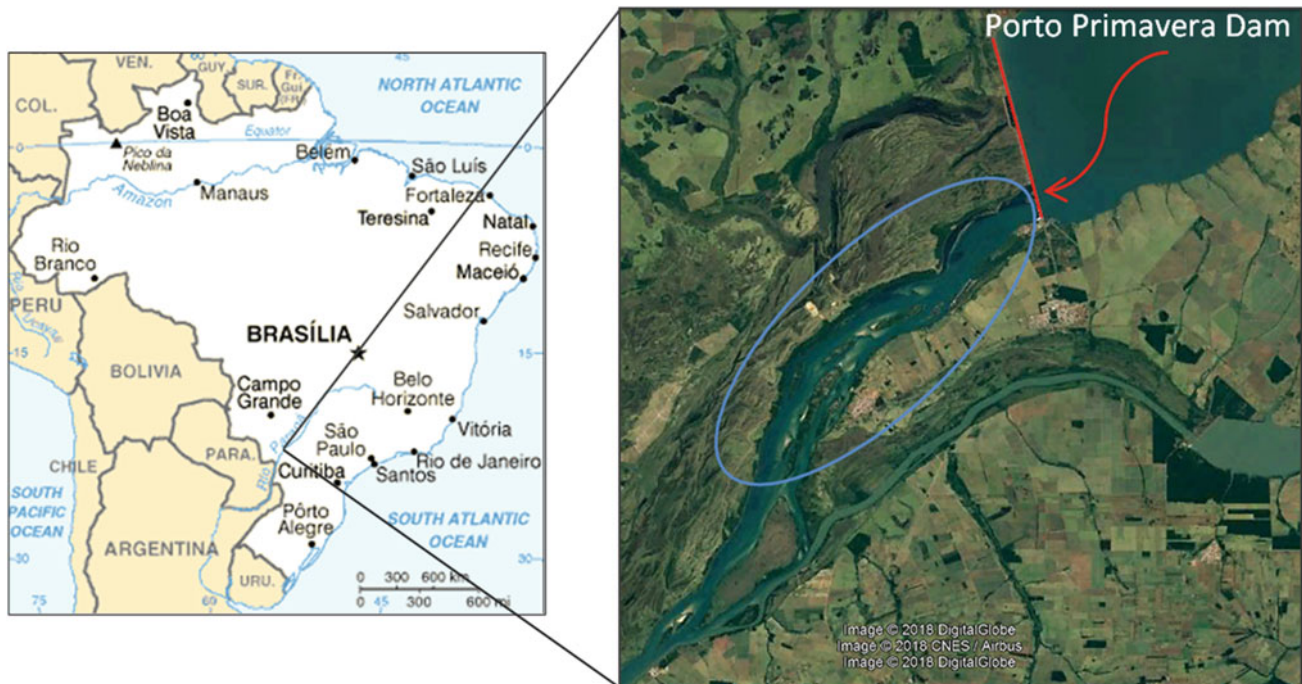


**Fig. 1** Location of the study river reach (blue ellipse), downstream of the dam, where the hydrodynamic and morphologic modeling were developed

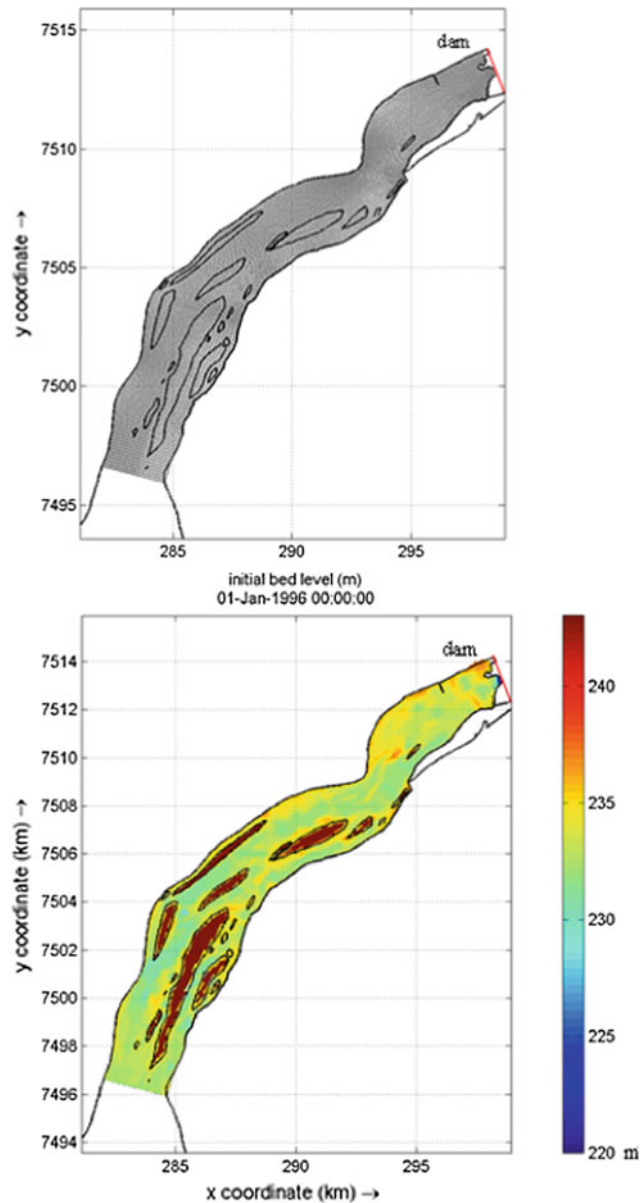
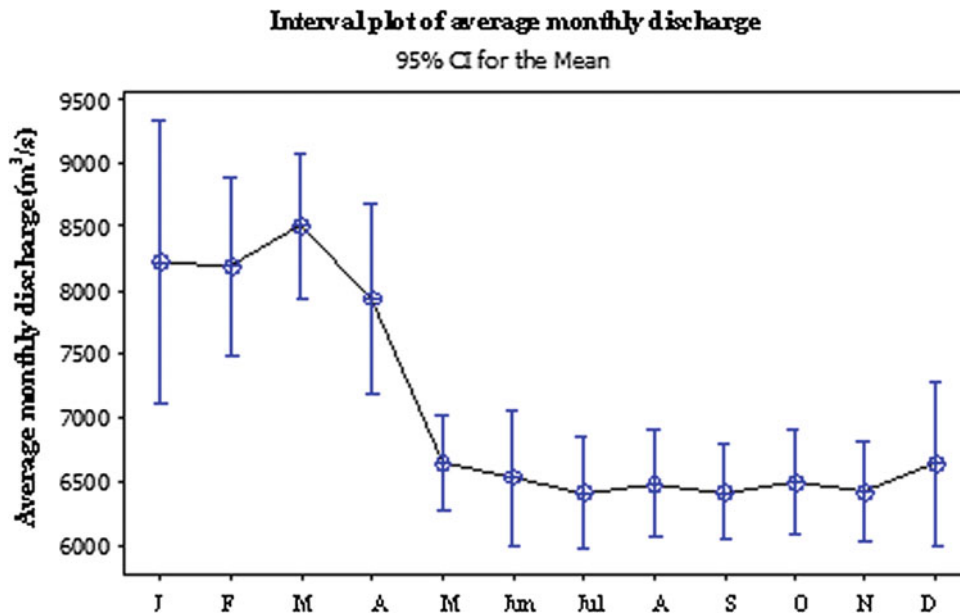


**Fig. 2** Delft3D model with grid and bathymetry (color bar)

process. This value agrees with the fluvial studies in the Porto Sao Jose station, downstream the Porto Primavera dam. Five different scenarios were conducted during the model calibration in order to evaluate the behavior of flow from turbines downstream the dam: 1—model not

considering the sediments of islands and sand banks, for hydrodynamic calibration and validation. 2—model considering the sediments information of sand banks. 3—model considering sand banks and bottom sediment information. 4—model considering all components—sand banks, bottom

**Fig. 3** Distribution intervals of the average monthly flow with a confidence interval of 95%



and islands sediment information. 5—model considering all components and applying morphological acceleration factor (MORFAC). MORFAC of 4 has been used. The dry season (May–December) lasts for twice the period of the flood (January–April). This means that the flood period was equivalent to one month hydrodynamic computation time and the dry period was equivalent to two months for each simulated year (morphological time), and the discharge forcing corresponds to the values measured for each season, for each simulated year.

## 4 Results and Discussion

The scenarios were conducted sequentially, for the calibration of each process: first the hydrodynamic were calibrated through the tests of roughness and velocities obtained, compared with measured data. From scenarios 2 to 3 the sand banks and bottom characteristics were applied and the model was calibrated through adjustments of flow as well as

thicknesses of bottom sediment classes. In scenario 5 the model became stable and realistic, based on the measured information's and other studies. It was possible to observe that the most intense currents are in the regions near and after the spillways, in the left bank of the river, in the right bank of the river (multichannel section), which agrees with the actual situation of the studied segment.

The results of morphological changes for scenario 5 are presented as plots of bed level changes, showing sedimentation (positive values) and erosion (negative values). The studied area was split in two segments: single channel and multichannel. Different scales of presentation were defined for each section, since the greater modifications occurred in the first stretch of the river. Figures 4 and 5 show the depth average flow velocity results and Figs. 6 and 7 present the observed changes for the 14 years simulated. Model results are therefore compared with the observed sedimentation and erosion for the period from 1996 to 2003, made by multitemporal aerial analyses (Fig. 8).



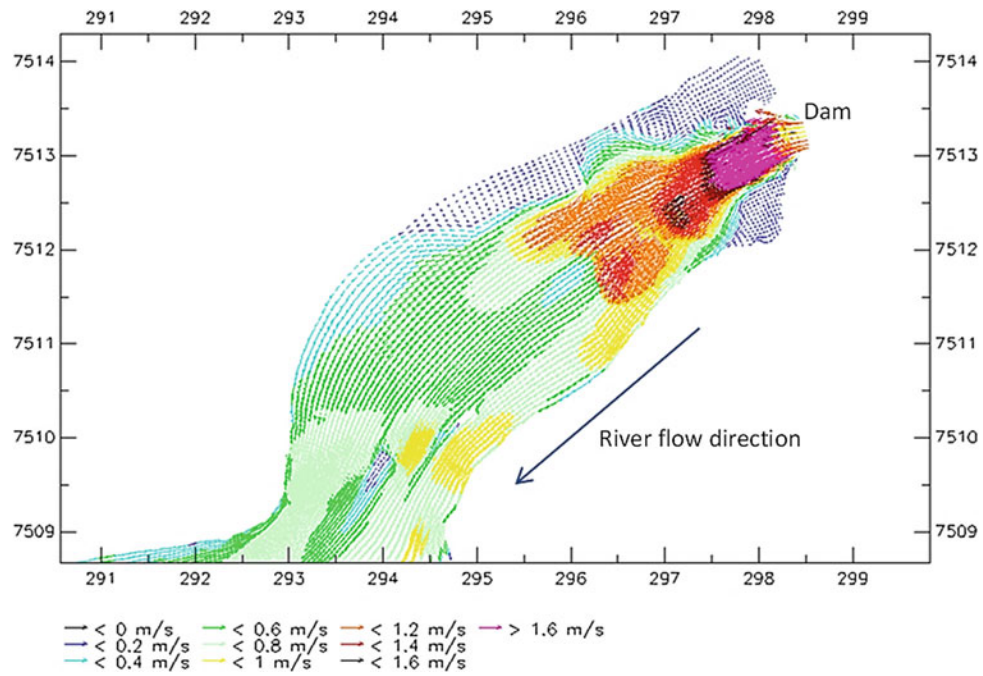


**Fig. 4** Depth average flow velocity for simulations in the single channel stretch of the river for scenario 5. The highest velocities are concentrated after the spillways and towards the left bank of the river

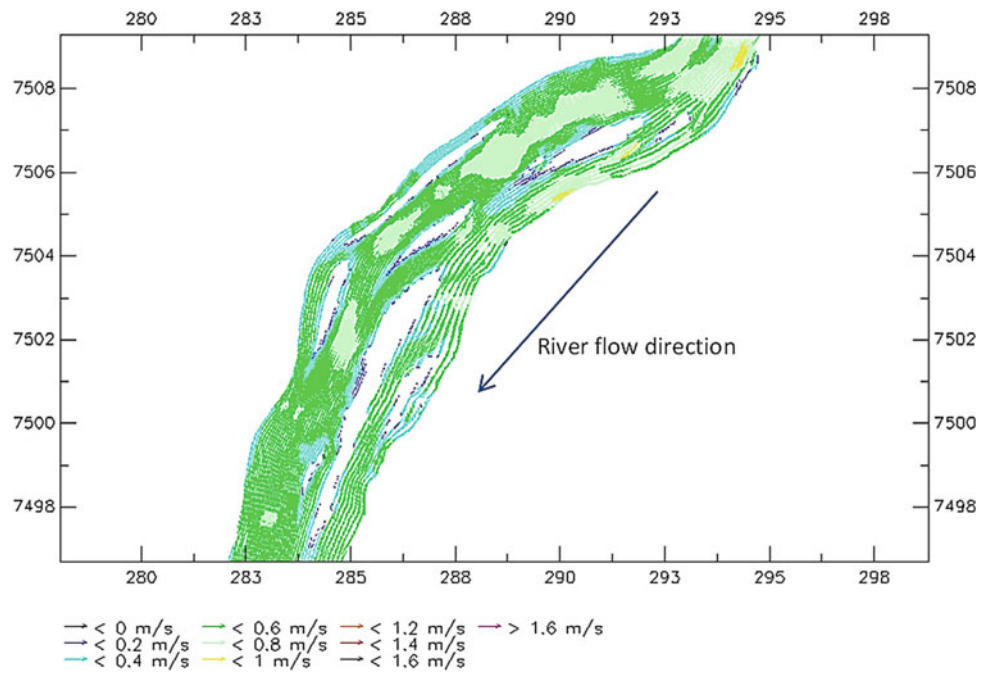


**Fig. 5** Depth average flow velocity for simulations in the multichannel stretch of the river for scenario 5. The highest velocities are concentrated in the left channel between islands and sand banks

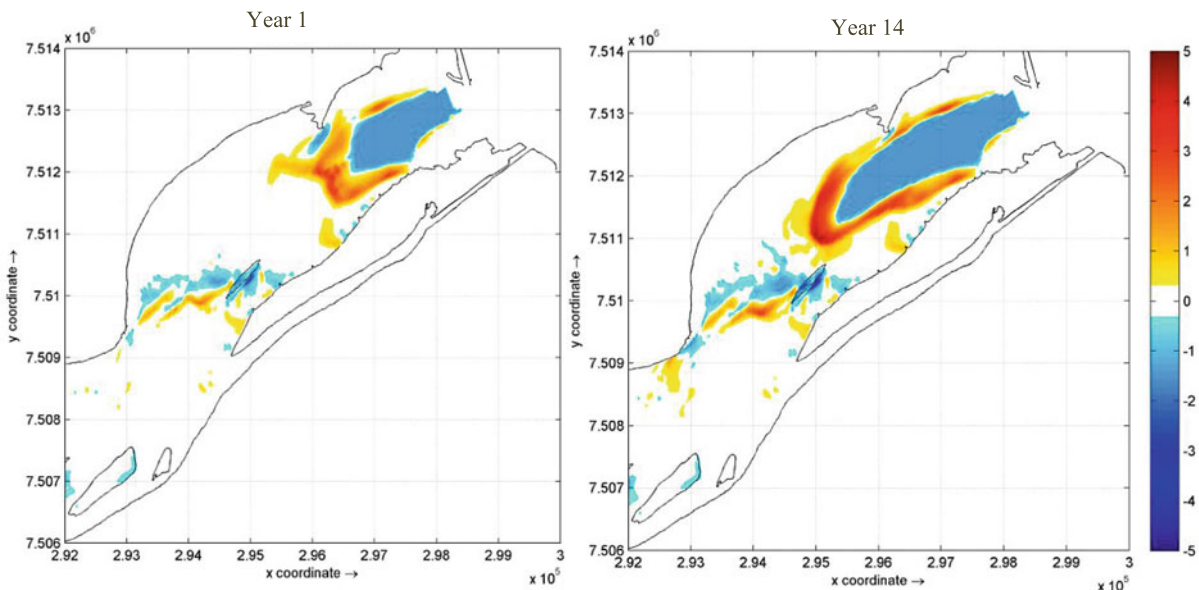


**Fig. 6** River changes after hydrodynamic simulations for 1 and 14 years in the single channel stretch. The images show the changes occurring in the river in each simulated period. Negative values indicate erosion and positive values indicate sediment deposition (in meters)

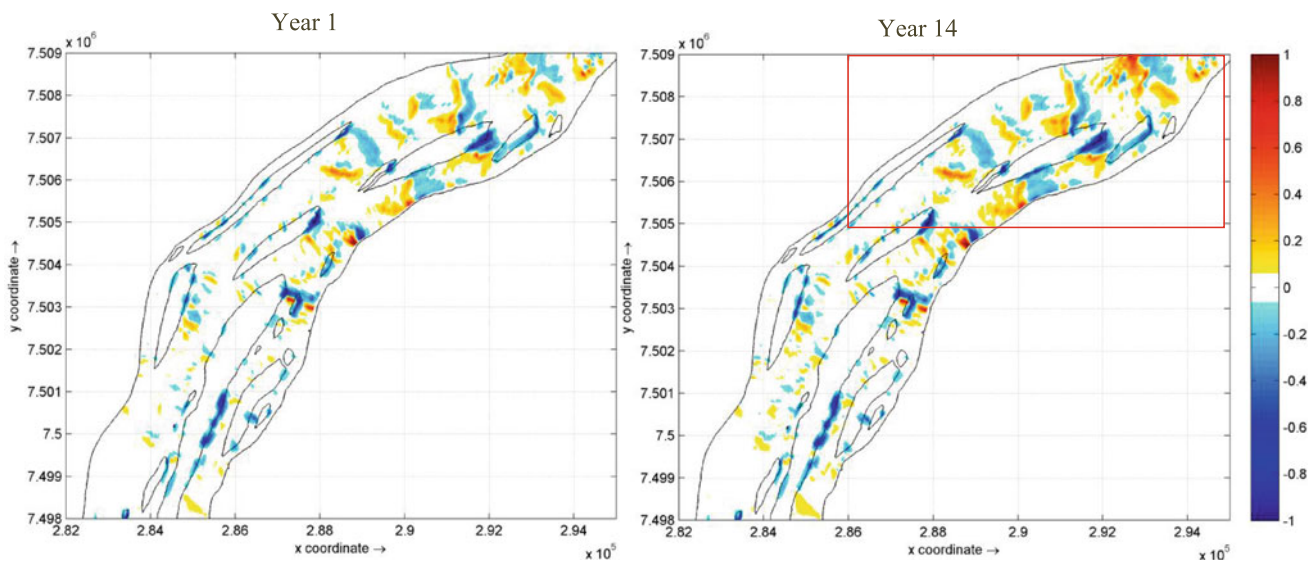


**Fig. 7** River changes after hydrodynamic simulations for 1 and 14 years in the multichannel stretch. Negative values indicate erosion and positive values indicate sediment deposition (in meters). This river

segment is further away from the dam (12 km) and the most significant modifications in the erosion-deposition pattern are in the red square area

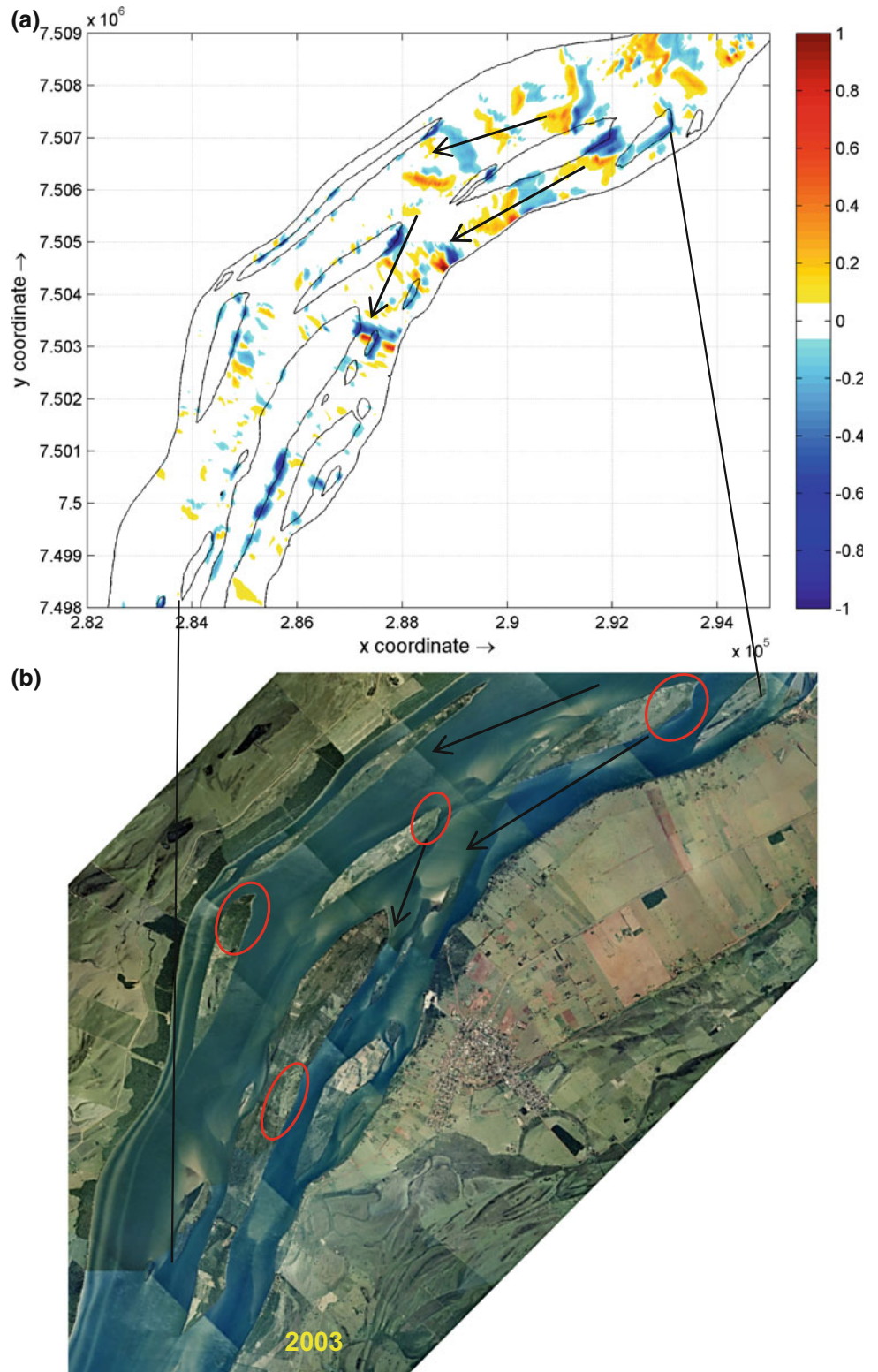
## 5 Final Considerations

This study presents an example of the use of numerical model to investigate the changes in sediment transport downstream of the dams. The hydrodynamic simulation was satisfactory and able to reproduce the reality downstream of

the reservoir, both in the sediment transport and deposition patterns of the sandbanks and in the erosion sites in the islands identified and monitored in the previously developed field studies by the researcher's team from the Institute for Technological Research, Brazil.

The results indicate that numerical models, when properly implemented, can provide a prediction of morphological

**Fig. 8** River changes after hydrodynamic simulations for 7 years in the multichannel stretch: **a** results of Delft 3D simulation **b** real situation in photogrammetric mosaics (2003). The arrows indicate the flow direction and the red circles the eroded sites (retreats of the islands' margins measured in the field by Siqueira et al. 2010). The results of Delft 3D Flow simulation are similar to those measured in the real situation. Negative values in color bar indicate erosion and positive values indicate sediment deposition (in meters)




changes and erosive/depositional patterns due to the installation of reservoirs and hydroelectric plants.

---

## References

- Celeri, A., Alves, C.F.C., Carvalho, N.O.: Reassessment of Porto Primavera reservoir sedimentation in view of updated sediment measurements. *Sediments budgets 2* (Proceedings of symposium S1 held during the seventh IAHS Scientific Assembly at Foz do Iguaçu, April, 2005). IAHS Public. **292**, 308–314 (2005)
- Institute for Technological Research.: Reservoir marginal slopes at Porto Primavera dam—Bank erosion monitoring program implementation. Technical Report 51.195, Sao Paulo, Brazil (2001) (in Portuguese)
- Institute for Technological Research.: Study of protection alternatives for the control of erosion on the margins of the Sergio Motta dam (Porto Primavera). Technical Report 130 968-205 (Research and Development funding CESP/Brazilian electric power agency—ANEEL—in Portuguese) (2012)
- Siqueira, A.G., Azevedo, A.A.; Dozzi, L.F.S., Kitahara, S.M.: Multitemporal analysis of the dynamic alteration on Paraná Riverbed, Downstream of Porto Primavera Dam, Brazil (2010)
- Wagner, R.C.: Results of a two-dimensional hydrodynamic and sediment-transport model to predict the effects of the phased construction and operation of the olmsted locks and dam on the Ohio River near Olmsted, Illinois. USGS—Water Resources Investigations, Report 03-4336, 68p (2004)

# Estimation of Continuity of a Fault Based on Composite Planar Fabric

Yasuhiko Wakizaka , Atsushi Kajiyama, Hiroyuki Watatani, and Mutsuo Kozuma

## Abstract

In Japan, there are many faults at dam sites, and a low-dip fault in particular can cause serious geological problems for the design and construction of a gravity type dam. It is difficult to estimate accurately the distribution and continuity of a fault due to the presence of composite planar fabric in a fault. Usually, Y shear, R1 shear and P foliation are observed in faults, and a fault extends to Y shear. However, the contact planes between a fault and its wall rock are not necessarily Y shear. When the contact planes between a fault and its wall rock are R1 shear or P foliation, the fault will not extend to the contact plane. Actually, all contact planes of a fault and its wall rock were estimated to be the Y shear based on drilled cores and data from borehole camera at dam sites in Japan, and the estimated distribution of faults did not match the actual distribution obtained by observing the excavated plane. Accordingly, identification of Y shear based on observation of high-quality drilled cores in Chichibu accretionary complex, which is a typical accretionary complex was performed. Y shear was identified one third of faults based on the combination of P foliation and R1 shear. Accurate estimation of the fault continuity is possible using the dip and strike of Y shear obtained by images from a borehole camera.

## Keywords

Dam • Low-dip fault • Composite planar fabric

## 1 Introduction

The Japanese Archipelago is located at the boundary of various plates, and as a result many faults are distributed in the area. Even if it is not active, a low-dip fault can cause serious geological problems for the design and construction of a gravity-type dam. This is because a low-dip fault may form a slip surface when the dam reservoir is filled, and the dam will then collapse due to a slip. The distribution of faults is usually estimated from surveys of outcrops, and observations of drilled cores and walls of adits. However, the information obtained by all of these surveys and observations is one dimensional or zero dimensional; it is difficult to obtain three dimensional information of faults for the following reasons:

1. The distances between boreholes are too long (the density of boreholes is too low) compared to the fault length.
2. The boundary between a fault and wall rock is disturbed in the case of ordinary drilled cores.
3. If cores are drilled by high-quality methods, the dip and strike of a fault are not determined using only the cores. To determine the dip and strike of a fault, data from a borehole camera is required.
4. The boundary between a fault and wall rock does not necessarily express elongation of the fault.

The first cause is a problem of borehole density, the second cause is attributed to drilling quality and the third cause is due to the fault dip and strike measurement method. Only the fourth cause is a geological problem, so this paper discusses the fourth cause.

## 2 Accuracy of Estimating the Location and Continuity of a Fault

The accuracy of estimating the location and continuity of a fault can be confirmed at a dam site, because the basement rock at the site is excavated. Figures 1 and 2 show the

Y. Wakizaka (✉)

Japan Dam Engineering Center, Ikenohata, Taito-ku, Japan  
e-mail: dora1026@peach.ocn.ne.jp; wakizaka@jdec.or.jp

A. Kajiyama

CTI Engineering Co., Ltd., Dosho-machi, Chuo-ku, Osaka, Japan

H. Watatani · M. Kozuma

CTI Engineering Co., Ltd., Daimyo, Chuo-ku, Fukuoka, Japan

distribution of faults before and after excavation of basement rock at two dam sites. The distribution of faults before excavation was estimated by geological investigations such as observations of outcrops, drilled cores and walls of adits.

Figure 1 shows an example of high dip faults. Basement rock of the A-dam site is Cretaceous gneiss. Faults Fa', Fi, F9 and Fe estimated before excavation were observed in the same locations after excavation, whereas the locations of the other faults estimated before excavation differed from the locations observed after excavation. Fault Ef did not appear when the basement rock was excavated. Figure 2 shows an example of low-dip faults at the B-dam site. The geology of the B-dam site is Miocene lapilli tuff. Eighteen low-dip faults were observed before excavation, and the continuity of all faults was estimated to be poor. However, eight faults indicated good continuity after excavation, as shown in Fig. 2. Estimation accuracy is not so good for high-dip and low-dip faults.

### 3 Geological Factors Affecting the Accuracy of Estimating the Continuity of a Fault

#### 3.1 Formation Process of Faults

The process of formation of faults was studied by Riedel (1929) by performing experiments on the formation of an artificial fault. He made a cut box which consisted of two parts, and filled the box with a mixture of sand and clay. In this box, the cut plane was the displacement direction of a

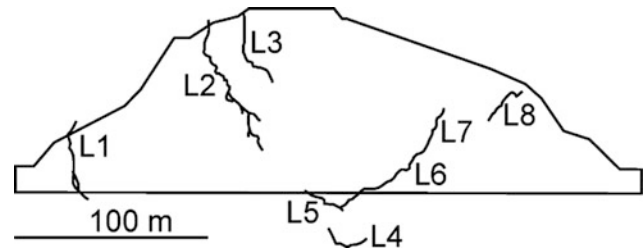


Fig. 2 Distribution of low-dip faults after excavation of basement rock indicated by the top view in B-dam, after Wakizaka (2015)

fault, and displacement could occur along the cut plane. At the stage of small displacement, staggered shear planes which crossed the displacement direction appeared, called Riedel shear planes. This experiment is called the Riedel shear test.

Tchalenko (1970) performed the Riedel shear test, and obtained the following results: staggered Riedel shear planes which crossed the displacement direction appeared when the displacement was small, other shear planes were formed in accordance with the progress of displacement, and finally each shear plane connected together and formed planes parallel to the displacement direction. Figure 3 shows the process of formation of a right lateral fault based on the test results of Tchalenko. The magnitude of displacement increased from (a) to (e). During the stage of development of the fault, the boundary between the fault and wall rock is not necessarily parallel to the direction of fault elongation as shown in Fig. 3(a) to (d).

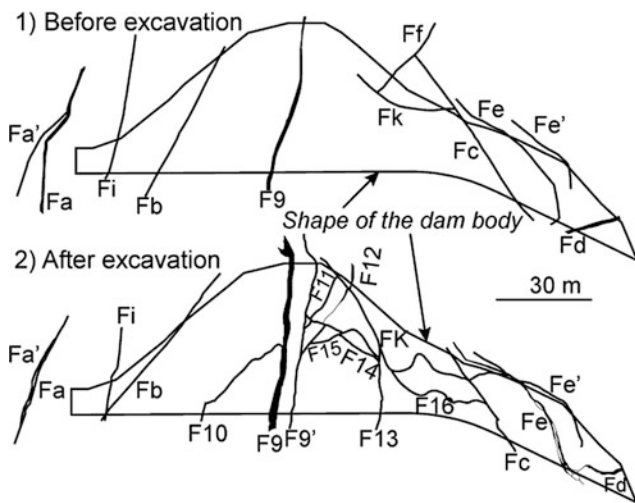


Fig. 1 Distribution of high-dip faults before and after excavation of basement rock indicated by the top view in A-dam, after Wakizaka (2015)

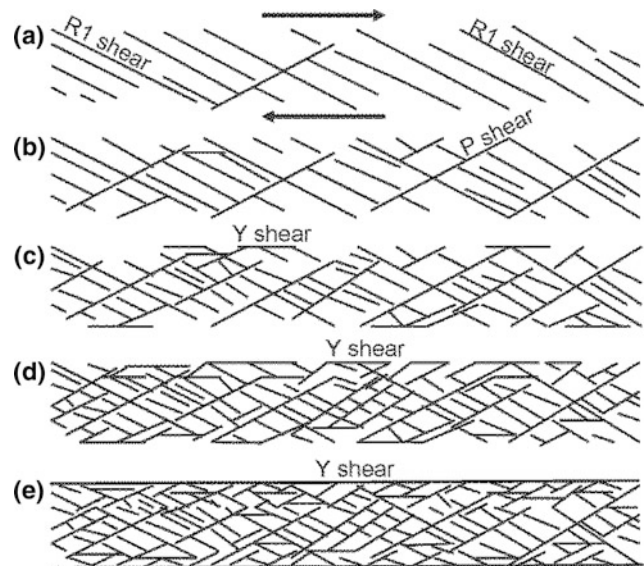


Fig. 3 Process of formation of a fault

### 3.2 Composite Planar Fabric and Continuity of a Fault

Various planes such as Riedel shear planes which appear during fault development are called composite planar fabric. Logan et al. (1979) gave the terms for each plane as shown in Fig. 4. Stearns et al. (1981) proposed a term of R instead of R1, and R' instead of R2. R1 or R and R2 or R' are Riedel shear planes, and Y, X and P are also shear planes. T is a tension crack. Among them, the direction of Y shear is that of elongation of the fault. P is not only a shear plane but also a foliated plane which consists of an arrangement of long axes of fragments or arrangement of mica. A shear plane of P is P shear, whereas a foliated plane of P is P foliation (Rutter et al. 1986). According to triaxial compression testing (e.g. Paterson 1978), the formation of a composite planar fabric is related to high confining pressure.

The boundary plane between a fault and wall rock in a developed fault may be composed of various planes such as Y, R1 and P shears, and the upper and lower surfaces of a fault in a drilled core show various planes. If the boundary plane between a fault and wall rock is P foliation or R1 shear, then the P foliation or R1 shear is mistaken for Y shear, and estimation of continuity of this fault is incorrect as shown in Fig. 5.

The boundary between a fault and wall rock does not necessarily express the elongation of the fault, as mentioned above. However, when the continuity of a fault is estimated by drilled cores, the direction of the boundary between a fault and wall rock obtained by the drilled cores is usually considered to be the direction of elongation, especially in the case of ordinary drilled cores without borehole camera data. The main geological factor affecting the accuracy of estimating the location and continuity of a fault is the presence of composite planar fabric in the fault.

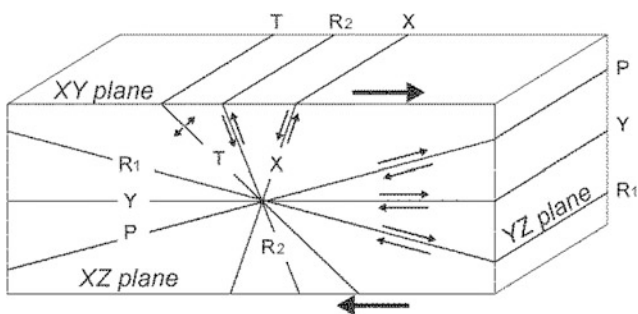


**Fig. 4** Composite planar fabric of a lateral fault and its terms after Logan et al. (1979)

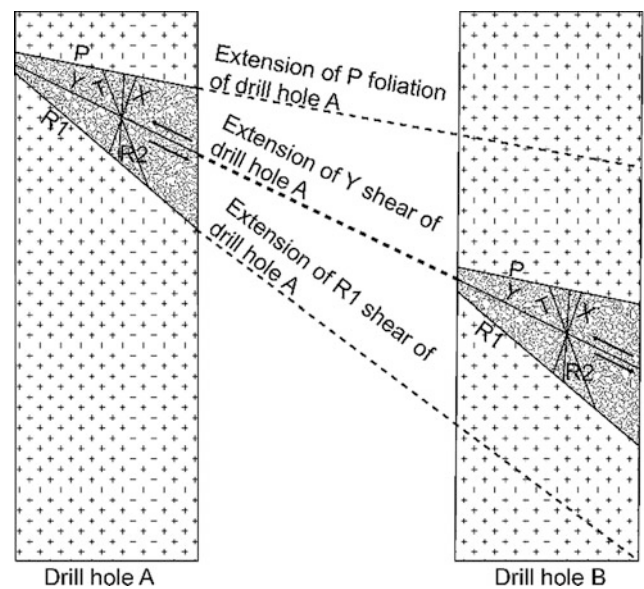


**Fig. 5** Relationships between composite planar fabric and continuity of faults

## 4 An Example Estimating the Continuity of a Fault Based on Composite Planar Fabric

### 4.1 Geological Settings

Chichibu accretional complex is distributed in the example area. In the example area, the origin of this complex is an olistostrom, and is mainly composed of sandstone, mixed rock (chaotic rock) of sandstone and slate, slate and chert. Many low-dip faults are distributed in sandstone, slate, and mixed rock of sandstone and slate. It is planned to construct a gravity type dam in this area.

### 4.2 Method

Seven high-quality drilled cores of diameter 70 mm were observed. These drill holes (A to G drill holes) were arranged on the same measured line. The positions of low-dip faults and detailed structures such as composite planar fabric of faults were observed. A low-dip fault was defined as a fault having dip of less than 35°. When fabric was determined, P foliation was initially recognized based on Fig. 6, because the displacement of each shear plane is not usually determined by a drilled core, so each shear plane is not

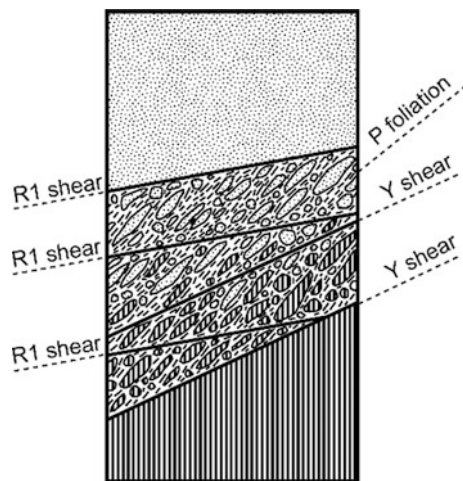


**Fig. 6** Determination of P foliation, R1 and Y shears in a drilled core

determined by displacement. P foliation is expressed by the arrangement of the long axis of fragments and/or mica minerals. The dip and strike of the shear planes and foliation were determined from images taken by a borehole camera. The dip and strike of planar fabric were plotted on a Schmidt net diagram to confirm the accuracy of determination of the shear planes and foliation and to divide the strike and dip of Y shear. Y shear was accurately determined when Y and R1 shears, P foliation and unspecified planes showed nearly the same range of strike within  $20^\circ$ . Accurate Y shears were divided into some groups based on their dip and strike. The apparent dip of Y shear was plotted in the section by the same dip and strike group. Finally, the continuity of Y shear which is the continuity of the low-dip fault was determined based on the section.

### 4.3 Results

#### Determined planar fabric

The numbers of observed low-dip faults were as follows: drilled core A: 15, B: 11, C: 17, D: 13, E: 11, F: 7, G: 11. Figure 7 shows apparent dips of the upper and lower surfaces of the low-dip faults. The upper and lower surfaces were determined by the upper and lower boundaries, respectively, between a fault and wall rock. Low-dip faults are mainly distributed in slate, and mixed rock of sandstone and slate. It is impossible to estimate the continuity of faults because the direction of the upper and lower surfaces is very complicated.

Figure 8 shows example photographs of the determined planar fabric. The arrangement of the long axis of fragments was observed in Fig. 8a, b, and the arrangement of mica minerals was recognized in Fig. 8b. These arrangements

were considered to be P foliation. The R1 and Y shears were determined by the P foliation and the relationships between planes as shown in Fig. 4. When P foliation was determined, the old P foliation which was formed in accretion was neglected. Rock that shows old P foliation. This rock is perfectly consolidated.

Y shear was confirmed by the relationships between its strike and the strike of other shear planes and foliation. The strike of the confirmed Y fabric had the same or nearly the same strike as the other shear planes and foliation. Figure 9 shows the dip and strike of the confirmed Y shear; the dip and strike was divided into two groups, group A and group B. The range of dip and strike of group A is  $10^\circ$ – $30^\circ$  and  $N10^\circ W$ – $N60^\circ E$  respectively, and that of group B is  $10^\circ$ – $32^\circ$  and  $N10^\circ W$ – $N60^\circ W$  respectively.

#### Distribution of Y shear

Figure 10 shows the apparent dips of Y shear and similar planes of Y shear of group A in geological section. Figure 11 also expresses the apparent dips of Y shear and similar planes of Y shear of group B. Y shear and similar planes of Y shear are called Y shear below. Comparing the apparent dips of Y shears in both groups with the apparent dips of the upper and lower surfaces of the faults as shown in Fig. 7, the apparent dips of Y shears naturally show the same direction.

## 5 Discussion

### 5.1 Continuity of Faults

The continuity of low-dip faults was estimated based on the distribution of the apparent dips of Y shears as shown in Figs. 10 and 11. In these figures, if Y shears are distributed at the elongation of the other Y shears, these Y shears are considered to be continuous with each other. However, measurement of the dip and strike of Y shears from the borehole camera images had some errors. Therefore, when estimating the continuity of Y shears, some width in the direction of elongation is required.

Figures 12 and 13 show the estimated elongation of the faults based on the apparent dip of Y shears of group A and group B, respectively. In group A, two faults are estimated to continue. One continues from the drill hole D to G in mixed rock of sandstone and slate, and the other is continues from drill hole D to F in slate. In group B, two faults are also estimated to continue. One is elongated from drill hole A to B in slate, and the other continues from drill hole C to D in mixed rock of sandstone and slate. The continuity of faults is accurately determined based on observation of Y shear.



**Fig. 7** Apparent dip of upper and lower surfaces of faults

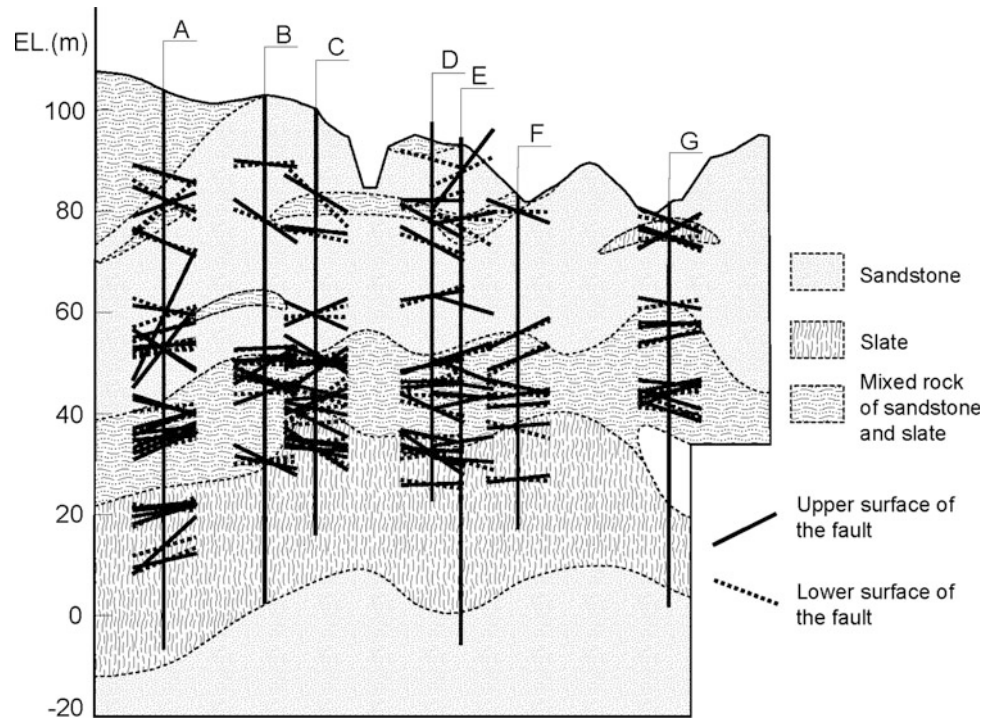


**Fig. 8** Examples of determined composite planar fabric

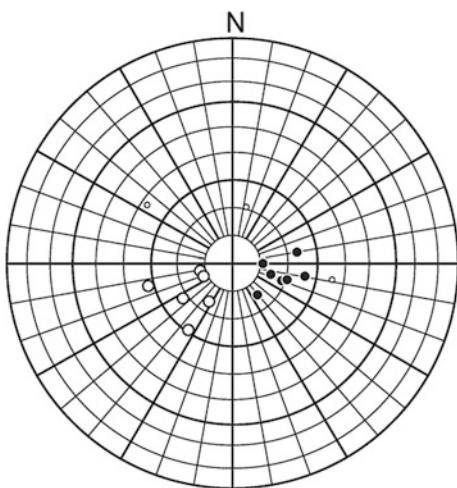
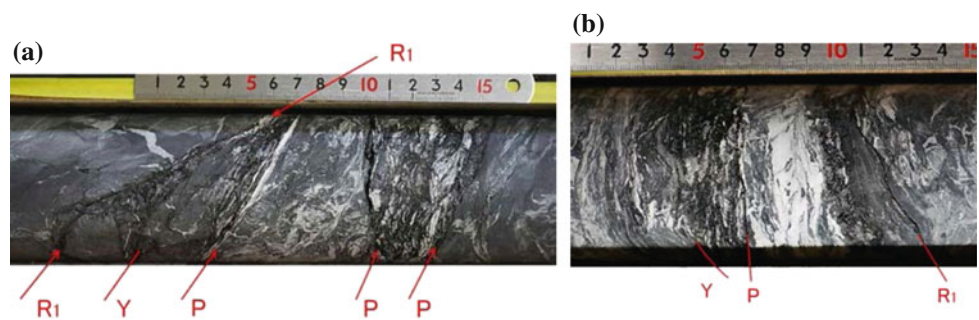


**Fig. 9** >Schmidt's polar net plots of Y shear dip and strike (lower-hemisphere projection). Solid circles: Y fabric of group A. Large open circles: Y fabric of group B. Small open circles: Y fabric of another group

## 5.2 Problems in Determining Composite Planar Fabric

There are some problems in determining composite planar fabric as follows.

1. Shear planes and foliation are not observed in the fault part, because the core is disturbed by drilling even though the core is high quality.
2. Shear planes and foliation are not present in the fault part, because the length of the fault is shorter than the interval between shear planes or foliation.
3. Shear planes are not specified, because P foliation is not present.

To the problems 1 and 2, all faults distributed in two drill holes next to each other are considered to be connected each other. To solve problem 3, all shear planes are considered to be Y shear.

**Fig. 10** Apparent dip of Y shears of group A

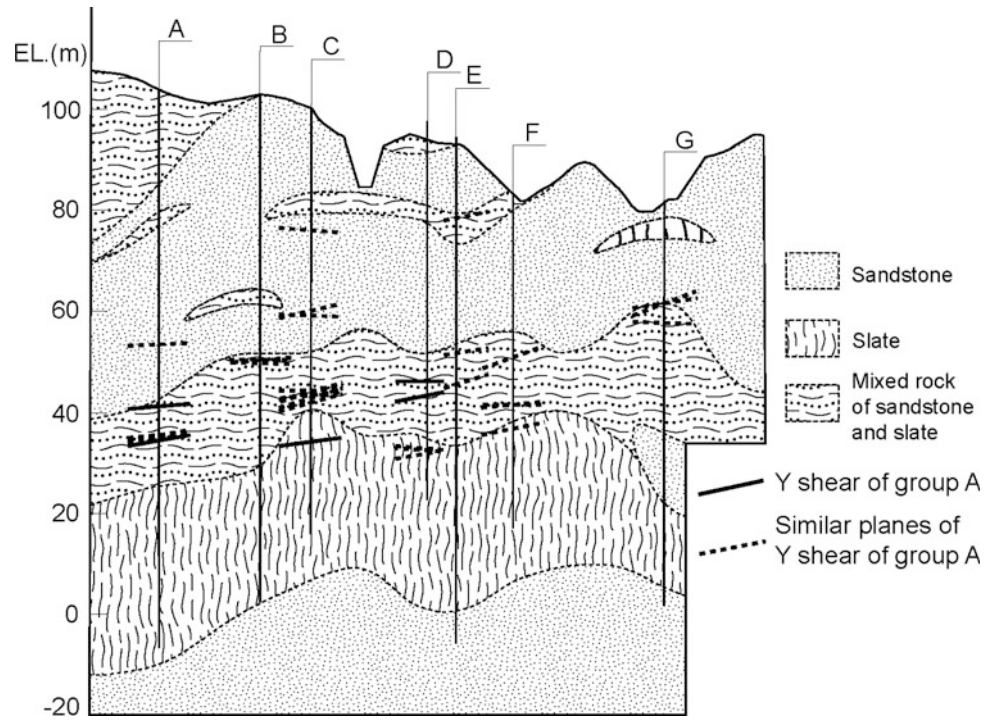


**Fig. 11** Apparent dip of Y shears of group B

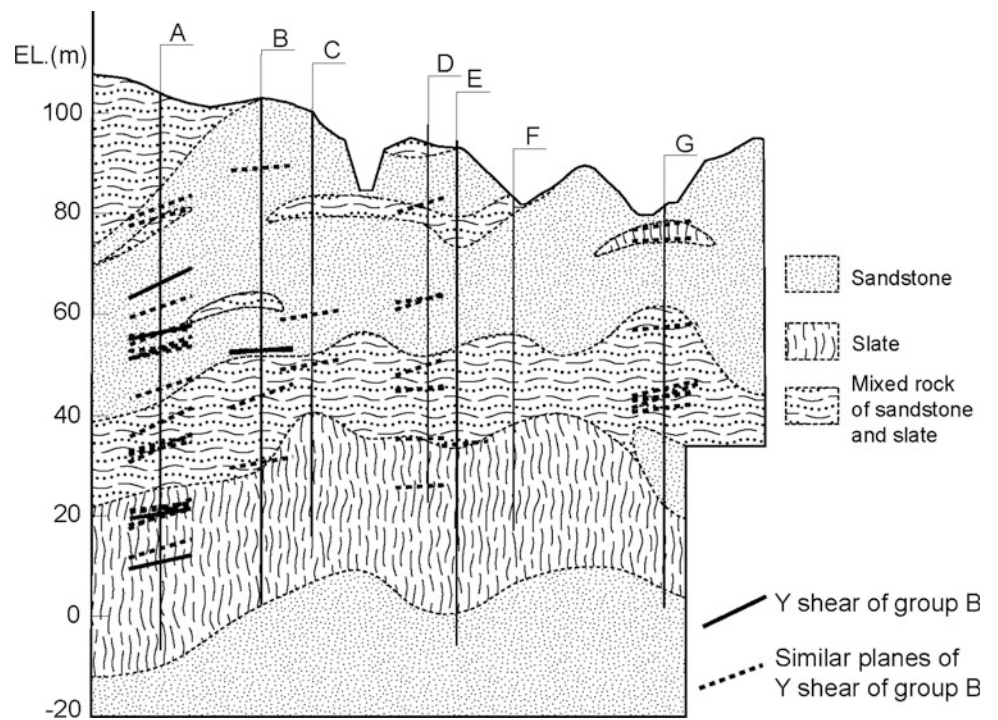


**Fig. 12** Estimated elongation of Y shears of group A

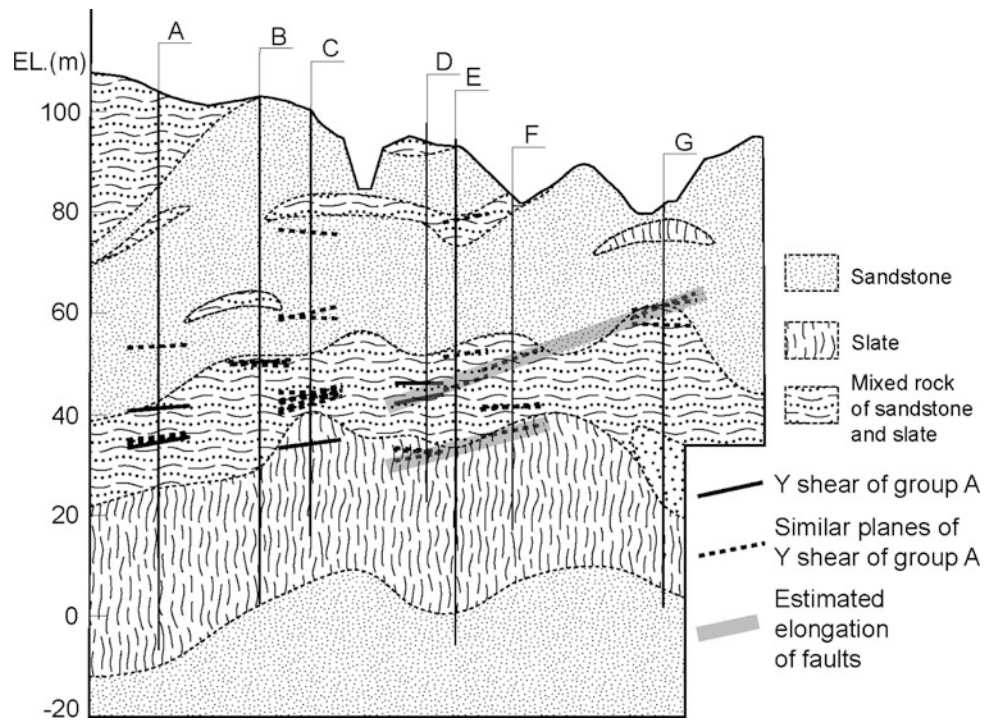
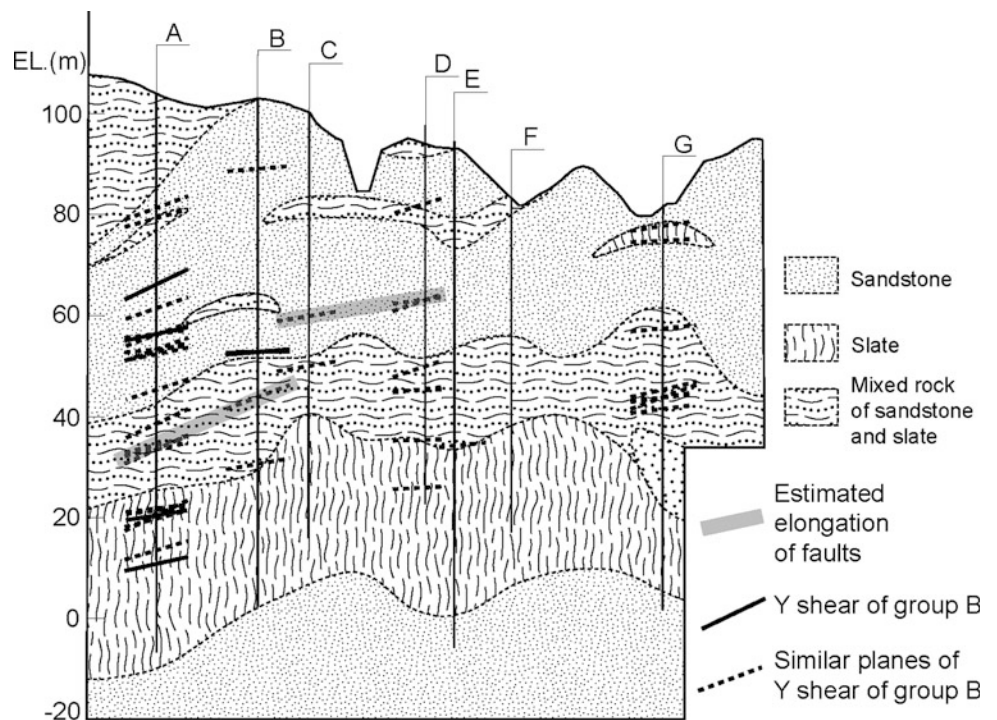


**Fig. 13** Estimated elongation of Y shears of group B



## 6 Conclusion

It is difficult to estimate the distribution and continuity of faults by drilled cores, because faults have composite planar fabric. A fault elongates along only the direction of Y shear.

The contact planes between a fault and its wall rock have various fabrics such as Y, R1 shears and P foliation, and so contact planes between a fault and its wall rock are not necessarily expressed by Y shear. Therefore, it is necessary to determine Y shear in order to accurately estimate the continuity of faults. Y shear and similar planes of Y shear

were determined using high-quality drilled cores in an example area belong to the Chichibu accretionary complex. It is considered that continuity was accurately estimated by determining Y shear and similar planes of Y shear.

---

## References

- Logan, J.M., Friedman, M., Higgs, N., Dengo, C., Shimamoto, T.: Experimental studies of simulated gouge and their application to studies of natural fault zones. USGS Open File Report 79-1239, pp. 305–343 (1979)
- Paterson, M.S.: *Experimental Rock Deformation, The Brittle Field*, 254p. Springer, Berlin (1978)
- Riedel, W.: Zur Mechanik geologischer Brucherscheinungen: ein Beitrag zum Problem der “Fiederspälten”: Zentralblatt für Mineralogie, Geologie, und Palaeontologie, Abt B, pp. 354–368 (1929)
- Rutter, E.H., Maddock, R.H., Hall, S.H., White, S.H.: Comparative microstructures of natural and experimentally produced clay-bearing fault gouges. *Pure. appl. Geophys.* **124**, 3–30 (1986)
- Stearns, D.W., Couples, G.D., Jamison, W.R., Morse, J.D.: Understanding faulting in the shallow crust: contributions of selected experimental and theoretical studies, In Carter, N.L., et al. (eds.) *Mechanical Behavior of Crustal Rocks, The Handin Volume*, vol. 24, pp. 215–229. American Geophysical Union, Geophysical Monograph (1981)
- Tchalenko, J.S.: Similarities between shear zones of different magnitudes. *Geol. Soc. Am. Bull.* **81**, 1625–1639 (1970)
- Wakizaka, Y.: Modeling of ground and points to note for modeling for engineering geology. In: *Proceedings of 2015 Symposium, Japan Society of Engineering Geology*, pp. 9–20 (2015) (in Japanese)

# Geologic Influences on Slope Stability and Foundation Design, Oroville Dam Spillway, California

Stephanie Briggs, Matthew Huebner, Hans AbramsonWard, Justin Cox, Jennifer Dean, Bryan Dussell, Holly Nichols, Brad von Dessonneck, Coralie Wilhite, and Justin Zumbro

## Abstract

Beginning in February 2017, California Department of Water Resources engineering geologists mapped newly exposed Middle to Late Jurassic Smartville complex rocks in the immediate vicinity of the eroded Oroville spillway. The purpose of the mapping was primarily to characterize rock strength, weathering properties, and discontinuities to support slope-stability analysis and foundation design. At the site, the Smartville complex consists of an assemblage of deformed, mafic metavolcanic rocks. Metamorphic fabrics consist of pervasive northwest-striking, moderately northeast-dipping foliation defined by alignment of characteristic greenschist-facies index minerals. Several orientations of prominent brittle shear zones were observed within the Smartville complex rocks; many of these appear to reoccupy pre-existing joint

sets and the pervasive northwest-striking metamorphic foliation. These shear zones strongly influence the slope stability and weathering profile of the foundation rock for two reasons: (1) they are often filled with clay, breccia, decomposed rock, or other weak material; and (2) these zones are planar discontinuities that permit water infiltration and concentrate chemical weathering within the adjacent metavolcanic rocks. This paper presents: (1) the magmatic, metamorphic, and deformational characteristics of the Smartville complex in the vicinity of the Oroville Dam; (2) an assessment of the geometry of mapped planar fabrics; (3) the nature of observed shear zones; and (4) potential crosscutting relationships that provide insight regarding the interpreted multi-phase deformation history at the Oroville dam site.

## Keywords

Smartville complex • Oroville • Spillway • Foundation mapping

S. Briggs (✉) · M. Huebner · H. AbramsonWard  
Lettis Consultants International, Walnut Creek, CA 94596, USA  
e-mail: briggs@lettisci.com

J. Cox · J. Dean · H. Nichols · B. von Dessonneck · J. Zumbro  
California Department of Water Resources, West Sacramento,  
CA 95691, USA  
e-mail: justin.cox@water.ca.gov

J. Dean  
e-mail: Jennifer.Dean@water.ca.gov

H. Nichols  
e-mail: Holly.Nichols@water.ca.gov

B. von Dessonneck  
e-mail: bradley.vonDessonneck@water.ca.gov

J. Zumbro  
e-mail: justin.zumbro@water.ca.gov

B. Dussell  
Division of Safety of Dams, California Department of Water  
Resources, Sacramento, CA 95818, USA  
e-mail: bryan.dussell@water.ca.gov

C. Wilhite  
U. S. Army Corps of Engineers, Sacramento, CA 95814, USA  
e-mail: coralie.p.wilhite@usace.army.mil

## 1 Introduction

Oroville Dam was constructed on the Feather River in the mid-1960s by the California Department of Water Resources (DWR) and is the largest dam and reservoir within the State Water Project. The dam structure contains two spillways: a gated, concrete-lined chute and a concrete monolith weir with an unlined spill area (Fig. 1). The gated chute is the primary spillway used on a regular basis (commonly referred to as the Flood Control Outlet, or the FCO Spillway) and the monolith weir is a backup structure designed for use in rare events (commonly referred to the Emergency Spillway) (Fig. 1).

On February 7, 2017, a hole formed in a portion of the concrete-lined spillway. Continued operation of the gated spillway caused extensive erosion and damage to the concrete structure. The areas of deepest erosion occurred in portions of the spillway that were mapped during original construction as

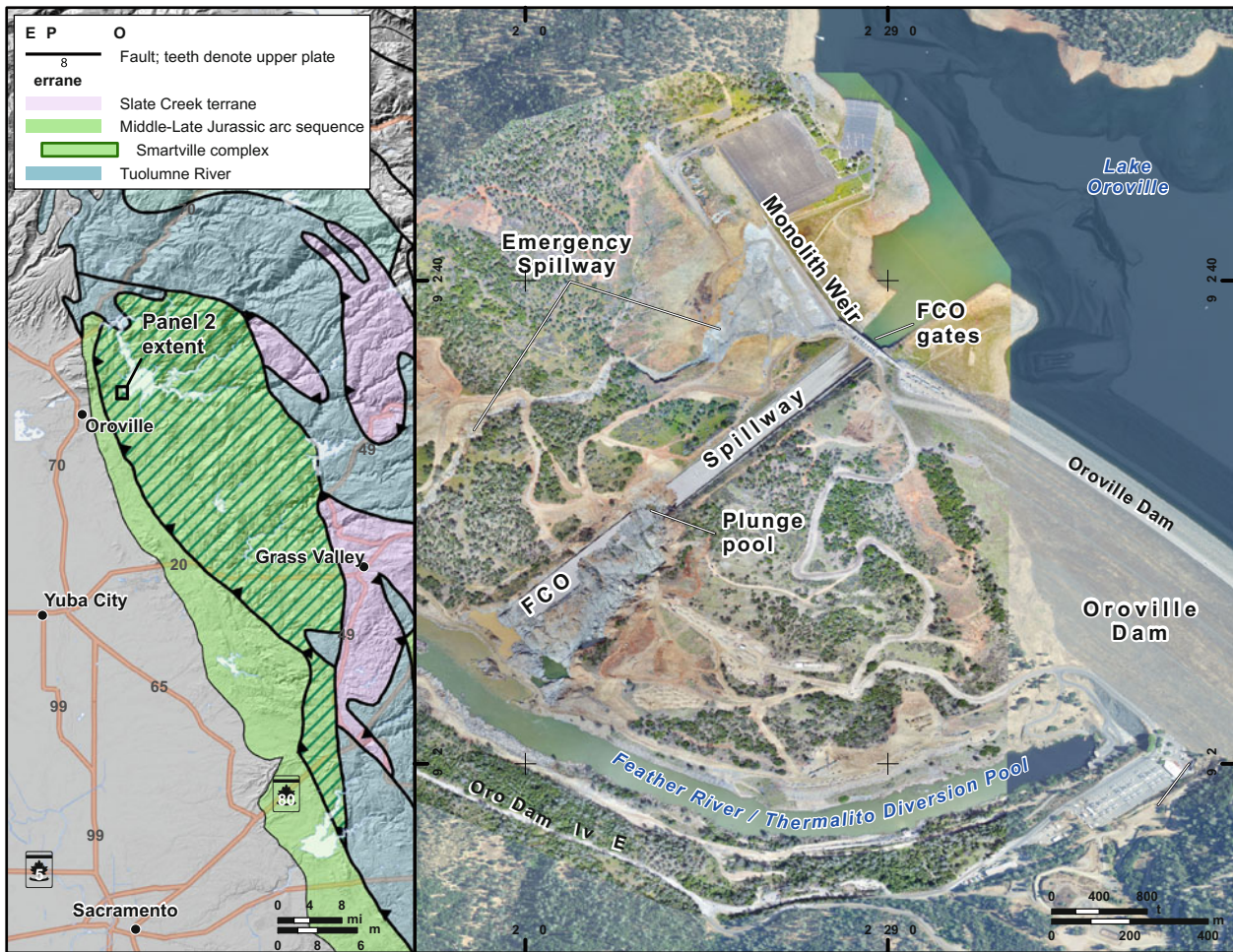


**Fig. 1** Tectonic map (Panel 1) and site location map (Panel 2). Tectonic map in Panel 1 modified from Snow and Scherer (2006)

strongly weathered to decomposed amphibolite rock. On February 12, 2017, during operation of the emergency spillway, rapid, deep headward erosion was observed in the northern portion of the unlined emergency spillway.

In March, DWR and its contractors began reconnaissance mapping of eroded exposures outside of the FCO chute. In May 2017, DWR began repair of the damaged gated chute and mitigation measures downstream of the monolith weir. During the 2017 construction season, DWR and consultant geologists documented geologic conditions exposed in final subgrade elevations through a detailed mapping program. The mapping of the FCO spillway for the 2017 construction season was completed in September 2017.

## 2 Geologic Setting

The Oroville Dam site is located in the western Sierra Nevada foothills within the Middle-Late Jurassic arc sequence of Snow and Scherer (2006; see Fig. 1), the westernmost belt of

rocks that comprise the Foothills Metamorphic belt. This sequence includes Jurassic-age ophiolitic rocks of the Smartville Complex (e.g., Schweickert and Cowan 1975; Menzies et al. 1980; Day and Bickford 2004). The Smartville Complex is bound to the east by the Wolf Creek fault (northern equivalent of the Bear Mountains fault zone of Clark 1960; see Edelman et al. 1989), which juxtaposes rocks of the Smartville Complex against the Tuolumne River and Slate Creek terranes (Edelman and Sharp 1989; Jura-Triassic arc belt of Snow and Scherer 2006). To the west, the Smartville Complex is juxtaposed above rocks of the Middle-Late Jurassic arc sequence along the Spenceville fault, which is interpreted by Schweickert (2015) as an east-dipping thrust fault. In general, the Smartville Complex consists of massive mafic lava flows, pillow basalts and sheeted dikes, and part of a plutonic suite (Menzies et al. 1980; Day et al. 1985). The Oroville Dam and spillways were constructed in an unnamed unit of the Smartville Complex; this unit consists of strongly foliated, greenschist-facies mafic metavolcanic rocks (amphibolite).

### 3 Methods

Geologic mapping was completed by teams generally consisting of two geologists. Base maps were created from drone-acquired aerial imagery immediately prior to geologic mapping; imagery was typically generated a few days prior to mapping as the exposure was cleaned. Mapping was conducted at a scale of 1:60. Map sheets were approximately 40 ft by 60 ft, and roughly 365 of these sheets were created and assigned a unique ID number that was tied to an overall project grid system. The primary objectives of the mapping were to characterize rock strength, weathering properties, and discontinuities to support foundation design and slope-stability analysis; data were recorded using the classification schemes employed by the DWR Project Geology Mapping Standards, modified from Barton and Choubey (1977), Brown (1981), Hoek (1996), and U.S. Bureau of Reclamation (USBR) (2001). Along with lithologic contacts and shear zones, zones of different weathering intensity and fracture density were mapped and assessed for continuity across map-sheet boundaries.

Geologists recorded attributes of every measured discontinuity, including width, shape, roughness, filling or coating, and any interpretation of past movement or sense of shear. Notable features in each map sheet were documented with photographs that included location, view direction, and a brief description. The GIS database developed for the project included aerial imagery, mapping linework, locations of each discontinuity measurement (~20/map sheet), attributes of each measured discontinuity, and locations of photographs.

## 4 Results

### 4.1 Geologic Mapping

#### Lithology

The dominant lithology exposed in the FCO spillway foundation consists of mostly fine- to medium-grained, greenish-gray to black mafic metavolcanic rocks that are locally porphyritic (Fig. 2a). Mineral assemblages consistently include characteristic greenschist-facies index minerals typical of a mafic volcanic protolith, and generally consist of:

chlorite + plagioclase + epidote + actinolite + quartz  
± carbonate ± sphene

Variations in mineralogy or texture are generally subtle and discontinuous, and can be traced along the strike of foliation over relatively short distances (meters to tens-of-meters); contacts between lithologic variations appear to be parallel to the pervasive foliation. Thin, discontinuous lenses of

medium- to coarse-grained metagabbroic rocks are common, and in places, are boudinaged (Fig. 2a). Volcanic flow boundaries, including basaltic flow breccias or pillow basalts, are not obvious in the exposures; however, pahoehoe-like structures are relatively common and occur along foliation planes (Fig. 2b). Additionally, thin interbeds of porphyritic mafic metavolcanic rocks occur throughout the FCO foundation; this interpretation is based on rounded plagioclase and amphibole ( $\leq 0.5$  mm) porphyroclasts, and relatively high quartz content (up to 20%).

### 4.2 Foliation

Exposed rocks in the FCO spillway foundation are strongly foliated. Foliation is relatively consistent throughout the exposure, generally oriented N15°W/65°NE (Fig. 3a). The foliation is defined by parallel alignment of elongate minerals, including chlorite and actinolite, which supports development of the foliation during greenschist-facies metamorphism.

### 4.3 Joints

The natural outcrops, water scoured exposures from February, and surfaces blasted during 2017 construction exhibit a blocky texture defined by the intersection of foliation and several joint sets (Fig. 2c). The most dominant joint set is subvertical with northeast-southwest strike (Fig. 3b). These joint surfaces are typically rough to slightly rough, and locally filled with calcite or iron-stained. Spacing of these surfaces vary from inches to approximately one to two feet.

Another dominant joint set strikes roughly east-west and dips approximately 25° to the south (Fig. 3b). This joint set typically has surfaces that are smooth to slightly rough, with common calcite to clay fillings with iron staining. This set is most obvious in vertical exposures such as along the edges of the FCO spillway. Joint spacing is roughly 3 ft or greater.

Additionally, joints commonly occur along foliation surfaces, striking northwest-southeast with ~60° dip, with conjugate joints forming at similar strike but with dips at high angles to the foliation surface (Fig. 3b). Foliation-parallel joints and the conjugate southwest-dipping set tend to be planar, slightly rough, and iron-stained, with spacing on the order of 3 ft or greater.

### 4.4 Shears

Many of the mapped discontinuities yield evidence for deformation or prior movement; these features are referred to as shears. Criteria developed to identify shears include:

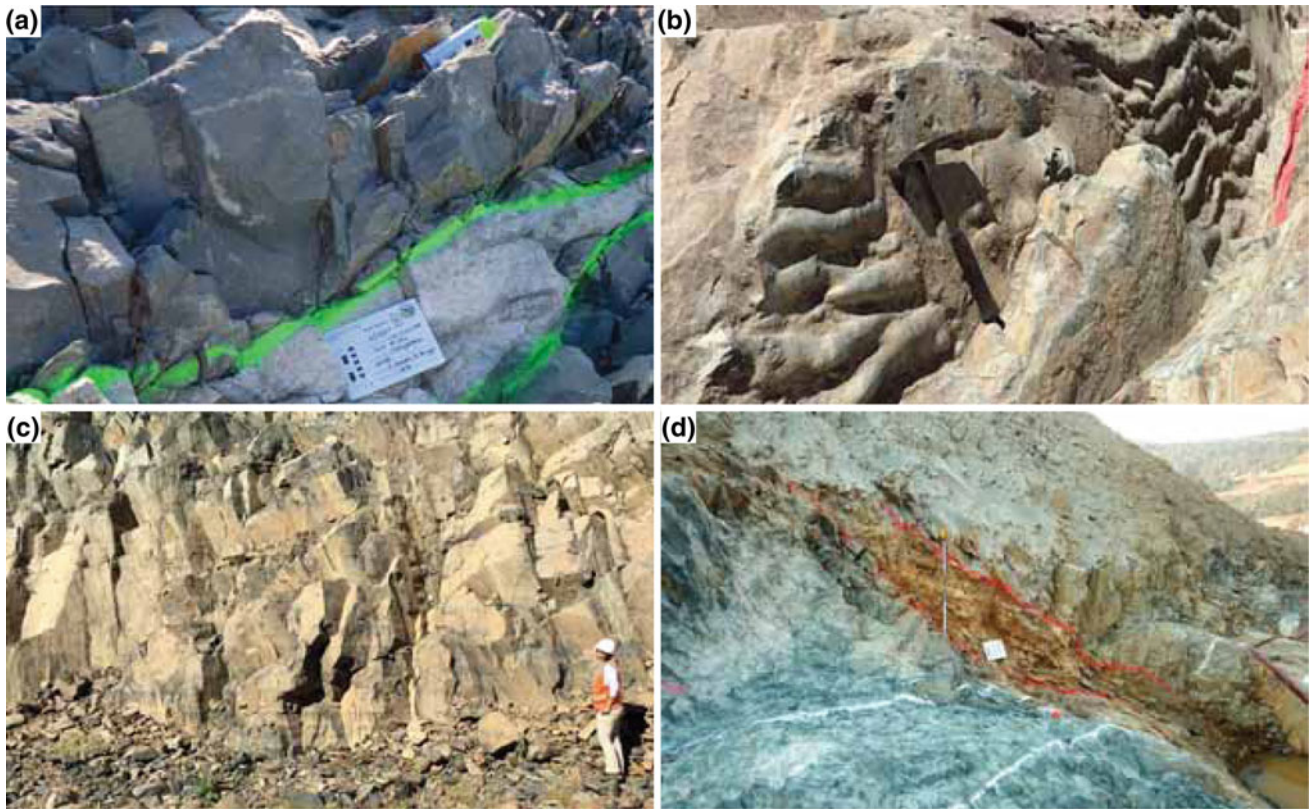


**Fig. 2** Outcrop photos. **a** Typical exposure of the fresh to slightly weathered amphibolite in the central and lower FCO spillway. The contact with a lens of metagabbro is painted green. View to the east, **b** primary volcanic pahoehoe-like structure on foliation plane. View to the southwest, **c** jointing within a vertical exposure of amphibolite yields a blocky texture. View to the northwest, **d** view to the south of intense weathering along a southwest-dipping shear zone in the FCO spillway wall

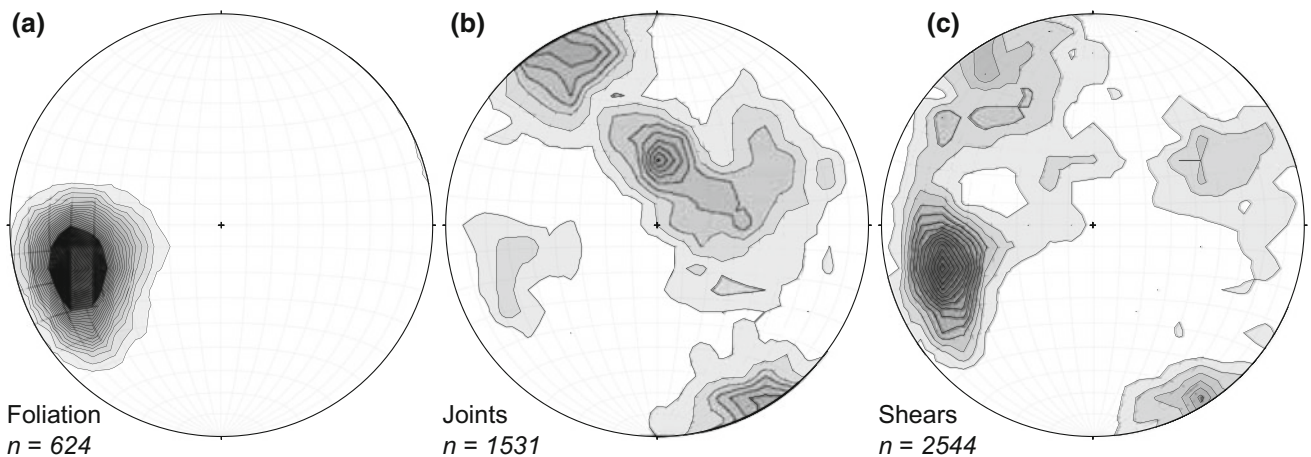


**Fig. 3** Contoured equal area stereonet projection of poles to discontinuities mapped in the FCO spillway. **a** Poles to foliation, **b** poles to joints, **c** poles to shears



(1) striations or slickenlines; (2) observed offset of bedding, joints, or other markers; (3) brittle secondary fracturing; or (4) textural evidence for mechanical grain-size reduction via cataclasis. The orientations of all mapped shears indicate four primary populations:

1. Shears striking N16°W, dipping 64°NE,
2. Shears striking N60°E or S60°W, with near-vertical dips ( $\geq 80^\circ$ ),
3. Shears striking N90°E, dipping gently 25°S, and
4. Shears striking S20–40°E, dipping 40–60°SW.

These populations indicate that many shears reoccupy existing planar fabric, (such as foliation or joint sets).

#### 4.5 Major Shear Zones

The vast majority of mapped shears had narrow apertures, are laterally discontinuous, and less than 2–3 in. in width. However, detailed mapping also revealed more prominent and well-developed shear zones throughout the FCO spillway (Fig. 4). These ‘major shear zones’ met one or more of the following criteria:

- Shear zone was continuous across tens to hundreds of feet
- Shear zone was greater than or equal to 6 inches wide and/or have associated zones of intensified weathering of greater than or equal to 1 foot, or

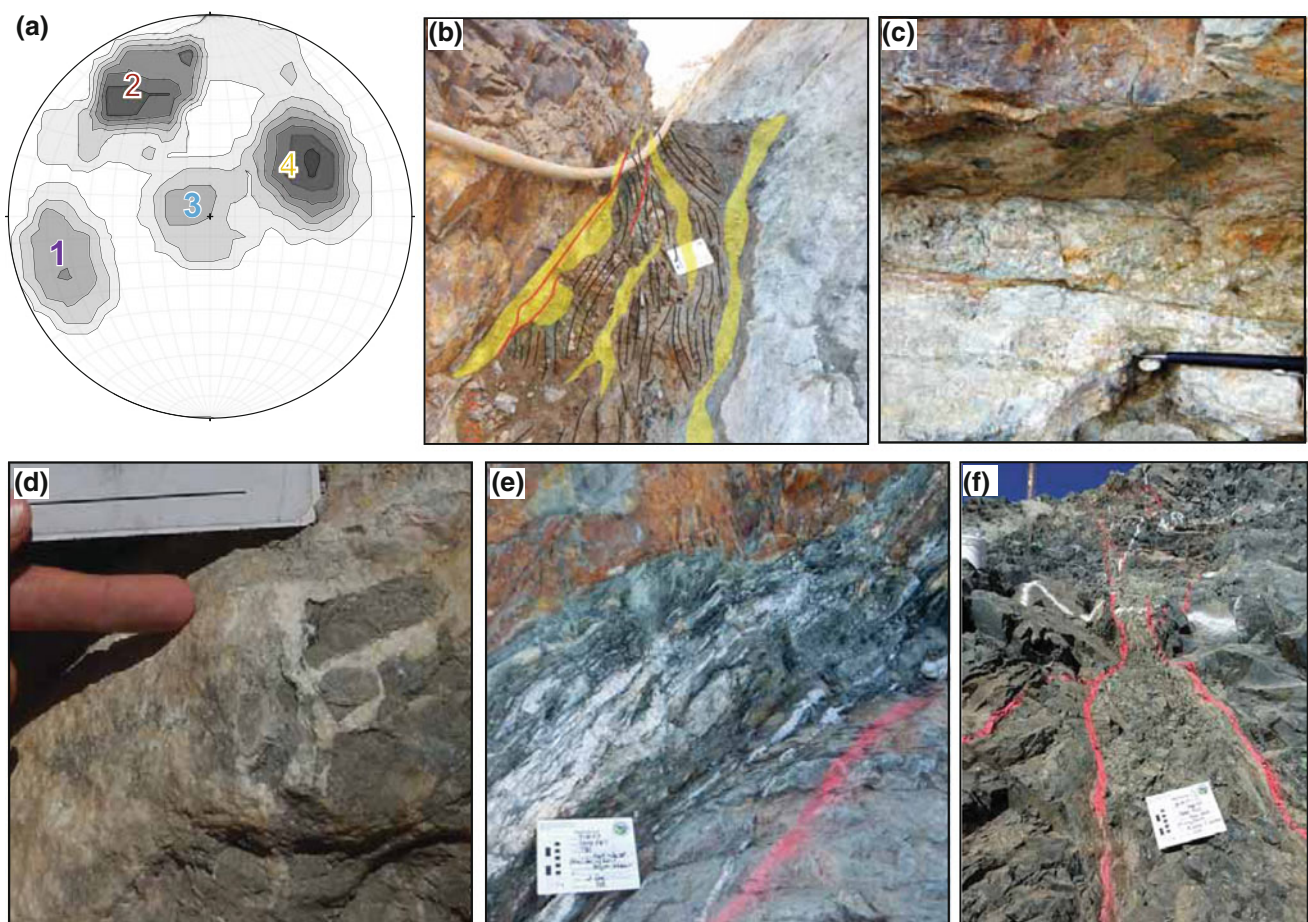


**Fig. 4** Major shear zones encountered in the FCO spillway. **a** Contoured equal area stereonet projection of poles to major shear zones. The colored numbers correspond to the shear zone populations discussed in the text. **b** View to the northwest of cohesive cataclasite developed along a southwest-dipping shear zone. **c** Cataclasite from shear zone shown in **b**, view to the southwest. **d** Photograph of brecciated amphibolite in matrix of quartz and calcite along a southwest-dipping shear zone. **e** View to the southeast of mylonite developed along a northeast-dipping shear zone. The photo board is approximately 9x12 in. **f** View to the north-northeast of slightly to moderately weathered, intensely fractured amphibolite along a northeast-striking shear zone. The shear zone is surrounded by darker gray, fresh to slightly weathered amphibolite that is moderately fractured (photo board approximately 9x12 in)

- Shear zone was associated with well-developed deformation-related features (e.g. Sibson 1977) that include mylonite, breccia, cataclasite, or gouge
- Shear zone was correlative with any of the shears identified in the foundation mapping conducted during the original FCO construction (DWR 1970).

Many of these shear zones extend across the full width of the FCO chute (approximately 200 ft), but some shears with orientations more spillway-parallel have been mapped across distances of up to 900 ft (Fig. 4f). These longer shear zones ranged from 0.5 to 5 ft thick, and were most commonly approximately 1 foot thick. Shear zone fabric indicates deformation occurred over a range of temperature and pressure conditions.

Mylonite zones mostly occur along foliation-parallel shear zones (Population 1), although less commonly occur along the moderately southwest-dipping shear zones (Population 4, Fig. 4a and e). Where present, mylonite zones include a steep (subparallel with dip of foliation) mineral stretching lineation primarily defined by elongate actinolite grains. Porphyroclast tails include chlorite and actinolite, which supports ductile deformation accompanied metamorphism at greenschist-facies conditions. Additionally, prominent quartz veins along a foliation-parallel mylonite zone include dynamic recrystallization textures that suggest crystal plastic deformation was accommodated via subgrain rotation, which suggests deformation temperatures between approximately 400 and 500 °C (e.g., Stipp et al. 2002).

Most of the mapped shear zones exhibit brittle characteristics that suggest cataclasis as the primary deformation mechanism (Fig. 4c). Shear-related rocks found within the mapped area are generally characterized by angular, brecciated pieces of amphibolite within a fine- to coarse-grained matrix of recrystallized quartz and calcite (Fig. 4d). Seams or anastomosing ribbons of clay within cataclasite zones likely represent weathering of fault gouge or fine-grained cataclasite.

#### *Orientations*

The major shear zones identified during detailed geologic mapping of the FCO chute can be grouped into four primary populations, based on orientation (Fig. 4a):

1. Northwest-striking, steeply northeast-dipping (foliation parallel, shown in purple). These shear zones locally include <1 m-thick mylonites (Fig. 4e). In many cases, mylonite zones are overprinted by brittle cataclastic fabric. Mineral stretching lineations in mylonites and slickenlines are typically subparallel to dip direction.
2. Northeast-striking, steeply dipping (shown in red). These shear zones are typically 1–2 ft wide, with clear evidence for brittle cataclasis and mechanical grain-size reduction

- (Fig. 4f). Chemical weathering along this group of shear zones is only slightly enhanced relative to surrounding rocks. Slickenlines and striations are typically down-dip.
3. Variably striking, gently dipping (shown in light blue). The gently dipping, low angle shear zones are most exposed in the deepest portions of the scoured plunge pool (see Fig. 4) that developed during operation of the FCO. These shear zones have variable traces on the topography of the scoured FCO spillway. These shear zones are characterized by brittle fault-rock fabrics, en echelon tension gash arrays, and thin veneers of lineated quartz veins along narrow ( $\leq 6$  in thick) exposures of amphibolite breccia. The lineations measured along these shear zones are sub-parallel to dip direction.
  4. Southeast-striking, moderately southwest-dipping (shown in gold). These shear zones are typically the most weathered, and of the mapped shear zones, most often contain decomposed rock and clay, and have the thickest zones of intensified weathering associated with them (Fig. 2d). Slickenlines are typically parallel to dip direction.

#### *Crosscutting Relationships*

The intersections of major shear zones were exposed at several locations within the mapped area. The clearest crosscutting relationship observed in the FCO foundation indicates an apparent 6 ft separation of a moderately southwest-dipping shear zone (Population 4) along a sub-vertical northeast-striking shear zone (Population 2). There are also many examples of a subvertical northeast-striking shear zone truncating the foliation parallel, northeast-dipping shear zones. However, in some locations the subvertical northeast-striking shear zones are truncated by foliation parallel, northeast-dipping shear zones (Population 1).

## 4.6 Weathering and Fracture Density

The depth and degree of chemical, in situ(?) weathering of the rock exposed within the foundation of the FCO spillway was variable. Detailed geologic mapping separated the degree of weathering into 6 categories, ranging from fresh to decomposed. Rock exposed in the portion of the FCO spillway downstream of the initial failure is characterized as the least weathered, typically ranging from fresh to slightly weathered rock, as the overlying, more weathered portions were weaker, and more likely to have been eroded and removed during operation of the FCO spillway between February and May, 2017. The rock in the central uppermost portions of the FCO spillway, where the spillway was demolished through blasting during construction, had much lower thicknesses of removed material, and thus was more likely to be moderately weathered. In general, the zones of

intensely weathered to decomposed material were confined to narrow, tabular zones along the major shear zones (see photo in Fig. 2d).

In most of the FCO spillway, the shear zones were easily recognized by their association with more intense weathering. Sheared amphibolite is typically discolored, weakened (in some cases it will crumble with light hammer blows or finger pressure), and iron stained in tabular zones parallel to and centered on a central shear zone (Fig. 2d). Gouge and the fine-grained portions of cataclasite are typically weathered to clay minerals. Weathering processes exploited these shear zones, most likely because greater fracture density provided a conduit for enhanced fluid flow (e.g., McCaig 1989).

---

## 5 Discussion

The foundation rocks of the Oroville FCO spillway have a geologic history that began with volcanism that occurred in or near an island arc oceanic setting proximal to Laurentia during the Middle to Late Jurassic Period (e.g., Menzies et al. 1980; Edelman and Sharp 1989; Day and Bickford 2004). Lithology and relict volcanic textures observed in exposures throughout the FCO spillway support the association with Jurassic Smartville volcanism, potentially with the “upper volcanic unit” of Menzies et al. (1980). Following deposition (or extrusion) of mafic volcanic and volcanoclastic rocks, the entire section was deformed and metamorphosed at greenschist-facies conditions. The pervasive foliation that dominates the exposure within the FCO spillway developed during metamorphism, based on the parallel alignment of greenschist-facies index minerals throughout the section. Foliation appears to be subparallel with lithologic contacts, and primary volcanic textures occur along foliation planes, which suggests transposition of primary and metamorphic fabric. Alternatively, rocks in the FCO spillway could represent a sheeted-dike complex that has undergone greenschist-facies metamorphism in an ocean-floor hydrothermal system (e.g., Mottl 1983), although this interpretation is not supported by (1) interbedded volcanoclastic rocks with contacts that are subparallel with foliation; (2) primary volcanic textures that occur along foliation surfaces; or (3) strong deformation that accompanied metamorphism.

During metamorphism, shear zones developed primarily along foliation planes, based on the occurrence of mylonites that include greenschist-facies index minerals within the fabric. Mylonites less commonly have been observed along the northwest-striking, moderately southwest-dipping shear

zones (see Fig. 4c). Steeply plunging, northeast-trending mineral stretching lineations and shallow, southeast-trending, short wavelength (<5 cm) crenulation axes along foliation planes are consistent with northeast-directed shortening.

The primary joint sets likely developed during exhumation of the section from depth. Northeast-directed shortening appears to have continued as the section was exhumed, based on (1) brittle overprint of cataclastic fabric on mylonites, and (2) steep (dip-parallel), northeast-southwest trending slickenlines on brittle shear surfaces that strike northwest, with dips to the northeast (foliation parallel) and southwest (moderate and shallow). The northeast-striking joints may represent tensile fractures that opened perpendicular to this northeast-directed shortening. Additionally, brittle shear zones that strike northeast (steep to subvertical dips) are compatible with this strain geometry, and may represent structures similar to tear faults. Cataclastic fabrics observed in brittle shear zones are typically cohesive (Sibson 1977), which suggests a minimum formation depth of 1–4 km. Mutually overprinting crosscutting relationships between the primary brittle shear zone populations indicates coeval deformation along these surfaces. Comparison of fabric diagrams of foliation (Fig. 3a), joints (Fig. 3b), and shear zones (Figs. 3c and 4a), in addition to numerous field observations, indicates that brittle shears and major shear zones reoccupied existing planar fabric within the exposed Smartville amphibolite. Lastly, contacts between weathering domains in the surrounding rocks are not offset at major shear zones. Thus, deformation along major shear zones likely pre-dates the development of the modern weathering horizon.

---

## 6 Summary

Geologic mapping used to document the lithology, structures, weathering, and fracturing of the Smartville complex exposed in the Oroville FCO Spillway foundation. The foundation rocks are Jurassic mafic metavolcanics that were metamorphosed at greenschist-facies conditions. Foliation developed during metamorphism, along with syn- to post-metamorphic shears and joints have approximately 4 primary populations: (1) northwest-striking, steeply northeast-dipping, (2) northeast-striking, near vertical dips, (3) east-striking, gently southwest dipping and (4) southeast-striking, moderately southwest-dipping. The observations from this mapping program, including the weathering designations, shear zone locations, and orientations of discontinuities have been utilized to inform the design and construction of the new spillway.

## References

- Barton, N., Choubey, V.: The shear strength of rock joints in theory and practice. *Rock Mech.* **10**(1–2), 1–54 (1977)
- Brown, E.T.: *Rock Characterization, Testing & Monitoring: ISRM Suggested Methods*, pp. 171–183. Pergamon Press, Oxford (1981)
- Clark, L.D.: Foothills fault system, western Sierra Nevada, California. *Geol. Soc. Am. Bull.* **71**, 483–496 (1960)
- Day, H.W., Bickford, M.E.: Tectonic setting of the Jurassic Smartville and Slate Creek complexes, northern Sierra Nevada, California. *Geol. Soc. Am. Bull.* **116**, 1515–1528 (2004)
- Day, H.W., Moores, E.M., Tuminas, A.C.: Structure and tectonics of the northern Sierra Nevada. *Geol. Soc. Am. Bull.* **96**, 436–450 (1985)
- Department of Water Resources, Project Geology, 1970, Final Geologic Report Oroville Dam Spillway, Project Geology Report C-38, 99p
- Edelman, S.H., Sharp, W.D.: Terranes, early faults, and pre-Late Jurassic amalgamation of the western Sierra Nevada metamorphic belt, California. *Geol. Soc. Am. Bull.* **101**, 1420–1433 (1989)
- Edelman, S.H., Day, H.W., Moores, E.M., Zigan, S., Murphy, T.P., Hacker, B.R.: Structure across a Mesozoic ocean-continent suture zone in the northern Sierra Nevada, California: Geological Society of America Special Paper 224, 56p (1989)
- Hoek, E.: Draft manuscript titled “Very poor quality rock masses” (1996)
- McCaig, A.M.: Fluid flow through fault zones. *Nature* **340**, 600 (1989)
- Menzies, M., Blanchard, D., Xenophontos, C.: Genesis of the Smartville arc-ophiolite, Sierra Nevada foothills, California. *Am. J. Sci.* **280**, 329–344 (1980)
- Mottl, M.J.: Metabasalts, axial hot springs, and the structure of hydrothermal systems at mid-ocean ridges. *Geol. Soc. Am. Bull.* **94**, 161–180 (1983)
- Schweickert, R.A.: Jurassic evolution of the Western Sierra Nevada metamorphic province. In: Anderson, T.H., Didenko, A.N., Johnson, A.N., Khanchuk, A.I., MacDonald, J.H. Jr. (eds.) *Late Jurassic Margin of Laurasia—A Record of Faulting Accommodating Plate Rotation*: Geological Society of America Special Paper 513, pp. 299–358 (2015)
- Schweickert, R.A., Cowan, D.S.: Early Mesozoic tectonic evolution of the western Sierra Nevada, California. *Geol. Soc. Am. Bull.* **86**, 1329–1336 (1975)
- Sibson, R.H.: Fault rocks and fault mechanisms. *J. Geol. Soc. (Lond.)* **133**, 191–213 (1977)
- Snow, C.A., Scherer, H.: Terranes of the western Sierra Nevada foothills metamorphic belt, California: A critical review. *Int. Geol. Rev.* **48**, 46–62 (2006)
- Stipp, M., Stünitz, H., Heilbronner, R., Schmid, S.M.: The eastern Tonale fault zone: a ‘natural laboratory’ for crystal plastic deformation of quartz over a temperature range from 250 to 700 °C. *J. Struct. Geol.* **24**, 1861–1884 (2002)
- U.S. Bureau of Reclamation (USBR): *Engineering Geology Field Manual, Second Edition: Volume 1*, 478p (2001)

# Microbial Changes of the Earth Dam Mechanical Properties and the Improvement of Them

Artem D. Demenev, Nikolay G. Maksimovich, Vadim T. Khmurchik, and Aleksey M. Sedinin

## Abstract

Earth dams are subject to raised liability because changes of their planned engineering and geological indices could lead to weakening or failure of the dam. Microbial processes are a significant but insufficiently studied factor affecting rock/soil properties. When large quantities of water-dissolved organic substances enter an earth dam, the increased activity of soil's microorganisms is able to cause a number of negative effects. We studied one of the largest earth dams in Perm region (Russian Federation) using a complex of field survey techniques. Some signatures of suffosion process were observed during field examination of the dam. Extensive laboratory investigations were carried out and the reasons of observed phenomena were determined. The study of microbial processes influence on dam's soil showed that its deformation modulus changed by a factor of two and more in some circumstances. Such changes of soil properties should be taken into account at planning stage of dam construction. Up-to-date microbiological techniques allow to improve properties of soils during exploitation of the dam. The laboratory experiment on biocementation (i.e. microbially induced calcite precipitation) of dam's soil showed 80% increasing of deformation modulus compared to natural untreated soil. This paper describes the results of laboratory investigations of dam's soil properties. The results of biocementation experiment are also discussed.

## Keywords

Soils • Microbiological influence • Mechanical properties • Biotechnology • Dam's stability

## 1 Introduction

Microbiological processes are a substantial but insufficiently studied factor affecting rock/soil properties. Microbiota activity influences solid, liquid and gaseous phases of soil, causing changes in acid-alkali and oxidative-reductive environment conditions and, consequently, physical and chemical soil properties (Bolotina and Sergeev 1987; Dashko et al. 2014; Demenev and Khmurchik 2014; Maksimovich et al. 2014, 2016; Radina 1973). When large quantities of organic substances enter the dam's body, rapid growth of microbiota could result in a number of negative processes and phenomena. Nevertheless, biotechnological methods of strengthening soils allow to improve their mechanical properties (DeJong et al. 2006; Weaver et al. 2011).

The purpose of this paper is to assess changes in mechanical properties of dispersive soils in the body and the basement of the earth dam caused by activation of microbiological processes, and to study the patterns of increasing deformation properties in sandy soils when biotechnological methods are used for their improvement.

## 2 Soils and Ground Water in the Study Area

The studied earth dam is constitutive part of one of the hydroelectric power stations of the Volga-Kama cascade and is located within an urban agglomeration in the Perm region. The dam was built by hydraulic inwash method and is composed of fine sands and gravelly sandy soils. The dam's basement is alluvial deposits represented by clays and heavy loams, fine sands and gravel-and-pebble formations. Clays and loams contain plant remains. The dam's basement also consists of lacustrine-boggy (bayou) sediments represented by clays and loams in high-plastic and fluid-plastic state, sludge deposits of the buried lake and bog muck. The thickness of alluvial deposits is about 14–17 m. Alluvial deposits (Q) cover the middle Permian (P<sub>2</sub>) and lower

A. D. Demenev (✉) · N. G. Maksimovich · V. T. Khmurchik  
A. M. Sedinin  
Natural Science Institute of Perm State University, Perm, Russian Federation  
e-mail: demenevartem@gmail.com

Permian ( $P_1$ ) rocks represented by interstratification of argillite, sandstone and limestone beds of varying thickness (see Fig. 1) (Mamenko 1967).

Waters in the dam's body have close hydraulic connection to alluvial horizon waters, which results in their similar hydrogeochemical content. Generally the dam body waters and alluvial swaters are calcium bicarbonate type, with up to  $1 \text{ g/dm}^3$  mineralization. In the areas where sulfates enter the alluvial water-bearing strata from underlying rock mass, anaerobic conditions induce the microbiological process of sulfate reduction identified by representative symptoms.

### 3 Methods

Examination of microbiological processes occurring in the earth dam from the engineering geology perspective would require the development of an integrated approach. Microbiological processes effect on geological environment is well-studied. But the universal approach to assessment of micriobiota activity effect on engineering geology indices is not developed. This paper focuses on the study of mechanical properties of soils and biotechnological method of their improvement; however, the entire bulk of the research includes an array of methods. Standard chemical analysis of 147 samples of water from the drainage system and from the observation wells in the dam was done by using 'Kapel'-104-T' capillary electrophoresis system (Russia) and UNICO spectrophotometer (USA). The gas-analyzer Drager X-am 7000 gas analyzer (Germany), Hanna (Germany) and Solinst (Canada) were used in soil gases survey. Mineralogical analysis of soils was performed on the X-ray diffraction analyzer "D2 Phaser" (Brucker, USA).

Physical-mechanical properties of the dam's soil were studied by using laboratory equipment measuring physical and mechanical soil properties. Laboratory microbiological studies of dam's water and soil were done also. Data were processed using special-purpose software: Surfer 8 (Golden Software), RockWorks 14, AutoCAD, Corel Draw etc.

Three wells deep were mechanically drilled in the dam up to 20 m: one well in the bed part and two wells in the plain part of the dam (see Fig. 2). Soils with undisturbed (monolith) and disturbed structure were sampled every meter in depth interval from 2 to 20 m to study their physical and strength properties A total of 45 soil samples was sampled and studied.

Up-to-date geomechanical conditions of the dam's body were studied. The simulation experiments were conducted to assess possible changes in physical and mechanical properties of loamy soils caused by activation of microbiological processes in the researched dam's body.

The first simulation experiment examined the effect of microbiological processes on mechanical properties of soils using enrichment cultures of aerobic heterotrophic and anaerobic sulfate reducing bacteria isolated from sampled soils. Soil samples were exposed to germ cultures up to 64 days during varying incubation periods.

This paper discusses the possibility to stabilize sands of the earth dam body using biocementation technology.

The second experimental set suggested exposure of the researched soils to additional urobacterial biomass to promote calcite sedimentation process. One of the sand biocementation method developments is application of a technology that uses native environment of soils sands introduction of external biomass (Gomez et al. 2014). The ability to decompose urea is generally inherent to

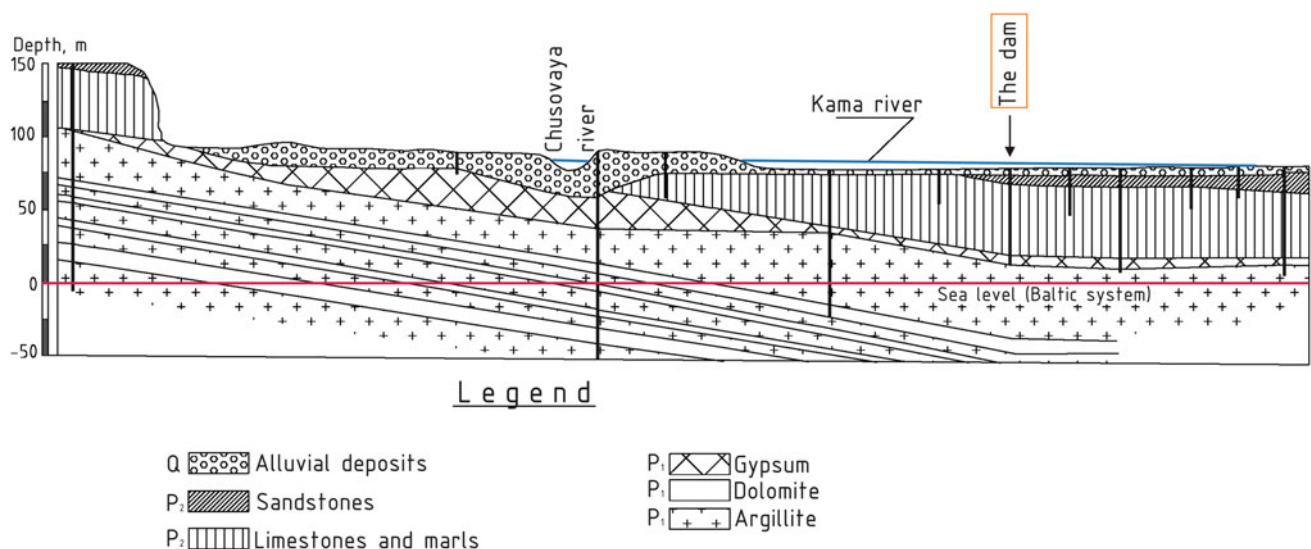


**Fig. 1** Geological cross-section of the study area



**Fig. 2** Location of wells in the dam

microorganisms; therefore experiments were conducted for improvement of sandy soils by way of calcite sedimentation due to the effect of native microbial flora, i.e. without introduction of additional biomass. Experimental soil samples were exposed to the solution in concentration of 60 ml per 1 kg of soil. The solution was prepared from distilled and river water and enriched with various concentrations of glucose, urea, calcium chloride ( $\text{CaCl}_2$ ), and solid beef-peptone extract as organic nutrient. In the first experimental set, additional biomass of urobacteria was also introduced. After 21 days of curing, soil deformation properties were determined by compression tests. In the course of the experiment, gas content was controlled in the artificial environment to determine intensity of microbiological processes. Upon completion of soils exposure, carbonate cementation and strength links formation was captured via microscopy.

#### 4 Results of Investigation

Active microbiological processes in the dam body are confirmed by nitrides concentration content in ground water. Their foci are scattered in the dam body, often in proximity to the lake buried during the dam construction, since the lake's bed deposits contained a lot of readily available organic matter for microorganisms. Based on the result of hydrochemical research, it was established that reservoir basin waters contain less total iron than waters in the dam's body. Besides, signature deposits of hydrous ferric oxides

were found at the drain bottom. In this case, iron can come from soils composing the dam base and body, containing iron in various forms. Active iron migration may occur in reducing conditions induced by microorganisms consuming oxygen in the course of their life-sustaining activity. It is notable that migration of mixed valence elements from soil may change their physical and mechanical properties, which, in its turn, impacts operational safety of the earth dam.

It has been established that bacterial exposure of soil samples, both to aerobic and anaerobic microorganisms, reduced soil modulus of deformation examined by compression tests (see Table 1).

For some soils two-fold reduction of the modulus of deformation has been observed as early as on the 29th day of the experiment (light clay—modulus of deformation changed from 3.41 to 1.56 MPa), while for other soils the modulus of deformation ( $E$ ) decreased only by 1.1 times even after 64 days of the experiment (light loam—modulus of deformation changed from 3.92 to 3.41 MPa). The instance of light silty clay demonstrates that exposure to anaerobic sulfate reducing microorganisms produced more effect on the soil modulus of deformation than exposure to aerobic heterotrophic microorganisms (as of the 29th day of anaerobic microbial exposure, the modulus of deformation decreased almost twice from 2.82 to 1.39 MPa, while the same level of the soil modulus of deformation change in the course of aerobic exposure was achieved only on the 64th day). After bacterial exposure, density of the soils has decreased, including dry unit weight.

**Table 1** Results of experiment to reduce of modulus of deformation

Well	Soil	Sampling depth (m)	Enrichment culture of microorganisms	Modulus of deformation (MPa)		
				Initial of test	After 29th day	After 64th day
1	Light silty clay	11.5	Anaerobic sulfate reducing bacteria	2.82	1.39	–
2	Light clay	6.2	Aerobic heterotrophic bacteria	3.41	1.56	–
3	Light sandy loam	6.5	Anaerobic sulfate reducing bacteria	3.92	–	3.41
3	Light silty clay	10.9	Aerobic heterotrophic bacteria	2.82	–	1.39

**Table 2** Results of experiment for improvement of sands using various concentrations of substances in solution

№	Base of solution	Concentration of substances (g/l)				Modulus of deformation (MPa)
		Glucose	CaCl <sub>2</sub>	Urea	Organic nutrient	
1	Distilled water	5	37.5	20	0.75	5.11
2	Distilled water	10	37.5	20	1.5	6.20
3	Distilled water	15	37.5	20	2.25	8.54
4	River water	10	37.5	20	1.5	9.49
5	Distilled water	20	37.5	20	3.0	8.68
6	Distilled water	20	75	40	3.0	8.03

Our results of the conducted experiments for improvement of soils using a biotechnological method showed that soils with introduced additional biomass had 35–80% higher modulus of deformation than abiotic controls.

Modulus of deformation value of sands improved without additional biomass is somewhat less but also effective as a method. Modulus of deformation (E) change has been compared via exposure to substances of varying concentration multiplicity. Substances from 1- to 4-fold concentration were introduced (see Table 2).

The amount of introduced components directly influenced the deformation modulus (E) increase in sands (modulus of deformation changed in several stages from 5.11 to 8.68 MPa with distilled water as solution base and 9.49 MPa when river water was used).

However, the samples with 4-fold concentration of substances in the solution manifested low increase of modulus of deformation versus 3-fold concentration (8.68 and 8.54 MPa respectively). This might be related to approximation to the maximum urea decomposition rate by microorganisms; hence further increase of urea concentration has no effect on increase of the modulus of deformation.

## 5 Conclusions

Our study reveals the tendency of soil mechanical properties to change due to microbiological exposure. It confirms the need to account for the possible changes in soils physical and chemical properties when ensuring safe operation of the dam or any other buildings and constructions, if their foundation suffers severe microbiological exposure. Meanwhile, not all microbiological processes produce negative effect on soil properties. The basics of microbiological process management, namely the activation of a certain group of native microbial population, allows to redirect the effect of microbiological processes and improve soils deformation properties due to carbonaceous biocementation. Two sets of experiments were conducted: with introduction of nutrient solutions and additional biomass into the researched soils, and with introduction of nutrient solutions sans additional biomass, i.e. by stimulating only the native microbial flora of the soils. Improved soils with additional biomass had 35–80% higher modulus of deformation versus abiotic controls. Modulus of deformation for sands improved without additional biomass is somewhat less but also effective as a method.



**Acknowledgements** The reported study was funded by RFBR according to the research project № 18-35-00042 and supported by the Ministry of Education and Science of the Russian Federation (Assignment No 5.6881.2017/8.9).

---

## References

- Bolotina, I.N., Sergeev, E.M.: Microbiological studies in engineering geology. *Eng. Geol.* **5**, 3–17 (1987) (in Russian)
- Dashko, R.E., Vlasov, D.Yu., Shidlovskaya, A.V.: *Geotechnical Engineering and Subsurface Microbiology*. MST, Saint-Petersburg (2014) (in Russian)
- DeJong, J.T., Fritzes, M.B., Nüsslein, K.: Microbially induced cementation to control sand response to undrained shear. *J. Geotech. Geoenviron. Eng.* **12**, 1381–1392 (2006)
- Demenev, A.D., Khmurchik, V.T.: The role of microorganisms in the migration of iron in clay soils. *Geology and Minerals of the Western Urals*, vol. 14, pp. 103–105. Perm State University, Perm (2014) (in Russian)
- Gomez, M., Anderson, C., DeJong, J., Nelson, D., Lau, X.: Stimulating in situ soil bacteria for biocementation of sands. *Geo-Congress* 1674–1682 (2014)
- Maksimovich, N.G., Khmurchik, V.T., Lazdovskaya, M.A., Demenev, A.D.: The complex of research methods to study microbiological activity in ground dams. *Vestnik of Saint-Petersburg University. Geol. Geogr.* **4**, 88–100 (2014) (in Russian)
- Maksimovich, N.G., Khmurchik, V.T., Demenev, A.D.: The role of microorganisms in elevating the turbidity of dam seepage water. *Power Technol. Eng.* **50**(1), 6–9 (2016)
- Mamenko G.K.: *Kama Dam on the Kama River*. Geology and Dams, vol. 5. Energy, Moscow (1967) (in Russian)
- Radina, V.V.: The role of microorganisms in the formation of ground properties and their tense state. *Hydrotech. Eng.* **9**, 22–24 (1973) (in Russian)
- Weaver, T.J., Burbank, M., Lewis, A., Lewis, R., Crawford, R., Williams, B.: Bio-induced calcite, iron, and manganese precipitation for geotechnical engineering applications. *Geo-Front.* 3975–3983 (2011)

---

**Part II**  
**Tunnels**

# Development of a System for Automatic Evaluation of the Geological Conditions of Tunnel Faces Using Artificial Intelligence and Application to a Construction Site

Ryosuke Tsuruta, Shinji Utsuki, and Masashi Nakaya

## Abstract

When constructing rock structures such as dams and tunnels, it is important to first ascertain in detail the geological conditions at the planned site during the preliminary survey stage, and to implement the optimal design according to these conditions. During construction, after evaluating the geological conditions found at the drilling surface and tunnel face, it will sometimes be necessary to sequentially revise the design and construction plans. In this respect, various studies using artificial intelligence (AI) have been carried out in recent years, and substantial advancement and labor-saving has been achieved in various evaluations, especially in industries outside of construction. This paper presents the details of investigations for constructing a system to automatically evaluate the geological conditions of tunnel faces by the convolutional neural network method, which is an AI image recognition technology that has been put to practical use in industries outside of construction, using face observation records and elastic wave velocities measured at the corresponding points as training data.

## Keywords

AI • Tunnel face • Elastic wave velocity • Automated evaluation

## 1 Introduction

When constructing rock structures such as dams and tunnels, it is important to ascertain the geological conditions at the planned site in detail, and to implement the optimal design and construction according to the conditions. Geological surveys and geophysical explorations at the survey and

design stage are conducted to evaluate the distribution of geological conditions of the planned site, and its engineering characteristics, and the structure (for example the dam foundation or tunnel support) is constructed based on the results. However, budgets for various investigations are limited at the survey and design stage, as is the precision of the above-mentioned geological survey and geophysical exploration itself. Thus, the detailed geological conditions are difficult to ascertain comprehensively at this stage (Civil Engineering Association Rock Mechanics Committee 1983; Civil Engineering Association Rock Mechanics Committee 1986).

By contrast, at the construction stage, the detailed geological conditions are verified directly at the actual drilling slope and tunnel face, and the differences between the conditions assumed in advance and the actual conditions are evaluated. It is important to sequentially review construction plans and designs, such as by considering additional construction measures in accordance with the situation.

Under such circumstances, various studies utilizing artificial intelligence (AI) have been carried out in recent years, and advancement and improved work efficiency have been achieved in various evaluations, especially in industries outside of construction (Nikkei Big Data 2017). Image recognition technology using AI is a method for automatically learning features of the appearance of the object to be evaluated from a large number of cases and optimizing and improving the recognition. This has been applied to applications such as automated driving, using automatic evaluation of onboard camera images, and the automated evaluation of carcinoma cells, which was previously carried out visually by doctors.

The convolutional neural network (CNN) method is an AI image recognition technology that is being utilized in industries outside of construction as described above. This paper presents details of investigations into the automation and advancement of evaluations of geological conditions at civil engineering work sites by applying the CNN method.

R. Tsuruta (✉) · S. Utsuki · M. Nakaya  
Hazama Ando Corporation, Tokyo, Japan  
e-mail: tsuruta.ryosuke@ad-hzm.co.jp

## 2 Issues Related to Geological Evaluations at Tunnel Construction Sites

- (1) Issues related to geological evaluations at the survey and design stage

Geological surveys of tunnels and large underground cavities begin with a literature search on prior geological surveys conducted in the area. With this information, geological surveys, such as ground surface surveys and boring surveys, are conducted according to the conditions present and the size of the structure, and geophysical explorations such as measurement of elastic wave velocity and resistivity are carried out in the ground. However, for extensive linear structures, including roads and railroad tunnels, depths of up to several hundred meters are planned, making it extremely difficult to ascertain the detailed geological conditions of the entire excavation site in advance due to survey costs and limitations on accuracy.

The New Austrian tunneling method (NATM) is used in tunnel design and construction. In this method, the tunnel is constructed by means of full tunnel face excavation. The most important task in this method is to cause the formation of a relieving arch in the mass, which turns it into a load-bearing element and replaces lining by installing deformable support (anchors, steel arches and shotcrete). For the design of the entire tunnel, engineering characteristics of rock deep underground at the tunnel excavation site are estimated based on the results of seismic prospecting and resistivity sounding from the ground surface. In this way, a wide range of geological conditions can be estimated relatively easily, and detailed investigations can be conducted of aspects such as the design of support patterns and evaluation of low speed zones and fault fracture zones. However, due to various limitations, there are many cases where differences between the support pattern established at the design stage and the result established after checking the geological conditions of the tunnel face during excavation result in design changes, which increases construction costs.

- (2) Issues related to geological evaluations at the construction stage

To deal with issues such as the design of tunnel support patterns, it is necessary to ascertain the geological conditions estimated at the preliminary survey stage prior to the start of construction, formulate an optimal construction plan according to the situation, and reliably evaluate differences from preliminary assumptions. Some cases require implementation of optimal additional measures according to the situation by observing the geological situation in more detail during excavation. The observation of geological conditions

during excavation is usually carried out by a trained and experienced engineering geologist once a day at intervals of several meters, and the results are organized as tunnel face observation data for evaluation items for the characteristic elements of the rock, as shown in Table 1. Then, because shotcrete is used at the drilling site, the condition in the vicinity of the excavation site is confirmed with reference to the tunnel face observation records when determining the rock on which to implement the study of the support pattern with the contractors on site. The evaluation is carried out using only the tunnel face for which the geological conditions can be directly confirmed. Although geological conditions at the site are appropriately processed in the observation record, each evaluation item such as compressive strength, crack frequency, and weathering of the rock (as shown in Table 1) is a quantitative evaluation with a range. In addition, as shown in Fig. 1, even though the correlation with the support pattern is verified for the tunnel face evaluation points calculated by weighting each evaluation item, the large scatter of the data is problematic. In contrast, in an increasing number of tunnel excavations, methods such as exploratory boring, drill logging, and various forward surveys of the tunnel face are applied to verify the condition of the tunnel face and the rock ahead of the tunnel face, in addition to the geological observations.

The location of ground sections unsuitable for tunnels such as faults and the distribution of large-scale spring water sources are predicted in advance, and the stability of the tunnel is secured by implementing additional countermeasures according to the situation. However, there are problems with this, such as cost, accuracy, and impact on the process from interrupting tunnel construction.

Based on the current situation and the issues described above, when constructing highly important underground structures in Japan, which has a particularly large overburden and complicated geological conditions, it is necessary to recognize that the information obtained from the preliminary geological survey results is limited. Also, it is necessary to conduct more efficient and effective construction according to the situation by ascertaining the actual geological conditions in more detail according to the geological information obtained during construction and geophysical exploration (Table 2).

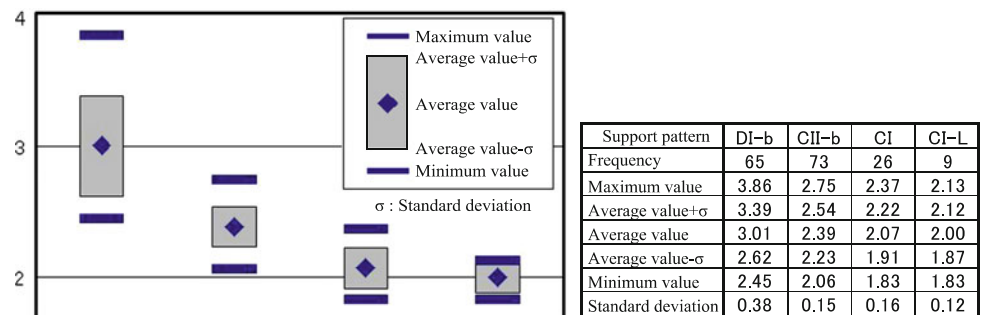
---

## 3 Development of an Automatic Evaluation System for Tunnel Face Geological Conditions and Application at Construction Sites

This section discusses the automatic evaluation system for tunnel face geological conditions. Various studies have been conducted in response to issues encountered at past tunnel

**Table 1** Example of geological condition evaluation items in a tunnel face observation record

	1	2	3	4
Compressive strength	Over 100 MPa You can not crush it with a hammer blow	100–20 MPa You can crush it with a hammer blow	20–5 MPa You can crush it with a light hammer blow	Under 5 MPa You can stab a hammer into it
Crack frequency	Over 1 m	1–20 cm	20–5 cm	Under 5 cm
Weathering	Not weathered	Discoloration along cracks Slight decrease in strength	Discoloration to the inside of the rock Significant decrease in strength	Being crushed Unconsolidated

**Fig. 1** Example of the frequency distribution of tunnel face evaluation

construction sites, as described in Sect. 2. We present details of (1) a study using past construction, carried out at the time of development; and (2) system development for actual operation at construction sites.

- (1) Study of an automatic evaluation system using past construction results

For this system, we performed system development with the training data taken from actual tunnel face observation records of the tunnel site and elastic wave velocities. These physical properties of the rock are measured at the excavation site and form the basis of support design. Here, we present an outline of the specific system and details of an actual investigation.

- (a) Outline of the evaluation system

The developed system uses AI image recognition technology and automatically evaluates the engineering characteristics of the rock from tunnel face photographs. During development, the AI was taught the relationship between the elastic wave velocity of the tunnel face obtained from a tunnel face tester survey (TFT survey) (Masashi et al. 2013), which is an elastic wave survey using a blast boring method that we developed, and tunnel face photographs at the corresponding points.

The Central Research Institute of Electric Power Industry (CRIEPI) rock classification is applied to the evaluation of

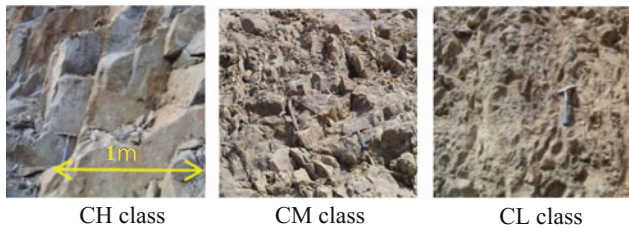
dam foundation rock and is still widely used in determining the engineering characteristics of rock (Koukichi 1990). This method ranks the engineering properties of rock from a combination of the following detailed evaluation items: the appearance of rock as empirically assessed by geological experts as graded on the scale of new rock (CH), weakly weathered rock (CM), and strongly weathered rock (CL) as shown in Fig. 2; the compressive strength of the rocky section as shown in Table 1; the frequency of cracking; weathering alteration and other changes. These are then grouped by class as shown in Fig. 2. In this rock grade classification, the relationship between strength, deformation, and other rock characteristics was confirmed from past rock test results as shown in Table 3, and the correlation with elastic wave velocity, which forms the basis of the tunnel design, is also found (Koukichi 1990).

The AI was taught the relationship between the tunnel face photograph showing the appearance of rock and its elastic wave velocity reflecting its engineering characteristics in accordance with the past evaluation method described above. The CNN method, which has been widely applied in other areas, was used for AI machine learning. This method iteratively learns based on the training data and automatically finds patterns hidden therein.

The CNN method uses a multi-layer neural network to construct, by computer simulation, a mathematical model that aims to recreate several characteristics seen in neural functioning. When images or other data are input to the CNN, learning is repeated in each layer as information is

**Table 2** An example of support pattern for road tunnels

Class of ground	Support pattern	Round length (m)	Rock bolt			Steel support			Spacing (m)	Thickness of shotcrete (cm)
			Length (m)	Spacing		Area of installation	Top heading	Bench		
				Circumferential direction (m)	Longitudinal direction (m)					
C I	C I	1.2	3.0	1.5	1.5	Top heading	–	–	–	10
	C I-L									
C II	C II-a	1.2	3.0	1.5	1.2	Top heading, bench	–	–	–	10
	C II-b						H-125	–		
D I	D I-a	1.0	3.0	1.2	1.0	Top heading, bench	H-125	H-125	1.0	15
	D I-b		4.0							

**Fig. 2** Example of rock grade classification

transmitted from an upper layer to a lower level. In this process, feature values that were previously set manually according to image, sound, or other data, are automatically calculated.

(b) Measurement of the elastic wave velocity training data by TFT survey

Generally, in an elastic wave survey using the refraction method, multiple geophones are installed on a survey line, elastic waves are generated by a small-scale blast, and the elastic waves arriving at each geophone are measured. The blasting device outputs an electric signal at the time of the blast, and the difference in the arrival time (initial shock arrival time) of elastic waves at the geophones is measured by starting the data logger simultaneously with the blast. Furthermore, a travel-time curve is created from the distance to the receiving point from the blasting point and the initial shock arrival time, the elastic wave velocity is calculated from the gradient.

The TFT survey system comprises a tunnel face tester, which aggregates measurement data and data from peripheral equipment (current sensor, seismometer, and IC recorder). The tunnel face tester outputs the signals from the current sensor and the seismometer to the IC recorder as a two-channel voltage signal. The current sensor is a non-contact sensor and, by being attached to the blast circuit, senses the current at the time of the blast and safely outputs a voltage to an independent circuit. Also, by using an IC recorder (DR-05, TASCAM; maximum resolution: 24 bits; maximum sampling frequency: 96 kHz) to record elastic wave data and placing it in a continuous recording state, it is possible to record the elastic waves and blast signals generated by blasting multiple times. The seismometer uses a geophone (GS-20DH, OYO; natural frequency: 28 Hz) in refraction seismic surveys. A rock bolt (usually  $L = 3\text{--}4$  m) placed in the sidewall as tunnel falsework is used as a waveguide and the seismometer is mechanically installed on the head of the rock bolt.

This method makes it possible to continuously measure the reflected waves from the front of the tunnel and the direct waves from the tunnel face blast point without interrupting tunnel construction.

The elastic waves generated in the tunnel excavation propagate through the rock around the tunnel, and the elastic wave velocity of the rock can be calculated from the distance between the tunnel face and the seismograph and the initial shock arrival time of the elastic wave. Figure 3 shows a conceptual diagram for the measurement of elastic wave velocity. Here, the elastic wave velocity between the tunnel

**Table 3** Relation between CRIEPI rock classifications and physical property values (Koukichi 1990)

Rock grade classification	Deformation coefficient ( $\text{kg}/\text{cm}^2$ )	Static modulus of elasticity ( $\text{kg}/\text{cm}^2$ )	Adhesive strength ( $\text{kg}/\text{cm}^2$ )	Internal friction angle ( $^\circ$ )	Elastic wave velocity ( $\text{km}/\text{s}$ )	Repulsion degree of the Schmidt test hammer	
A–B	Over 50,000	Over 80,000	Over 40	55–65	Over 3.7	Over 36	
$C_H$	50,000–20,000	80,000–40,000	40–20	40–55	3.7–3	36–27	
$C_M$	20,000–5000	40,000–15,000	20–10	30–45	3–1.5	27–15	
$C_L$	D	Under 5000	Under 15,000	Under 10	15–38	Under 1.5	Under 15

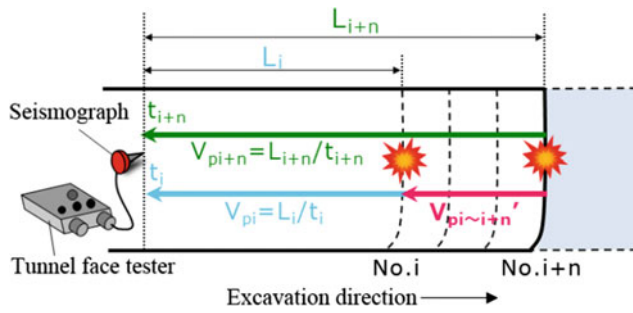


**Fig. 3** Conceptual diagram of elastic wave

face and the seismograph ( $V_{pi}$ ) is expressed by the following relation among the distance between the seismograph and the tunnel face ( $L_i$ ) and the arrival time of the initial motion of the elastic wave ( $t_i$ ).

$$V_{pi} = L_i/t_i \quad (1)$$

When elastic waves from a tunnel face advancing on a single straight line as the excavation progresses are measured without changing the position of the seismograph, the elastic wave propagation paths are considered to be the same as in prior measurements, and the elastic wave velocity at that time is considered to be a combination of the already measured section and the section with new progress. The section elastic wave velocity  $V_p'$  in the case where excavation has progressed  $n$  excavation lengths from the already measured section can be expressed by the following equation.

$$V'_{pi \sim i+n} = (L_{i+n} - L_i)/(t_{i+n} - t_i) \quad (2)$$

When the position of the seismograph is unchanged, the section elastic wave velocity  $V_p'$  can be obtained from the travel-time curve when the relationship between the measured distance  $L$  (tunnel face to seismometer) and the initial arrival time  $t$  of the elastic wave (travel-time curve) has a

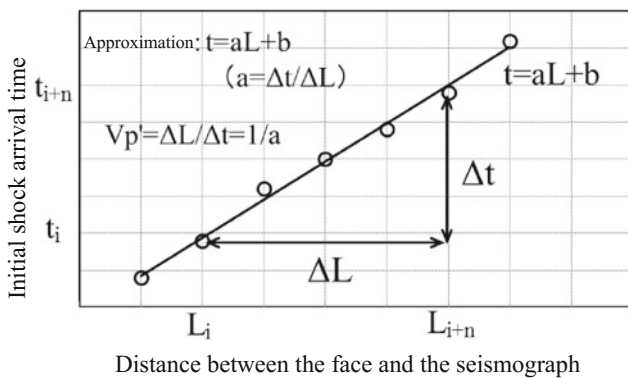


**Fig. 4** Travel-time curve

linear form, as shown in Fig. 4. The travel-time curve and the interval elastic wave velocity, respectively, are represented by the following equations.

$$t = aL + b \quad (3)$$

$$V_p' = dL/dt = 1/a \quad (4)$$

(c) Evaluation method using tunnel face observation records and elastic wave velocity

This study used 134 tunnel face observation records for a 1.2 km tunnel excavated in granite (a previous project by our company) to verify the validity of the evaluation results produced by the system. After letting the AI learn the relation between the photographs and the acoustic wave velocities at the tunnel face, a new facial photograph was evaluated. The AI extracted the similarity between the learned image and the features of the new facing, and instantaneously determined the elastic wave velocity. In an investigation such as the one described above, several tens of thousands of learning results are required. Thus, square frames with side lengths 0.5, 1.0, and 2.0 m were treated as one unit in a tunnel face photograph, and these were shifted by several tens of centimeters. By studying 280 points in a tunnel face, the required number of study points was secured. Within one frame, as shown by Table 1 and Fig. 2, rock grade was determined as a combination of compressive strength, crack interval, and degree of weathering of the rocky portion. Focus was placed on the crack interval, and the frame was set to be 50 cm or more, which can cover an interval of less than about 10 cm in geologically defective zones and intervals of more than about 20 cm in good zones.

For AI learning, the images were separated into three groups (CI, CII, and DI) based on acoustic wave velocity, and each group was divided into 3–4 subgroups. The automatic evaluation of feature similarities with images within the same category and differences from images in other groups were automatically evaluated. When making a determination using a new unknown image, after learning the required number of pieces, the group whose classification is most similar to the image is determined, and the relationship with the elastic wave velocity obtained at the point is regarded as the accuracy rate.

(d) AI elastic wave velocity automatic evaluation results

Table 4 shows the investigation results for frame sizes of 0.5, 1.0, and 2.0 m. The recognition rate of the three classifications indicates whether the relationship between the determination result and the actual elastic wave velocity is within the correct range of the three categories when the

**Table 4** AI elastic wave velocity automatic evaluation results

Frame size	Color mode	Classification	Accuracy rate (%)
32 × 32	RGB	3 categories	84.6
		10 subcategories	41.0
		10 subcategories (learned in advance)	77.6
64 × 64	RGB	3 categories	86.7
		10 subcategories	56.5
		10 subcategories (learned in advance)	99.1
128 × 128	RGB	3 categories	85.8
		10 subcategories	61.0
		10 subcategories (learned in advance)	97.0
64 × 64	Gray	3 categories	76.3
		10 subcategories	41.5
		10 subcategories (learned in advance)	95.9

trained AI makes a determination from an unlearned picture of a tunnel face. The recognition rate is about 85% in all frames, but the accuracy rate is highest in the 1.0 m frame. Thus, this investigation confirms the feasibility of evaluation of the ground to be carried out for each support pattern.

We confirmed the accuracy rate when each group was divided into 3 or 4, for a total of 10 subcategories, and found that there was an accuracy rate of about 40–60% for the subcategories. A trend was observed where the accuracy increased with increasing the size of the investigation frame. The accuracy rate for the training image obtained when letting the AI recognize a tunnel face photograph learned in advance is about 77% for a 0.5 m frame, but a high accuracy rate, 97% or more, was achieved for both the 1.0 m and 2.0 m frames.

In addition, to confirm the extent to which the AI is evaluating the color of the rock, an investigation was conducted on a 1 m frame with black and white versions of images used in the above investigation. As a result, the accuracy rate for the unknown image decreased by about 10 percentage points and by about 3 percentage points for a trained image as compared with a color image. Although the AI uses the color tone of the rock shown in Fig. 2 as determination data, better rock has more pronounced crack intervals and greater irregularities in form, whereas poorer rock has finer crack intervals and less irregularity in form. It is likely that the AI uses this as the primary determination data.

## (2) Construction of the site operation system

Based on the investigation using the past construction records, we constructed a system for practical on-site operation. Tunnel face photographs are taken immediately after completion of blasting, excavation, and shaping of the tunnel. When a photograph is transferred to the data center, the AI browses past construction cases and uses the relationship between the geological condition of the tunnel excavation

part, elastic wave velocity, and other factors to promptly return the estimated elastic wave velocity for the tunnel face.

As a result, the difference between the geological condition of the excavated part can be quantitatively evaluated directly in front of the tunnel face and the point in question. This makes it possible to receive qualitative judgments immediately after blasting, such as the necessity of spraying the tunnel face boundary, determination of the blast hole arrangement, and evaluation of the validity of the support pattern. Conventionally, these are made by on-site technicians and miners after conducting various investigations and surveys.

Immediately after an excavation, the AI automatically judges the tunnel face elastic wave velocity. It then compares this with the results of TFT survey by referring to exploration results at several points, as shown in Fig. 4, when the excavation has progressed several tens of meters. The data are accumulated sequentially in the machine learning server once the results are known. Then the AI once again learns the difference between the speed estimated immediately after excavation and the actual value, and the learning result is successively reflected in the real-time assessment of a new excavation site.

We have begun pilot operation of the above-mentioned system at one of our tunnel construction sites. In the future, we will continue to improve the system based on the needs of the site as confirmed during practical use, and we will establish a configuration to manage all 20 of our tunnel construction sites.

## 4 Conclusions

In this paper, we presented an outline of an AI system for automatic evaluation that aims to accelerate, streamline, and advance the geological evaluation of tunnel faces in tunnel



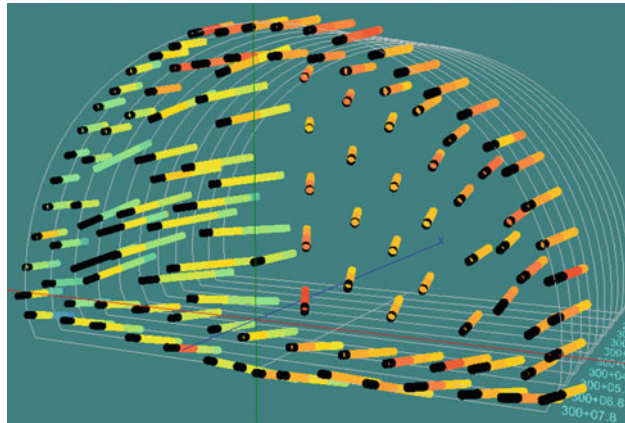


**Fig. 5** Drilling energy distribution map during construction of an excavation blast hole



**Fig. 6** Tunnel face image by RGB color model (left) and its weathering evaluation by hyper-spectral camera (right)

sites. We reported the results of investigations using data from existing tunnel in granite. In the future, we will increase our experience with various types of rock and continue to improve the system according to needs identified during on-site operations.

This study was carried out using tunnel face photographs taken with ordinary digital cameras. In the future, we will regularize factors such as the conditions of the camera and lighting at all sites and train the AI to recognize characteristic element images of the rocks shown in Table 1, such as drilling energy distribution maps mainly showing the hardness of the rock (Fig. 5) and spectral camera images showing weathering characteristics (Fig. 6). In this way, we will increase the accuracy rate of the system.

By conducting such study, it will be possible to optimize construction by automatically and instantaneously evaluating the geological conditions during tunnel excavation at a higher level of detail and then reflecting the results in setting the support and blast specifications. We intend to develop this system to realize automation of geological evaluations of slopes in dam base excavations and construction sites, and to achieve acceleration, automation, and advancement of evaluations and determinations at various other non-geological construction sites.

Through this, it may be possible to automatically conduct evaluations for selecting aspects such as tunnel supports and the protective surface for the excavation. Such evaluations have been mainly carried out by civil engineers at construction sites in the past, without a geological engineer present on site.

## References

- Civil Engineering Association Rock Mechanics Committee: Geological Survey of dam, p. 2. Japan Society of Engineering Geology, Tokyo (1986)
- Civil Engineering Association Rock Mechanics Committee: Rock Measurements and Geological Survey of Tunnels, p. 1. Japan Society of Engineering Geology, Tokyo (1983)
- Koukichi, K.: Introduction to Geological Engineering, p. 115. Doboku-kougakusha, Tokyo (1990)
- Masashi, N., Hiroyuki, Y., Shinji, U., Kazuhiro, O., Masayuki, S.: Development and illustration of system which evaluating geological condition around tunnel cutting face by the excavation blasting. Report on Tunnel Engineering Committee of Japan Society of Civil Engineers, vol. 23, pp. 209–215. Japan Society of Engineering Geology, Tokyo (2013)
- Nikkei Big Data: Learning from Google Deep Learning. Nikkei BP Inc., Tokyo (2017)

# Wear Phenomena in Tunnel Boring Machine (TBM) Hard Rock Drilling—Reasons and Consequences

Peter Ellecosta, Heiko Käsling, and Kuroschi Thuro

## Abstract

In hard rock tunnel boring machine (TBM) drilling, wear issues play a crucial role in the success of a tunneling project. Thus, excavation tools must be selected carefully and adapted to ground conditions. The shape and the material-quality of the cutters have to be adjusted and possible alterations of the tool, caused by the excavation process, must also be taken into account. This is because of the stress applied on the steel during the drilling process. Due to the knowledge of the wear processes by the interaction of the steel with the rock surface and the resulting material changes, it is possible to draw conclusions about the choice of the ideal excavation tool. In our paper, five basic macroscopically wear types will be distinguished: (1) abrasive/normal wear, (2) tapering, (3) mushrooming as (4) brittle failure of the cutter ring and (5) blockade of the roller bearing. These basic wear types lead to distinct cutter ring shapes which allow deriving some fundamental characteristics of the interacting rock types. In addition to an assessment on this macroscopic level, a microscopic analysis is necessary too. For this purpose, the surfaces and associated metallographic sections of worn disc cutters are analyzed. As a result, the tribological processes under the disc cutter, leading to tool wear, can be better understood. In summary, the investigations may contribute to a better understanding to make it easier choosing the proper TBM disc cutter for a distinct rock type in order to minimize the risk of tool related downtimes.

## Keywords

TBM • Hard rock TBM • TBM disc cutter • Wear • Wear phenomena

## 1 Introduction

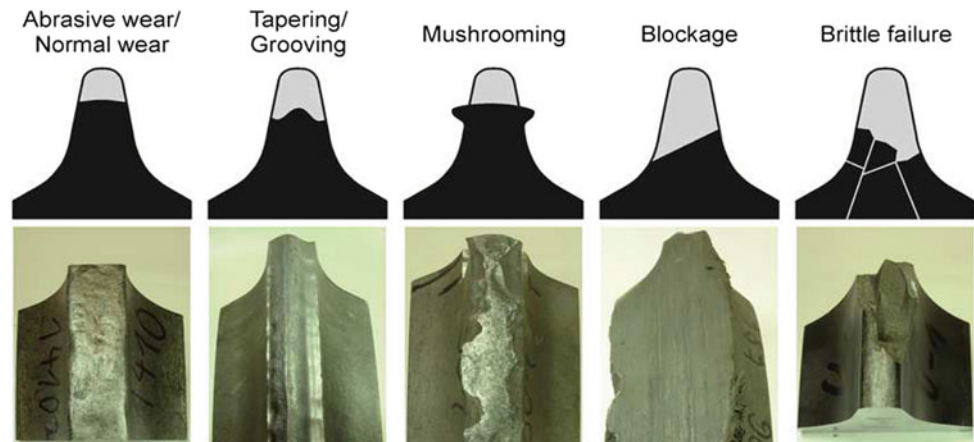
Hard rock tunnel boring machines (TBMs) have earned a pronounced distribution in modern tunnel construction. Hence, the prediction of the TBM tool wear and penetration have improved over time and reached a high level. However the requirements for such a prognosis are constant homogeneous and reliable ground conditions. This prognosis can reach an insufficient level if the ground is heterogeneous and variable. Firstly, this may lead to a selection of an inappropriate excavation tool and secondly to under- or overestimation of wear. Due to this, tool replacement, which is one of the major expense factors, can increase tremendously. The right choice of tools also plays an important role. In addition to shape and quality, the strength and hardness of the TBM disc cutters is crucial as well, but their characteristics are usually not given by the manufacturers yet. It is still common practice to select cutting tools on the basis of experience values. Another aspect, often underestimated and little noticed, is the transformation process that happens to the material after it comes into contact with the rock mass. This paper will present the disadvantages of choosing of an unsuitable tool and also wants to highlight the fact that a tool regarded as optimal still has certain vulnerabilities.

## 2 Macroscopic Wear Analysis

In TBM hard rock drilling, five basic wear types can generally be detected and distinguished visually even during operation in the installed conditions. This makes it possible to draw conclusions about the rock and the rock mass, even if the tunnel face is only poorly accessible or totally inaccessible. These five basic shapes (Fig. 1) include:

P. Ellecosta (✉) · H. Käsling · K. Thuro  
Technical University of Munich, Arcisstraße 21, 80333 Munich,  
Germany  
e-mail: p.ellecosta@tum.de

**Fig. 1** In the case of a visual wear analysis, five basic wear types can be distinguished. From these, conclusions on rock type (including some basic characteristics) and rock mass quality can be deduced



- Abrasive wear/normal wear (sometimes also asymmetrical)
- Tapering (sometimes with grooving and sometimes also asymmetrical)
- Mushrooming/formation of an impact head (sometimes with chipping)
- Special type I: blockage
- Special type II: brittle failure.

The *abrasive wear/normal wear* type is considered optimal because of its high degree of utilization, since the steel of the disc cutters is uniformly removed. Sometimes, the wear occurs asymmetrically because of unilateral load, especially in the caliber region (Thuro 2003; Käsling 2009). This wear type typically appears in compact rock mass, which consist of strong rock (classification according to ISRM—International Society for Rock Mechanics (1978)). Anisotropies in the rock and the rock mass are usually rather small.

A sharpening of the disc cutters (type *tapering*, sometimes with *grooving*) is characteristic for loose rocks or very weak to medium weak rocks (classification according to ISRM—International Society for Rock Mechanics (1978)) and very poor grain binding. Depending on the design of the cutter head and type of the tunnel boring machine, this wear type can also show an asymmetry in the wear pattern. Figure 1 also shows that if the width of the cutter has already increased as a result of progressive wear, it can also lead to *grooving*. This mainly depends on the cutter tip width, the penetration depth and the self-sharpening effect of the respective rock.

The formation of an impact head on the cutting ring, or also called *mushrooming* occurs when rock has very strong to extremely strong unconfined compressive strength (UCS) (classification according to ISRM—International Society for Rock Mechanics (1978)). Due to high UCS values, contact pressure has to be very high for an effective rock-cutting and -chipping. This results in a secondary and

cold forging of the cutting ring. When this happens, the steel is stressed and deformed beyond its yield point or elasticity limit and irreversible, plastic deformation occurs. If this mushroom-shaped deformation is very high, *chipping* may also happen, depending on the steel properties (hardness, strength and toughness, adjusted during heat treatment). In this case, large steel chips break off laterally in sizes from mm to cm (Fig. 1 center below). If this happens, there is a disproportionate loss of material which leads to significantly shortened service life.

In addition to the normal wear types, special shapes can also occur, which are not or only minimally dependent on geological conditions. The roller bearing might be blocked (special wear type I: *blockage*), so that the cutting ring cannot rotate anymore and is abraded on one side only. This can happen when stone-dust and stone-flour penetrate the seal and get into the bearing or lubricating oil leaks out. If a bearing becomes too hot and the oil can not sufficiently lubricate, it also blocks the cutting ring. The *blockage* wear type is therefore a blockage of the bearing and is caused by a problem of the base body.

The second special wear type is *brittle failure*. This means, bigger parts or the complete cutting ring crack suddenly and unpredictably due to brittle fracturing. Even if only a few parts of the cutting ring break off, the functionality is usually reduced to such an extent that the entire cutter needs to be replaced (also necessary in order to avoid major damage, for example, at the bearing or the cutter head). A rupture of the steel can be due to a faulty or insufficient heat treatment of the cutting ring during the manufacturing process. Another possibility is that the heat treatment, i.e. the adjustment of the hardness, strength and toughness, is not adapted to the lithological conditions. It is also possible that falling metal parts, e.g. built-up welds, wear-protective material or disc fragments are rolled over by the tools. This is an extreme dynamic overload that can lead to total failure of the cutting ring. However, we have found a certain correlation with geological conditions in a highly fractured rock

mass involving very hard and solid rock. In this combination, the tunnel-face is blocky. An explanation for this effect can be high primary stresses. In order to be able to excavate these kinds of rocks at all, very high contact-pressures and -forces must be applied to the cutting ring. However, since only parts of the chisels come into contact with the tunnel face due to its blockyness, the permitted force per cutter is exceeded, and thus the failure of the chisel is promoted.

### 3 Microscopic Background

In a current alpine tunnel project involving complex geological conditions, a research project conducted in cooperation with the contractor allowed us to analyze a large number of worn cutting rings. The advantage of this project was that the excavated rocks were weak to very strong and also cutting rings from different manufacturers were used. This gave us the opportunity to compare different manufacturers with a large number of diverse rocks together. Thus, we found all five macroscopic wear types during excavation works, that were mentioned in the previous chapter (Fig. 1). Over a total length of about 10 km, 20 areas were examined more closely. Of these, 32 disc cutters were taken at 9 areas and subjected to intensive microscopic analysis (Table 1). The procedure of sampling was that the worn and exchanged cutters were ordered by their macroscopic wear type. Based on this selection, up to 4 cutting rings per wear type were subsequently selected for micro-

scopic analysis as a representative sample. The results are summarized in this chapter.

The focus was to investigate the reason for the cutting ring alteration due to its interaction with the rock mass. With the help of reflected-light microscopy on metallographic cross-sections, possible changes (alterations) in the steel structure got visible. Moreover, these alterations can also be determined qualitatively to semi-quantitatively with the aid of hardness tests, what is briefly discussed below.

*Heavy duty (hd)* cutting rings are usually used in hard rock tunnel boring. The following details will refer to this cutting ring quality since this quality was present in the tested samples. The typical thing about *hd* cutting rings is that the material used is an easily hardened steel type which is hardened and tempered. Partially, the quench- and temper-process also occur several times e.g. to get a very fine-grained structure. An example for this is shown in Fig. 2. The microstructure in this image is fine-grained as well as isotropic and is called martensitic to bainitic. Comparing cutting rings from different manufacturers showed that there were slight variances: the steel structure was highly martensitic to pure bainitic and showed a difference in grain size. This means that there is a clear difference in the production process (forging and heat treatment) and thus a difference in quality.

When the cutting ring forms an impact head, a plastic material flow is macroscopically recognizable towards the flanks. This is also visible under the microscope (Fig. 3). This figure shows a clear more or less horizontal alignment

**Table 1** Overview of the investigations made

	Rock strength in the study areas (according to ISRM—International Society for Rock Mechanics (1978))			
	Weak–medium strong	Medium strong–strong	Strong	Strong–extremely strong
Investigated areas	3	6	4	7
Macroscopic wear type	Mainly tapering	Combination of tapering and abrasive wear	Mainly abrasive wear	Mainly mushrooming
Areas with detailed microscopic analysis	2	2	2	3
Cutter changes	4/7	5/9	15/11	34/16/21
Examined cutters per area	3× tapering/3× tapering	2× combination of tapering and abrasive wear/3× combination of tapering and abrasive wear	3× abrasive wear, 1× brittle failure, 1× blockage/3× abrasive wear	4× mushrooming, 1× brittle fracture, 1× blockage/2× mushrooming, 1× blockage/3× mushrooming, 1× brittle fracture
Presented examples	–/–	–/–	Fig. 2/ Fig. 4, Fig. 5	Fig. 3/–/–

**Fig. 2** Metallographic cross-section from the inside of a worn cutting ring (wear type: *normal wear*) with a martensitic to bainitic microstructure

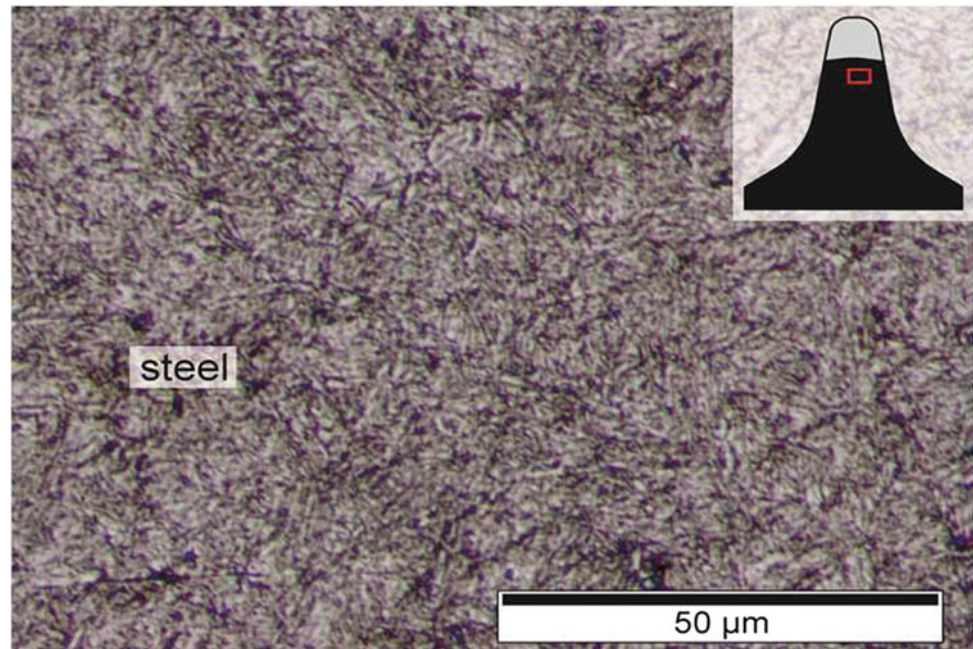
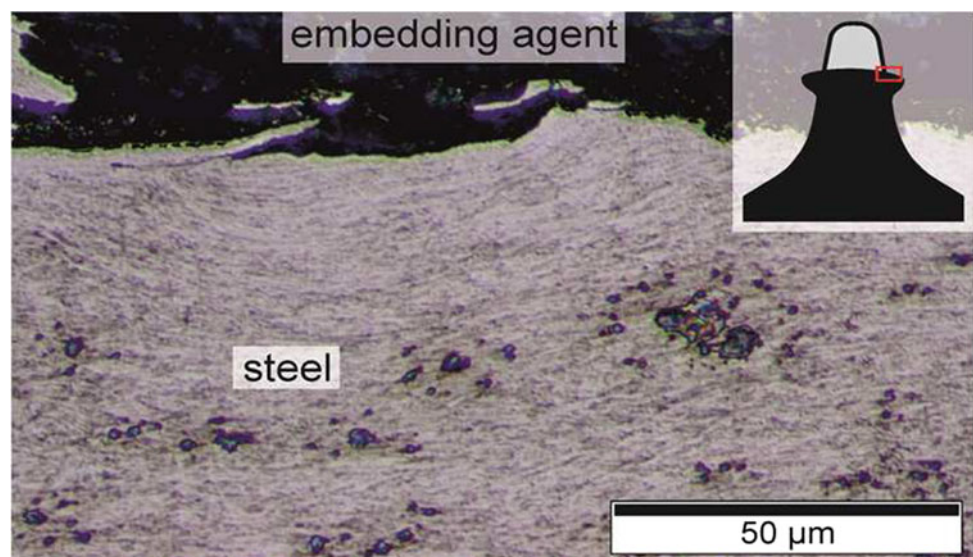


**Fig. 3** Metallographic cross-section from the edge of a worn cutting ring with the wear type *mushrooming*. The structure shows a clear horizontal alignment



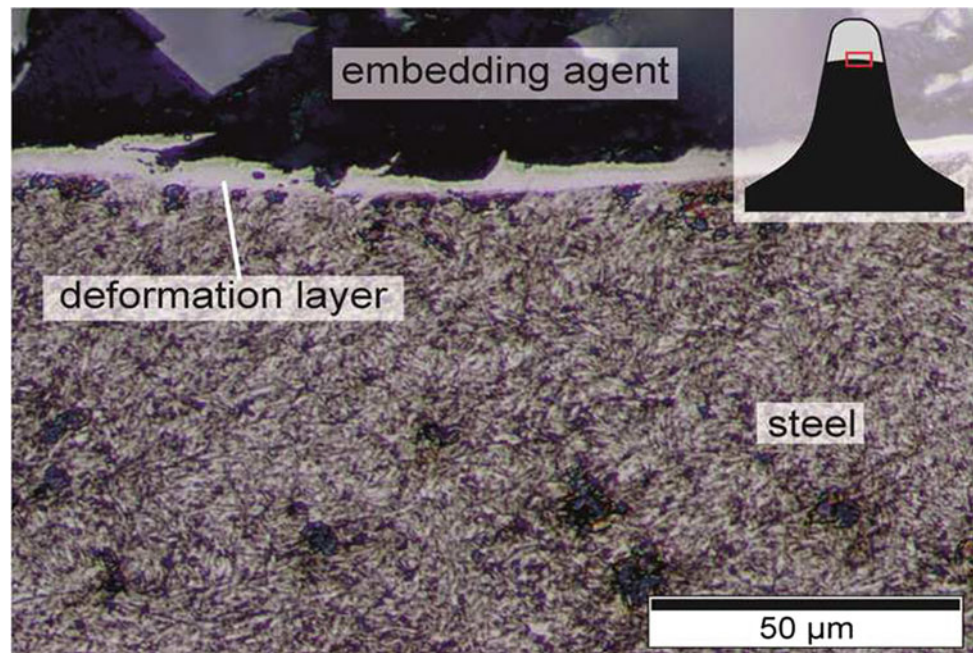
of the crystallites. At this point, the steel has a distinct anisotropy in the otherwise typically isotropic structure.

When looking at Fig. 4, it is noticeable that the microstructure at the edge of the cutting ring is very similar to the microstructure in the center: It also possesses the isotropic, martensitic to bainitic microstructure. However, a bright and structureless deformation layer of up to 10 µm is located on the former contact area between the cutting ring and the rock mass. This deformation layer was extremely deformed and heated up during use. This process is comparable to overheating that happens during grinding (*grinding burn*). These phenomena have often occurred on cutting rings with the macroscopic *abrasive wear* shape.

Excavated rocks in the analyzed project were mica-rich gneisses which typically had low to medium abrasive values but are classified as strong (classification according to ISRM—International Society for Rock Mechanics (1978)) with a medium unconfined compressive strength of 60–80 MPa. Reducing or even avoiding unwanted *grinding burns* altogether could be achieved by reducing the cutting wheel revolution number (RPMs) and lowering the tool temperature by a cutter wheel sprinkling during operation.

The contact area of a cutting ring with *abrasive wear* is shown on the two images of Fig. 5. The last excavated rock of the shown cutting ring was a mica-rich and strong gneiss (classification according to ISRM—International Society for

**Fig. 4** Metallographic cross-section from the edge of a worn cutting ring with *abrasive wear*. The structure is martensitic to bainitic, while a distinct deformation layer is located on the former contact surface of the tool



Rock Mechanics (1978)). Figure 5a shows a ground seepage like shear plane on the right, which was caused by a mineral grain penetrating into the steel. EDX analysis shows that it is a quartz grain. Due to the low reflectivity of quartz, the grain appears almost black on the upper image (reflected-light microscopy). On the SEM image (Fig. 5b), the material contrast between steel and quartz can be clearly seen by the back-scatter electron contrast method. It was also found that this phenomenon of mineral particles penetrating into the steel is not a rarity: this can also occur in combination with quartz- and feldspar-bearing rocks in the case of *mushrooming* and *tapering*.

## 4 Consequences

The effects resulting from cutting ring wear are manifold and often superimposed, which makes a systematic analysis difficult, especially in real construction operations. In general, cutting rings typically have a fine-grained isotropic structure after their production, including heat treatment. That means the steel is extremely strong, tough and hard and there is primarily no preferential direction for material failure. The discussed phenomena occurred only during the interaction with the rock surface.

To be able to understand the material-altering processes of the steel during the excavation process, the behavior of steel under load must be investigated in the laboratory. Figure 6 shows a schematic stress-strain diagram of a tensile test. As soon as the steel is stretched, the stress increases uniformly up to the (upper) yield strength, which is also

called the elastic limit. This is the range of elastic deformation. Only when this point is exceeded, *yielding*, i.e. plastic deformation can occur, depending on the steel structure and heat treatment of the material. The length of *yielding* is called *yield point elongation* or *Lüders elongation* (Gottstein et al. 2014). From a certain point onward, yielding ceases and the stress begins to rise again. This starts the zone of *strain hardening*, which is characterized by an arched curve and a plastic, permanent deformation. If there is no *Lüders elongation*, depending on the steel type, *strain hardening* begins as soon as the curve leaves the linear range. The plastic deformation can be shown microscopically in an alignment of the crystallites. In addition, the dislocation density, i.e. the number of defects in the atomic lattice increases. All of this leads to irreversible strain hardening while the residual formability is reduced. As a result, the hardness and brittleness increase as well, while the toughness decreases. The peak of the stress-strain curve corresponds to the tensile strength of the material. This is also the onset of *necking* in the tensile test. When this happens, the curve slowly diminishes until the final fracture happens, and material completely fails. The onset of *necking* corresponds to the point from which an overload occurs. This leads to (uncontrolled) crack growth (Ilschner 2016). Furthermore, pores and cavities can also form shortly before final fracturing.

If this behavior is transferred to the *mushrooming* wear type, it can be concluded that the range of plastic deformation is assigned to the range of *strain hardening*. Our own, as-yet unpublished investigations have shown that hardening of the material occurs. Unfortunately, this also includes a

**Fig. 5** Metallographic cross-section from the edge of a worn cutting ring with *abrasive wear*. **a** A quartz grain, penetrated into the steel, causes a ground seepage like shear plane in the steel. **b** SEM image (back-scatter electron contrast)

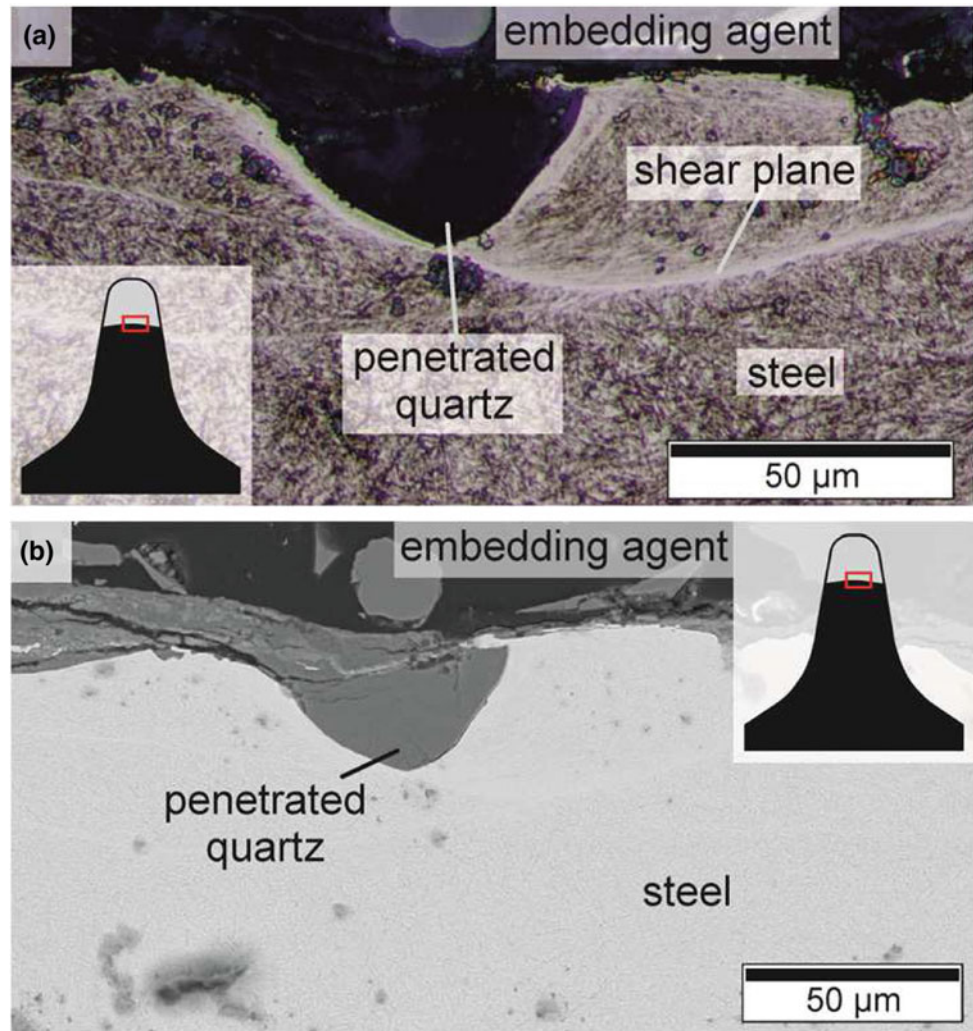
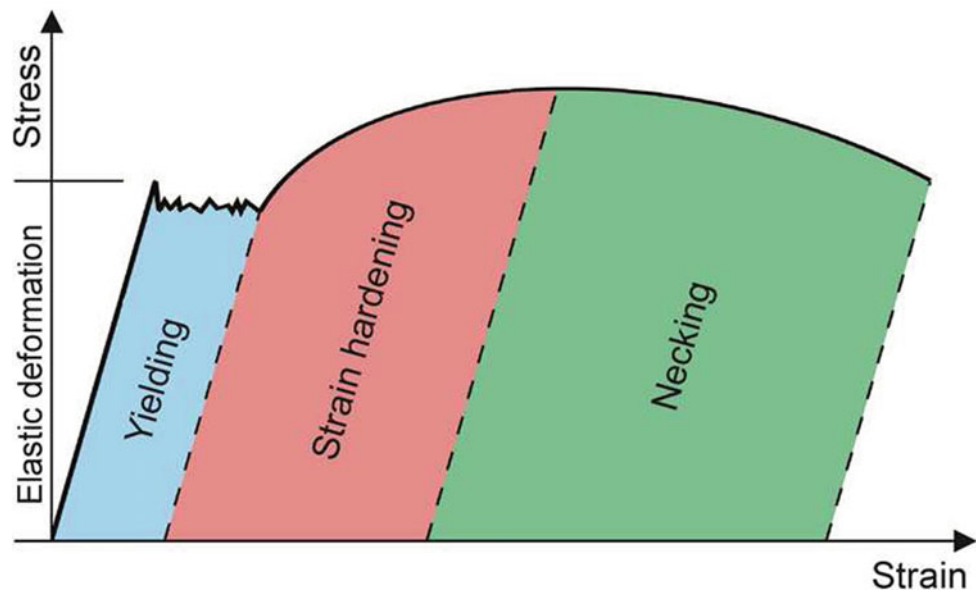


**Fig. 6** Schematic diagram of a tensile test with the typical areas that occur during loading (according to Weißbach and Dahms (2015))



reduction in toughness. In part, the deformation even extended to the point that the *necking* area was reached and clear cracks formed. This then led to premature, locally limited material failure due to *chipping*.

The formation of a deformation layer (Fig. 4) shows extreme deformation and heating on a microscopic scale in the rock contact area which reduces the hardness significantly. In addition to formation of this kind of bright and structureless deformation layer, there was a formation of a new hardening zone with higher hardness values below this deformation layer. In such zones, the hardness increased by an average of 5–15%. Due to higher hardness values, brittleness also increased significantly and results in a higher susceptibility to wear due to impact stress. As mentioned in the previous chapter, the phenomenon of a bright and structureless deformation layer intensified with strong but slightly abrasive rocks. This means that this deformation layer is probably also formed by other wear types and rocks, but removed by the higher wear immediately after formation. The low hardness of the deformation layer thus leads to increased material removal.

The penetration of mineral particles into the surface of the cutting rings is in principle possible if these minerals have a higher hardness than the steel. Own investigations showed that common *heavy duty* cutting rings have a mean Vickers hardness of 680–700 HV. Feldspar and quartz are mentioned as examples of common and harder minerals with a Vickers hardness of 720 (alkali feldspar) and 1280 HV (quartz) (according to Tourenq (1966)). As already mentioned, this phenomenon was observed in quartz- and feldspar-rich rocks and all macroscopic wear types. The problem with penetrating mineral particles is that it comes to intermittent stress and overloading of the steel by material displacement and a ground seepage like shear plane is formed (see Fig. 5). This leads not only to plastic deformation but also to hardening and embrittlement along this shear plane. Thus, the shear plane acts as a predetermined breaking point during continuous load by the usage. Because of crack growth, the chip is gradually released, which corresponds to markedly increased and unintended wear.

It must also be mentioned that the mechanical properties of steel are temperature-dependent. The resultant friction and wear during usage creates heat. Our measurements show temperatures exceeding 100 °C on caliber disc cutters (Rauch 2016). Punctual and for a short time, a significantly higher temperature is assumed and could be proven with the formation of a *grinding burn*-like deformation layer (Fig. 4). Because of the increase in temperature, the tensile strength

might initially increase, but would then gradually decrease again (Seidel 2014). In addition, the amount of elastic strain decreases in favor of a higher plastic deformation.

---

## 5 Conclusion

This paper demonstrates that that cutting rings with the same macroscopic wear shape are also very similar microscopically and that the altered properties of the steel in the contact area with the rock differ significantly from those in the rest of the cutting ring. Deformation and reshaping results in plastic deformation. These deformation areas often have increased hardnesses, which in principle should be regarded as positive in terms of wear. However, this also affects the toughness of the steel since the brittleness also increases, which has a negative effect on the tool wear. This material behavior leads to a failure of often larger areas in the cutting ring, e.g. for breaking of steel chips. Since this takes place during the cutting process, it cannot be prevented and ultimately represents a compromise between the material characteristics hardness, strength and toughness. The formation of a *grinding burn*-like deformation layer is the result of overheating, which can be reduced at least by a cutter wheel sprinkling during operation and reducing the cutting wheel RPMs.

Research and development are still necessary to improve cutting rings. A better understanding of the tribological influences and the processes occurring in the contact area between tool and rock should be developed. From our point of view, the wear processes for hard rock tunnel boring machines (hard rock TBMs) are still not sufficiently understood. While the effects and signs of wear are known in principle, there is still a lack of systematic and detailed investigations at a microscopic scale.

In practice, it is difficult to study the contact area of TBM disc cutters at tunnel face during active tunnel drive and advance. Due to the high contact pressures and the rotational movement of the cutter head and the cutting rings themselves, it is extremely difficult to install sensors or measuring devices or to route sensor signals backwards to a data logger. First attempts were made, e.g. by Entacher et al. (2013) and Schuller et al. (2015).

In addition, research must be carried out in cooperation with ongoing excavation works without interrupting the operation procedure. Another problem is the restricted manufacturer information policy regarding material characteristics of the cutting rings and heat treatment. This makes it



difficult to compare the tools of different manufacturers objectively, based solely on material characteristics. Thus, the suitability of different cutting rings only becomes apparent during use.

## References

- Entacher, M., Winter, G., Galler, R.: Cutter force measurement on tunnel boring machines—implementation at Koralmtunnel. *Tunn. Undergr. Sp. Technol.* **38**, 487–496 (2013)
- Gottstein, G.: *Materialwissenschaft und Werkstofftechnik*. 4th edn. 634pp. Springer, Berlin (2014)
- Ilschner, B., Singer, R.F.: *Werkstoffwissenschaften und Fertigungstechnik*. 6th edn. 511pp. Springer Vieweg, Berlin (2016)
- ISRM—International Society for Rock Mechanics: Suggested methods for the quantitative description of discontinuities in rock masses. *Int. J. Rock Mech. Min. Sci. Geomech. Abstr.* **15**(2), 319–368 (1978)
- Käsling, H.: *Bestimmung der Gesteinsabrasivität*. Unpub. Diploma thesis, Technical University of Munich, Munich (2009)
- Rauch, R.: *Einfluss des Gebirges auf die Vortriebsleistung und den Diskenschleiß beim tiefliegenden TBM-Vortrieb am Koralmtunnel (Österreich)*. Unpublished Masters thesis, Chair for Engineering Geology, Technical University of Munich, 73 pp. Munich (2016)
- Schuller, E., Galler, R., Barwart, S., Wenighofer, R.: The transparent face—development work to solve problems in mechanized hard rock tunnelling. *Geomech. Tunn.* **8**, 200–210 (2015)
- Seidel, W.W., Hahn, F.: *Werkstofftechnik*. 10th edn. 473pp. Hanser, Munich (2014)
- Thuro, K., Plinninger, R.J.: Klassifizierung und Prognose von Leistungs- und Verschleißparametern im Tunnelbau. In: *Dt. Ges. Für Geotechnik E.V. (eds.) Taschenbuch für den Tunnelbau 2003*, vol. 27, pp. 62–126. Glückauf, Essen (2002)
- Tourenq, C.: La dureté vickers des minéraux et des roches. *Bulletin Liaison Laboratoires des Ponts et Chaussées*, 19, réf 332 (1966)
- Weißbach, W., Dahms, M., Jaroschek, C.: *Werkstoffkunde*. 2nd edn. 597 pp. Springer Vieweg, Wiesbaden (2015)

---

**Part III**  
**Groundwater Resources**

# Diagenesis of the Upper Jurassic Carbonate Rocks Within Deep Geothermal Boreholes of the North Alpine Foreland Basin in Germany

Elena Mraz, Markus Wolfgramm, Inga S. Moeck, and Kuroschi Thuro

## Abstract

Upper Jurassic carbonates serve as a geothermal reservoir within the north Alpine foreland basin (so-called Molasse basin). The pore space development of the Upper Jurassic is an important factor for the success of geothermal projects or any other reservoir production. Hitherto, successful geothermal projects have cumulated in the area around Munich (Germany), as porosity and permeability of the southward dipping strata decrease with depth towards the Alps. The porosity decline can be caused by a change in facies or by a different grade in diagenesis, which has not been sufficiently analyzed yet. The diagenesis of the Upper Jurassic, especially the porosity, was analyzed in the southern part of the Molasse basin at depths less than 3.500 m. The first step in our approach was the microfacies analysis of rock samples to characterize the primary pore space. The microfacies results show a change in facies (transition zone) southwards, indicated by planktonic organisms in black, low porosity carbonate rocks. Due to Alpine tectonics and the formation of the typical wedge shaped north Alpine foreland basin, synsedimentary fractures and fault zones developed in the carbonates. Compared to the matrix those fracture and fault systems provide the main pathways for fluid flow. In the second step, diagenetic fluids were analyzed by fluid inclusion and cathodoluminescence measurements within calcite and dolomite crystals at different cement phases to understand the diagenesis of those deep buried carbonates. The microfacies analysis is important

for the identification of high porosity domains and should be considered in reservoir exploration.

## Keywords

Reservoir characterization • Diagenesis • Geothermal production • Carbonate rocks • Pore space

## 1 Upper Jurassic Carbonate Reservoir

### 1.1 Deep Geothermal Energy in Bavaria

The geothermal reservoir in Bavaria (south-east Germany) is provided by Upper Jurassic carbonate rocks, which host a warm to hot fluid within fractures and pore space. The Upper Jurassic is explored as a low enthalpy hydrothermal resource (Agemar et al. 2014) within the north Alpine foreland basin, the so-called Molasse basin. Hitherto, deep hydrogeothermal projects are concentrated in the area around Munich, Germany. There, the Upper Jurassic (Malm) reservoir is reached at depths of 2.500 to 3.500 m b.l.s. with fluid temperatures ranging between 65 and 150 °C. Due to the wedge shape of the foreland basin, the Upper Jurassic strata dips to the south, and therefore shows an increase in temperature and pressure southwards. However, the porosity and permeability of the strata decrease towards the Alps. Hence, for the success of geothermal projects, the pore space development of the Upper Jurassic carbonate rocks needs to be understood.

This paper aims to analyze and understand the porosity decline of the Upper Jurassic carbonates with depths towards the south. Nowadays, there are two theories about this decline; first it can be caused by a change in facies (depositional environment), and secondly by a different grade in diagenesis. Up to now, these possible causes have not been sufficiently analyzed for the deep buried Upper Jurassic, depths lower than 3.500 m. In the first part, the depositional

E. Mraz (✉) · K. Thuro  
Technical University of Munich, Arcisstr. 21, 80333 Munich,  
Germany  
e-mail: e.mraz@tum.de

M. Wolfgramm  
Geothermie Neubrandenburg GmbH, Seestr. 7A, 17033  
Neubrandenburg, Germany

I. S. Moeck  
Leibniz Institute of Applied Geophysics, Stilleweg 2, 30655  
Hannover, Germany

environment of the Upper Jurassic carbonate rocks is described, which were then affected in a second step by diagenesis.

## 2 Geology and Tectonic Evolution of the Molasse Basin

Today, the north Alpine foreland basin is composed of an Upper Jurassic and Cretaceous basement, which is underlain by Permo-Carboniferous troughs and Variscan crystalline complex (Lemcke 1988). The basin is filled by Cenozoic sedimentary rocks, alternating sequences of sandstone with claystone. The Upper Jurassic carbonates were deposited within an epicontinental sea connected to the northern part of Tethys. The carbonate rocks encompass limestones, marlstones and dolostones, which interfinger with each other (Meyer and Schmidt-Kaler 1989). The Upper Jurassic is further subdivided into a bedded and massive facies in southern Germany. The bedded facies contains alternating layers of limestone and marlstone, whereas the massive facies, also called reef facies, is built by reef and reef-like organisms, and can additionally be dolomitized. The dolomitization is a diagenetic process, which affects the carbonate rocks differentially. During the Cretaceous, the Upper Jurassic sediment rocks were exposed and eroded; consequently the Upper Jurassic strata could be partially karstified (Koschel 1991). Nowadays, the Upper Jurassic crops out at the Franconian and Swabian Alb in the north of

the Molasse basin and is reached at depths of around 5.000 m at the northern Alpine boundary.

The epicontinental Upper Jurassic sea (Franconian platform and Helvetic shelf) (Fig. 1) was connected by the Hessian Seaway to the north with the northern German Basin, to the west with the Paris Basin and to the south with the Tethys (Ziegler 1990). To the east and north east, the sea was restricted by the Bohemian massif and to the north and northwest by the Rhenish massif (Ziegler 1990) (Fig. 1). Accordingly, the biostratigraphy can be parallelized to the Paris Basin and the northern boreal realm of the Tethys. The depositional environment is a limestone sedimentation which is interrupted by marlstone layers. In the area around Munich, a large ooid platform is described by Meyer and Schmidt-Kaler (1989). The Upper Jurassic strata and reservoir can reach a thickness of up to 400 m (Pomoni-Papaioannou et al. 1989).

The Upper Jurassic depositional environment can be subdivided into five facies realms in the Molasse basin (Fig. 1). The two facies realms, Swabian and Franconian, are described at the type regions at the Swabian and Franconian Alb respectively in the north. To the south, the Swabian and Franconian facies merge into the Helvetian facies, which was deposited on the Helvetic shelf and not anymore on the Franconian platform (Fig. 1). To the west, the Swabian facies intersects with the northern facies of the Rauracien and the southern Argovian facies, in the area of Switzerland today. The Argovian facies further merges into the Helvetian facies to the south. The five facies realms are

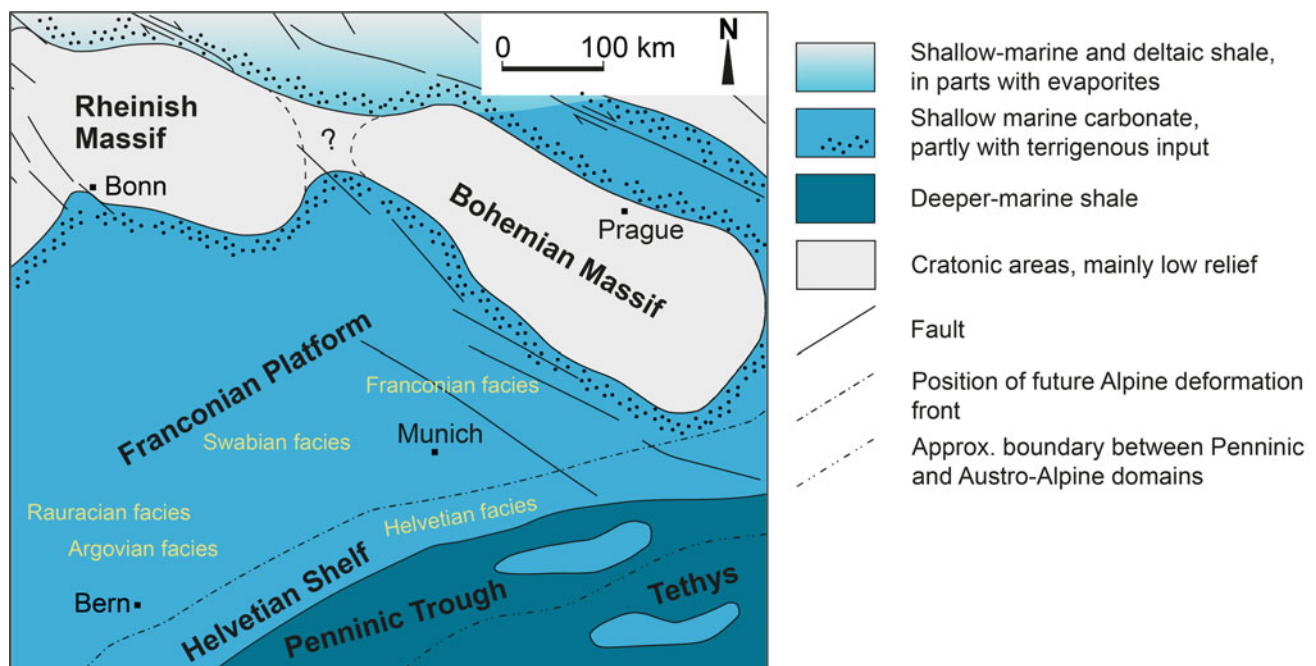


**Fig. 1** Paleogeography of southern Europe during the Kimmeridgian to Tithonian (middle to late Upper Jurassic) [after Ziegler (1990)]

classified by lithostratigraphy and the Rauracien and Argovian facies are additionally classified by the biostratigraphy after Gygi (2012). The lithostratigraphy is not applicable at boreholes, where rock chips are the only rock samples and bigger fossils, such as the ammonites necessary for the biostratigraphy, are rarely included. Consequently, the lithostratigraphy and biostratigraphy cannot be applied at the deep boreholes where only rock chips are available.

During the Upper Jurassic, the Franconian platform was located at the passive northern margin of the Tethys and was affected by synsedimentary tectonics parallel to the passive margin (Ziegler 1990). During the latest Jurassic and early Cretaceous, the landmass was uplifted and the Penninic ocean was closed (Ziegler 1990). At the beginning of the Cenozoic, the Alpine orogeny started, which developed the wedge shape foreland basin in the north and south of the Alps. Consequently, the Upper Jurassic strata was influenced by Alpine tectonics, which caused synsedimentary fractures and fault zones (Büchi et al. 1965). Those fractures and fault zones were in part reactivated during the Cenozoic and strike east-west, parallel to the Alps.

---

### 3 Diagenesis

The porosity development of carbonate rocks is mainly influenced by diagenesis. Up to now, diagenesis of the Upper Jurassic has been studied (Liedmann 1992; Liedmann and Koch 1990; Reinhold 1996, 1998b) at outcrops at the Swabian and Franconian Alb, around 200 km northwest of Munich. Those studies are now extended to the southern part of the Molasse basin with the Upper Jurassic at depths lower than 3.500 m. The southern, deeper part of this study is around 50 km south of Munich.

The diagenesis encompasses multiple processes which form a sedimentary rock from a sediment. Carbonate rocks are altered by diagenesis (Machel and Buschkuehle 2008; Reinhold 1998a), around one meter below the sediment surface, very early in the process. In the Upper Jurassic carbonate rocks, mineralization is the main diagenetic factor, containing recrystallization processes such as dolomitization and calcification, as well as silification and hydrocarbon migration. The mineralization occurs in the pore space of the matrix and is linked to fractures, evident by partly or completely filled calcite fractures.

Pore space can be increased by up to 13% by the process of dissolution or by dolomitization (Böhm et al. 2011; Machel 2004), resulting in an effective porosity of around 20% (Beichel et al. 2014). However, it can also decrease by recrystallization and precipitation. Therefore, it is necessary to characterize the influencing processes.

In addition, there is the process of karstification, which needs to be separated from the term dissolution. Karstification phenomena, such as caves, are described for Upper Jurassic carbonate rocks by Frisch and Huber (2000), very critically by Villinger (1988) for outcrops, and were assumed for one borehole within the Molasse basin. However, karstification is not present within the Upper Jurassic rocks of the Molasse basin.

For precipitation of crystals and for some recrystallization reactions, fluid flow is necessary, like the process of dolomitization with  $Mg^{+2}$ -rich fluids. Those fluids can be stored in fluid inclusions within the crystals. Primary fluid inclusions contain the present fluid during the growth of the crystals. On the other hand, secondary fluid inclusions are along former fracture planes, and represent fluids at a later stage. In addition, the relative age of the fluid inclusions is analyzed by cathodoluminescence. Cathodoluminescence of crystals is caused by characteristic lattice defects of foreign atoms during diagenesis (Boggs and Krinsley 2006).

---

### 4 Methods

To analyze and characterize the processes which cause the porosity decline, rock samples of the Upper Jurassic in the Molasse basin were used. The rock samples were either rock chips (cuttings) or drill cores. The rock chips were produced in the drilling mud during drilling and were influenced by the drilling process. Rock samples of the Upper Jurassic carbonate rocks were from deep boreholes distributed all over the Molasse basin. Drill cores and cuttings were made to thin sections, which were half-colored with Alizarin Red S. The thin sections were analyzed by a polarization microscope and described according to rock color, microfossils, and texture (Dunham 1962; Folk 1959, 1962). The microfacies was analyzed by microfossils to determine the depositional environment, and further the primary pore space was described.

The diagenetic fluids were evaluated in fluid inclusions using microthermometry combined with cathodoluminescence. The fluid inclusions were located within calcite or dolomite crystals along growth zones or at former fracture planes. Therefore, it was possible to describe the evolution of the diagenetic fluids. In addition, the cathodoluminescence could determine, using a cold cathode, the relative age of the different cement generations. Using microthermometry at salty aqueous two-phase fluid inclusions, the salt content and minimal trapping conditions (T, P) could be measured (Goldstein 2001). The minimal trapping conditions were determined by the homogenization temperature, where the vapor phase homogenizes to the liquid phase in a

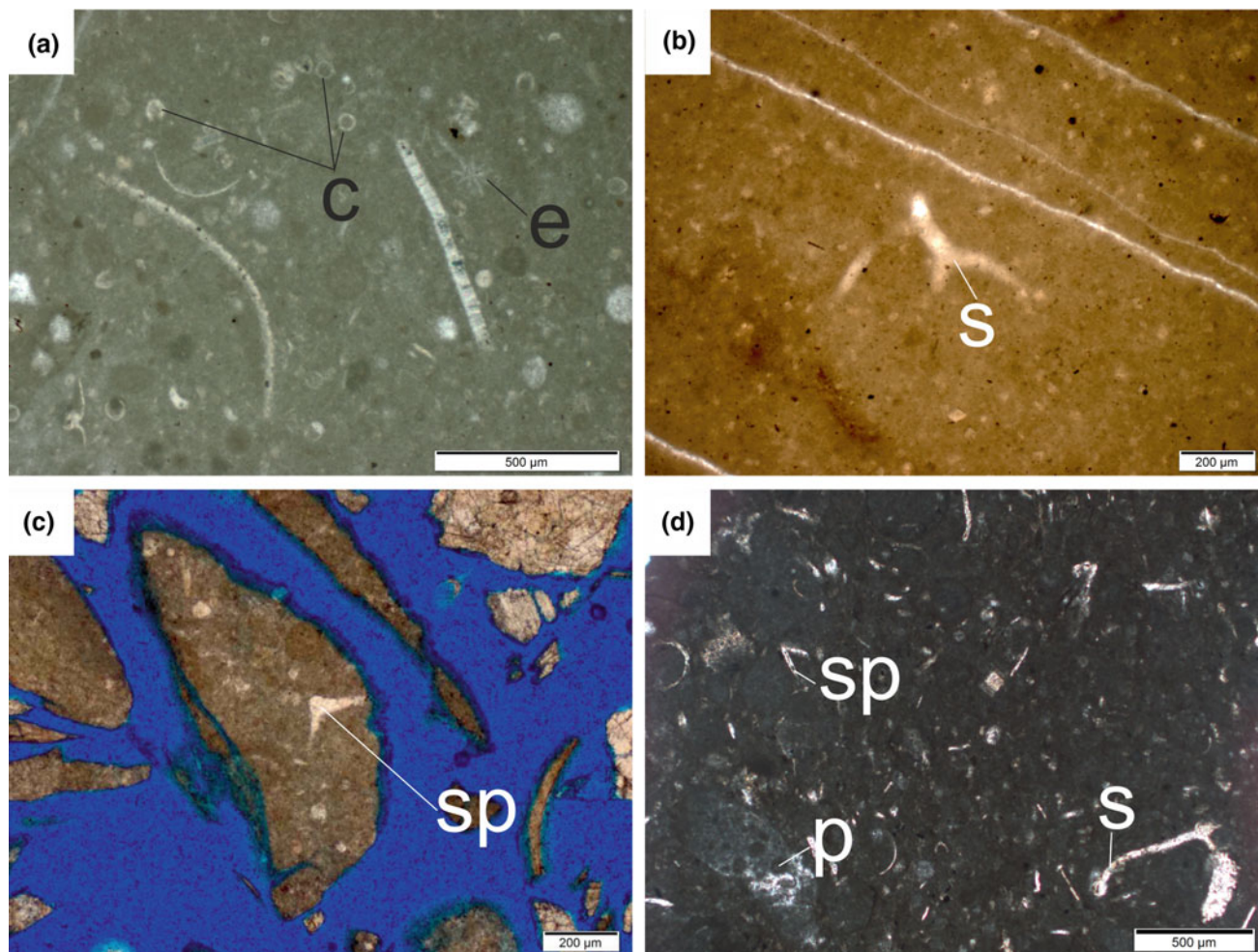


**Fig. 2** **a** Quinten-Fm. (wackestone) with characteristic microfossils, the calpionellids (c), and bioclasts like echinoderms (e); **b** Transition zone wackestone with abundant *Saccocoma* (s); **c** Cuttings of a transition zone wackestone with sponge spiculae (sp); **d** Transition zone

wackestone with peloids (p) sponge spiculae (sp), and *Saccocoma* (s). Thin section photos in transmitted light, **c** dyed with blue resin. Photos Elena Mraz

liquid-vapor system. The salt content was calculated from the ice-melting temperature after Driesner (2007); Driesner and Heinrich (2007).

## 5 Results

The microfacies analysis in the southern area of the north Alpine foreland basin indicates a change in depositional environment compared to the typical developed Franconian and Swabian facies. The depositional environment in the south of Munich shows a pelagic sedimentation due to an increase in planktonic organisms, like the planktonic crinoid *Saccocoma* (Fig. 2), for the early Upper Jurassic. Further, reef organisms are preserved as bioclasts within a fine-grained limestone with no visible porosity in regard to the thin sections (Fig. 2c, d). Accordingly, the bioclasts were

transported as reef debris to the southern area. In addition, the encountered Upper Jurassic carbonates rocks in the deep, southern area show a grey to black rock color, no porosity, and no productivity. Still, the Helvetian facies (Quinten-Fm.), with characteristic calpionellids (Mohr and Funk 1995) (Fig. 2a), is not encountered within the analyzed boreholes of the Molasse basin. In addition, the Argovian facies (Wildeggen-Fm.) is visible by clastic intermediated layers in a deep analyzed borehole east of Lake Constance (Fig. 3). Therefore, a transition from the Franconian platform to the Helvetian shelf is assumed in the area south of Munich and depicted in Fig. 3. Consequently, the depositional environment changes with increasing depth and becomes more diverse than was previously assumed.

The diagenetic fluids within the analyzed calcite and dolomite crystals showed a relative similar trend for the basin. All measured homogenization temperatures were

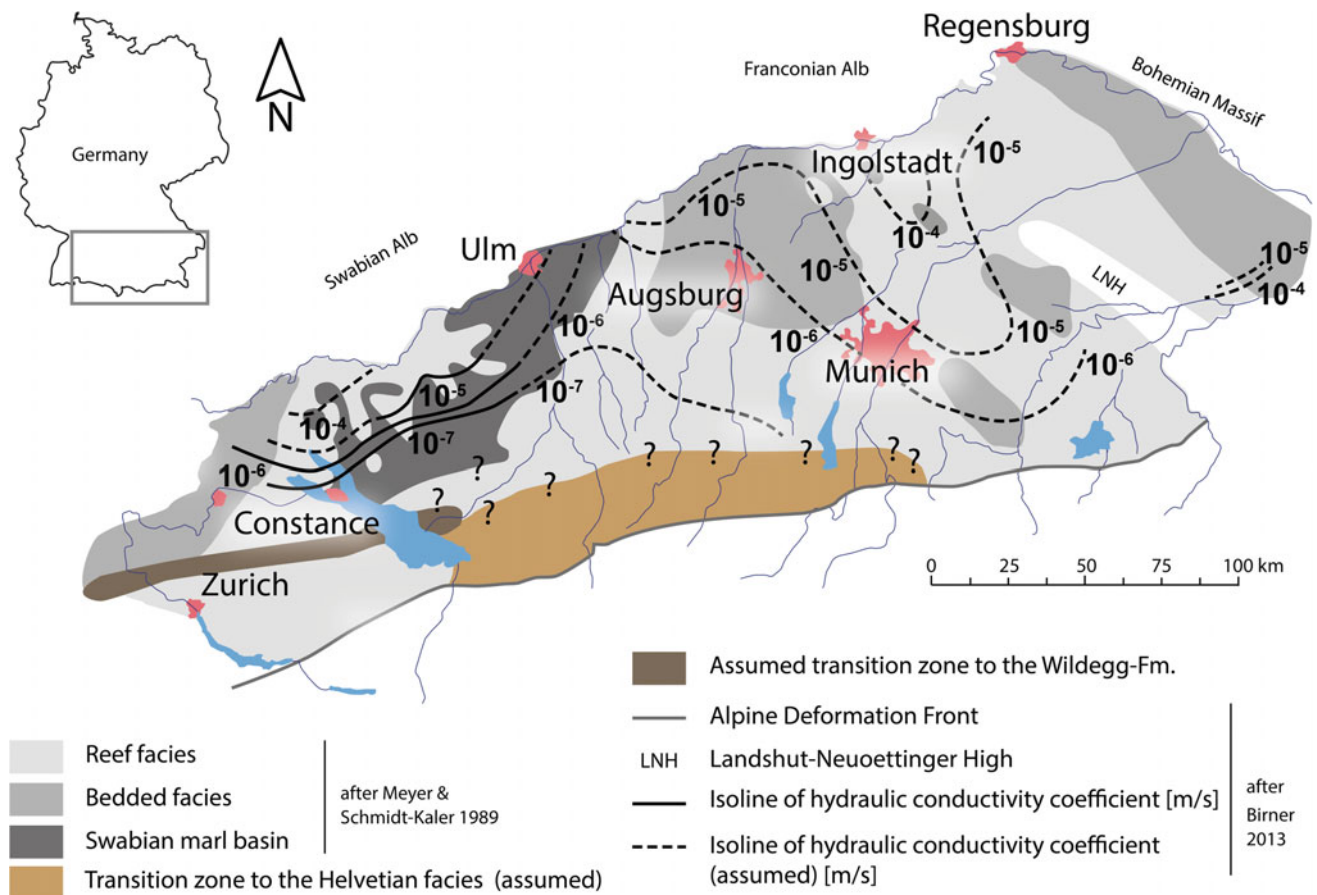


**Fig. 3** Geological overview of the new facies distribution from the Franconian platform to the Helvetian shelf within the Molasse basin and coefficient of hydraulic conductivity during the late Oxfordian (Birner 2013; Meyer and Schmidt-Kaler 1989)

above the recent reservoir temperature. Additionally, the salt content of the fluid inclusions was diluted compared to the sea water present during the sedimentation within the Tethys.

## 6 Discussion

In some literature less intense karstification is named as a cause for the decline in porosity towards the south (Koschel 1991). Other studies named the Helvetian facies as a possible cause, due to its low porosity and black rock color (Lemcke 1988). However, the current microfacies studies show that the black carbonate rocks, intersected at the deep boreholes, contain no calpionellids and cannot be classified by the Helvetian facies. Hence, for the black, low porose Upper Jurassic carbonate rocks with planktonic organisms a new classification is needed, the so-called transition zone facies. The transition zone represents the change of the Franconian platform to the Helvetian shelf in the south, and thereby the change in depositional environment. Therefore,

the Helvetian facies is suggested not to be the cause for the porosity decrease. It can be assumed that the transition zone might be the cause for the lowly porous limestones.

Higher homogenization temperatures than recent reservoir temperatures can either be caused by a change in the geothermal gradient or by an influx of hot fluids, perhaps from deeper formations. The two possible causes will be further analyzed by applying additional methods, such as isotope signatures. The dilution of the salt water, the former sea water of the Tethys, can be caused by a meteoric groundwater flow, as it is discussed in previous research (Prestel et al. 1991). The dilution of the former seawater indicates fluid flow within the low porous aquifer and is evident in calcite filled fractures. The matrix shows no visible porosity, therefore, fractures provide the main pathways for fluid flow in the Upper Jurassic reservoir.

The results indicate a porosity control by the facies type, as the platform to shelf transition facies is aligned with the low porosity domain, evidenced by low productivity wells. Hence, fluid flow is dominated by fractures within the transition zone in the deep southern basin, explaining the

low reservoir productivity. The microfacies analysis is crucial for reservoir characterization and the localization of successful wells.

## 7 Summary

The rock sample analysis combined with fluid inclusions measurements shows that the matrix and thereby the facies (depositional environment) have a minor influence on the porosity and productivity of the Upper Jurassic carbonate rocks. Consequently, fractures and fault systems provide the main pathways for fluid flow. However, the change in depositional environment cannot be the only cause for the porosity decline.

There are differences in the pore space development between the area of Munich and the southern part of the Molasse basin, which need to be further characterized. One still unclear process is the dolomitization depending to a high extent on the supply of magnesium-rich fluids.

The microfacies analysis is a basic method in reservoir characterization and helps to determine high and low porosity domains. The presented results are important for hydrocarbon and geothermal exploration, as well as for subsurface storage.

**Acknowledgements** This research is supported by the Federal Ministry of Economic Affairs and Energy on the basis of a decision by the German Bundestag with the support code 0324004.

## References

- Agemar, T., Weber, J., Schulz, R.: Deep geothermal energy production in Germany. *Energies* **7**, 4397–4416 (2014)
- Beichel, K., Koch, R., Wolfgramm, M.: Die Analyse von Spülproben zur Lokalisierung von Zuflusszonen in Geothermiebohrungen. Beispiel der Bohrungen Gt Unterhaching 1/1a und 2. (Süddeutschland, Molassebecken, Malm). *Geol. Blätter NO-Bayern* **64**, 43–65 (2014)
- Birner, J.: Hydrogeologisches Modell des Malmaquifers im Süddeutschen Molassebecken. Berlin, Freie Universität Berlin, 86 pp (2013)
- Boggs, S., Krinsley, D.: Application of Cathodoluminescence Imaging to the Study of Sedimentary Rocks. Cambridge University Press, 165 pp (2006)
- Böhm, F., Birner, J., Steiner, U., Koch, R., Sobott, R., Schneider, M., Wang, A.: Tafelbankiger Dolomit in der Kernbohrung Moosburg SC4: Ein Schlüssel zum Verständnis der Zuflussraten in Geothermiebohrungen des Malmaquifers (Östliches Molasse-Becken, Malm Süddeutschland). *Z. Geol. Wiss.* **39**, 117–157 (2011)
- Büchi, U., Lemcke, K., Wiener, G., Zimdars, J.: Geologische Ergebnisse der Erdölexploration auf das Mesozoikum im Untergrund des schweizerischen Molassebeckens. *Bulletin der Schweizerischen Vereinigung von Petroleum-Geologen und-Ingenieuren* **15**, 7–38 (1965)
- Driesner, T.: The system H<sub>2</sub>O-NaCl. Part II: correlations for molar volume, enthalpy, and isobaric heat capacity from 0 to 1000° C, 1 to 5000 bar, and 0 to 1 X NaCl. *Geochim. Cosmochim. Acta* **71**, 4902–4919 (2007)
- Driesner, T., Heinrich, C.A.: The system H<sub>2</sub>O-NaCl. Part I: correlation formulae for phase relations in temperature–pressure–composition space from 0 to 1000° C, 0 to 5000 bar, and 0 to 1 X NaCl. *Geochim. Cosmochim. Acta* **71**, 4880–4901 (2007)
- Dunham, R.J.: Classification of carbonate rocks according to depositional texture. In: Ham, W.E. (ed.) *Classification of Carbonate Rocks—A Symposium*, AAPG Memoir, 1, pp. 108–121. American Association of Petroleum Geologists, Tulsa, Oklahoma (1962)
- Folk, R.L.: Practical petrographic classification of limestones. *AAPG Bull.* **43**, 1–38 (1959)
- Folk, R.L.: Spectral subdivision of limestone types. In: *Classification of Carbonate Rocks—A Symposium* (Ed W.E. Ham), AAPG Memoir, 1, pp. 62–84. American Association of Petroleum Geologists, Tulsa, Oklahoma (1962)
- Frisch, H., Huber, B.: Ein hydrogeologisches Modell und der Versuch einer Bilanzierung des Thermalwasservorkommens für den Malmkarst im Süddeutschen und im angrenzenden Oberösterreichischen Molassebecken. *Hydrogeologie und Umwelt* **20**, 43 (2000)
- Goldstein, R.H.: Fluid inclusions in sedimentary and diagenetic systems. *Lithos* **55**, 159–193 (2001)
- Gygi, R.A.: Quantitative Geology of Late Jurassic Epicontinental Sediments in the Jura Mountains of Switzerland. Springer Science & Business Media (2012)
- Koschel, G.: *Geologischer Überblick—Hydrogeologische Randbedingungen*, München, Freiburg i. Br. (1991)
- Lemcke, K.: *Das Bayerische Alpenvorland vor der Eiszeit: Erdgeschichte, Bau, Bodenschätze*. Geologie von Bayern I. Schweizerbart, Stuttgart (1988)
- Liedmann, W.: Diagenetische Entwicklung Süddeutscher Malmkarbonate - unter Berücksichtigung lumineszenzpetrographischer, fluid inclusions und geochemischer Untersuchungsmethoden. Dissertation Universität Heidelberg, Heidelberg, 307 pp (1992)
- Liedmann, W., Koch, R.: Diagenesis and fluid inclusions of upper Jurassic sponge-algal reefs in SW Germany. *Facies* **23**, 241–267 (1990)
- Machel, H.G.: Concepts and models of dolomitization: a critical reappraisal. *Geol. Soc. London Spec. Publ.* **235**, 7–63 (2004)
- Machel, H.G., Buschkuehle, B.E.: Diagenesis of the Devonian Southesk-Cairn Carbonate Complex, Alberta, Canada: marine cementation, burial dolomitization, thermochemical sulfate reduction, anhydritization, and squeegee fluid flow. *J. Sediment. Res.* **78**, 366–389 (2008)
- Meyer, R.K.F., Schmidt-Kaler, H.: *Paläogeographischer Atlas des süddeutschen Oberjura (Malm)*. Schweizerbart, Stuttgart, 77 pp (1989)
- Mohr, H., Funk, H.: Die Entwicklung der helvetischen Karbonatplattform in der Ostschweiz (Tithonian-Berriasian): Eine sequenzstratigraphische Annäherung. *Eclogae Geol. Helv.* **88**, 281–320 (1995)
- Pomoni-Papaioannou, F., Flügel, E., Koch, R.: Depositional environments and diagenesis of upper Jurassic subsurface sponge- and tubiphytes reef limestones: Altensteig 1 well, western Molasse Basin, Southern Germany. *Facies* **21**, 263–283 (1989)
- Prestel, R., Wolf, M., Eichinger, L., Salvamoser, J.: Gaszusammensetzung von Ölfeldwässern und Grundwässern im Malm des süddeutschen Molassebeckens, München, Freiburg i. Br. (1991)



- Reinhold, C.: Prozesse, Steuerung und Produkte komplexer Diagenese-Sequenzen in süddeutschen Malm-Karbonaten - Die oberjurassische Massenkalk- und Bankkalkfazies bei Geislingen/Steige (Oxford/Kimmeridge, östliche Schwäbische Alb). Dissertation Technische Universität Berlin, Berlin, 255 pp (1996)
- Reinhold, C.: Die Massen- und Bankkalk bei Geislingen/Steige (Kimmeridge, östl. Schwäbische Alb)-Mikrofazies, Ablagerungsraum und diagenetische Entwicklung. *Jh. Ges. Naturkde. Württemberg*, 154, 75–106 (1998a)
- Reinhold, C.: Multiple episodes of dolomitization and dolomite recrystallization during shallow burial in Upper Jurassic shelf carbonates: Eastern Swabian Alb, Southern Germany. *Sed. Geol.* **121**, 71–95 (1998b)
- Villinger, E.: Bemerkungen zur Verkarstung des Malms unter dem westlichen süddeutschen Molassebecken. *Bulletin der Vereinigung schweizerischer Petroleum-Geologen und-Ingenieure* **54**, 41–59 (1988)
- Ziegler, P.A.: *Geological Atlas of Western and Central Europe*. Shell Internationale Petroleum Mij. and Geol. Soc. of London (1990)

# Assessment of the Hydrogeological Windows Impact on Groundwater Contamination in Moscow

Irina Galitskaya, Irina Pozdnyakova, Irina Kostikova,  
Oleg Mironov, and Leonid Toms

## Abstract

This paper presents the results of assessing the hydrogeological windows impact on the Podol'sko-Myachkovskii aquifer contamination in Moscow as the most important reserve source of drinking water supply. In the areas of hydrogeological windows, the contamination of the Podolsko-Myachkovskii aquifer can occur due to rapid mixing of contaminated groundwater of the overlying above-Jurassic aquifer and pure groundwater of the Podolsko-Myachkovskii aquifer. The study consisted of analyzing the water chemistry data of these aquifers; choice of the elements—indicators of groundwater contamination; analysis of the indicators distribution schemes in the studied aquifers and comparison with the boundaries of hydrogeological windows. The research results testified to the significantly elevated concentrations of contamination indicators in the Podolsko-Myachkovskii aquifer at the sites of hydrogeological windows allocated within the specific geostructural, hydrogeological and tectonic conditions.

## Keywords

Hydrogeological windows • Groundwater contamination • Low-permeability deposits • Vertical leakage • Hydrogeological conditions • Aquifer vulnerability

## 1 Introduction

Significant anthropogenic contamination of groundwater is one of the most pressing problems that our world faces today, and the various aspects of this problem is actively

researched by scientists of all countries. Particular attention is paid to the study of groundwater contamination hazard in the territories of hydrogeological windows location. By the hydrogeological windows are meant the zones in the geological environment within which contaminants can penetrate rapidly from near-surface into more deep aquifers in the areas where continuity of separating low-permeability deposits is disturbed and their permeability is relatively high.

Numerous publications have been devoted to the study of the hydrogeological windows role in groundwater contamination [for example, the study of groundwater quality features in areas of increased permeability in the Tobolskii artesian basin (Vsevolodzkaya and Galitskaya 1980), oil products migration through hydrogeological windows (Pozdnyakova et al. 2016), groundwater chemistry change in the mining area in Upper Silesia (Rozkowski 1993)]. Studies related to the mapping of hydrogeological windows are conducted in Sergeev Institute of Environmental Geoscience, Russian Academy of Sciences (IEG RAS) since 2008. In 2013–2014, a research group of IEG RAS has developed “Map of the Boundaries of Hydrogeological Windows” in some districts of the city at a scale of 1:10000 (Pozdnyakova et al. 2016). This map is compiled for the first time by an original method, combining large-scale mapping of the geological structure, hydrogeological and structural-tectonic conditions, groundwater flow calculations, and the analysis of monitoring data on groundwater level and chemistry. The map is based on a large body of data obtained from official sources with the application of modern computer technologies. The integrated approach used in the study allows the hydrogeological windows to be identified, mapped, and compared in terms of the travel time of the most common pollutants from them into the Podol'sko-Myachkovskii aquifer, which is of strategic significance for drinking water supply.

The aim of our study is to assess the hydrogeological windows impact on the Podol'sko-Myachkovskii aquifer contamination in Moscow. The choice of the study object is determined by the following. Firstly, the Podol'sko-Myachkovskii aquifer is the most important reserve source

I. Galitskaya (✉) · I. Pozdnyakova · I. Kostikova  
Oleg Mironov · L. Toms  
Sergeev Institute of Environmental Geoscience Russian Academy  
of Science (IEG RAS), Moscow, 101000, Russia  
e-mail: galgeoenv@mail.ru

of drinking water supply in the capital, and secondly, the presence of hydrogeological windows can have a considerable significance for groundwater quality for this aquifer. The research is carried out within the framework of the project of the Russian Foundation for Basic Research. At the first stage, for data visualization, the maps of the pollution indicator distribution in the groundwater were compiled in the areas of hydrogeological windows and outside them. The obtained results are presented and discussed in this article.

## 2 Geological and Hydrogeological Setting

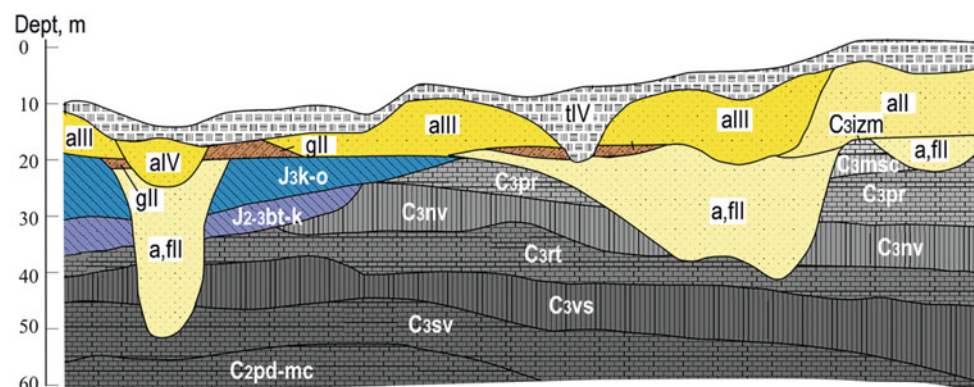
The geology of the area is heterogeneous. The geological conditions are represented by two different types of rocks: Precambrian crystalline rocks of the basement and Palaeozoic, Mesozoic and Cenozoic sedimentary cover rocks. The total thickness of the sedimentary cover rocks is about 1000 m. Due to geological processes of erosion and denudation, the Triassic and Dyas rocks were washed out and are not represented in the Moscow area. Palaeozoic sedimentary rocks are represented by Devonian limestones, clays and sandstones; Carboniferous limestones and Jurassic clays. Cretaceous rocks of the Mesozoic, portrayed on elevations of Moscow, are similarly absent in the geological section of the disposal fields area. Quaternary rocks are mostly represented by the Moscow River deposits. The variability of geology is due to the existence of a network of buried erosion troughs in bedrocks of Carboniferous and Jurassic, filled with sand-clay Quaternary deposits. The geology and the hydrogeological structure of the stratum that overlays the main Podol'sko-Myachkovskii aquifer varies depending on the presence and depth of ancient erosion troughs (Fig. 1).

Hydrogeological conditions of the city area shows up to 10 and more aquifers in the zone of active water exchange. In this interval, it is common to identify a higher water bearing stratum in sands, clays, and other deposits of Quaternary and Mesozoic and a lower stratum in carbonate rocks

and clays of Carboniferous (Pozdniakova et al. 2013). At the major portion of the territory, except for the valleys of the Moskva River and its tributaries, the upper and lower strata are separated by low permeability Middle and Upper Jurassic ("Jurassic") clays, which serve as a regional aquitard. In the upper stratum, in the zone of occurrence of moskovskaya and donskaya moraines, the aquifers and the low permeability deposits that separate them are combined into the above-moraine aquifer system, while the entire water bearing stratum overlaying the "Jurassic" clays is combined into the "above-Jurassic" aquifer system. The above-Jurassic aquifer system is ubiquitous; it is represented most fully on the right bank side of the Moskva River, where it consists of 5 and more aquifers in Quaternary (alluvial, fluvio-glacial), Cretaceous and Upper Jurassic deposits. In the floodplain of the Moskva River and its tributaries, the above-Jurassic aquifer system contains a single aquifer in alluvial deposits, immediately overlaying the Carboniferous deposits. In the places where there is no "above moraine" aquifer system, the above Jurassic aquifer system is the first from the surface; those systems show close hydraulic interaction in the rest of the territory.

According to the "Map of the Boundaries of Hydrogeological Windows" (Pozdnyakova et al. 2016) hydrogeological windows of different orders were defined based on the results of the vertical filtration time calculation for contaminants, migrating from the above-Jurassic aquifer to the deeper Podol'sko-Myachkovskii aquifer and the lifetime of drinking water supply wells, I—<400 days (survival time of pathogenic microorganisms in groundwater), II—<1000 days (half-life of oil products), III—3–15 years (decomposition time of more than 60 organic compounds and tritium half-life), IV—15–25 years (design lifetime of drinking water supply wells), V—25–50 years (actual lifetime of drinking water supply wells), VI—50–100 years (characteristic migration time, considering the sorption retention of heavy metals, ammonium ions, radionuclides (cesium and strontium), and nitrates (with denitrification taken into account) (Fig. 2).

**Fig. 1** Geological structure of the strata separating the above-Jurassic and Podol'sko-Myachkovskii aquifers



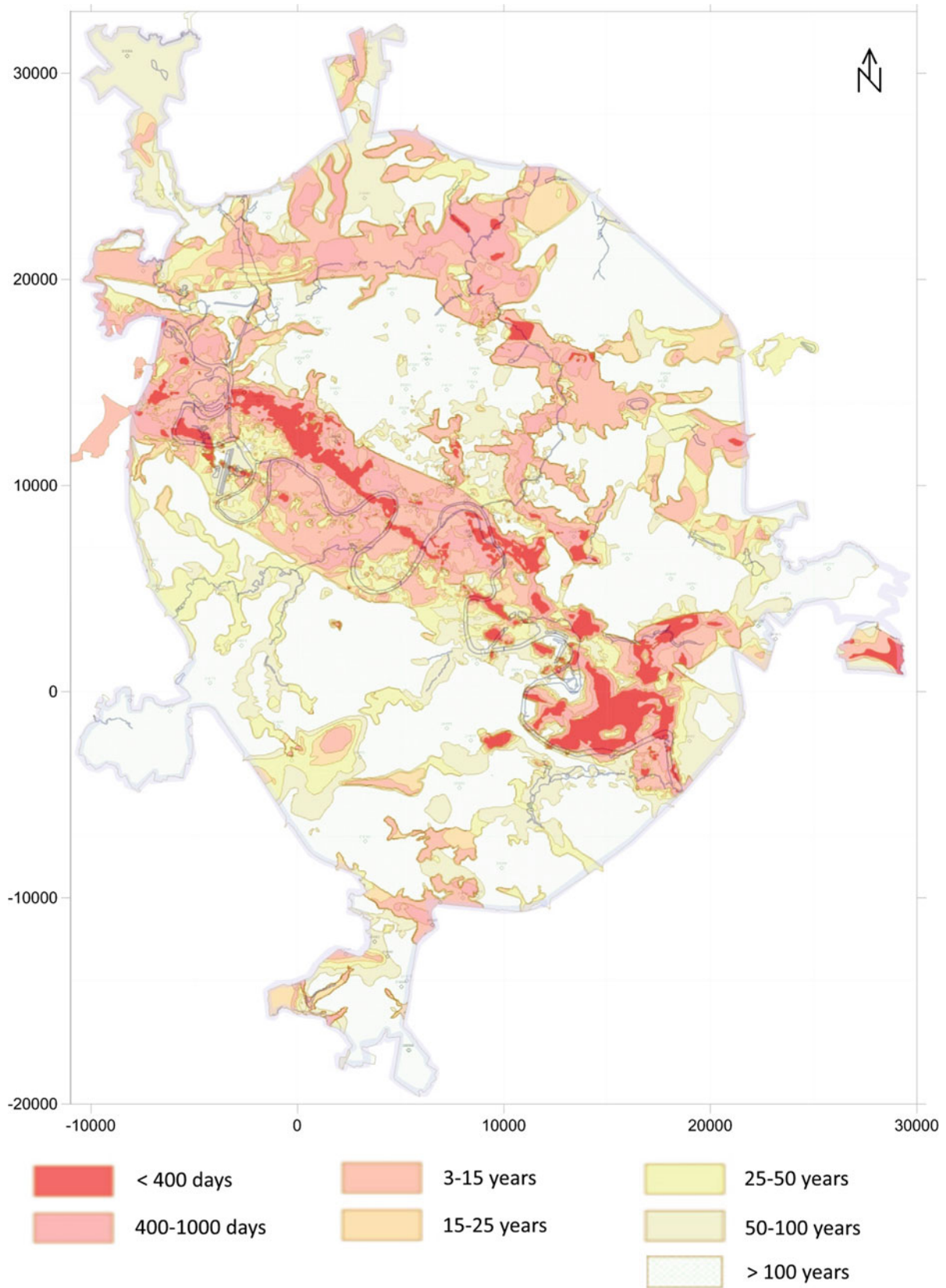


**Fig. 2** Schematic map of hydrogeological windows

In addition, according to tectonic features the potential hydrogeological windows have been identified, which are areas associated with zones of intersection of lineaments, tears, geodynamically active zones and other structural elements in which the permeability of rocks can be increased due to increased fracturing.

### 3 Materials and Methods

Studying the hydrogeological windows impact on groundwater contamination in the Podol'sko-Myachkovskii aquifer consisted in analyzing the water chemistry data of the above-Jurassic and Podol'sko-Myachkovskii aquifers; choice of the elements—indicators of groundwater contamination on the basis of the study on the water chemistry genesis in the above-Jurassic aquifer; construction and analysis of the elements—indicators distribution schemes in the above-Jurassic and Podol'sko-Myachkovskii aquifers and their comparison with the “Map of the Boundaries of Hydrogeological Windows”. Groundwater samples were collected from monitoring wells in above-Jurassic aquifer and water wells in Podol'sko-Myachkovskii aquifer. These data were provided by OAO Geotsentr-Moskva.

The data were statistically processed, the unauthentic data was rejected, and then the most representative time periods for mapping were selected. When assessing the degree of the natural groundwater chemistry disturbance, the data on background elements concentrations were used and the assessment of groundwater contamination was performed by using the values of maximum permissible concentrations for drinking water. When constructing the schemes of contaminants—indicators distribution the software package “Surfer” was used and the most acceptable result (for a given sampling network) was obtained by Kriging method.

## 4 Results and Discussion

### 4.1 The Choice of the Elements—Indicators of Groundwater Contamination

Analysis of the groundwater in the above-Jurassic aquifer showed that the natural chemical composition is substantially disturbed by technogenic processes, that is expressed in significant excess of the background concentrations of components and change of the natural hydrocarbonate water type to sulfate or chloride types. Groundwater showed the following concentrations (Table 1).

Exceeding the maximum permissible values was recorded for a wide range of components: chlorides, sodium, ammonium, nitrates, oil products, iron, and heavy metals. The highest levels of groundwater contamination were observed for oil products, manganese and, in particular, for iron. Elevated concentrations of chloride, sulfate, ammonium, nitrate, oil products are associated with infiltration of contaminated sewage and surface runoff, whereas water contamination by iron and manganese is due mainly to interactions in the water-rock system.

Indicators of contamination can serve components primarily of technogenic origin—ammonium, nitrates, oil products, phenols, surfactants, as well as chloride ion and sodium, significantly higher concentrations of which, compared to the background, also have anthropogenic genesis (the application of anti-icing products). As the main indicator of contamination, it is advisable to use chloride ion, which, unlike other components, is not sorbed by rocks, practically does not undergo physical and chemical transformations, and is characterized by a fairly stable character of the concentration change in the study area. Other components of technogenic genesis—oil products, phenols, surfactants, nitrogen compounds, can be used as additional indicators to obtain a more complete picture of the influence

**Table 1** Concentration of chemical substances in the above-Jurassic and Podol'sko-Myachkovskii aquifers

Element	Concentration, mg/L above-Jurassic aquifer	Concentration, mg/L Podol'sko-Myachkovskii aquifer
Chloride	0.5–12259	<0.05–293.0
Sulfate	0.1–748.9	<0.01–440.0
Nitrate	0.04–83.85	<0.01–37.2
Sodium	0.2–7778	4.4–1069.0
Ammonium	0.05–236	<0.05–183.0
Calcium	0.5–1900	3.2–250.5
Magnesium	0.27–350	0.01–141.0
Oil products	0.005–53.0	<0.005–113.0
Iron	0.1–1693	<0.01–14.2
Manganese	0.001–22.9	<0.01–1.02

of the polluted waters penetration from the above-Jurassic aquifer to the Podol'sko-Myachkovskii aquifer, and also to elucidate the possibility of using the chemical composition of groundwater as hydrogeochemical sign of the hydrogeological windows.

#### 4.2 Changes of Groundwater Chemistry in the Podol'sko-Myachkovskii Aquifer in the Sites of the Hydrogeological Windows

The results of study showed that the baseline groundwater chemistry in the Podol'sko-Myachkovskii aquifer to be only slightly disturbed by technogenic processes. The water-rock interactions form hydrocarbonate and sulfate-hydrocarbonate water of natural genesis. Chloride-hydrocarbonate groundwater of natural-technogenic genesis are less common, and located within the Moskvoretskaya geodynamically active zone. The concentrations of technogenic components are much less than in the above-Jurassic aquifer (Table 1).

The distribution of the contamination indicators concentrations in the Podol'sko-Myachkovskii aquifer shows that higher concentrations of chloride ion (Fig. 3), nitrate ion, oil products, and ammonium ions correlate with the occurrence areas of hydrogeological windows in the valleys of the Yauza and Moskva rivers. The highest concentrations (mg/L) of the contamination indicator confined to the identified hydrogeological windows of the first and second orders: chloride ion, up to 293; sulphate ion, up to 440.0; nitrate ion, up to 37.2; oil products, up to 0.113; and ammonium, up to 183. Therefore, the hydrogeological windows of the first and second orders are among the most dangerous. In these areas there are no weakly permeable deposits separating the Podolsko-Myachkovskii and the above-Jurassic aquifers, and where the aquifers form a single aquifer. In this stratum, contamination of the Podol'sko-Myachkovskii aquifer occurs due to the mechanisms of rapid mixing of contaminated groundwater of the above-Jurassic aquifer and pure groundwater of the Podol'sko-Myachkovskii aquifer.

The most clearly the effect of hydrogeological windows on groundwater contamination in the Podol'sko-Myachkovskii aquifer can be seen in the scheme of chloride ion distribution (Fig. 4). A preliminary assessment of correlation coefficients of filtering time and indicators concentrations showed that the highest values are observed for chloride ion—0.74, less significant—for sulphate ion—0.61, nitrate ion—0.52, ammonium ion—0.56, which apparently can be associated with chemical processes and requires further research.

## 5 Conclusions

Minimizing the adverse effect on the main reserve source of potable water, i.e., Podolsko-Myachkovskii aquifer in Carboniferous deposits appears to be one of the major problems in Moscow urban planning. Assessment and mapping of groundwater protection degree are of great importance for the choice of sites with the minimal groundwater contamination risk when placing the objects of infrastructure and industry. Podolsko-Myachkovskii aquifer is the most vulnerable to contamination within the sites of hydrogeological windows, where fast contaminant transport from the polluted above-Jurassic aquifer to deep aquifers is possible due to the high discontinuity and permeability in the separating layer.

The results of this study lead to the conclusion that the hydrogeological windows can effect on the groundwater chemistry in the Podolsko-Myachkovskii aquifer. Groundwater pollution indicators are mostly components of technogenic origin, including ammonium ion, nitrates, oil products, phenols, SAS, and, primarily, chloride ion. Elevated concentrations of contaminants were characteristic for the areas of hydrogeological windows in the valleys of the rivers Yauza and Moscow, allocated according to geological structure, hydrogeological and tectonic conditions. Therefore, the hydrogeochemical criteria, notwithstanding the objective restrictions of applications, can be used to identify hydrogeological windows in the zones of higher permeability and lower thickness of low-permeability Jurassic clays. The accuracy of the method can be improved by the introduction of hydrogeological monitoring in the zones of both identified and potential hydrogeological windows, the data on which are insufficient now.

The system of measures for the preservation of the groundwater drinking quality should involve the identification of areas most vulnerable in terms of contamination penetration into them, the inventory of potential pollution sources, the assessment of groundwater pollution, and the development of special regulations on the economic activities in such areas. Of greatest importance is the development of environmental regulations on the use of the zones of hydrogeological windows, primarily, the most hazardous and unprotected hydrogeological windows of the first and second orders. For these areas, it should be recommended to remove industrial plants or modernize underground services, treatment facilities, etc.; eliminate landfills and technogenic soil dumps, modernize the sewage networks in residential areas, reduce motor transport emissions by introducing special types of fuel and electric transport; modernize road storm-water drains; introduce groundwater monitoring with obligatory allocation of observation wells at ecologically hazardous facilities; prohibit the construction of new

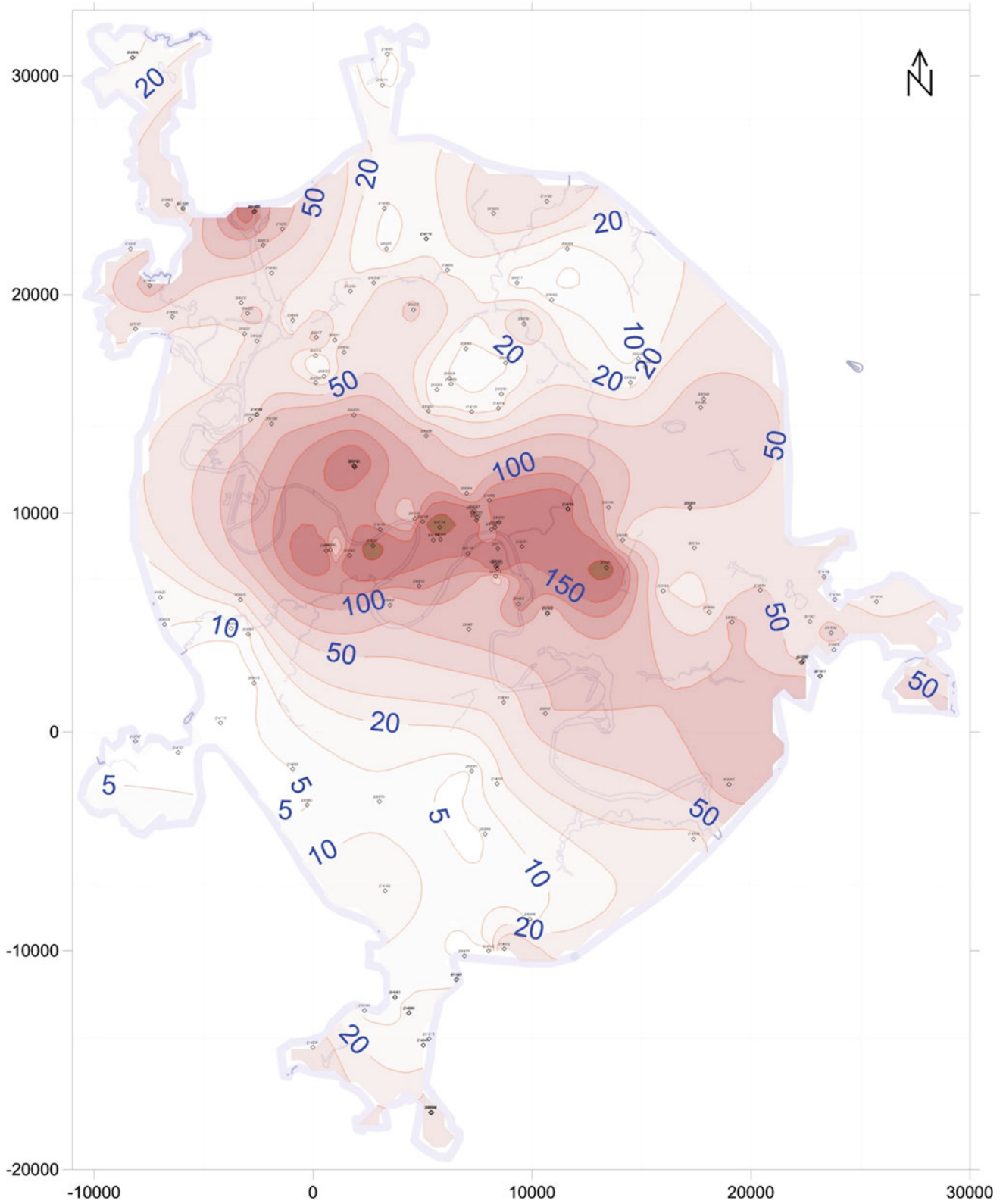


**Fig. 3** Schematic map of the distribution of chloride ion in groundwater of the Podol'sko-Myachkovskii aquifer, mg/L

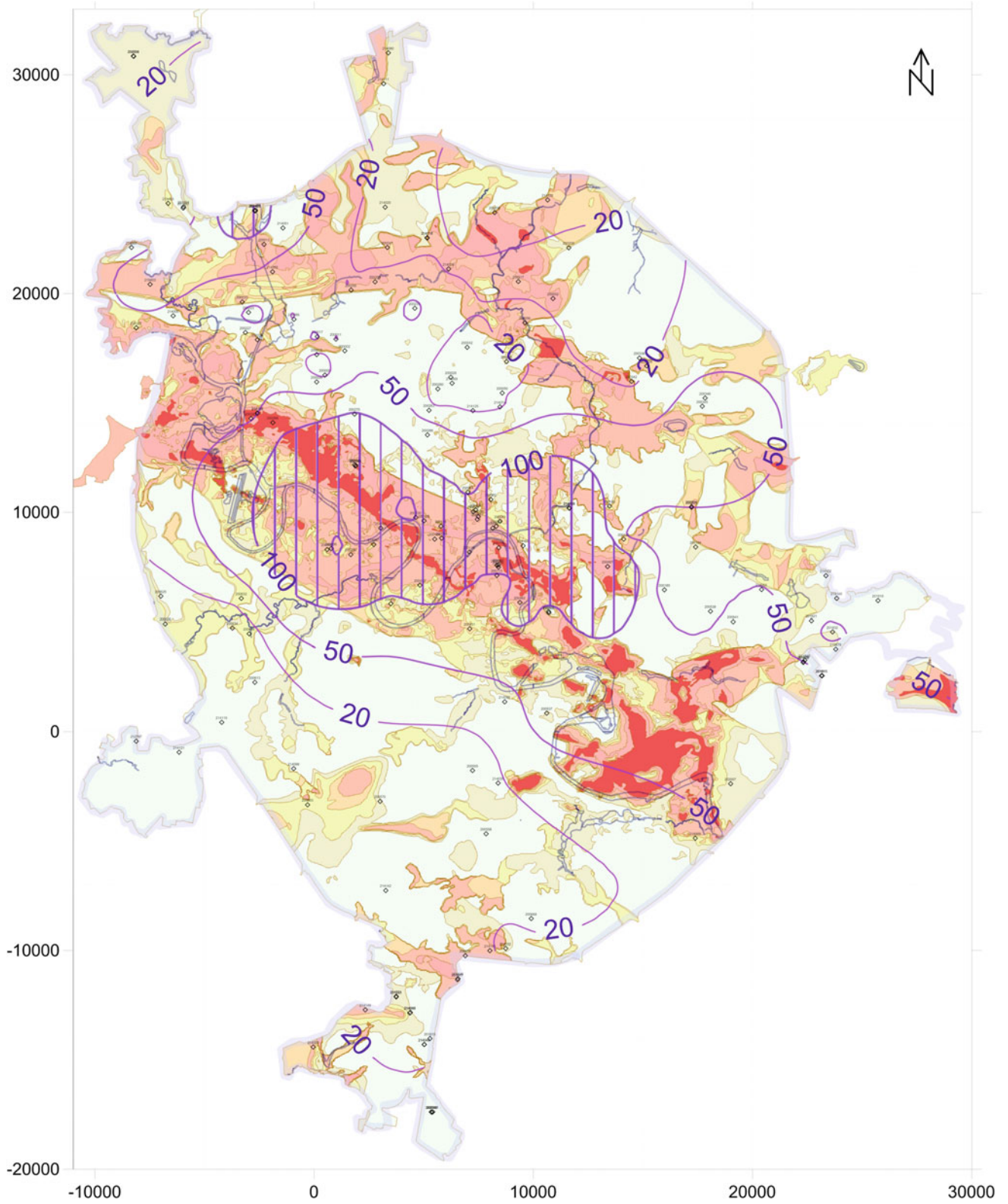


**Fig. 4** Schematic map of the distribution of chloride ion in groundwater of the Podol'sko-Myachkovskii aquifer, mg/L in the sites of hydrogeological windows



industrial facilities (except for the critical life-supporting facilities), petrol stations, auto washing, etc. The possibility to allocate a potential groundwater pollution source in zones of hydrogeological windows must be substantiated by the results of forecasting groundwater pollution in the Podol'sko-Myachkovskii aquifer by numerical simulation of groundwater flow.

**Acknowledgements** The research was financially supported by the project of the Russian Foundation for Basic Research (RFBR) № 17-05-01016.

---

## References

- Pozdniakova, I.A., Kozhevnikova, I.A., Kostikova, I.A., Toms, L.S.: Groundwater interaction assessment based on the large-scale mapping of geological and hydrogeological conditions in Moscow. *Water Resour.* **40**(7), 695–705 (2013)
- Pozdnyakova, I.A., Galitskaya, I.V., Mironov, O.K., Kostikova, I.A., Dorozhko, A.L., Batrak, G.I., Matveeva, L.A., Fesel, K.I.: Identification of hydrogeological windows based on large-scale mapping of the geological and hydrogeological conditions in Moscow. *Water Resour.* **43**(7), 1012–1022 (2016)
- Rozkowski, A.: Impact of mining on the groundwater chemistry in the Upper Silesian Coal Basin (Poland). *Mine Water Environ.* (Annual issue) **12**, 95–106 (1993)
- Vsevolodzkaya, M.A., Galitskaya, I.V.: Estimation of mass transfer in marine genesis clay under seepage. In: *Materials of Conference of Chemical Society GDR*, pp. 80–85. Dresden technological university (1980)

# On the Differing Role of Contact Obstacles on Variably Saturated Flow in Vertical and Horizontal Fractures

Brendon R. Jones, J. Louis Van Rooy, and Matthys A. Dippenaar

## Abstract

A series of flow visualization experiments is developed in order to observe the different role that contact obstacles have on variably saturated flow in a vertical fracture compared to a horizontal fracture. The model fractures consist of a single rough-walled quartzite fracture wall mismatched with a second transparent smooth replica wall. Results drawn from this research show that contact obstacles result in longer flow paths of between 4 and 14%, with longer flow paths observed in horizontal fractures. Furthermore, contact obstacles result in different unsaturated flow mechanisms when present in vertical compared to horizontal fractures under low flow rates. Contact obstacles enhance the variably saturated flow process in vertical fractures, but act as choke points in horizontal fractures.

## Keywords

Vadose zone • Roughness • Fracture flow • Unsaturated flow

## 1 Introduction

The vadose zone typically comprises soil underlain by fractured rock. Often, groundwater parameters are readily available, but variably saturated flow through soil and rock is oversimplified or estimated as input for hydrological models. Current key research questions identified for the intermediate fractured vadose zone, are the influence of fracture or discontinuity geometry, as well as partial saturation

(Berkowitz 2002; Neuman 2005). In this unsaturated zone, the most notable implication of partial saturation of fracture networks is that gravity does not necessarily force water down near-vertical discontinuities (Dippenaar and Van Rooy 2016). Recently, Jones et al. (2017) presented experimental results that indicate that the conventional practice of water exerting isotropic pressures may be incorrect, as saturation within the fractured vadose zone is highly anisotropic and not uniform. Inevitably, this may contribute to extensive engineering applications, which includes stability analyses conducted for mining and civil geotechnics.

Pyrak-Nolte et al. (1988) state that fracture permeability is controlled by the largest connected channel within the system, and that flow through that channel is controlled by its narrowest aperture, or choke point. Under partial saturation, relatively large amounts of fluid are forced to pass through zones of narrow aperture, which act to restrict flow. This causes large localized pressure drops, and therefore localized variations in channel width, which act to decrease permeability in a fracture (Nicholl and Glass 2007). Additionally, increased flow path lengths also contribute to this decrease in permeability, with Kishida et al. (2013) finding that flow path lengths are 3–9% longer than the straight-line distance. Within topographic depressions, fluid moves as thick pendular regions, whilst thin pendular films occur at topographic ridges, or at choke points (Tokunaga and Wan 1997; Tokunaga et al. 2000). When considering inclined fractures, the effects of gravity can destabilize a wetting front, leading to the development of fingers oriented in the direction of gravity (Nicholl and Glass 2007). Jones et al. (2017) found that, in unsaturated conditions, preferential flow occupies the minority of cross-sectional area in a smooth, clean, open vertical fracture, despite large fluid supply from a saturated horizontal fracture.

The research presented in this paper aims to investigate the different roles that contact obstacles play in governing flow in vertical compared to horizontal fractures. A series of flow visualization experiments are developed on fractures consisting of a single quartzite fracture wall mismatched

---

B. R. Jones (✉)  
GaGE Consulting, Johannesburg, South Africa  
e-mail: bren.r.jones@gmail.com

J. L. Van Rooy · M. A. Dippenaar  
Engineering Geology and Hydrogeology, Department of Geology,  
University of Pretoria, Pretoria, South Africa

with a second transparent smooth replica wall in order to observe flow behaviour under intermittent influx.

## 2 Experimental Set-up and Procedure

The fractures are selected in the field such that the Joint Roughness Coefficient (JRC) ranges between 8 and 10 (5th profile of Barton and Choubey 1977), with a large (open) mean mechanical aperture ( $e$ ) of 1–3 mm. The experimental set-up consists of two fracture models: Model 1 is vertical, and Model 2 is horizontal, with the respective set-up illustrated in Fig. 1. Each fracture surface is scanned to produce a surface and contour profile of the fracture. Thereafter, the JRC is more precisely approximated by measuring the maximum amplitude,  $a$ , of the roughness, over the measured profile length,  $L$  (see for e.g. Barton 1982; and Barton and de Quadros 1997). Model 1 (vertical) consists of 100 mm height  $\times$  150 mm width quartzite fracture, characterized by a JRC of 8.1, and a mean mechanical aperture ( $e$ ) of approximately 1.35 mm. The fracture used in Model 2 (horizontal) measures 265 mm length  $\times$  150 mm width  $\times$  100 mm height, characterised by a JRC value of 9.81, and a mean mechanical aperture ( $e$ ) of approximately 2.54 mm. The intention was not to model the vertical and horizontal fractures exactly but ensure that their respective characteristics fell within typical field ranges.

Model preparation begins by fixing a single Plexiglas L-section sheet against the model quartzite fracture, which is thereafter placed in a strongbox. A transparent grid is placed on the outside of the Plexiglas L-section, to assess the geometry of the flow paths. A water inlet container is constructed around the fracture entrance, with potassium

permanganate crystals scattered to dye the water. An overhead bracket with a water inlet pipe and a solenoid valve (electronic tap) is installed above the fracture, while basal drains in the strongbox act as the outlet. Cameras are placed to record the experiment. The experimental procedure commences when the solenoid valve is opened, and influx is introduced as individual droplets at approximately 0.6 l/h. The experiment is stopped when the solenoid valve is closed after 5-min for Model 1 and 10-min for Model 2, respectively.

## 3 Results

### 3.1 Model 1: Vertical Fracture

During the wetting of the vertical fracture, an initial sliding droplet travels vertically down the fracture. Thereafter, several smaller liquid bridges continue to slide down this wetted flow path and reach the wetting front of the droplet at 6 s. Once the sliding droplet spans the vertical length of the fracture, the snapping behaviour ceases, and a continuous rivulet establishes. The flow path taken is approximately 83.5 mm in length, which is 4% longer than the compared straight-line distance of 80 mm. At 45 s, a second fluid finger invades at the top of the fracture, adjacent to the initial finger. In measuring the flow path taken by the second fluid finger, from entry to exit points, the length is approximately 87 mm, approximately 8.7% longer than the straight-line distance of 80 mm. As this finger develops, the resulting flow path is visibly influenced by the geometry of the quartzite fracture walls as shown in Fig. 2 and described as follows:

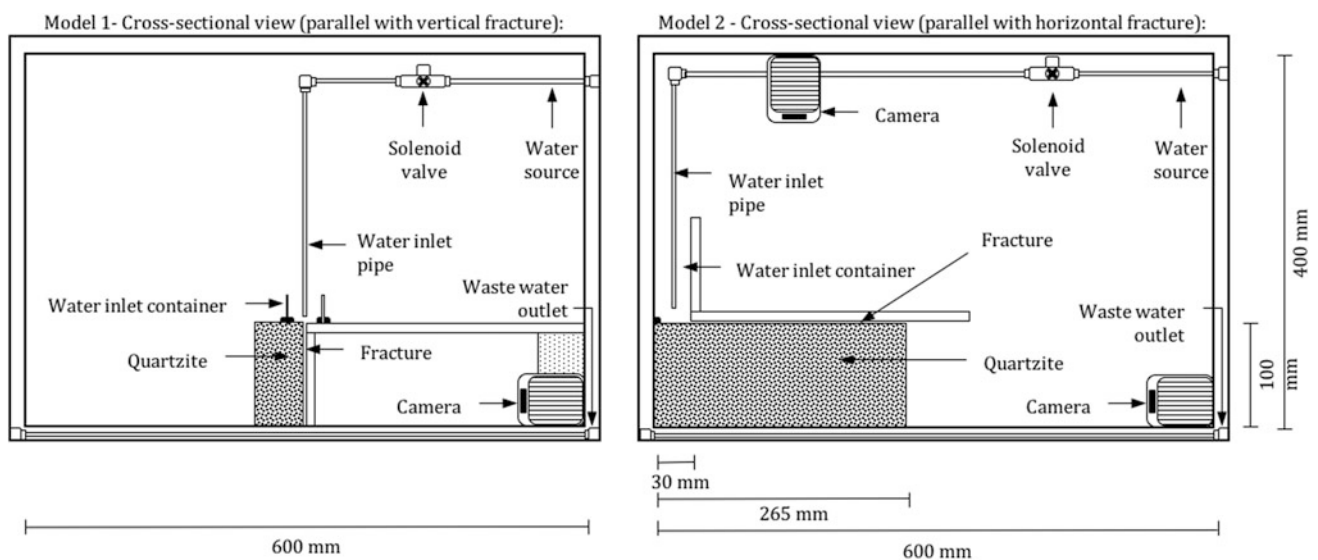
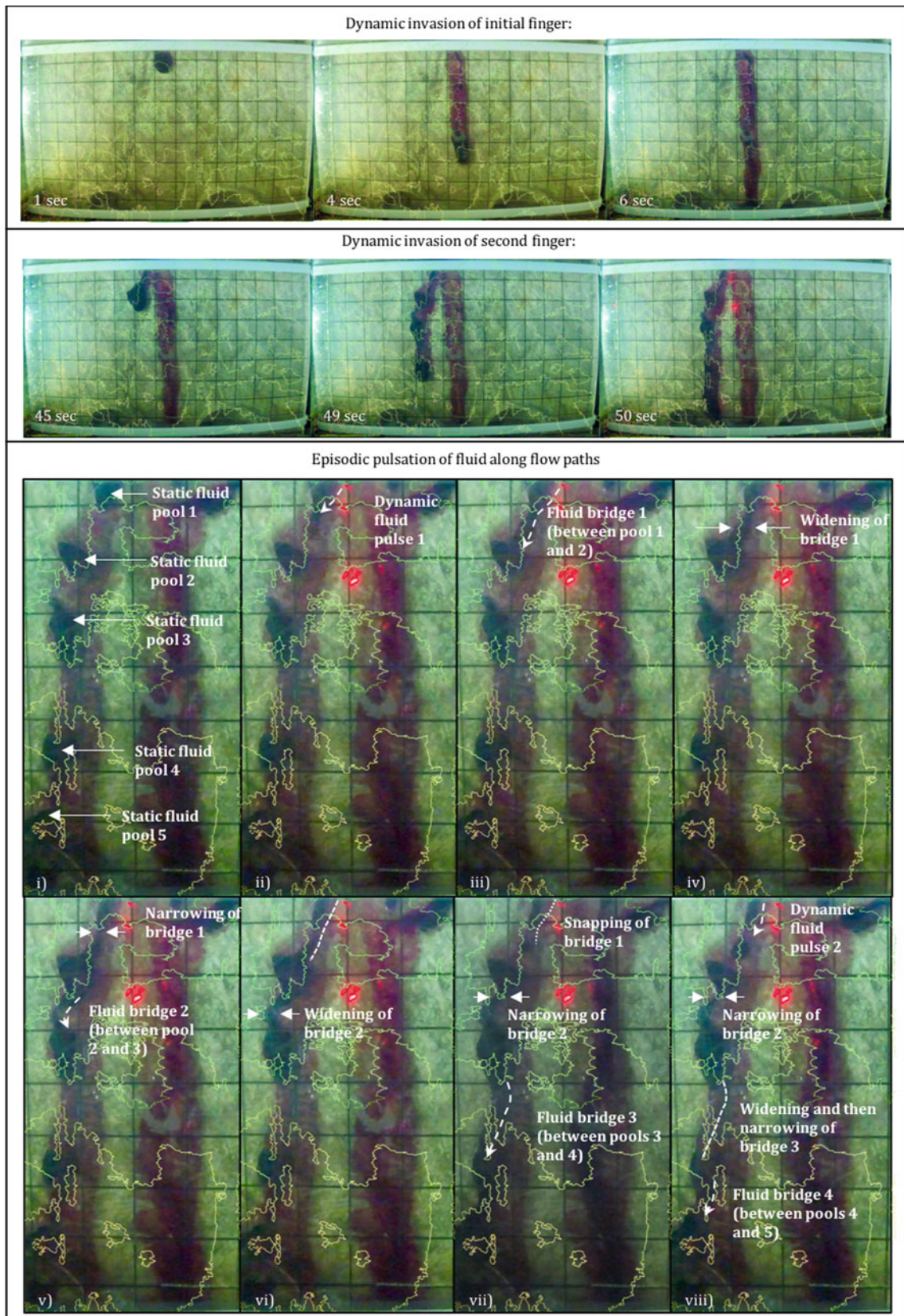


Fig. 1 Model set-up for the Model 1: vertical fracture (left), and Model 2: horizontal fracture (right)



**Fig. 2** Model 1 (vertical fracture): Invasion of initial and second fingers during wetting, with integrated dynamic flow occurring along the second finger (10 mm × 10 mm grid). Static pools are present where contact obstacles occur within the fracture

- i. Five static pools are observed along the second finger;
- ii. A dynamic pulse of fluid moves vertically downward from the top pool (1);
- iii. Fluid pulse 1 moves towards the underlying static pool 2, and joins the two pools via an aperture-spanning fluid bridge (1);
- iv. Fluid bridge 1 widens as fluid is transferred between pools 1 and 2;
- v. Fluid bridge 1 narrows as the fluid has been transferred, and concurrently a second fluid bridge (2) develops between static pool 2 and static pool 3;
- vi. Fluid bridge 2 widens as fluid is transferred, while fluid bridge 1 continues narrowing;
- vii. Fluid bridge 1 snaps and pools 1 and 2 disconnect, whilst at the same time fluid bridge 2 narrows, and a third fluid bridge (3) develops between the static pool 3 and 4;
- viii. Fluid bridge 2 continues narrowing (but never snaps), whilst a fourth fluid bridge (4) develops between pools 4 and 5. A second dynamic pulse of fluid is now seen developing at fluid pool 1, and the process repeats itself.

### 3.2 Model 2: Horizontal Fracture

A visual summary of the experiment and the observed flow mechanisms is shown in Fig. 3. During the first 5-min of the test, fluid pools invade the fracture as two wetting fronts into the back-right and back-left corner of the fracture. For the next minute thereafter, the wetting fronts do not obviously advance along the length of the fracture, as both fluid pond fronts are contained by a ridge on the fracture where a narrowing of aperture occurs. This period of no advancement of the wetting front occurs during the addition of 8.4 ml of fluid to the inlet container. At approximately 6 min into the test, the fluid pond in the back-right breaches this ridge, and fluid rapidly spills into a depression in the central-right of the fracture. Based on the geometry of the depression, approximately 5.2 ml of fluid occupies this depression, within the 30 s that it develops. A minute thereafter the depression continues to fill at a slow rate, but there is again no advancement of the wetting front until a minute later, where the process of filling and spilling repeats itself, albeit much less discernible due to the lack of such a tight aperture as previous.

At 9:20 min into the test, the fluid pool reaches the vertical exit wall, where fluid exists from the horizontal fracture as a single advancing sliding droplet. This droplet does not snap, and instead establishes a continuous rivulet along the right side

of the vertical exit wall. The fluid pools within the horizontal fracture continue expanding slightly, for the next 2 min, until this process stops and the system seems to be in equilibrium. This flow path that the fluid took is measured from the centre of the ridge and depression, being 268 mm in length, which is 14% longer than the straight-line distance of 235 mm.

## 4 Discussion and Conclusion

Results on both models show that flow path lengths are between 4 and 14% longer for the rough-walled quartzite fractures with contact obstacles, which is similar to the findings of Kishida et al. (2013). Furthermore, the orientation of the fracture influences the length of the flow paths, whereby flow paths in the horizontal fracture are longer than those in the vertical experiment.

In open, clean, rough-walled, mismatched horizontal fracture walls, this can be explained by the findings of Nicholl and Glass (2007) where flow is forced to pass through the choke point and the conductivity is dependent thereof. This leads to a fill and spill process, similar to that described by Tokunaga and Wan (1997) and Tokunaga et al. (2000). Here, thick pendular regions form within topographic depressions and thin pendular films at the topographic ridges (choke points). Flow occurs into depressions where the fluid rapidly invades, whilst fluid is contained by choke-points, formed at ridges in the roughness profile of the fracture. Once the fluid pool reaches the elevation of the choke point, it breaches and spills into the next depression and the cycle continues.

This is in contrast to the role that choke points have on unsaturated flow in vertical fractures, where instead of a choke point constraining flow (Pyrak-Nolte et al. 1988), they dictated flow paths under intermittent influx conditions. Here, the fluid travels between the fluid bridges that develop around the contact points. This flow mechanism displays a hysteric behavior, whereby the narrower aperture of the fracture is wetted and subsequently drains with fluid pools remaining due the influence of capillary forces, instead of needing to overcome larger gravitational forces in the larger apertures that drain quicker.

In aiming to understand discrete fracture flow at partial saturation, it becomes increasingly evident that a more fundamental knowledge gap exists in the understanding of not *how much* water flows through fractures, but rather *how* water flows through fractures per se. Using black box model approaches (i.e. bulk flow methods) can generally be estimated with a fair amount of confidence. However, the problem faced relates to how water is transferred through individual fractures. Clearly, while there is improvement in

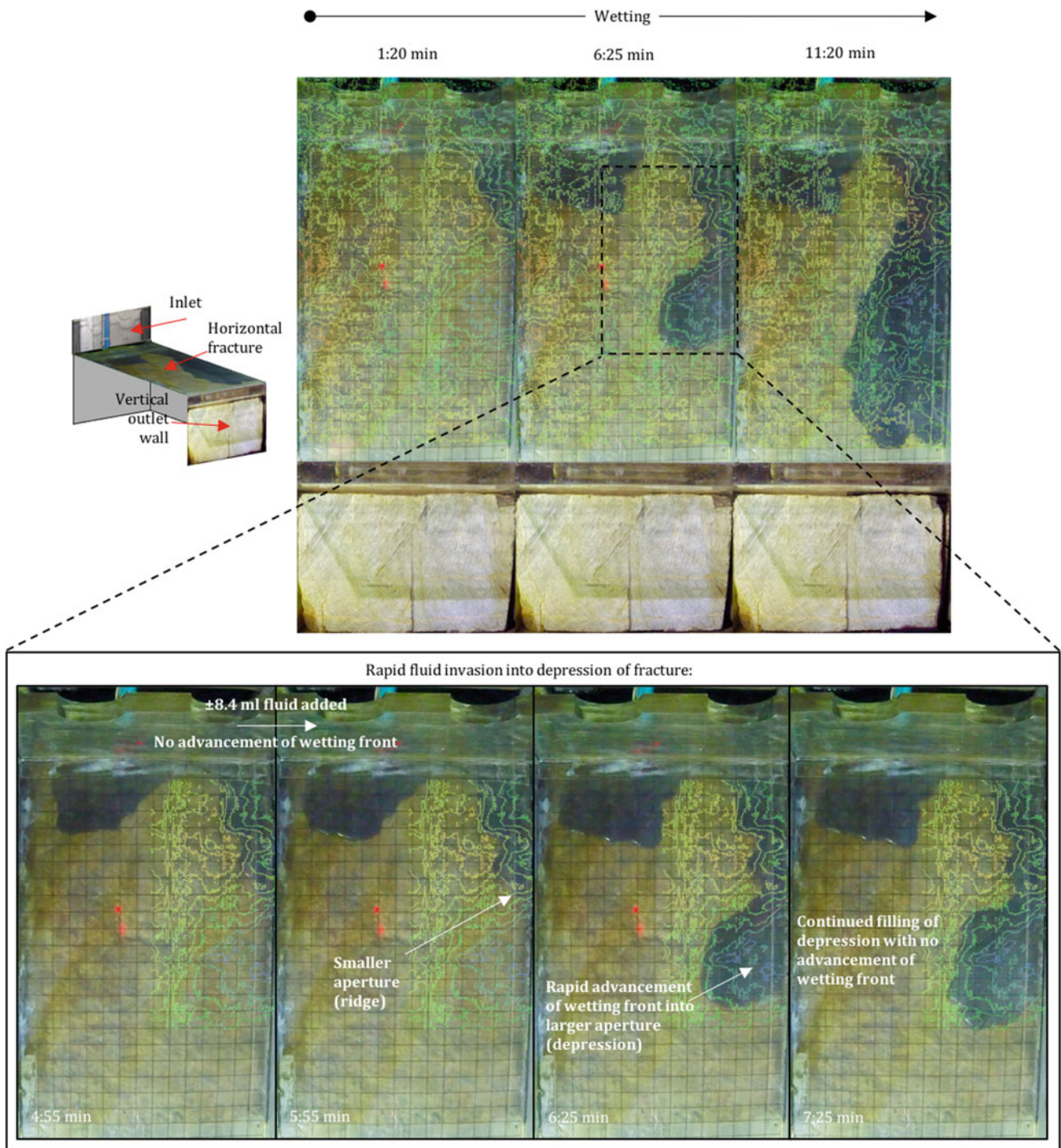


**Fig. 3** Model 2 (horizontal fracture): Summary of the wetting and observed flow mechanisms of the horizontal fracture (10 mm × 10 mm grid). Blue contours indicate larger apertures, and orange contours indicate narrower apertures

the understanding of the science behind partially saturated flow, the implications of poor understanding and interpretation are only now starting to manifest themselves. Although significant progress has been made, there is still a long way to go to properly anticipate the role of highly variable moisture content in fractured systems.

## References

Barton, N.: Modelling rock joint behavior from in situ block tests. Implications for nuclear waste repository design (1982)  
 Barton, N., Choubey, V.: The shear strength of rock joints in theory and practice. *Rock Mech.* **10**, 1–54 (1977)

- Barton, N., de Quadros, E.F.: Joint aperture and roughness in the prediction of flow and groutability of rock masses. *Int. J. Rock Mech. Min. Sci.* **34**, paper no. 252 (1997). [http://dx.doi.org/10.1016/S1365-1609\(97\)00081-6](http://dx.doi.org/10.1016/S1365-1609(97)00081-6)
- Berkowitz, B.: Characterizing flow and transport in fractured geological media: a review. *Adv. Water Resour.* **25**, 861–884 (2002). [https://doi.org/10.1016/S0309-1708\(02\)00042-8](https://doi.org/10.1016/S0309-1708(02)00042-8)
- Dippenaar, M.A., Van Rooy, J.L.: On the cubic law and variably saturated flow through discrete open rough-walled discontinuities. *Int. J. Rock Mech. Min. Sci.* **89**, 200–211 (2016). <https://doi.org/10.1016/j.ijrmms.2016.09.011>
- Jones, B.R., Brouwers, L.B., Dippenaar, M.A.: Partially to fully saturated flow through smooth, clean, open fractures: qualitative experimental studies. *Hydrogeol. J.* (2017). <https://doi.org/10.1007/s10040-017-1680-3>
- Kishida, K., Sawada, A., Yasuhara, H., Hosoda, T.: Estimation of fracture flow considering the inhomogeneous structure of single rock fractures. *Soils Found.* **53**, 105–116 (2013). <https://doi.org/10.1016/j.sandf.2012.12.007>
- Neuman, S.P.: Trends, prospects and challenges in quantifying flow and transport through fractured rocks. *Hydrogeol. J.* **13**, 124–147 (2005)
- Nicholl, M., Glass, R.: Wetting phase permeability in a partially saturated horizontal fracture. In: *Proceedings of 5th Annual International Conference on High Level Radioactive Waste Management*, pp. 22–26 (2007)
- Pyrak-Nolte, L.J., Cook, N.G.W., Nolte, D.D.: Fluid percolation through single fractures. *Geophys. Res. Lett.* **15**, 1247–1250 (1988). <https://doi.org/10.1029/GL015i011p01247>
- Tokunaga, T.K., Wan, J.: Water film flow along fracture surfaces of porous rock. *Water Resour. Res.* **33**, 1287–1295 (1997)
- Tokunaga, T.K., Wan, J., Sutton, S.R.: Transient film flow on rough fracture surfaces. *Water Resour. Res.* **36**, 1737–1746 (2000)

# Experimental and Numerical Study of the Groundwater Quality in Altered Volcanic Rock Area

Takehiro Ohta, Shuichi Hattori, Yoshihiro Kikuchi, and Dai Shimofusa

## Abstract

Groundwater geochemistry associated with the Hakkouda Tunnel in the Sankaku-dake Mountains, Aomori prefecture, northern Japan, was surveyed in an experimental and numerical study to understand the mechanism forming the groundwater quality in altered volcanic rock mass. We already made clear that the groundwater quality in this area corresponds with the mineral assemblages in the rock masses. Altered volcanic rock samples were tested by batch-leaching test to estimate rock-water reaction model in equilibrium conditions, in which 100 g crushed rock samples, under 10 mm in diameter, were shaken with 500 g pure water. The results of this test show that the chemical quality of the leaching water from an altered rock sample is similar to that of groundwater distributed in same rock mass. The numerical simulations using PHREEQC verified the results of the leaching test for altered volcanic rock samples. The calculation results support that the water reacts with rock (minerals) in equilibrium. From these results, we can estimate that the quality of fissure groundwater in hard rock mass depends on the equilibrium reaction with co-existing minerals in aquifer and that the geochemical homogenization of

groundwater by diffusion and/or dispersion do not influence the groundwater quality.

## Keywords

Groundwater quality • Altered volcanic rock • Leaching test • Thermo-dynamic simulation

## 1 Introduction

Recently groundwater pollution caused by the heavy metal elements from natural rock mass becomes serious issue, and is widely noticed. It is well known for example that the seepage water from mines has strong acidity and has high heavy metal elements concentration (Saskatchewan Environment and Public Safety Mine Pollution Control Branch 1992). It is suggested that the wide area arsenic pollution of groundwater depend on the hydrogeology of aquifer (Shimada 2003). On the other hand, it is afraid that concrete materials such as lining of tunnels are deteriorated by the long-term seepage of acid groundwater and that agricultural environment around tunnels is influenced by constant alkaline water seepage.

The groundwater quality will be changed by the reaction between water and minerals and will attain to chemical equilibrium condition in the aquifer. It is probable therefore that the geology of aquifer influence to groundwater quality (Seki et al. 1999). It is expected that acidification and concentration of heavy metal are occurred in groundwater contacting ore-vein around the mines. We summarized the influence of mineral assemblage to form groundwater quality from the result of comparison between water quality and mineral assemblage in spatial at Hakkouda Tunnel (Ohta et al. 2015).

We will discuss how the groundwater quality is make up by mineral-water reaction based on leaching test and thermo-dynamics simulation combined with field survey results.

T. Ohta (✉)

Division of Earth Science, The graduate School of Science and Technology for Innovation, Yamaguchi University,  
Yoshida 1677-1 Yamaguchi, Japan  
e-mail: takohta@yamaguchi-u.ac.jp

S. Hattori

Japan Railway Construction, Transport and Technology Agency,  
Yokohama, Japan

Y. Kikuchi

Japan Mining Engineering & Training Center, Tokyo, Japan

D. Shimofusa

NS Environmental Science Consultant Corporation,  
Yamagata, Japan



## 2 Geological Setting and Groundwater Quality

The Neogene formations distribute around the Hakkouda Tunnel, and the Neogene intrusive rocks intrude into these formations (Fig. 1) (Ohta et al. 2015). The Quaternary pyroclastic flow deposits from the Hakkouda volcano cover these Neogene rocks. The structure of the Neogene formations around this tunnel is an anticline to extend the axis from north to south at the summit of this tunnel. There are many abandoned mines, e.g. the Kitakami Mine, around this tunnel. The abandoned mine to be distributed over less than 3 km from this tunnel is 11 mines, e.g. the Taisei Mine (Fig. 1). These abandoned mines classified as ore vein type mines, which consist of pyrite, chalcopyrite and sphalerite mainly (Ohta et al. 2015).

We already reported the groundwater quality in each formation distributed around the Hakkouda Tunnel (Shimofusa et al. 2003). We collected and analyzed 1006 primitive groundwater samples that were gushed out from the cutting face and the pilot drilling to confirm the spatial distribution of the groundwater quality. The groundwater around the Hakkouda Tunnel is classified into calcium-bicarbonate and/or calcium-sulfate type and is in range from 7.5 to 9.5 in pH. Some groundwater showing extreme feature of calcium-sulfate type shows low pH below 4.5.

## 3 Groundwater Quality Controlled by Mineral Assemblage

The representative samples were examined by X-ray powder diffraction (XRD) in order to grasp the influence of the mineral assemblage on the groundwater quality (Ohta et al. 2015). We examined 580 rock samples collected from cutting faces and pilot drilling cores.

The diffracted intensity of each mineral detecting in samples by X-ray powder diffraction is divided into 4 grades qualitatively. Figure 2 indicates the spatial distribution of the diffracted intensity of each mineral. In this figure the diffracted intensity shows as proximity average grade of 20 samples approaching it. Because it is not a sampling of the equal distance, the proximity average of the number of the uniform samples does not express correct qualitative grade. However, we can understand the distribution of the diffracted intensity of minerals in a large sense at the wide spatial range shown in Fig. 2.

We can classify type of alteration of rock mass based on the mineral assemblage getting from XRD results. Two sections, i.e. 639–640 km and 645–646 km, have mineral assemblage in acidic altered zone, such as kaolinite and pyrophyllite. From 642 to 645 km and from 651 to 653 km, the mineral assemblages of rock mass are of alkaline altered zone, e.g. zeolite and smectite. Other sections are classified in neutral altered zone, but some area have high contents of

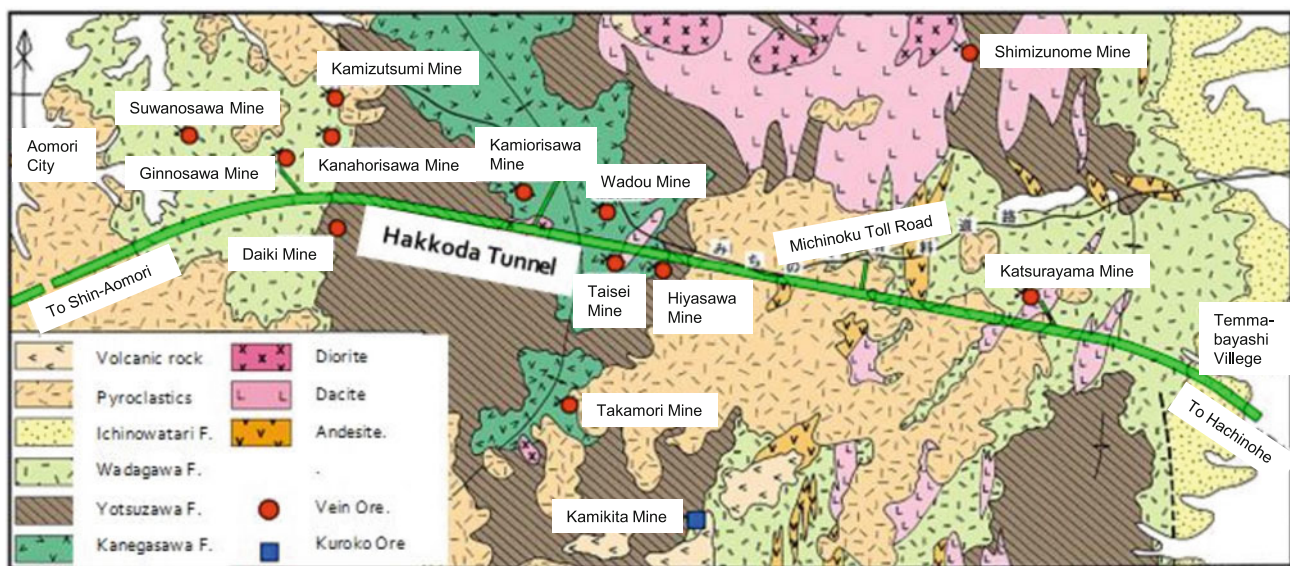
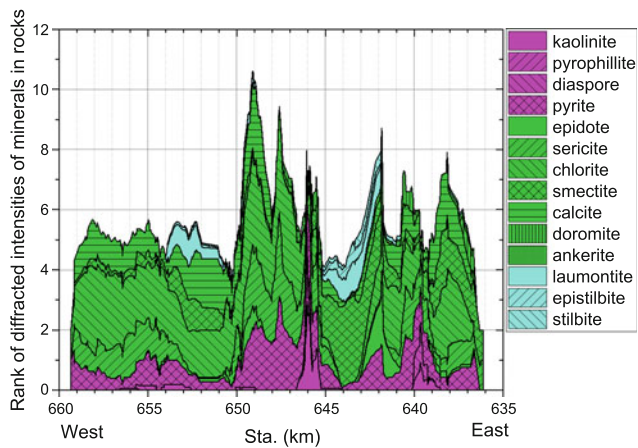


Fig. 1 Geological map around the Hakkouda Tunnel (Ohta et al. 2015)



**Fig. 2** Spatial distribution of mineral assemblage (Ohta et al. 2015)

pyrite, e.g. 640–641 km, 646–650 km, 653–656 km and 658–660 km.

To understand the spatial distribution of groundwater quality in a large sense, we illustrate the spatial variation of proximity average values of pH, electrical conductivity (EC), cations and anions concentrations of 10 samples coming close to in Fig. 3 (Ohta et al. 2015). The groundwater distributed in the area in which diagenesis was the dominant alteration process is in range from 8.0 to 9.0 in pH and ranges from 10 to 30 mS/m (Ohta et al. 2015). At the areas affected by both hydrothermal alteration and diagenesis with many pyrites the EC of groundwater exceed 40 mS/m (Ohta et al. 2015). If the rock masses include calcite with pyrite at the same level especially, e.g. 640–641 km, 648–650 km, around 655 km, the groundwater has more than 80 mS/m of EC (Ohta et al. 2015). On the other hand, the groundwater in rock masses affected by remarkable acidic alteration, 645–646 km, indicates strong acidity, lower than 4.0 of pH. The pH of groundwater at 639–640 km including acidic alteration minerals becomes lower than that of peripheral groundwater (Ohta et al. 2015). If the calcite and pyrite of quantity at same level are contained in rock mass, the concentration of  $\text{Ca}^{2+}$  and  $\text{Mg}^{2+}$  in the groundwater becomes higher than peripheral area (Ohta et al. 2015). The concentrations of  $\text{Na}^+$ ,  $\text{Ca}^{2+}$  and  $\text{Mg}^{2+}$  in the groundwater are slightly low at the area in which the mineral assemblages of neutral to alkaline alteration, such as zeolite, are recognized (Ohta et al. 2015).  $\text{SO}_4^{2-}$  concentrations in groundwater become high at the area in which acidic altered minerals distribute and at the diagenesis alteration area which contain many pyrite (Ohta et al. 2015).  $\text{SO}_4^{2-}$

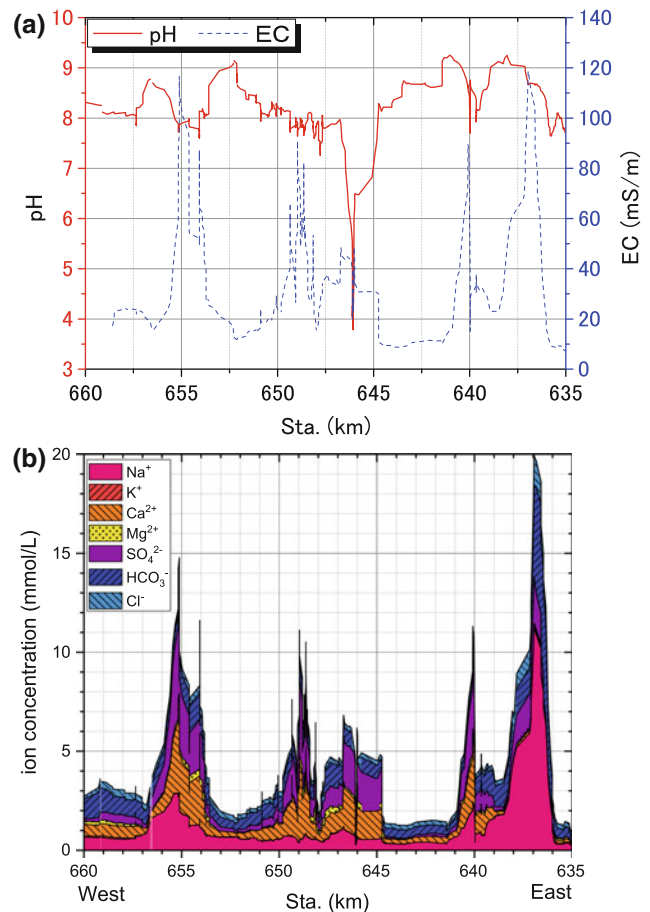


**Fig. 3** Spatial distribution of groundwater chemistry (Ohta et al. 2015). **a** pH and electrical conductivity, **b** ion concentration

concentration in the groundwater at neutral and alkaline alteration zone indicates low value.

From above mentioned results, groundwater chemistry is controlled by the alteration type of rock mass defined due to mineral assemblage. From Figs. 2 and 3, we can understand that the groundwater chemistry changes remarkably at the boundary of alteration types. This fact indicates that the groundwater does not mix each other beyond the boundary, or that the groundwater inflowing to an alteration zone is equilibrated with peripheral rock mass instantly.

#### 4 Batch Leaching Test

To verify the water quality equilibrated with rock materials, water quality of leachate was examined after batch leaching test of rock samples obtained from the Hakkouda Tunnel.

## 4.1 Testing Method

The procedure of this test is as follows (Hattori et al. 2003).

- (1) The rock samples are crushed to grains smaller than 10 mm in size after dried.
- (2) Portions of 100 g of the crushed samples are mixed with 500 ml-distilled water and the mixture samples are shaken for three minutes.
- (3) The pH and electric conductivity of the leachate are measured after 10 min, 1 h, 24 h, 7 days, 28 days and 56 days.
- (4) The concentrations of cations ( $\text{Na}^+$ ,  $\text{K}^+$ ,  $\text{Ca}^{2+}$ ,  $\text{Mg}^{2+}$ ) in the leachate after 56 days are determined by ICP emission spectrometry (Shimazu ICPS-7500). The  $\text{SO}_4^{2-}$  content and  $\text{Cl}^-$  content in the leachate are determined by the ion chromatography, and the  $\text{HCO}_3^-$  content is measured by the sulfate titration method.

## 4.2 Results of Batch Leaching Test

Figure 4 shows the spatial distribution of leachate water chemistry after 56 days leaching, which indicates as proximity average values of 50 samples approaching it. In this figure, the spatial variation of proximity average values of groundwater chemistry of 10 samples coming close is illustrated to compare with the spatial distribution of leachate water chemistry.

The results of Fig. 4 illustrates mostly the same spatial distribution of water chemistry between groundwater and leachate. This fact suggests that the groundwater chemistry is controlled by rock mass chemistry due to mineral assemblage and that the groundwater will become equilibrium with peripheral rock mass instantly. However, we can recognize that some cases need long time to become equilibrium state because partly groundwater chemistry of pyrite dominant area differ from leachate chemistry, i.e. 653–656 km.

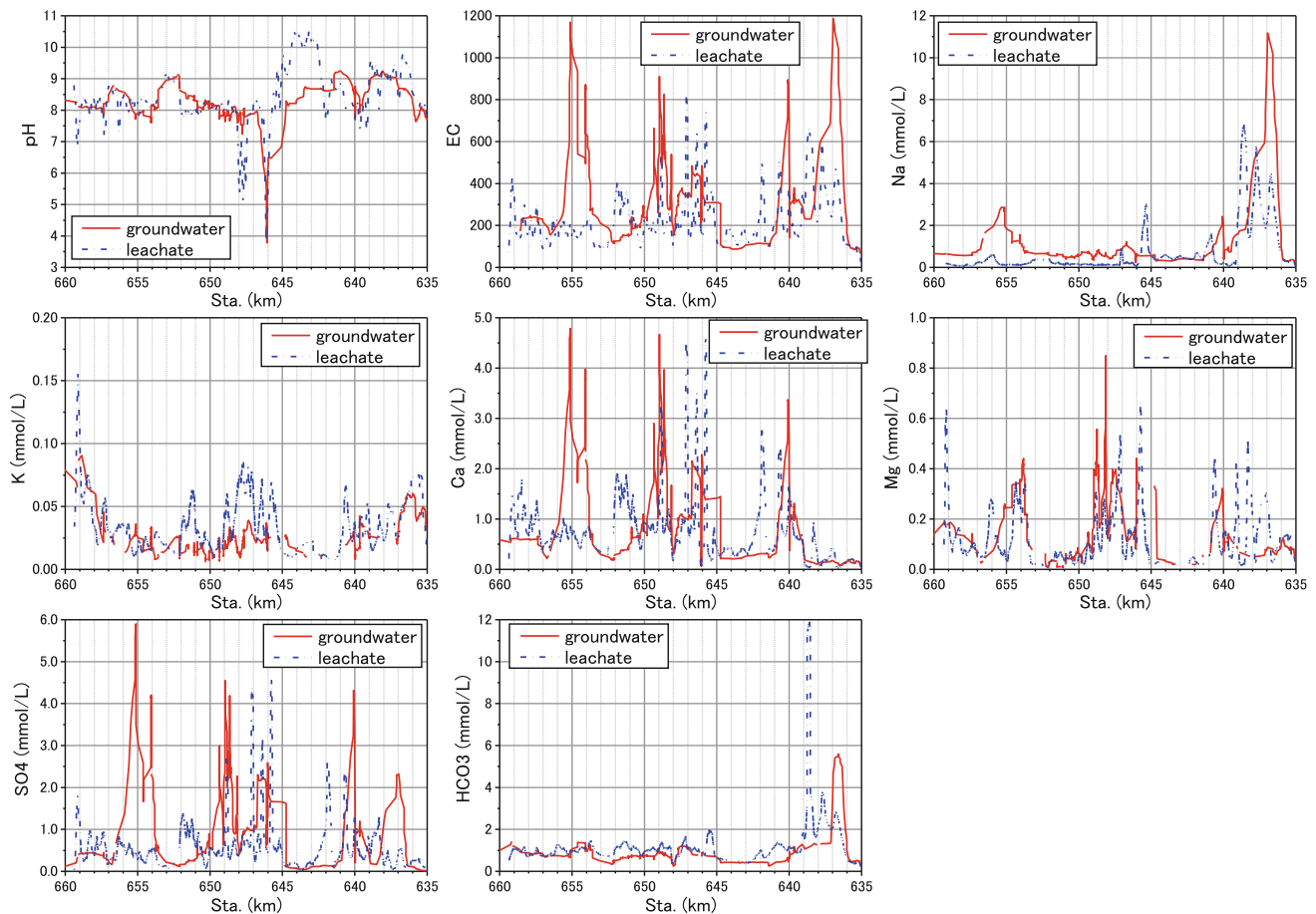


**Fig. 4** Comparison between groundwater chemistry and leachate chemistry

## 5 Thermo-dynamic Simulation

As mentioned above, the facts that the groundwater chemistry harmonize with mineral assemblage and agree with leachate chemistry, suggest that the groundwater quality is formed under the condition equilibrated with peripheral rock mass. We therefore try to verify equilibrium reaction between groundwater and minerals by geochemical code PHREEQC (Parkhurst and Appelo 1999) using thermo-dynamic theory.

### 5.1 Simulation Model

The thermo-dynamic calculations simulated the water-mineral reaction under the batch-leaching test conditions, i.e. 100 g crushed minerals mixed with 500 ml-distilled water under atmospheric  $\text{CO}_2$  gas partial pressure ( $[P_{\text{CO}_2}] = 10^{-3.5}$ ), 25 °C and 6.0 in pH.

Some chemical species will be removed from aqueous phase as colloidal compounds or low crystallinity compounds under the condition of water-mineral reaction in leaching test, if the compounds concentration will come to saturation state. In the simulation model, we set up these compounds, i.e. ferrihydrite ( $\text{Fe}(\text{OH})_3$ ), gibbsite, cerussite, tenorite, smithsonite, willemite, as precipitation phase by EQUILIBRIUM keyword in PHREEQC. The partial pressure of  $\text{CO}_2$  gas was set up by same command.

Sorption was modeled as surface complexation onto ferrihydrite and gibbsite. The equilibrium constants of surface complexation onto ferrihydrite and gibbsite suggested by Parkhurst and Appelo (1999) and Karamalidis and Dzombak (2010) respectively are adopted. We used 0.2 mol weak site and 0.005 mol strong site per mol Fe, a surface area of  $5.33 \times 10^4 \text{ m}^2 \text{ mol Fe}$  for ferrihydrite, and used 0.033 mol per mol Al, a surface area of  $2500 \text{ m}^2 \text{ mol Al}$  for gibbsite. These parameters were set up by SURFACE keyword in PHREEQC.

Reacting minerals assemblage and amount of each mineral in the leaching test were estimated from bulk chemistry of rock samples based on the method suggested by Ohta et al. (2013). The reaction of estimated minerals with water in the leaching test were modeled by REACTION keyword in PHREEQC as the irreversible reactions. The reacting primary minerals and secondary minerals were presumed 0.1 and 0.001 mm in diameter respectively, and both were presumed as sphere shape.

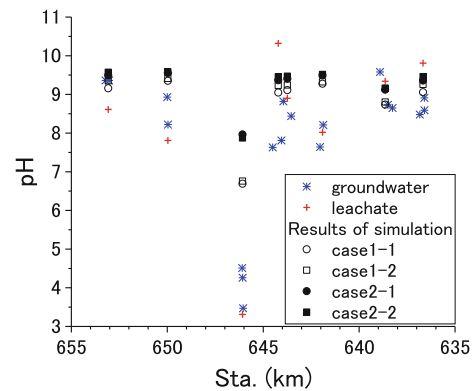


**Fig. 5** Spatial distribution of pH in groundwater, leachate and calculated result for the leaching test. Case 1, equilibrium with ferrihydrite and gibbsite; Case 2, equilibrium with ferrihydrite and gibbsite; case x-1, all Fe in rock samples as ferric; case x-2, 80% of Fe in rock samples divided to ferrous

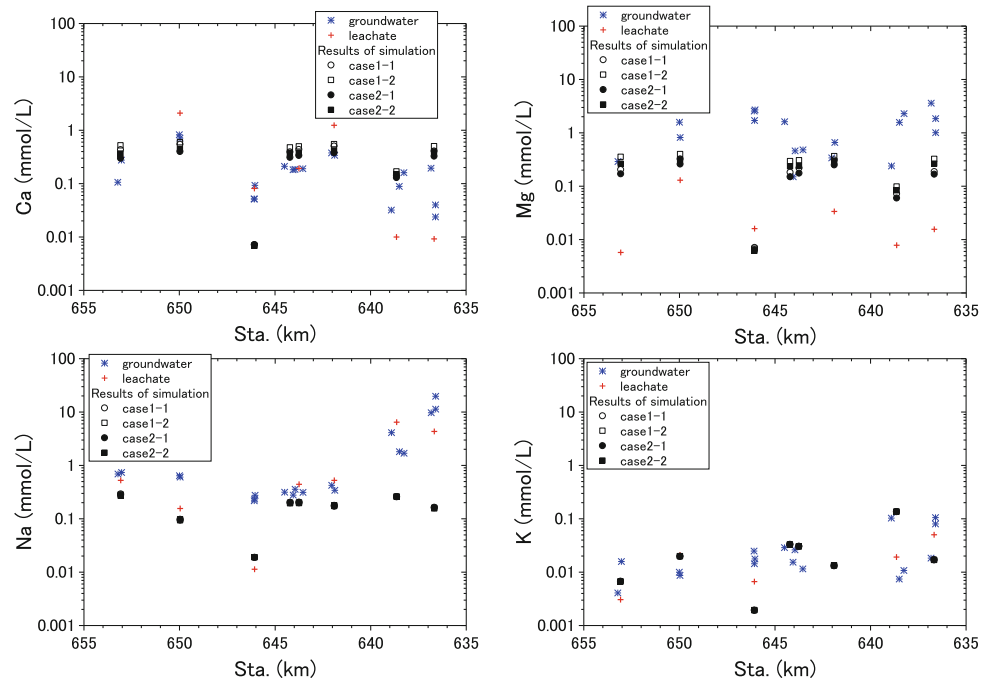
### 5.2 Results of Simulation

Figure 5 shows spatial distribution of pH's of groundwater, leachate and calculated result of the leaching test. We can recognize that spatial changes of pH indicate similarity among groundwater, leachate and simulation result. At around 646 km, groundwater and leachate are lower 5.0 in pH, and calculated pH shows below 7.0, which is higher than groundwater and leachate. However, because the calculated pH at 646 km is remarkably lower than pH values of other area, it seems that the calculation can simulate pH of leachate.

Cation concentrations calculated by the simulation are close to the concentration of leachate and groundwater at most area (Fig. 6). However, calculated concentration both of calcium and sodium from 635 to 640 km are differ from the concentration of leachate and groundwater. Total amount of calcium and sodium can be simulated at this area as with other area. Because smectite and sericite are dominant mineral phase at 635–640 km, we can consider that the cation exchange causes the difference of concentration in Ca and Na between calculation and leachate, groundwater.

Calculated sulfate concentrations show extreme low than the concentration of leachate and groundwater (Fig. 7). But spatial changing trend of calculated sulfate concentration is similar to the trend of leachate and groundwater.

From the above-mentioned results, we can grasp that the calculation model can simulate the water chemistry forming



**Fig. 6** Spatial distribution of cations in groundwater, leachate and calculated result for the leaching test. Case 1, equilibrium with ferrihydrite; Case 2, equilibrium with ferrihydrite and gibbsite; case

x-1, all Fe in rock samples as ferric; case x-2, 80% of Fe in rock samples divided to ferrous

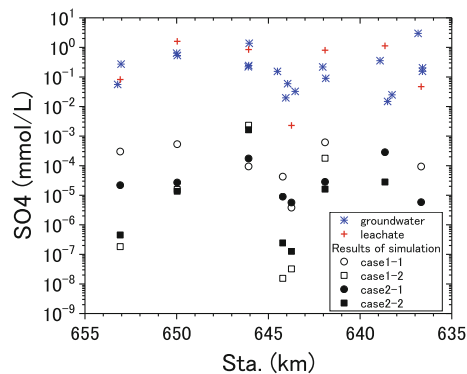


**Fig. 7** Spatial distribution of sulfate concentration in groundwater, leachate and calculated result for the leaching test

mechanism of leachate and groundwater. This means that the groundwater chemistry is formed by equilibrium reaction between water and mineral assemblage in rock mass.

## 6 Conclusions

To understand water quality forming mechanism in altered volcanic rock area, we examined the relationship among the groundwater chemistry, the mineral assemblage, the leachate water quality in leaching test and calculated leachate water quality by thermo-dynamic simulation. The examination leads the results as follows;

1. The comparison between groundwater quality and mineral assemblage shows that groundwater chemistry is controlled by the alteration type of rock mass determined by mineral assemblage. And the groundwater inflowing to an alteration zone is equilibrated with peripheral rock mass instantly (Fig. 8).
2. The results of leaching test suggest that the groundwater chemistry is controlled by rock mass chemistry caused by

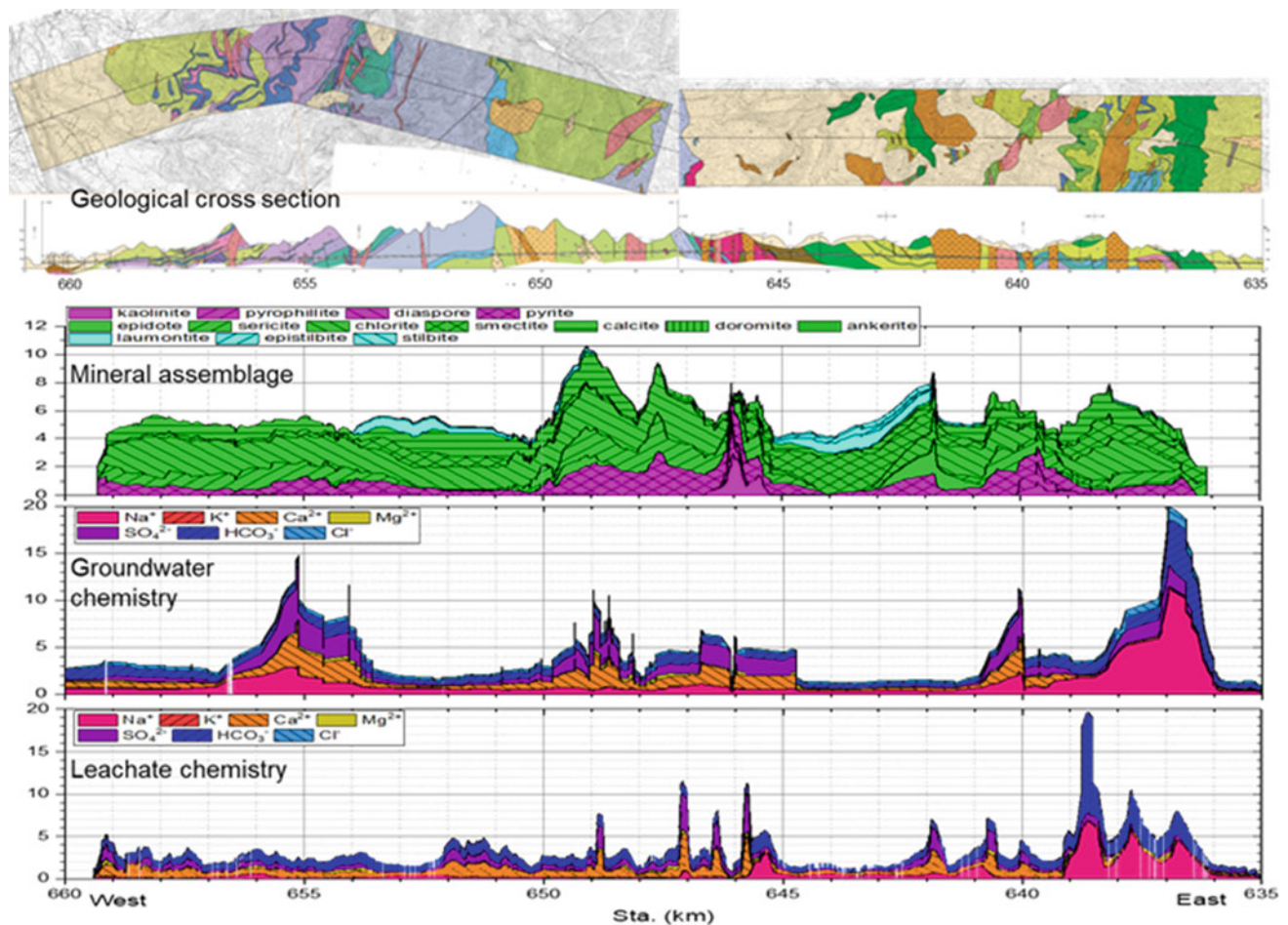


**Fig. 8** Tunnel zoning map of geology, mineral assemblage, groundwater chemistry and leachate chemistry

mineral assemblage and that the groundwater will become equilibrium with peripheral rock mass instantly (Fig. 8).

3. The thermo-dynamic simulation supports the above results.

## References

- Saskatchewan Environment and Public Safety Mine Pollution Control Branch: Mine Rock Guidelines, Design and Control of Drainage Water Quality. Steffen Robertson and Kirsten (B.C.) Inc. (1992)
- Shimada, N.: Arsenic in groundwater: the chemical behavior, source and relevant problems. *Shigen-Chishitsu*. **53**(2), 161–172 (2003)
- Seki, Y., Kanai, Y., Kamioka, H., Tsukimura, K., Hamasaki, S., Kanazawa, Y., Nakajima, T.: Relationship between geology and water quality of rock seepage from quarries—a case study around the Yamizo mountains. *Bull. Geol. Surv. Jpn.* **50**(11), 683–697 (1999)
- Ohta, T., Hattori, S., Kikuchi, Y. and Shimofusa, D.: Influence of mineral assemblage to form the groundwater quality in altered rock area. In: *Proceedings of 10th Asian Regional Conference for IAEG*, Tp3–P19 (2015)
- Shimofusa, D., Ohta, T., Hattori, S.: The relationship between groundwater qualities from the Neogene formations in the Hakkouda Tunnel and their geology. In: *Proceedings of the JSEG 2003* (2003)
- Hattori, S., Ohta, T., Kiya, H.: Engineering geological study on exudation of acid water from rock mucks—evaluation methods of rocks at the Hakkouda tunnel near mine area. *J. Japan Soc. Eng. Geol.* **43**(6), 359–371 (2003)
- Parkhurst, D.L., Appelo, C.A.J.: User's guide to PHREEQC (version 2) —a computer program for speciation, batch-reaction, one-dimensional transport, and inverse geochemical calculations. *Water-Resources Investigations Report 99-4259*, U.S. Geological Survey (1999)
- Karamalidis, A.K., Dzombak, D.A.: *Surface Complexation Modeling* Gibbsite. Wiley (2010)
- Ohta, T., Marumo, K., Atsuta, S.: Thermo-dynamic simulation of batch leaching tests for soils and rock samples. In: *Proceedings of 13th Japan Symposium on Rock Mechanics & 6th Japan-Korea Joint Symposium on Rock Engineering* (2013)

# Secondary Groundwater Resources Exploited by Traditional Knowledge Systems in a Semiarid Region of Southern Italy

Vincenzo Simeone and Antonio Graziadei

## Abstract

Devices used to catch secondary groundwater resources are common in inland southern Italy, though little known to Italian technical literature. They are an interesting example of how the local non-technically-codified knowledge allows for exploiting the water resources. This paper presents the case study of the drainage tunnels (locally called *cape d'acqua*) of Casino Rago, near the town of Ferrandina, in Basilicata region. Despite its similarities to other underground collection systems that can be found in the region, the device presented here has some unique features within its structure and because it drains water in an area where the dominant outcropping geological formation is silty clay. This tunnel, together with other *cape d'acqua* and other underground water catchment systems, played a very important role in the development of many agricultural areas in Basilicata. Unfortunately, most of them are no longer in use for their original purpose, so they are slowly undergoing an abandonment process. Recognising the role that structures of this kind have had in the formation of the traditional landscape is the only way to ensure the continuation of a sustainable technique of water management and the transmission of the landscape values to the future.

## Keywords

Secondary groundwater resources • Draining tunnels • Traditional knowledge • Traditional landscape

## 1 Introduction

Draining tunnels is a generic term that identifies a wide variety of systems for water catchment which allow using groundwater to supply urban and agricultural areas. The tunnels are dug almost horizontally beneath the Earth's surface and can grow to a few metres or several kilometres (Laureano 2001).

These water collection systems can also be found in Italy where, among others, the *qanat* of Palermo (Todaro 1988) and the Etruscan tunnels (Ravelli and Howarth 1984) are known to be. In Basilicata, examples of them are found in Irsina (Graziadei 2015), where a system of underground tunnels, named Bottini, still collects the groundwater and carries it to the underlying monumental fountain, and onto the near farming areas. In Tricarico (Graziadei 2015) such a structure was identified, though partially damaged and altered in its original function. Other examples of similar structures in Basilicata such as Casino Laudati tunnel are found in the territory of Ferrandina (Graziadei 2015), where they are called "*cape d'acqua*", and their water production in the past used to support small irrigated areas within more extended olive plantations.

The case study presented here comes from Ferrandina and, for its building characteristics and planimetric design, is an important example of a draining tunnel in the Basilicata region.

## 2 Geological Characteristics and Groundwater

Geologically the area of Ferrandina, Fig. 1, is part of the Bradanic Foredeep (Galeandro et al. 2013, 2017), a large tectonic trough, filled since the end of Pliocene up to the end of Pleistocene. This shows a significant thick sequence of clayey silts, evolving in the upper part into sands and finally top regressive conglomerates. The sedimentary sequence,

V. Simeone (✉)

Department of Civil, Environmental and Construction Engineering and Chemistry, Technical University of Bari, via E. Orabona 4, 70125 Bari, Italy  
e-mail: vincenzo.simeone@poliba.it

A. Graziadei

Architect, Paesaggi Meridiani, via Pienza, 24, 85100 Potenza, Italy

Fig. 2, going upward, is made by Sub-apennine clays. These contain: silty clays and clayey marly silts, rich of carbonates, up to 40%, characterized by a grey-blue colour. The high content of carbonates makes these clays particularly hard and compact. Within the clay outcrops, the top is characterized by a ochraceous-brown colour, for a thickness ranging between few meters to 10–12 m. The top of the sequence is constituted by regressive sandy conglomerate deposits, like Monte Marano sands and Irsina conglomerate. These deposits constitute the top of the plate on which Ferrandina town is located, where the thickness of this layer is 90 m at most. This plate is the remaining relic of a wider plate, which was progressively disrupted by large landslides. These landslides produced large disarticulated masses, which lay on the right side of river Basento valley close to Ferrandina.

The flank of river Basento valley are strongly disturbed by deep gravitative phenomena, at local and large scale. The slopes are covered by shallow deposits, up to a few meters thick, constituted by silty sands. Along the whole side of the slope, and in particular in the higher part, it is possible to identify large blocks, made of yellowish sands and reddish conglomerates, dipped into the clay mass or as detritus. These constitute the shallow layer of the slope. The clayey over-consolidated masses on the slope are severely disturbed by tectonic and gravitative large phenomena. These affected the slope, originating fractures and dividing those masses into

blocks. These clays blocks evolved, due to gravitative phenomena. Along the flanks of the blocks, runoff generated erosion, which is particularly intense where the blocks are steep and poorly permeable. The blocks of the rocks at the top act as rainfall water tanks, which once released infiltrates the poorly cemented layers and then the fractures of the clay. This causes a water circulation, which is very high, if compared with that expected in such poorly permeable terrains.

The investigated site shows several springs, which are drained by some tunnels, located in the higher part of the slope going from the ridge between Ferrandina and Salandra town towards the river Basento. The springs are located close to Casino Rago. The investigated spring is located on a morphological jump, downstream the trench originated by an ancient landslide, constituted by a large mass of closure deposits, i.e. sands and gravels, fallen from the slope. The spring is likely originated by the infiltrated rainfall through the shallow layers of the trench and then drained by the aforementioned large permeable mass. Spring water is rich of calcium carbonate, as shown by the large number of concretions in the draining system. This abundance of carbonates is consistent with the circulation inside calcareous sands and silts and in fissured marly masses, which allow rainfall water to deteriorate the calcium carbonate within the rocks. The flow path is likely long, this is consistent with the high content of carbonates as well as the poor variability of spring discharge during the year.

**Fig. 1** Study area and track of the geological cross section

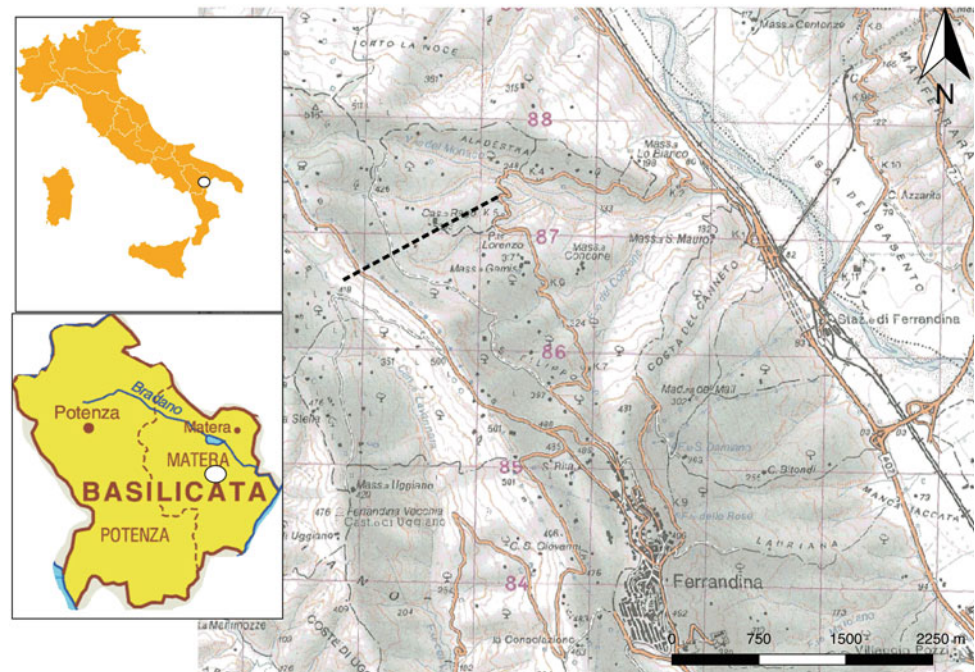
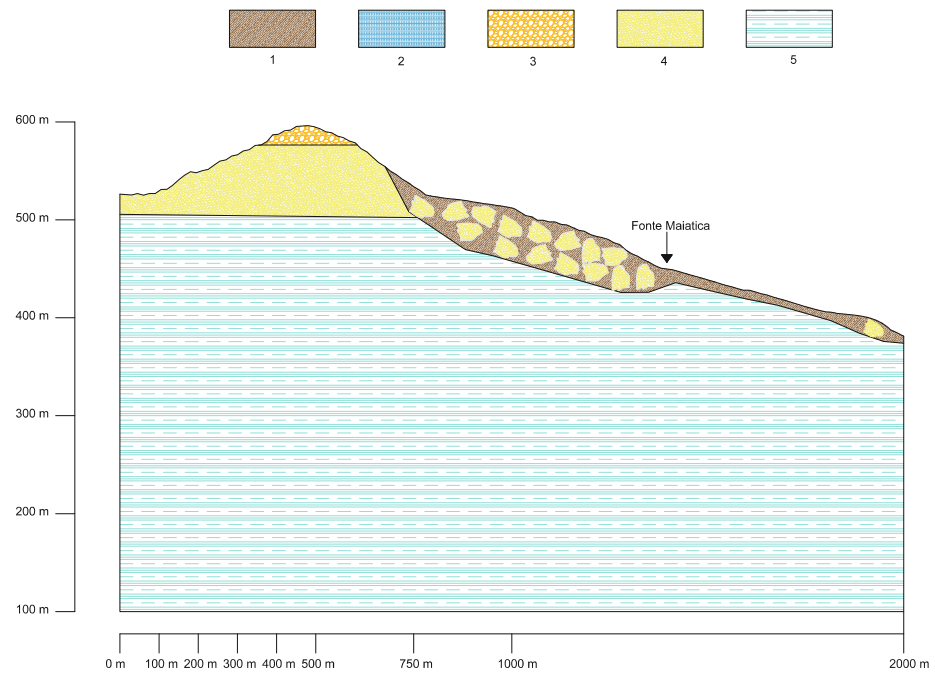




**Fig. 2** Geological cross section. 1 Colluvial debris. 2 Alluvial deposits. 3 Irsina conglomerates. 4 Monte Marano Sands and sandstone. 5 Sub-apennine clay and silty clay



### 3 The System of Draining Tunnels Near the Rago Casino

A short distance from the main building of the estate, a modern rammed earth reservoir collects water in part, by a system of draining tunnels which develops upstream of the water storage. Figure 3 shows the entrance of the tunnel and the surrounding landscape. The catchment system is accessed through a doorway from which, almost perpendicular to

each other, the two main tunnels branch out, to the directions east-west and north-south, respectively, Fig. 4.

The tunnel aligned with the entrance (A) penetrates the front side of the hill, so that the distance between the bottom of the structure and the outer surface increases as one moves away from the entrance. The other branch (B), instead, develops roughly in parallel to the contour lines, and depth remains roughly constant with respect to the ground level.

The first tunnel (A), oriented east-west, has a length of about 20 m, Fig. 3a. The path is quite regular, except for a



**Fig. 3** Entrance of the tunnel and surrounding landscape

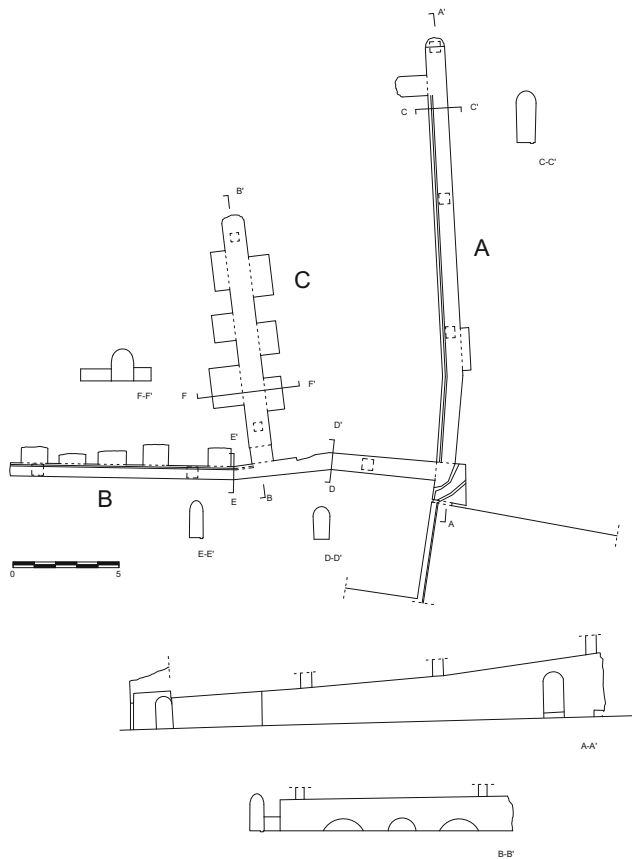


**Fig. 4** Survey of the drainage system: plan and cross sections

slight change of direction at about 4.20 m from the entrance. The cross section, except from the height, also remains roughly consistent along the route of the tunnel. The width at 1.50 m from the ground varies between 85 and approximately 105 cm, while it narrows slightly toward the floor, where the measurements are between 80 and 90 cm. This way, the section presents a slight tapering of the side walls up to springer of the vault.

The latter has a profile that varies, depending on the different proportions between the springer width and the rise, from the semi-circular arch to the pointed arch to the elliptic one. In any case, these are slight differences in geometry and the passage from one configuration to another is gradual, so that there are no points of discontinuity. The height of the structure goes from 1.35 m at the entrance to about 2.95 m on the bottom.

Along the same wall, traces of other three arches, now walled up, are visible between the recess bottom of the tunnel and the niche, while a fourth walled arch is between the niche and the mouth of the tunnel. The upstream arch is not completely closed, like the others are, and has, at the bottom, three openings from which water emerges.

At the springing line of the vault, and for all its linear development, there are symmetrical holes evidently functional to the construction of the structure.

The tunnel has three vertical ventilation shafts in communication with the outside, of which, currently, only the most upstream is open, while the others have been intentionally closed with stone slabs, Fig. 5b. The second tunnel (B), oriented north-south, has also an overall length of just over 20 m. The inner profile also in this case is rather constant over the entire length of the tunnel, Fig. 6a. The width varies from 85 cm in the final portion to about 65 cm in the upstream. The tapering towards the inside of the side walls is more evident in the end portion, where the difference between the width from the floor and from the springing line is about 10 cm. The geometry of the vault is similar to that of the first tunnel, mostly elliptical or round arch. The height of the tunnel ranges from around 1.40 at the mouth to 1.75 m upstream.

The executive aspects of this branch appear to be similar to those of the first one. In the left wall there are five arches that define as many functional niches, letting the main duct communicate with other water outcrops. As in the first tunnel, even on the floor of this one there is a draining channel, the same size of the other branch, and currently recognisable only in the innermost portion.

Here too the vault has, at the springing line, holes in sizes and shapes similar to those of the other tunnel, and three vertical shafts. On the left wall a niche gives access to a side branch (C) of the tunnel, Fig. 6b. It runs for about 11 m from east to west, with an almost parallel direction to the first tunnel. Just past the lower connecting arch, the height becomes about 1.50 m, reaching approximately 1.70 m in the inner part. The width of this third tunnel is slightly greater than the other two, and is about 1.05 m along its whole length. Here too, the vault has an elliptical or round profile and the features and executive aspects are very similar to those of the other two tunnels. Even the C branch presents niches, once again formed as small barrel vaults in bricks, opening on both the side walls. The tunnel has two vertical shafts.

#### 4 Some Considerations on Function and Evolution of the System

One of the significant characteristics of the Rago Casino catchment system appears to be the presence of lateral niches to the tunnels. From the analysis of the primary aspects, there seems to be a pretty clear coincidence in time between the building of the tunnel system and the construction of the side arches. The latter may have been made near the major

**Fig. 5** **a** The drainage system: branch A. **b** Vertical shaft in the branch A



**Fig. 6** **a** The drainage system: branch B. **b** Vertical shaft in the branch B



outflows of water, in order to create a wider area of drainage of the soil, and thus to collect greater amounts of water. The niches in the A tunnel, with the exception of those further

upstream on both walls, do not seem to be productive. Their infill can probably be put in relation to static issues that may have affected the tunnel. If the presence of lateral niches and

secondary branches can be put in relation to similar features in other systems such as the Bottini of Irsina, the niches of the Rago Casino catchment system have the peculiarity to develop in depth up to constitute, in some cases, small side rooms to the tunnels.

## 5 Draining Tunnels and Traditional Landscape in Ferrandina

The water caught by the system is no longer used for traditional forms of irrigation or for the original purpose it had during the construction of the draining tunnels. The intensification of olive cultivation on the one hand, the substantial non-use for residential purposes of farms or casini and their service facilities on the other, as well as the disappearance of the agricultural production of family type, has led to a move away of the traditional catchment systems. It so happens that many of the “cape d’acqua” in the area of Ferrandina are no longer repaired, kept efficient or cleaned of debris.

Therefore, it is important to recognise the role that structures of this kind have had in the formation of the traditional landscape, and may still have in its management. This is the only way to ensure the continuation of a

sustainable technique of water management and the transmission of the landscape values to the future.

## References

- Galeandro, A., Doglioni, A., Guerricchio, A., and Simeone, V.: Hydraulic stream network conditioning by a tectonically induced giant deep seated landslide along the front of the chain and its influence on landslide and flooding hazard. *Nat. Hazards Earth Syst Sci. EGU*. **13**, 1269–1283. <https://doi.org/10.5194/nhess-13-1269-2013>. (2013)
- Galeandro, A., Doglioni, A., and Simeone, V.: Statistical analyses of inherent variability of soil strength and effects on engineering geology design. *Bull. Eng. Geol. Environ.* **77**(2) 587–600. <https://doi.org/10.1007/s10064-016-0859-5>. (2017)
- Graziadei, A., Landscapes of water in southern Italy. Catchment tunnels, traditional knowledge and cultural landscapes. In: Semsar Yazdi, A.A., Bahri, A. (eds.) *Proceedings of Second IWA Workshop on Evolution of Qanat and Relevant Hydraulic Technologies*, pp. 199–212. Yazd, Iran, 8–10 Nov 2015
- Laureano, P.: *Atlante d’acqua: conoscenze tradizionali per la lotta alla desertificazione*. Bollati Boringhieri, Torino (2001)
- Ravelli, F., Howarth, P.J.: Etruscan cuniculi: tunnels for the collection of pure water. In: *Transactions of the Twelfth International Congress on Irrigation and Drainage*, vol. II. Fort Collins, CO, USA (1984)
- Todaro, P.: *Il sottosuolo di Palermo*. D. Flaccovio, Palermo (1988)

---

**Part IV**  
**Climate Change**

# Effects of Climatic Changes on Groundwater Availability in a Semi-arid Mediterranean Region

Angelo Doglioni and Vincenzo Simeone

## Abstract

The effects of climatic changes on rain amount and distribution during the year, together with the consequences on availability of water resources, are ongoing challenges. These problems are particularly striking in semi-arid regions, which are traditionally affected by water scarcity. The Mediterranean basin is characterized by semi-arid climate; moreover, some Mediterranean regions have high-permeability karst areas, with poor availability of shallow water. Therefore, in these regions groundwater constitutes the main autochthonous water resource. Aquifers are mostly fed by direct rainfalls, whereas these produce an effective infiltration. However one effect of climatic changes is the decreasing amounts of precipitations and the change of their distribution during the year, conditioning the amount of infiltrating water. This is due to the increasing number of high intensity rainfall events as well as to the increasing of summer precipitations. These events notoriously produce high runoff, while infiltration is quite limited. Here this issue is investigated looking at long timeseries of precipitations and piezometric data for two aquifers in south Apulia, southeast Italy.

## Keywords

Climatic change • Rainfall • Infiltration • Groundwater • Timeseries • Semi-arid • Mediterranean basin

## 1 Introduction

Climatic changes and their effects on rain precipitations is an important topic for those areas where water scarcity is endemic and shallow water resources are quite rare (Siegfried and Kinzelbach 2006). The Mediterranean basin and in particular south Italy is progressively experiencing a constant evolution on the precipitation trends, both in terms of intensity of the events and in term of rain volumes, besides in time distribution (Galeandro et al. 2015; Doglioni and Simeone 2017; Doglioni et al. 2012; Polemio and Casarano 2008). This is affecting water availability, since it is related to the recharge supplied by rain events. Apulia is a region located in south east of Italy, characterized by relatively poor precipitations, with an average total amount ranging between 300 and 800 mm per year, with a very limited presence of shallow water resources (Cristino et al. 2015; Doglioni et al. 2015b). Therefore, the main water reserve is constituted by groundwater, which is mostly stored in a large karst aquifer and by relatively small shallow porous aquifers (Doglioni and Simeone 2014, 2017). Given the importance of groundwater, these aquifers are traditionally monitored, therefore a widespread data availability, in terms of time series of data, is available, with series covering up to 60 years. Here an analysis of the effects of rain precipitations on groundwater availability is proposed both for the deep karst aquifer and the shallow porous aquifers of Apulia. It is shown how the evolution of precipitations across the last six decades affected the piezometric levels of groundwater due to the variation of rain water supply. It is also analysed the effect of the amount of precipitations on the karst and porous aquifers, whereas different lags between precipitations and groundwater levels oscillations are shown. The outcome of this analysis will show that the actual variations of rain precipitations are causing a progressive evolution towards a new scenario for groundwater availability, which ought to be necessary accounted for groundwater use.

A. Doglioni (✉) · V. Simeone  
Department of Civil, Environmental and Construction Engineering  
and Chemistry, Technical University of Bari, via E. Orabona 4,  
70125 Bari, Italy  
e-mail: angelo.doglioni@poliba.it

## 2 The Investigated Aquifers

Salento Peninsula is the Southern part of Apulia region in the extreme south-east of Italy, see Fig. 1. It is a sort of lowland, characterized by a Mesozoic calcareous and calcareous dolomitic basement that outcrop in the higher part of the peninsula. The basement is strongly fractured and karstified thus showing quite high permeability and hosting a really large coastal karst aquifer, described by Grassi and Simeone (2002) and Cotecchia et al. (2005). This aquifer is partially supplied by the northern part of the Apulian karst coastal aquifer (Murgia) and mainly by direct rainfall where the basement outcrop. The calcareous basement is diffusely covered by Paleogene, Miocene and Plio-Pleistocene sedimentary deposits of transgressive-regressive cycles that can host small porous aquifers. One of these is that one in the area of Brindisi in the northern part of Salento peninsula. It is a small porous shallow aquifer (Doglioni and Simeone 2017) hosted in the Plio-Pleistocene deposit filling the graben that separate the northern part of Apulia calcareous basement (Murgia) from the southern one (Salento). This aquifer is supplied only by direct rainfall. The deep coastal karst aquifer is investigated using groundwater level and rainfall data measured at the town of Lecce (Doglioni et al. 2015a), while the porous aquifer is investigated using rainfall data from Brindisi rain gauge station and groundwater levels measured by a phreatimetric gauge station located 6 km west of Brindisi. For both groundwater level and rain gauge stations, long and reliable time series of data ranging between 1952 and 2002 are available, see Fig. 2a, b.

Both cases are interesting because they are relatively straightforward hydrogeological systems and consisting of aquifer recharged almost only by direct rainfall and thus they serve as an ideal object for studying the relationship between groundwater level and precipitation.

Precipitation data show as Brindisi and Lecce, that are quite close to each other (their distance is about 40 km), have similar climate conditions characterized by a typical semi-arid Mediterranean climate. This is characterized every year by a single dry period and a single wet period.

## 3 Climatic Analysis and Results

The first stage of the proposed climatic analysis is the linear correlation between moving averages of rainfall heights and piezometric levels. The original timeseries are constituted by monthly data: in particular total monthly volume of rainfall and average monthly piezometric levels. The original measures, from which monthly data are implemented, are daily total rainfalls and piezometric levels measured every three days. Data are processed using moving averages of rain precipitation for the following time windows: 3, 5, 10, 20 and 30 years. Moving averages are considered both on the entire hydrological year, i.e. 1st September to 31st August, and limiting the total annual values to the winter/fall semester, i.e. October to March, which is the typical recharging period of the investigated aquifers. Here for brevity the most promising time windows are shown. In particular, these moving averages are 5 and 30 years for both the aquifers.

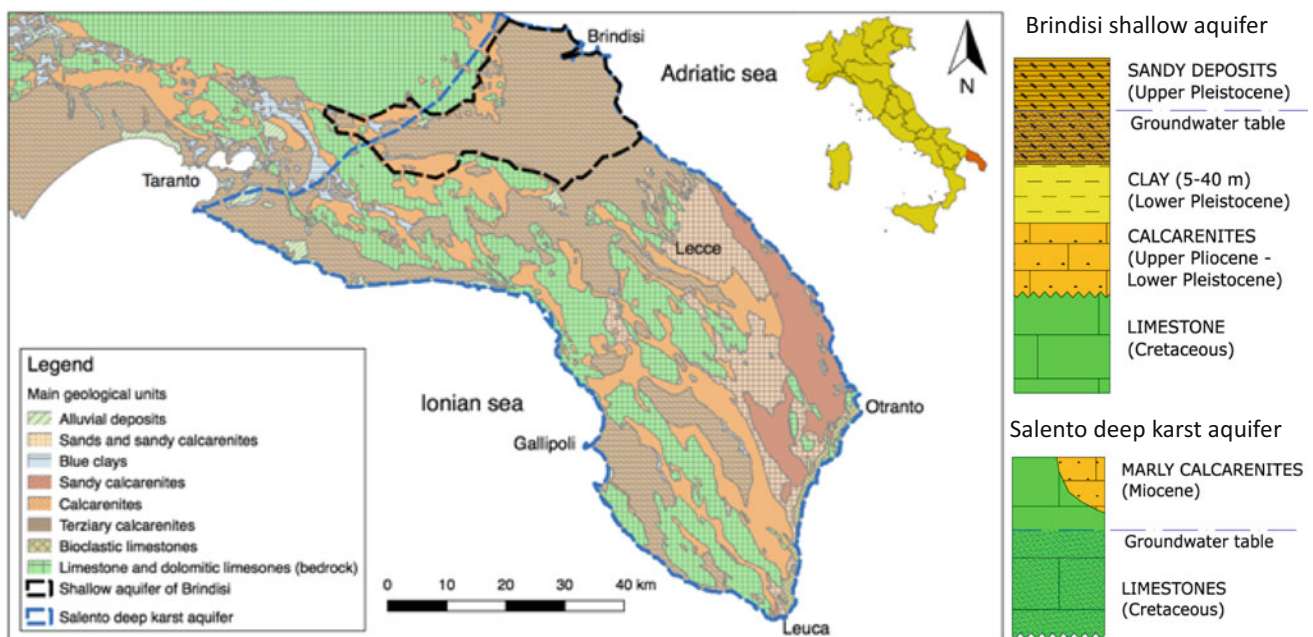


**Fig. 1** Simplified geological map of the investigated area and extension of the aquifers

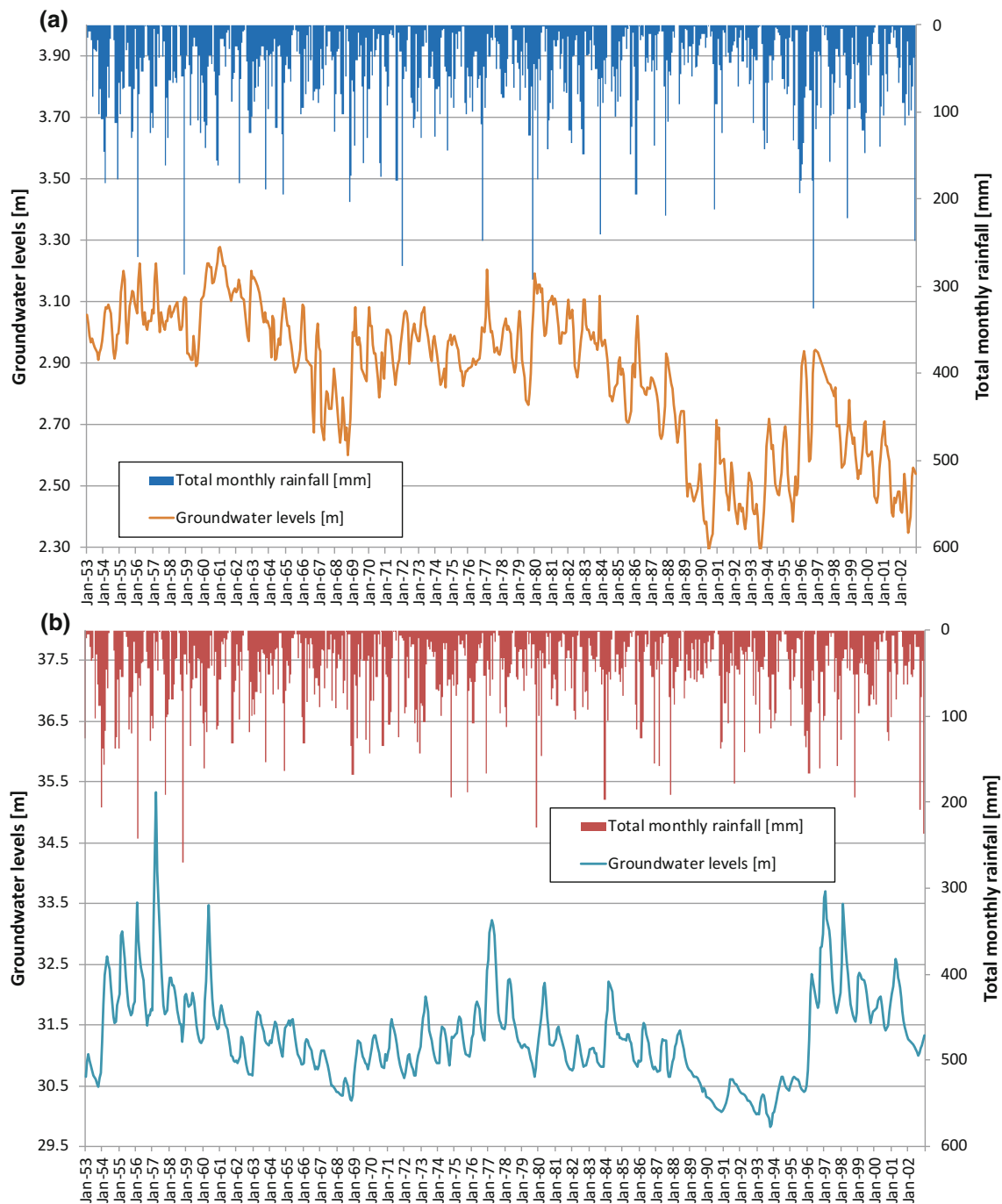


**Fig. 2** Time series of the investigated wells and raingages: **a** Salento karst aquifer; **b** Brindisi shallow aquifer

It is noteworthy that the time series of precipitations are continuously available since late 19th century, therefore even 30-years moving average is made of a number of data equal to the number of average winter levels of the aquifers.

The analyses are made on the winter/fall semester, i.e. October to March, which is the typical recharging period of the investigated aquifers. The obtained results are consistent with what expected, in particular for 30-years moving

averages, with a maximum R value equal to 0.84 for the Lecce data, i.e. large karst aquifer, consistent with the large dimensions of this aquifer. The case of Brindisi shallow porous aquifer is slightly different, since the highest R value is equal to 0.78, corresponding to 5-years moving averages, which is consistent with the limited dimensions of this aquifer. Figure 3 shows the scatter plots of these two cases.



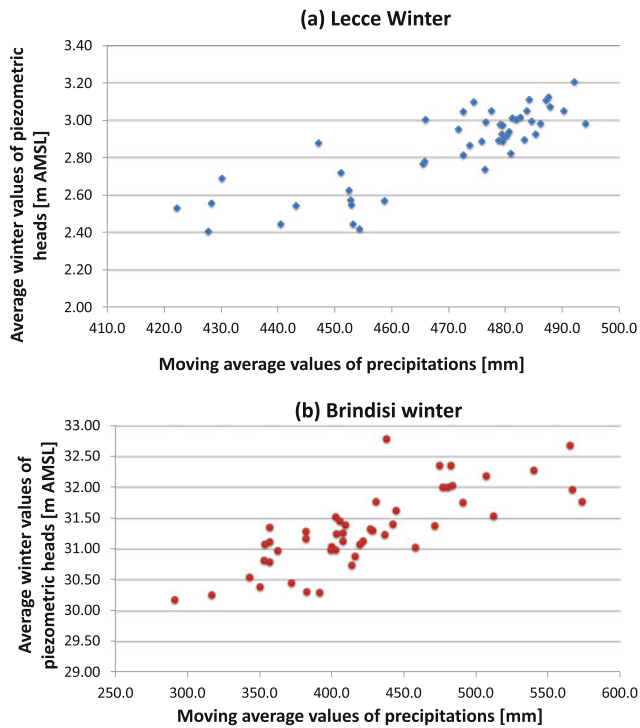
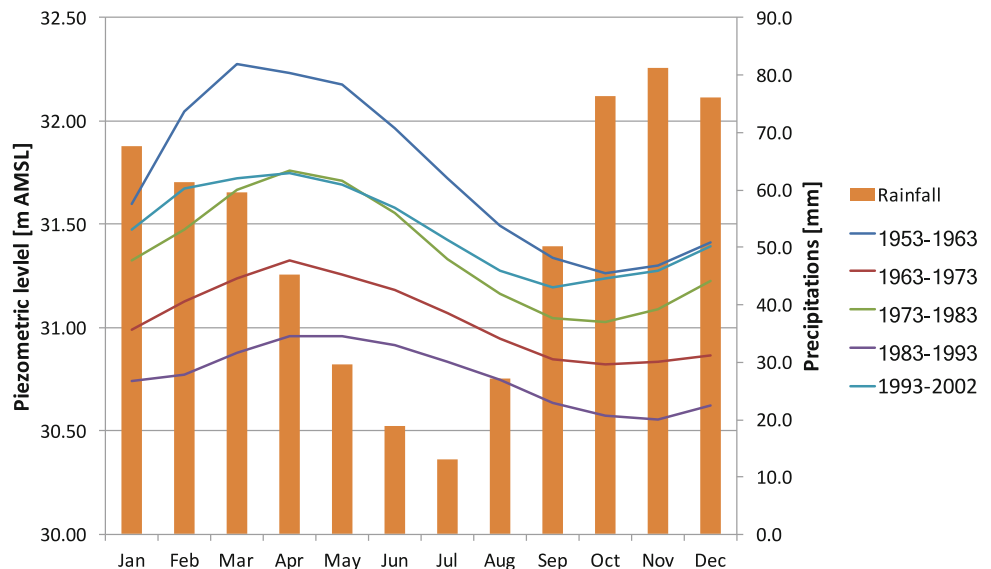


**Fig. 3** Scatter plots of 30-years moving average of Lecce data (a) and 5-years Brindisi data (b)

The next step is the subdivision of the investigated timespan of 50 years into 5 decades, where average monthly values of piezometric heads are estimated. Figure 4 shows the results of this analysis, with some interesting results. In this case, the average monthly precipitations are estimated accounting for the same timespan for which piezometric data are available.

**Fig. 4** Average monthly values of piezometric head of Brindisi shallow porous aquifer subdivided per decades

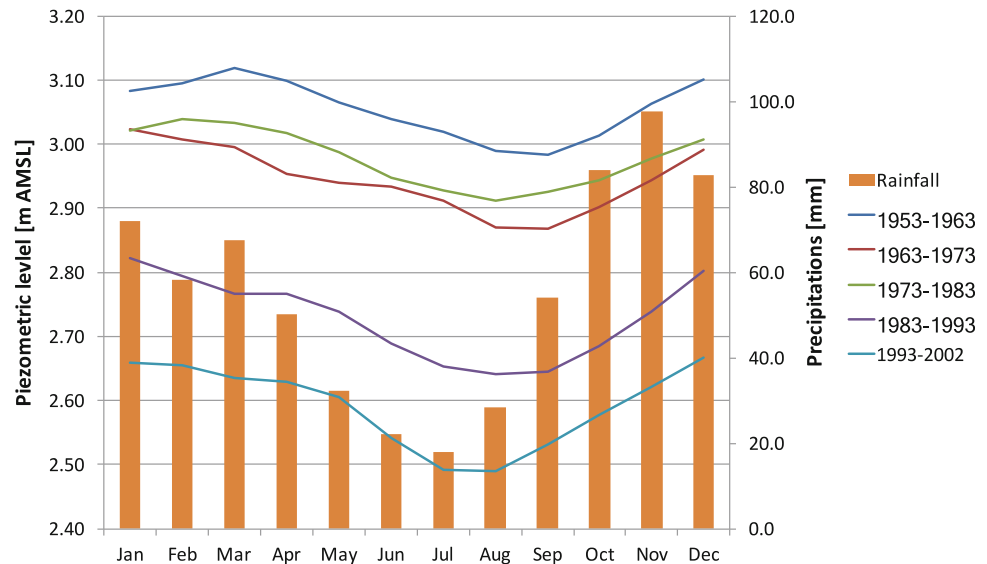


Brindisi shallow aquifer is characterized by a clear decreasing of average levels during the decades ranging between 1953 and 1993, with the annual peak of March gradually moving towards April.

After these decades, denoted by a sharp decreasing of precipitations, these progressively increased, thus causing a general increase of piezometric heads as well as the annual peak trendily moved back to March. Once again this relatively quick recover of Brindisi aquifer with the increase of precipitations is related to its small dimensions, and its relatively easy replenishment.

Figure 5 shows the same analysis on single decades for Lecce large karst aquifer. In this case the situation is different, since the negative trend of levels is not changed even by the increasing of precipitations during the latest decade of available data. This is consistent with the dimensions of the aquifer, which do not foster a quick recharge process, therefore in order to observe an increasing of levels a long positive trend of precipitations is guessed. This also emphasizes how such largely extended aquifer is particularly vulnerable to long dry periods, where the situation can be even worsened by potential increasing pumping activities. A further critical issue of this aquifer is related to its relatively low piezometric head, in fact during the period 1953–2002 the average level decreased of 50 cm on 3 m. Being this a coastal aquifer, this decreasing caused an estimated uprising of the transition zone between fresh and salt water of 15–20 m, according to the Ghyben-Herzberg theory (De Wiest 1998), with a serious risk of salt contamination. Moreover, it also noteworthy that the critical peak, in terms of drought, was between 1983 and 1993; therefore, ten years of seriously unbalanced ratio between pumping and recharge caused a damage which will not be optimistically recovered before 30 years.

**Fig. 5** Average monthly values of piezometric head of Lecce large karst aquifer subdivided per decades



## 4 Conclusions

This work presented a preliminary analysis of the impact of variations of rainfall on groundwater resources in a semi-arid Mediterranean area in south-east Italy. This analysis emphasizes how during the period ranging between 1953 and 2002 occurred first an absolute decreasing of precipitations with a peak between 1987 and 1993 and then, during the last decade, a relative increase. It is also interesting to remark that the measured increase of rainfall amount is partly due to high intensity rainfall events, typical of late summer. In this scenario, those regions like Apulia, in south-east Italy, which have almost exclusively groundwater resources are strongly penalized. In fact, on the one hand shallow and low potentiality aquifers seem to have a quite good capacity to recover when dry periods are followed by wet periods. On the other hand, the large karst aquifer, which represent the largest groundwater reservoir, is severely affected by such events, being poorly resilient to climatic changes. In fact, they are sensitive to long-term recharging, determined by multiple decades of regular or abundant winter precipitations, while high intensity events do not determine any recharge. This is the real critical effect of the climatic changes affecting the Mediterranean basin, since increasing summer temperatures, with high peak of evaporation, determine consistent effects on shallow reservoirs and on agriculture, with a massive use of groundwater. Therefore, the stress on the large aquifers makes their recharge even more difficult. This should foster a careful use of groundwater and the implementation of management policy for avoiding the qualitative and quantitative deterioration of this precious resource.

**Acknowledgements** This work was partly funded by the Apulian Regional Government as part of the project Future in Research, Data Driven models for groundwater management and the geomorphic analysis of landscape, project number 4A46U38.

## References

- Cotecchia, V., Grassi, D., Polemio, M.: Carbonate aquifers in Apulia and seawater intrusion. *G. Geol. Appl.* **1**, 219–231 (2005)
- Cristino, M.C., Doglioni, A., Simeone, V.: Notes on morphological characters of ephemeral streams in apulia region, south Italy. In: *Engineering Geology for Society and Territory—Volume 3: River Basins, Reservoir Sedimentation and Water Resources*, pp. 185–188 (2015). [https://doi.org/10.1007/978-3-319-09054-2\\_37](https://doi.org/10.1007/978-3-319-09054-2_37)
- De Wiest, R.J.M.: Ghyben-Herzberg theory. In: *Encyclopedia of Hydrology and Lakes*. Encyclopedia of Earth Science. Springer, Dordrecht (1998). [https://doi.org/10.1007/1-4020-4497-6\\_104](https://doi.org/10.1007/1-4020-4497-6_104)
- Doglioni, A., Simeone, V.: Data-driven modeling of the dynamic response of a large deep karst aquifer. *Proc. Eng.* **89**, 1254–1259 (2014). <https://doi.org/10.1016/j.proeng.2014.11.430>
- Doglioni, A., Simeone, V.: Evolutionary modeling of response of water table to precipitations. *ASCE J. Hydrol. Eng.* **22**(2), Art. no. 04016055 (2017). [https://doi.org/10.1061/\(asce\)he.1943-5584.0001465](https://doi.org/10.1061/(asce)he.1943-5584.0001465)
- Doglioni, A., Galeandro, A., Simeone, V.: Evolutionary data-driven modelling of Salento shallow aquifer response to rainfall. In: *Engineering Geology for Society and Territory—Volume 3: River Basins, Reservoir Sedimentation and Water Resources*, pp. 281–285 (2015a). [https://doi.org/10.1007/978-3-319-09054-2\\_58](https://doi.org/10.1007/978-3-319-09054-2_58)
- Doglioni, A., Galeandro, A., Simeone, V.: The generation of runoff through ephemeral streams. In: *Engineering Geology for Society and Territory—Volume 3: River Basins, Reservoir Sedimentation and Water Resources*, pp. 181–184 (2015b). [https://doi.org/10.1007/978-3-319-09054-2\\_36](https://doi.org/10.1007/978-3-319-09054-2_36)
- Doglioni, A., Simeone, V., Giustolisi, O.: The activation of ephemeral streams in karst catchments of semi-arid regions. *Catena* **99**, 54–65 (2012). <https://doi.org/10.1016/j.catena.2012.07.008>

- Galeandro, A., Doglioni, A., Simeone, V.: Success of reclamation works and effects of climatic changes in Taranto area: South Italy. In: *Engineering Geology for Society and Territory—Volume 1: Climate Change and Engineering Geology*, pp. 165–168 (2015). [https://doi.org/10.1007/978-3-319-09300-0\\_31](https://doi.org/10.1007/978-3-319-09300-0_31)
- Grassi, D., Simeone, V.: Different hydrogeological characters recognized in the same Mesozoic limestone platform of Apulia region. In: *International Groundwater Conference*. IAH International Association of Hydrogeologists, Darwin, Australia, 12–17 May 2002
- Polemio, M., Casarano, D.: Climate change, drought and groundwater availability in southern Italy. *Geol. Soc. Spec. Publ.* **288**, 39–51 (2008)
- Siegfried, T., Kinzelbach, W.: A multiobjective discrete stochastic optimisation approach to shared aquifer management: Methodology and application. *Water Resour. Res. AGU* **42**(2), W02402 (2006). <https://doi.org/10.1029/2005wr004321>

# Estimating Sustainability Benefits from Use of Blended Cements and Slag Cement at Geotechnical Projects

Josh Patterson and Charles M. Wilk

## Abstract

Portland cement, blended hydraulic cement, and slag cement are all cementitious materials used in deep soil mixing, subsurface grouting, and slurry walls. Portland cement is the “default” cementitious material used in geotechnical applications due to its known properties and history of good performance. Production of portland cement results in life cycle impacts. Blended hydraulic cement and slag cement are composed of industrial byproducts. Much of life cycle impact of these industrial byproducts has already been borne by the industries that generated them. Life Cycle Assessments are a means to quantify life cycle impacts and can be used to compare the relative life cycle impacts of one cementitious material or mix design to another. Owners, engineers and contractors can contribute to the sustainability of a geotechnical project by increasing the use of blended hydraulic cements and slag cement in geotechnical projects while attaining the project’s performance standards. Two case studies are presented that demonstrate the sustainability impacts of different cement mixtures. Sustainability contributions may competitively position a proposed geotechnical application or cementitious material mix design against less sustainable proposals.

## Keywords

Sustainability • Cement • Slag cement • Blended cement • Life cycle assessment • Geo technical

## 1 Introduction

Portland cement (PC) has historically been a “default” cementitious material used in deep soil mixing, subsurface grouting, and slurry walls. The use of PC can be expected to continue due to the proven track record and engineering acceptance in these in geotechnical applications. Sustainability is defined as the quality of not being harmful to the environment or depleting natural resources. Production of PC at cement plants uses natural resources (e.g., fossil fuels, limestone, shale, clay). PC production also results in environmental impacts such as emission of carbon dioxide (CO<sub>2</sub>) into the atmosphere.

Blended hydraulic cements (BHCs) can be interground or otherwise blended mixtures of Supplementary Cementitious Materials (SCMs) with PC. Commonly used SCMs include fly ash, ground granulated blast furnace slag (GGBFS) and limestone. Examples of industrial byproducts commonly used in geotechnical work include coal combustion residuals (CCR) (aka fly ash), and GGBFS. GGBFS is commonly known as slag cement (SC) as described by American Concrete Institute’s publication ACI 233R-03.

Much of life cycle impact of these SCMs and industrial byproducts have already been borne by the industries that generated them. There is increasing awareness to life cycle impacts and sustainability of different materials used on projects. This is evident in the application of the Leadership in Energy and Environmental Design (LEED) program. The savings in environmental impact with the use of SCMs and industrial byproducts can make proposed use of these materials in a geotechnical project more attractive in terms of sustainability.

Owners, design engineers and contractors can contribute to the sustainability of a project by increasing the use of BHCs and industrial byproducts. These lower-impact materials displace some of the PC in a mix design.

J. Patterson  
Lehigh Hanson Inc., San Ramon, CA 94583, USA  
e-mail: josh.patterson@lehighhanson.com

C. M. Wilk (✉)  
SolidStable Remediation Consulting Inc.,  
Arlington Heights, IL, USA  
e-mail: solidstable@gmail.com

## 2 Life Cycle Assessment and Environmental Product Declaration

Production of materials usually consumes natural resources and energy, and produces waste. Life Cycle Assessment (LCA) is a standardized system to quantify the environmental impacts of subject materials across the full life cycle: from raw materials acquisition through manufacturing, use and final disposition. Information developed from an LCA on a subject material is presented on an Environmental Product Declaration (EPD). The EPD provides data on environmental impacts, consumption of material resources and energy, and waste generated caused by the subject material. LCA when carefully considered, can provide a means to compare impacts between subject materials. Most product LCA's tend to be cradle-to-gate as a subject material's use cannot always be defined beyond the product's manufacturing plant gate. The methods used in LCAs and reporting on EPDs have been somewhat standardized to allow some simple comparisons. This is true of some of the

cements used in geotechnical work including deep soil mixing, subsurface grouting, and slurry walls. We researched for existing Type III EPD for materials that could be used in these geotechnical applications and found that portland cement, blended hydraulic cement and slag cement each had an industry-wide EPD. A Type III EPD means the document has third party verification and certification by an EPD program operator (in these cases by ASTM).

## 3 Comparison of Cement's Life Cycle Assessments

Owners, design engineers and contractors involved in deep soil mixing, subsurface grouting, slurry wall have an opportunity to increase the sustainability of a project by selecting cements that have lower environmental life cycle impacts.

Comparisons can be made between cements using data reported on the latest industry wide EPDs that are now

**Table 1** Sample comparison of life cycle assessment results of cements

Category indicator	Unit	Portland cement 1 metric ton	Blended hydraulic cement 1 metric ton	Slag cement 1 metric ton
Global warming potential	kg CO <sub>2</sub> eq.	1040	892	147
Acidification potential	kg SO <sub>2</sub> eq.	2.54	2.26	2.1
Eutrophication potential	kg N eq.	1.22	1.11	0.27
Smog creation potential	kg O <sub>3</sub> eq.	48.8	42.3	26.5
Ozone depletion potential	kg CFC 11 eq.	2.61E-05	2.48E-05	1.69E-05
<i>Total primary energy</i>				
Non-renewable (incl. fossil and nuclear)	MJ	5595	5071	2434
Renewable (incl. solar, wind, biomass, hydroelectric and geothermal)	MJ	292	172	76
<i>Material resources consumption</i>				
Non-renewable materials	kg	1420	1240	11
Renewable materials (incl. recovered materials)	kg	7.64	3.42	1105
Net fresh water	L	9700	9240	32
<i>Total waste generated</i>				
Non-hazardous	kg	8.99	10.5	0.3
Hazardous	kg	0.0518	0.0511	0.02

### Data sources

PC and BHC Portland cement association [www.cement.org/structures/manufacturing/environmental-impact-reporting](http://www.cement.org/structures/manufacturing/environmental-impact-reporting)

SC Slag cement association [http://www.slagcement.org/pdf/197.EPD\\_for\\_Slag\\_Cement\\_Association\\_Industry\\_Average\\_EPD\\_for\\_Slag\\_Cement.pdf](http://www.slagcement.org/pdf/197.EPD_for_Slag_Cement_Association_Industry_Average_EPD_for_Slag_Cement.pdf)

*Note about cements described in this table* Cementitious materials are produced by a great number of facilities. Available published EPDs were developed by industry-wide direct participation by many companies in the sector, but not all. Therefore, to use the data recorded on an EPD, your supplier's company would need to be listed as participating in the industry-wide developed EPD. This is to ensure that the EPD is relevant to your project. PC is described as common general use (GU) portland cement. BHCs vary based on producers. The BHC data this table is for an "industry average" BHC. These blended cements meet the ASTM C595 which include Type IP (fly ash or pozzolan), IS (slag), IT (ternary) and IL (portland limestone cement) being produced in the USA. The SC is ground granulated blast furnace slag (GGBFS)

*Caution note* Care must be taken when deciding to compare the results of material's EPDs that are made according to different Product Category Rules (PCR) to ensure the boundaries are somewhat similar as to what is included or is not included in the LCA for the product you are reviewing

publicly available. The cements compared on Table 1 include:

- Portland Cement
- Blended Hydraulic Cement
- Slag Cement.

Table 1 illustrates that the environmental impacts decrease with the use of SCMs and industrial byproducts. Greater use of SCMs and/or industrial byproducts in cements increases the sustainability of a project.

## 4 Sustainability Strategies

### 4.1 Comparing Life Cycle Impacts

Owners, design engineers and contractors involved in deep soil mixing, subsurface grouting, slurry walls may use the LCA data to position a proposed geotechnical application and/or mix design as a more sustainable alternative.

It is necessary to know the proportion of materials used in mix designs to quantify the contributions to sustainability of an alternate mix design. Supplemental cementitious materials or industrial byproducts are rarely used to completely replace PC in a mix design. Typically, SCMs and industrial byproducts replace a portion of PC in a design. Cement producers make this “replacement” when they produce BHCs. A geotechnical contractor can make this “replacement” by combining materials from separate silos at project

site. Example storing and blending PC and SC at a project site. Two or more EPDs could be used when a geotechnical contractor combines material at the project site. The percent proportions of the material and reported EPD data would be used in a calculation for project site-combined mixes.

The most sustainable mix design could be generally determined by comparing the LCA of the different cementitious material components and their proportions in one complete mix to another complete mix. Obviously, the most sustainable mix design would still be required to meet the project’s performance specifications. Enhanced sustainability may also be accomplished by performance optimization with the use of GGBFS or SC leading to a reduction of the total cementitious materials needed to meet project specifications. The cementitious combination or performance optimization along with costs and material availability would continue to be considerations in developing the final mix design.

As described in Table 2, environmental life cycle impacts of BHC and SC are significantly lower than PC. Industrial byproducts are “raw materials” in the production of BHC and SC. This recovery or reuse of industrial byproducts generates significantly less environmental impacts and consumes significantly less energy and non-renewable materials compared to production of PC. For example, production of BHC generates 86% and SC generates 14%, of the amount of CO<sub>2</sub> generated by a like amount of PC. Since the production of SC is principally the processing of the industrial byproduct GGBFC, the production of SC recovers 145 times more renewable material compared to PC.

**Table 2** Sample environmental impacts of BHC and SC compared to PC

Category indicator	Portland cement	Blended hydraulic cement	Slag cement
Global warming potential	1	0.86	0.14
Acidification potential	1	0.89	0.83
Eutrophication potential	1	0.91	0.22
Smog creation potential	1	0.87	0.54
Ozone depletion potential	1	0.95	0.65
<i>Total primary energy</i>			
Non-renewable and renewable energy	1	0.89	0.43
<i>Material resources consumption</i>			
Non-renewable materials	1	0.87	0.008
Renewable materials (incl. recovered materials)	1	3.42	145
Net fresh water	1	0.95	0.003
<i>Total waste generated</i>			
Non-hazardous	1	1.17	0.03
Hazardous	1	0.99	0.38

## 4.2 Relationship to LEED

There is increasing awareness to LCA and sustainability of different materials used on projects. This is evident in the application of the Leadership in Energy and Environmental Design (LEED) program devised by the U.S. Green Building Council. For projects enrolled in the LEED program, points toward a higher-level LEED certification are awarded when more transparency on sustainable materials and technologies are used. For example, a LEED point is awarded when an enrolled project building is constructed on a former contaminated industrial property or brownfield (High Priority Sites). Use of deep soil mixing to solidify and stabilize the hazardous contaminants in soil or use of a slurry wall to prevent groundwater contamination may facilitate the use of the brownfield. The High Priority Sites in the Location and Transportation (LT) credit category is worth up to 2 points. A design engineer or contractor proposing these geotechnical applications with materials that have an industry-wide EPD can also help the project obtain points in the new Materials and Resources (MR) credit category within LEEDv4. Before proposing this advantage to the project be sure to read if your suppliers were involved with the slag or cement industry work on the EPD published. Another way that owners, engineers and contractors can help contribute to a project's LEED rating, may be in the Sustainable Sites (SS) credit. Using soil mixing, grouting, or slurry walls to improve ground conditions and assist a chosen building site development to be able to accommodate greater density (below ground parking, etc.) and preserve more natural land area.

**Table 3** Sample approximate life cycle savings when using 4940 metric tons of 90/10 SC/PC compared to using 4940 metric tons of PC

Category indicator	LCA savings/benefits use of 4940 metric tons of 90/10 blend SC/PC compared to 4940 metric tons of PC
Global warming potential	Emitted 3970 fewer metric tons of CO <sub>2</sub> equivalents
Total primary energy	Consumed 15 million fewer megajoules of energy
Non-renewal materials	Consumed 6260 fewer metric tons of non-renewable materials
Renewable material use incl. recovered materials	Reused/recovered 4880 metric tons more material
Fresh water	Consumed 43 million fewer liters of fresh water

**Table 4** Sample approximate life cycle savings when using 767 metric tons of 85/15 SC/PC compared to using 767 metric tons of PC

Category indicator	LCA savings/benefits by use of 767 metric tons of 85/15 blend SC/PC compared to 767 metric tons of PC
Global warming potential	Emitted 581 fewer metric tons of CO <sub>2</sub> equivalents
Total primary energy	Consumed 2.2 million fewer megajoules of energy
Non-renewal materials	Consumed 920 fewer metric tons of non-renewable materials
Renewable material use incl. recovered materials	Reused/recovered 715 metric tons more material
Fresh water	Consumed 6.3 million fewer liters of fresh water

## 5 Example Projects: Estimating Sustainability Benefits by Using SC to Replace a like Amount of PC

### 5.1 San Antonio Backup Pipeline Sunol Valley, CA

A pipeline contractor used a cement and bentonite clay slurry as backfill for a portion of the San Antonio Backup Pipeline project in Sunol Valley, CA. during 2013. The cement portion of the slurry mixture was a blend of 90% SC and 10% PC. The total amount of SC used was approximately 4450 metric tons, with a calculated total of SC and PC used as 4940 metric tons.

Using the LCA data in Table 1, approximate life cycle impacts can be calculated when using 4940 metric tons of a 90/10 blend of SC/PC compared to PC (Table 3).

### 5.2 Deep Soil Mixing Port of Los Angeles Berth 142

Deep soil mixing was used to improve the bearing capacity of soil at Berth 142 of the Port of Los Angeles during 2014. In situ soil mixing used 767 metric tons of cementitious material. The cementitious mixture was 85% SC and 15% PC.

Using the LCA data in Table 1, approximate life cycle impacts can be calculated when using 767 metric tons of an 85/15 blend of SC/PC compared to PC (Table 4).

## 6 Conclusions

Owners, engineers, and contractors involved in geotechnical work can contribute to a sustainable built environment by selecting cements with the lowest environmental impacts. Some portion of PC in mix designs may be replaced by SCMs and/or industrial byproducts. Much of life cycle impacts of these SCMs and industrial byproducts have already been borne by the industries that generated these materials.

Results of an LCA for cements are reported on an EPD. The relative environmental impact or sustainability of a cementitious material may be compared by using the EPDs of the materials with similar product category rules [PCR].

The impact to sustainability of a project by the selection of cementitious material can be substantial as depicted by our estimates of the completed projects described. Project design engineers and contractors may be able to use their more sustainable solution to position their geotechnical application and/or mix design against competing proposals.

## Bibliography

- ACI Committee 233: Slag Cement in Concrete and Mortar. ACI 233R-03. American Concrete Institute, Farmington Hills, Michigan, USA (2003)
- Blended Cements—Environmental Product Declaration: Portland Cement Association, p. 11. Skokie, Illinois, USA (2016)
- Brownfield Remediation (n.d.): U.S. Green Building Council, <http://www.usgbc.org/credits/neighborhood-development-plan-neighborhood-development/v4-draft/slc2?view=resources>. 12 May 2017
- Concrete's Contribution to LEED v4, Concrete Sustainability Report: National Ready Mixed Concrete Association, p. 8. Silver Spring, Maryland, USA (2014)
- Kosmatka, S.H., Wilson M.L.: Design and Control of Concrete Mixtures. EB01, 16th edn., p. 632. Portland Cement Association, Skokie, Illinois, USA (2016)
- Portland Cement-Environmental Product Declaration: Portland Cement Association, p. 11. Skokie, Illinois, USA (2016)
- Slag Cement-Environmental Product Declaration, p. 16. ASTM International, West Conshohocken, Pennsylvania, USA (2015)



---

## Author Index

### A

AbramsonWard, Hans, [33](#)

### B

Briggs, Stephanie, [33](#)

### C

Cox, Justin, [33](#)

### D

Dean, Jennifer, [33](#)  
Demenev, Artem D., [3](#), [41](#)  
Dippenaar, Matthys A., [83](#)  
Doglioni, Angelo, [105](#)  
Dussell, Bryan, [33](#)

### E

Ellecosta, Peter, [57](#)

### F

Fiedler, M. F. M., [9](#), [17](#)

### G

Galitskaya, Irina, [75](#)  
Graziadei, Antonio, [97](#)

### H

Hattori, Shuichi, [89](#)  
Huebner, Matthew, [33](#)

### J

Jones, Brendon R., [83](#)

### K

Kajiyama, Atsushi, [25](#)  
Käsling, Heiko, [57](#)  
Khmurchik, Vadim T., [3](#), [41](#)

Kikuchi, Yoshihiro, [89](#)

Kostikova, Irina, [75](#)

Kozuma, Mutsuo, [25](#)

### M

Maksimovich, Nikolay G., [3](#), [41](#)  
Mironov, Oleg, [75](#)  
Moeck, Inga S., [67](#)  
Mraz, Elena, [67](#)

### N

Nakaya, Masashi, [49](#)  
Nichols, Holly, [33](#)

### O

Ohta, Takehiro, [89](#)

### P

Patterson, Josh, [111](#)  
Pozdnyakova, Irina, [75](#)

### S

Sedinin, Alexey M., [3](#), [41](#)  
Shimofusa, Dai, [89](#)  
Simeone, Vincenzo, [97](#), [105](#)  
Siqueira, A. G., [9](#), [17](#)  
Sousa, L. A. P., [9](#)

### T

Thuro, Kurosch, [57](#), [67](#)  
Toms, Leonid, [75](#)  
Tsuruta, Ryosuke, [49](#)

### U

Utsuki, Shinji, [49](#)

### V

Van Rooy, J. Louis, [83](#)

von Dessonneck, Brad, [33](#)

**W**

Wakizaka, Yasuhiko, [25](#)

Watatani, Hiroyuki, [25](#)

Wilhite, Coralie, [33](#)

Wilk, Charles M., [111](#)

Wolfgramm, Markus, [67](#)

**Y**

Yassuda, E. A., [9](#), [17](#)

**Z**

Zumbro, Justin, [33](#)